AB_2O_6 OXIDES: POTENTIAL THERMOELECTRIC AND MAGNETIC MATERIALS

Ebénézer Tetsi

Thesis submitted in accordance with the requirements of the University of Liverpool for the degree of Doctor of Philosophy

December 2017

Declaration

This thesis is submitted by the undersigned for examination for the degree Doctor of Philosophy at the University of Liverpool. It has not been submitted as an exercise for a degree at any other University or other degree-giving institution.

This thesis, apart from the advice, assistance and joint effort mentioned in the acknowledgements, is entirely my own work.

Ebénézer Tetsi

Abstract

AB_2O_6 oxides: potential thermoelectric and magnetic materials

Ebénézer Tetsi

The search for environmentally friendly and more sustainable energy sources is an ever-growing global concern. It is mainly due to global warming associated with fossil fuel sources which threatens our eco-system and ultimately our existence. Among the viable technologies for renewable energy, thermoelectric (TE) modules are of increasing interest because these solid-state devices can harness the waste heat given off from sources such as power production, factories, motor vehicles or computers into electricity using the Seebeck effect. However, because of their low efficiency the state-of-the-art TE materials (Bi_2Te_3, Sb_2Te_3, PbTe) have found limited commercial application. In addition, most of the best TE materials are non-stable at high temperature. Due to to their abundance, low cost and minimal environmental impact oxide materials attract increasing interest for the replacement of the standard TE materials. Besides, the spin degrees of freedom exhibited by some oxides lead to unique and fascinating properties which can be tuned for other applications.

AB_2O_6 oxides are interesting materials to study, due to the wide range of compositions and crystal structures. The investigation of the structural-property relationship in these systems may lead to high temperature thermoelectric applications. This said, some AB_2O_6 exhibit exotic magnetic features whose understanding raises questions regarding some fundamental physics. The thesis is organised in two parts. The first part discusses the thermoelectric properties of two AB_2O_6 oxides whereas the magnetic structures of other AB_2O_6 compounds are investigated in the second part. In this thesis there is the report, for the first time, of the temperature dependence of the thermopower of Y-doped $CdSb_2O_6$ and WV_2O_6. The negative sign of the Seebeck coefficient of these two materials indicates their n-type character. The temperature dependence of their electrical conductivity data reveal that these compounds behave as semiconductors. Henceforward Y-doped $CdSb_2O_6$ and WV_2O_6 are *n*-type semiconductor materials. Their power factors are comparable to that of some established TE materials such as $Cu_{0.98}Ni_{0.02}Nd_2O_4$. Analysis of the thermal conductivity of tungsten divanadate oxide demonstrates that the lattice contribution dominates the electronic contribution. Furthermore, there is the report of the ordering of Ni^{2+} ions within the magnetic lattices of $NiTa_2O_6$ and $NiNb_2O_6$. For the columbite $NiNb_2O_6$ a new model is proposed for its magnetic structure. Two propagation vectors are needed to describe the antiferromagnetic ordering below the Néel temperature. The 2-$\vec{k}$ sublattice magnetisation is characterised by non collinear magnetic moments. Eventually, in this thesis there is the determination of a new magnetic structure of $NiTa_2O_6$. As previously never done before for this antiferromagnetic compound, both a Shubnikov group and a magnetic structure are attributed to the ordering of the magnetic moments within its magnetic lattice. The study on the trirutile $NiTa_2O_6$ also illuminates the discrepancies between the novel model and the previous two models for its sublattice magnetisation.

"The truth is that as a man's real power grows and his knowledge widens, ever the way he can follow grows narrower: until at last he chooses nothing but does only and wholly what he must do."

Ursula K. Le Guin, A Wizard of Earthsea

Acknowledgements

I am very grateful to those who contributed in anyway to my doctorate in physics at the University of Liverpool.

Firstly, I would like to express my sincere thanks to my primary supervisor **Dr. Jonathan Alaria** for giving me the opportunity to do the PhD; and also for giving me the freedom and help to work on some exciting projects. Your expertise in a various fields (diffraction, magnetism, thin films and so forth) is remarkable! I would also like to thank **Dr Vin Dhanak** my secondary supervisor for constantly checking up on my progress and for the fruitful discussions over the four years. A gratitude goes out to the EPRSC and the University of Liverpool for providing the funding for my work.

During the my PhD I have had the opportunity to work with people who are experts in their fields: I acknowledge and thank **Dr. Florence Porcher** and **Dr. Françoise Damay** who are knowledgeable and passionate scientists at the Laboratoire Léon Brillouin in Saclay (France). They both helped me to perform neutron diffraction on my nickel-based powders with the 3T2 and G4.1 diffractometers, respectively. I still remember Florence (an amazing crystallographer) staying up late to fix the neutrons counting system of a diffractometer, for which she was not even responsible!

I would like to thank **Dr. Eric Don** for helping me with and installing the MMR instrument for the measurement of the Seebeck coefficient. Thank your prompt responses via emails and on the phone. There is still a mystery regarding the system as I have not been able to reach 80K with a better pressure than the one required stated in the manual .

I am grateful to **Dr. John Claridge** and **Dr. Matthew Dyer**. John, thank you for helping me understand concepts on neutron diffraction, magnetic structures and crystallography. Matthew, thank you for calculating the electronic structure and density of states of WV_2O_6.

I am thankful to **Dr. Hongjun Niu** and **Dr. Stanislav Savvin** for their effort, time and patience. Stan, thank you for your help regarding the measurement and the fitting of the thermal conductivity of WV_2O_6. Hongjun, a passionate scientist,I would like to thank you for being reliable and training me on various equipment.

I am indebted to **Dr. Václav Petříček** - a fantastic crystallographer - who helped me during the proceedings of the powder neutron diffraction data. I was and still am inspired by your expertise, passion and enthusiasm on magnetic structures. Thank you for clarifying some concepts of group theory, crystallography and magnetic structures. I would also like to thank you as you introduced me to **Pr. Harold T. Stokes**, **Pr. Branton J. Campbell** and **Pr. Manuel J. Perez-Mato** who are among the best when it comes to crystallography and magnetic structures. Of the many fond memories I particularly enjoyed a Saturday afternoon's skype in which you used your hands and head, together, to talk about a two-$\vec{k}$ magnetic structure!!! I hope Jana is more stable and is compatible full time with ISODISTORT.

I would also like to acknowledge some terrific people I have met at the Stephenson Institute for

Renewable Energy. The place with great facilities where the majority of my research took place. I am grateful to **Vincent Vasey** and **Keith Williams** for your help, efforts and time regarding some laboratory setups. You are the modern Leonardo Da Vincis. But also thanks for introducing me to the British culture and the scouse's lifestyle. Keith, I still remember your glittering eyes when I gave you the little bicycle. Thank you for introducing me to the following legends: **Kevin McCormick**, **George Sim**, **Daniel Hollywood**, **Paul Sinclair**, **Ozzy Mapar** and **Mark Whitley**. Vince, a man with great heart, I absolutely love your sense of humour. Of the many funny memories I particularly remember your joke about France not having cable ties because I didn't know that "serre-cables" are called cable ties in English!!

And also to **Jonathan Lee** and **Graeme O'Dowd** for their help and support. It was great sharing the Lab 5 with you during the last four years. Graeme, thank you for expertise regarding microscopy (SEM images and energy-dispersive x-rays analysis) and also proofreading some of my thesis. It was great fun sealing tubes with you. Jon (The Big Jon), you are a rock. Thanks to you the team now works in an environment which respects the safety regulations. I am indebted to you for introducing me to Buckfast and for your fantasy football tips!!

A special mention must be made to **Phil Benzie** and **Anne T. Coleman** for proofreading this thesis. I would like to thank you for your time, effort and patience. I apologise for destroying the English language. Kota, I am sorry for spreading the commas like droplets of rain. I loved the following side comments you wrote: the cat's mother and dumbo. Thanks to **Dawn McCullough** and **Wellington Franca** who introduced you to me. Thanks to Phili, a wonderful organist, for making me discover "In Our Time" and explore the country side of Wales. Of our many terrific discussions I particularly enjoyed when we stated all the stations between Chester and Bangor: Fflint, Prestatyn, Rhyl,... .

I extremely grateful to **Dr Jianli Zou** and **Dr Max Birkett**. You are both my mentors and friends. Max, an expert in optical properites of semiconductors, I am indebted for your constant help throughout the PhD regarding reports, CV, emails, Matlab, thesis, proofreading and many more. I'm sorry to have so often taken some of your time when you were about to leave. It was a pleasure discussing about physics, philosophy and the British culture. I still remember our discussion about existentialism and humanism!! Jianli, a battery expert, I am indebted to you for urging me to work hard. Your advice, support and wisdom were very important as they gave the strength to continue. I miss our philosophical conversations about the East and West, the concept of work, the spiritual and so forth. I hope I will see your masterpieces in a gallery someday. The highlight that stands out about our relationship has to be the book of Ursula K. Le Guin entitled A Wizard of Earthsea. The world needs more remarkable people like you two.

I would like to thank everyone in the Stephenson and espacially the following persons: Pr. Ken Durose, Pr. Ronan McGrath, Dr. Jonathan Major, Dr. Gilberto Teobaldi, Dr. Jamie Walsh, Dr. Nick Drewett, Dr. Laura Cabo-Fernandez, Dr. Gary Harlow, Dr. Elizabeth Cocklin, Dr. Iain Aldous, Dr. Gaia Neri, Dr. Arturas Adomkevicius, Dr. Henry Wu, Dr. Mark Forster, Filipe Nogueira Braga, Michael Graham, Thomas Galloway, Petar Radjenovic, Giorgos Papageorgiou, Marios Michailidis, Nikolas Antonatos, Thomas Whittles, Peter Yates, Joshua Fogg, Tom Baines, Jack Swallow,

Jessica Stoner, Scott Lewis, Lisa Rhodes-Martin and the brilliant Silvia Mariotti.
I also remain thankful to my friend **Christopher G. Sole**. Chris, being your housemate for three years and a half was a wonderful experience. Thank you for your constant patience, support and advice. I am also grateful to you for encouraging me to work hard. Thank you for easing my way into the British's lifestyle. I'll miss our long philosophical discussions, trips to Woolton for the bagpipe's lessons with **Filipe** (top lad) and the pipers: **Bernard Prendergast**, **Lawrence McClemens** and **David Anwyl**; I will also miss your compositions on your keyboard and of course your delicious Lasagna. Thank you for advising me to go to the beautiful city of Cordoba!! One of my favorite memories was a discussion at about 2 a.m on the Monty Hall's problem. Although you explained it over and over I wouldn't agree with the solution we both had a look at the wikipedia page.

Finally, I am ever grateful to my family for their invaluable love. I am thankful to you for having filled my life with happiness and for instilling some values of *la joie de vivre* in me. Thank you for being there and supporting me ... always!!!

Contents

Chapter 1

Introduction

Electricity is the most common and convenient form of energy in today's world society and economy. Many household appliances, industrial processes and communication devices rely on electricity, causing our society to be highly dependent on electricity. World population continues to rise year after year, with global population expected to exceed 10 billion by 2050 [1,2,3]. This population growth will lead to an increased demand on energy dependent services by a factor of 2-2.5 [2].

During the past two decades fossil fuels have provided most our energy requirements. The use of this energy source is threatening our eco-system and, ultimately, the existence of mankind. Some of the main environmental issues are the deterioration of the stratospheric ozone, water pollution and the global climate change. For instance, the use of fossil fuels in transportation of freight using aeroplanes (kerosene), shippings (diesel) and heavy goods vehicles (diesel) is directly related to the emission of pollutants. Among these toxic substances is CO_2: a harmful greenhouse gas which contributes to the depletion of the stratosphere. With population growth and its resultant pressure of increased demands for energy along with rising concerns about climate change there is a desire in the research community and general population to find new ways to produce clean, cheap and environmentally friendly energy.

In almost half of all the industrial processes more than half of the energy inputed into the process is turned into waste heat [4,5]. This holds true from a home kitchen kettle to manufacturing processes and industrial power production. Automobiles fueled with gasoline only utilise about 25 % of the initial input energy for vehicle mobility and accessories; the remainder is lost in the form of waste heat in the exhaust and coolant, as well as friction and parasitic losses [6]. One way of producing clean energy consists of capturing and re-utilizing the waste heat via a device in order to produce electricity. These devices are based on the principles of thermoelectricity, where there is direct conversion of heat into electricity. A phenomenon called the Seebeck effect [7,8], creates a voltage over a temperature gradient causing electricity to flow. The reverse effect, for which a material generates a temperature gradient when subjected to a difference of potential is also possible, this is called the Peltier effect [8,9,10]. The production of electric power via a thermoelectric (TE) module is a process

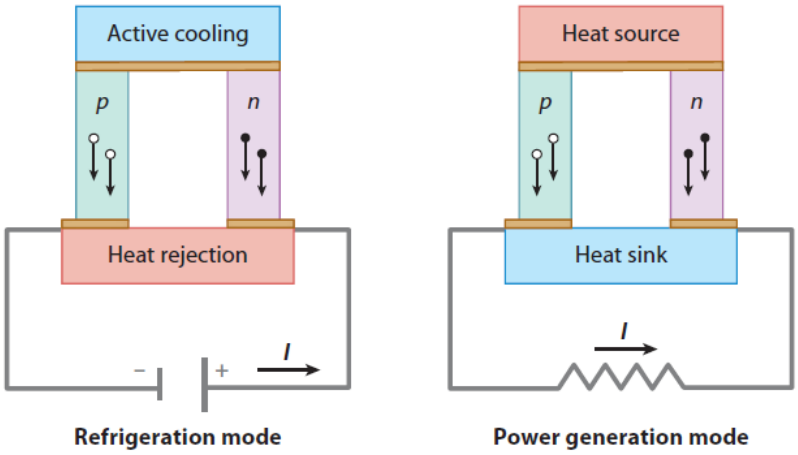

Figure 1.1: Typical thermoelectric modules. The module illustrates the Peltier effect, whereas the Seebeck effect is represented by the module on the right. Red denotes hotter temperatures, and blue denotes colder temperatures. Both modules are made of p- and n-type semiconductors. The latter are represented by green and magenta legs, respectively. They are linked-up by substrates, typically metallic pads [11].

without moving parts nor greenhouse gas emissions.

TE devices for power generation are also known as thermoelectric generators (TEGs) and those for cooling are called Peltier devices, see Figure 1.1. In practice a TE module is made of multiple pairs of n-type and p-type semiconductor legs connected to each other through metallic pads. In n-type semiconductors the majority of carriers are electrons, whereas holes are the majority of carriers in a p-type semiconductor. In order to minimise electrical resistance losses p-type and n-type arrays are put electrically in series and thermally in parallel; this configuration increases the operating voltage and reduces the electrical current of the system.

In order to determine the ability of a material at converting a temperature difference into electricity one evaluates its figure of merit ZT. This dimensionless physical quantity is given by the following formula:

$$ZT = \frac{\alpha^2 \sigma T}{\kappa} = \frac{\alpha^2 T}{\rho \kappa}, \tag{1.1}$$

where σ is the electrical conductivity, ρ is the electrical resistivity, α is the Seebeck coefficient and T is the mean operating temperature. The thermal conductivity κ of material is a physical quantity which measures how a material conducts the heat. The motion of free-carriers throughout the lattice and coherent lattice vibrations (phonons) are both responsible for the heat conduction in a solid. Hence, κ can be described by the equation (1.2):

$$\kappa = \kappa_e + \kappa_l. \tag{1.2}$$

The first term on the right hand side of equation (1.2) κ_e is the electronic contribution of the thermal conductivity. The lattice contribution is represented by κ_l. One can rewrite equation (1.1)

as:

$$ZT = \frac{\alpha^2 \sigma T}{\kappa_e + \kappa_l}. \tag{1.3}$$

A figure of merit, of about 1, $ZT \approx 1$, is the standard performance for a TE material in the thermoelectrics community. Bi_2Te_3 and PbTe [11,12,13] have a figure of merit, of about 1 at room temperature.

Thermodynamics defines the efficiency of a device as being the ratio between the net power output and the power input within the system. For instance, an TEG operating within two temperatures T_H and T_C has the following efficiency:

$$\eta = \frac{Q_H - Q_C}{Q_H}. \tag{1.4}$$

The efficiency of a TE module is the power input to the load (W) over the net heat flow rate (Q_H). From the figure of merit of a TE module the efficiency can then deduced as

$$\eta = \frac{W}{Q_H} = \frac{T_H - T_C}{T_H}\left(\frac{\sqrt{1 + ZT_M} - 1}{\sqrt{1 + ZT_M} + \frac{T_C}{T_H}}\right). \tag{1.5}$$

T_H and T_C correspond to the temperatures at the hot and the cold side of the TE module, respectively. Thus T_H has a higher value than that of T_C in both equation (1.4) and equation (1.5). Q_H represents the heat flow from the source to the sink and therefore is positive. T_M is equal to $\frac{T_C + T_H}{2}$. For instance, let us consider T_C as room temperature (300 K) and a $ZT = 1$. As a consequence, η corresponds to 5% conversion efficiency at $T_H = 400$ K and almost 15% conversion efficiency at $T_H = 900$ K. It demonstrates that stability at high operation temperature, is equally important as high ZT values of the thermoelectric materials to achieve greater heat to electricity conversion efficiency, as seen in Figure 1.2 on page 5.

Furthermore, according to equation (1.1) a good thermoelectric material must have a large thermopower or Seebeck coefficient, a high electrical conductivity and a low thermal conductivity. Indeed a high value of σ minimises the ohmic losses and facilitates the flow of electric current from one end of the material to the other one. In order to maintain the temperature gradient a low κ is required. One of the challenges within thermoelectric research is that κ, σ and S are all dependent of the carrier concentration of the free-carriers, as seen Figure 1.3 on the next page.

Figure 1.3 illustrates the difficulty of identifying materials with good thermoelectric properties, as improvements in one physical property (electrical conductivity) often results in drawbacks in another property (Seebeck coefficient). For example, metals - materials characterised by zero bandgap - have by far the highest electrical conductivity but small thermopower values [14,15,16]. On the contrary thermal insulators - materials characterised by a large bandgap - exhibit the lowest thermal conductivity and high Seebeck coefficients but are also electrical insulators [14,15,16]. It is due to the fact that both σ and κ_e are governed by the electron's behavior. σ and κ_e are tied through the Wiedemann-Franz

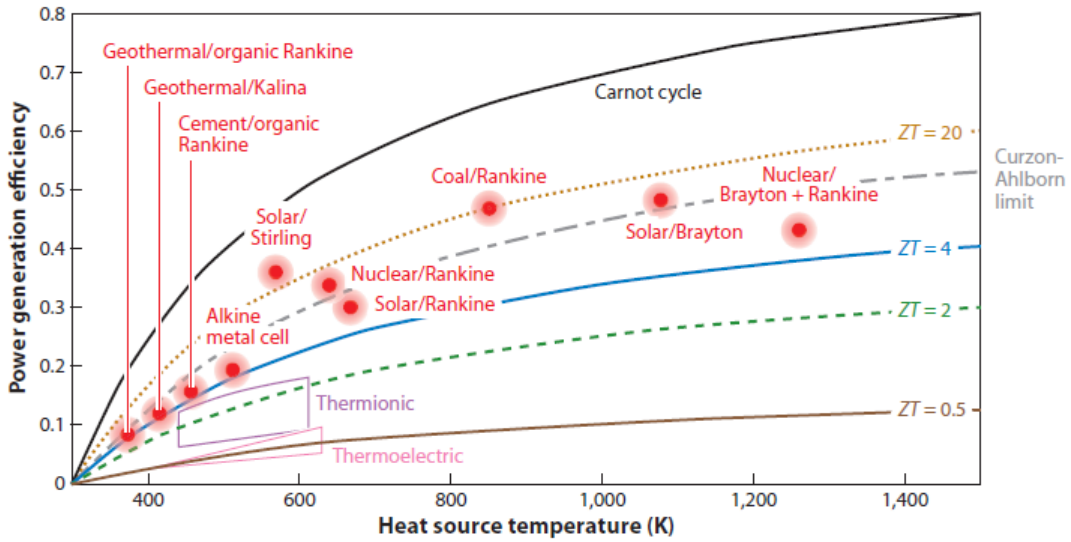

Figure 1.2: Thermoelectric power generation efficiency versus T_H. Comparison of Carnot efficiency η of various sources of energy[13]. The temperature of the cold side T_C is 300 K.

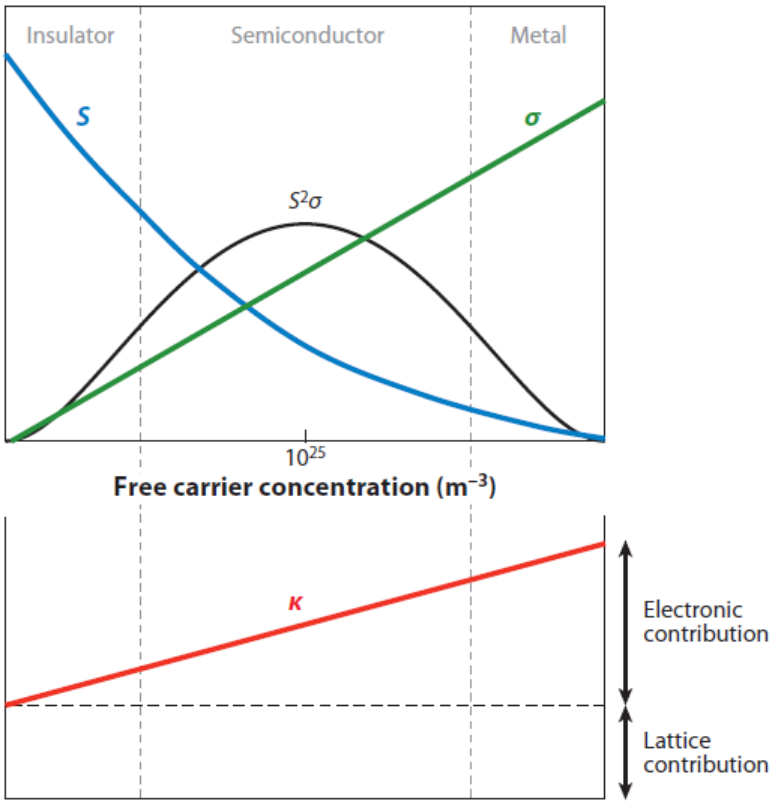

Figure 1.3: Comparison of the thermoelectric properties of insulators, semiconductors and metals. Seebeck coefficient, electrical conductivity and thermal conductivity behavior are mapped as function of the free-carrier concentration[13].

law which states that the ratio between κ_e and σ is constant at a given temperature, T, according to the following relation:

$$\frac{\kappa_e}{\sigma} = (\frac{\pi^2 k_B^2}{3e^2})T. \tag{1.6}$$

The constant on the right hand side of equation (1.6) corresponds to the Lorentz number (L). L is equal to $2.48 \times 10^{-8}\,\mathrm{V^2\,K^{-2}}$ for metals and is usually taken as $L = 2.0 \times 10^{-8}\,\mathrm{V^2\,K^{-2}}$ for degenerate semiconductors. Therefore materials in which thermal conductivity is dominated by lattice phonon contribution are more promising for thermoelectric application, since the phonon thermal conductivity can be decreased without affecting the electrical conductivity.

The curves in Figure 1.3 indicate that semiconductors are the most promising materials for the use in thermoelectric applications. In most semiconductors the major contribution to the thermal conduction comes from κ_l (phonons). As a consequence κ can be reduced without causing too great of a reduction of the electrical conductivity. In the 1950s tremendous amounts of work (experimental and theoretical) was conducted in order to identify semiconducting materials with a high ZT. For instance, the work of Ioffe[17] exposed that heavily doped semiconductors made the best TE modules, due their high free-carriers concentration. Elsewhere Mahan and Sofo[18] derived the thermopower, the electrical and thermal conductivities, as integrals of the transport distribution. These investigations and other studies have lead to the establishment of guidelines on materials suitable for TEGs. The criteria for the determination of potential TE materials are the following criteria:

- The first criterion focuses on the free-carriers concentration. Semiconductors with a carrier concentration $n \approx 10^{18} - 10^{20}\,\mathrm{cm^{-3}}$ are good candidate materials for thermoelectric power generation applications. As illustrated in Figure 1.3, these materials possess the optimal electrical conductivity and Seebeck coefficient to achieve a high power factor PF.

$$PF = \alpha^2.\sigma = \frac{\alpha^2}{\rho} \tag{1.7}$$

- Materials with good figure of merit are those for which the band gap Δ is of the order 10 $k_B T_o$ (the operating temperature of the thermoelectric material).
- Materials with high symmetry crystal structure (high band-degeneracy) and with small electronegativity difference among the constituent elements are good TEs. The aim is to minimise the scattering of charge carriers by optical phonons.
- Low thermal conductivity κ_l is often found in materials made up of heavy elements and/or with many atoms per unit cell. The scattering of phonons by heavy elements leads to a deterioration of the thermal conductivity of these materials. The same applies for structures made up of many atoms per unit cell.

The bipolar effect

The bipolar effect occurs in semiconductors in which both electrons and holes, have similar concentration and mobility, and then can both participate to the electric conduction. This is typically the case of wide-gap semiconductors at elevated temperatures or narrow-gap semiconductors at ordinary temperatures.

When a *n*-type semiconductor is subjected to an electric field and temperature gradient, the current density for electrons, i_n [7,11], is given by:

$$i_n = \sigma_n(\frac{dV}{dx} - \alpha_n \frac{dT}{dx}), \tag{1.8}$$

where σ_n and α_n represent the electric conduction and the thermopower associated to electrons. Similarly for a *p*-type semiconductor one has the following equation

$$i_p = \sigma_p(\frac{dV}{dx} - \alpha_p \frac{dT}{dx}). \tag{1.9}$$

One can then derive the respective Seebeck coefficient of the system:

$$\alpha = -\frac{dV}{dT} = -\frac{dV}{dx}.\frac{dx}{dT}. \tag{1.10}$$

In order to evaluate $\frac{dV}{dx}$ one sets up the temperature gradient to be equal to zero. Hence, combining equation (1.8) and equation (1.9) leads to:

$$i_n + i_p = \sigma_n \frac{dV}{dx} + \sigma_p \frac{dV}{dx} \tag{1.11}$$

$$= \frac{dV}{dx}(\sigma_n + \sigma_p). \tag{1.12}$$

Therefore, the electric field is given by:

$$\frac{dV}{dx} = \frac{i_n + i_p}{\sigma_n + \sigma_p}. \tag{1.13}$$

Inserting this relation into equation (1.11) gives

$$\alpha = \frac{i_n \frac{dx}{dT} + i_p \frac{dx}{dT}}{\sigma_n + \sigma_p}. \tag{1.14}$$

The thermopower of the system can then be rewritten as

$$\alpha = \frac{\alpha_n \sigma_n + \alpha_p \sigma_p}{\sigma_n + \sigma_p}. \tag{1.15}$$

Equation (1.15) demonstrates that the thermopower of the material is a weighted average of the Seebeck coefficients associated with the two types of carrier [7]. The carrier concentration of electrons

and holes are in the same order of magnitude in an intrinsic narrow semiconductor at ordinary temperatures or wide bandgap semiconductor at high temperatures. The Seebeck coefficient values for the two types of carriers are of opposite signs (+ or -). As a consequence one has $\alpha \to 0$. In order to avoid a deterioration of the thermopower in such materials, because of the bipolar effect, one typically dopes these materials with either donor or acceptor states. The doping then allows extrinsic conduction of the appropriate carrier type, electrons or holes, respectively [11]. The overall aim is to have either a predominantly *n*- or a predominantly *p*-type semiconductor material with an optimal Seebeck coefficient. A large direct band gap - typically on the order of10 $k_B T_o$ - is recommended to minimise the minority carrier contributions to the Seebeck coefficient. T_o is the operating temperature of the material [11].

1.1 State-of-the-art thermoelectric materials

Following the above guidelines, the search for the state-of-the-art TE materials was directed towards degenerate semiconductors and alloys materials. These materials, with covalently bonded characters (for high mobility) and with high-symmetry crystal structures (for low mobility), contain one or more of the following heavy elements: Bi, Pb, Te, or Sb. Gaultois, Seshadri *et al.* [19] created a large database of thermoelectric materials, by abstracting information from over 100 publications.This data mining has over 18 000 data points from multiple classes of compounds, whose relevant TE properties have been measured at several temperatures. One can then gain certain insights on a studied sample, by comparing its TE properties with that of the best materials in the database. The current best *n*- and *p*-type TE materials are for instance Bi_2Te_3, Sb_2Te_3, Bi_2Se_3, PbTe and SiGe. The temperature dependence of their figure of merit is displayed in Figure 1.4, found in the next page. *n*-type TE materials are exposed in the top diagram in Figure 14. The figure of merit (ZT), of bismuth telluride [20,21,22], is ≈ 1 at room temperature up to 200 °C. SiGe is by far the best *n*-type material for high temperature thermoelectric applications, as its $ZT \sim 1$ at temperatures between 800 and 1000 °C.

The bottom diagram in Figure 1.4 on the next page illustrates the figure of merit of the best *p*-type materials. At room temperature, in place of Bi_2Te_3 is antimony telluride Sb_2Te_3, whose ZT approximates 1 at 25 °C. The appropriate *p*-type material for a high-temperature TEG is $Yb_{14}MnSb_{11}$, because its figure of merit is about 1 around 1000 °C. TAGS refers to $(GeTe)_{0.85}$ $(AgSbTe)_{0.15}$. The standard TEGs (Bi_2Te_3, Sb_2Te_3, TAGS, etc) have an efficiency between 5 and 8 %. The best TE modules are used in various waste heat recovery applications, which are classified in the following five categories [23]:

- Electricity generation in extreme environments. In this instance thermoelectric devices are used in the space industry as radioisotope generators (RTG) [23]. The cold end is the vacuum, whereas the heat originates from the natural radioactive decay of a plutonium 238. The RTGs are made of PbTe, PbSnTe and TAGS [23].
- Decentralised domestic power in combined heat and power generation systems [23]. The aim is to produce electricity by installing TE modules (mostly Bi_2Te_3) on domestic ovens [24,25].

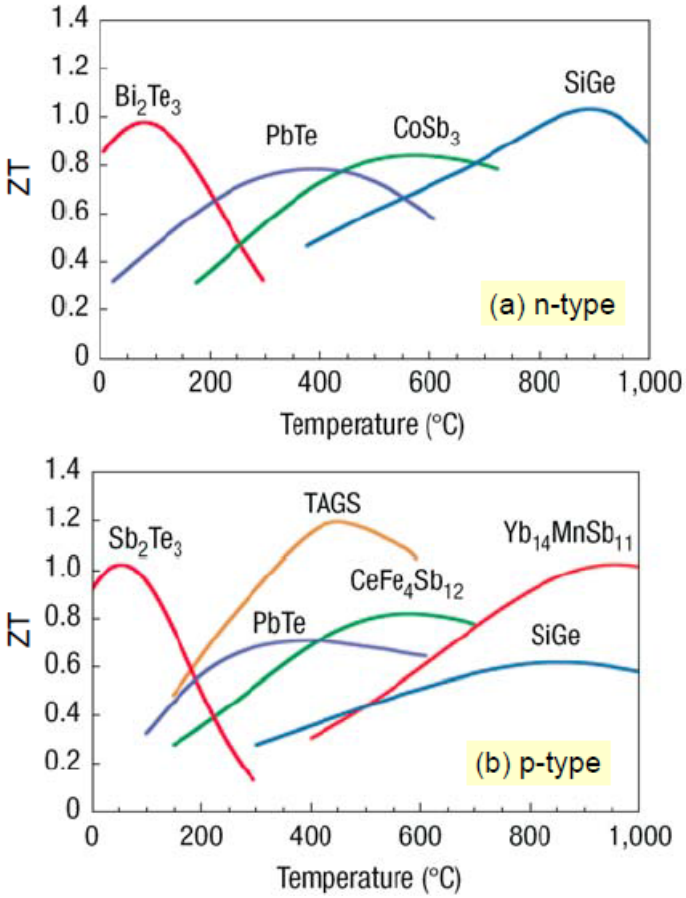

Figure 1.4: Figure of merit of some of the state-of-the-art thermoelectric materials as function of the operating temperature. The latter corresponds to the temperature of the hot side of a TE module[14].

- Micro-generation for sensors, microelectronics. TEGs are utilised to power micro-instruments (sensors, micro-controllers, etc). For this type of applications the heat source can be ovens, motors, hot fluid pipes, etc.
- Solar thermoelectric generator (solar TEG)[26,27]. The heat source is the sun. A TEG is installed on the rear side of photovoltaic panel to collect the waste heat in order to produce electricity. The idea is to increase the efficiency of the combined solar/thermoelectric system to convert the solar radiation into electricity.
- Power generation in the automotive sector. TEGs (Bi_2Te_3, PbTe) are typically installed on a vehicle to capture the waste heat and convert it into electricity.

1.2 Thermoelectric oxides

This section provides a review on the use of oxides for thermoelectric purposes. First there is a discussion on the main issues related to the state-of-the-art TE materials, which is then followed by a review of the thermeoelectric properties of some of TE oxide materials.

1.2.1 Merits of TE oxides

Some of the key-elements in the high-ZT materials are not abundant[28] in the Earth's crust. This is typically the case of tellurium (Te), which has an abundance of 0.001 ppm by weight. Te is by far the most commonly used element in TEGs. The abundance of antimony (Sb) and germanium (Ge) are 0.2 ppm and 1.4 ppm, respectively. One of the factors to take into account regarding a material's usage for technology is its price, especially when it comes to large-scale production. There has been a comparison between the crustal abundance and the price for most elements by many economic geologists[29].

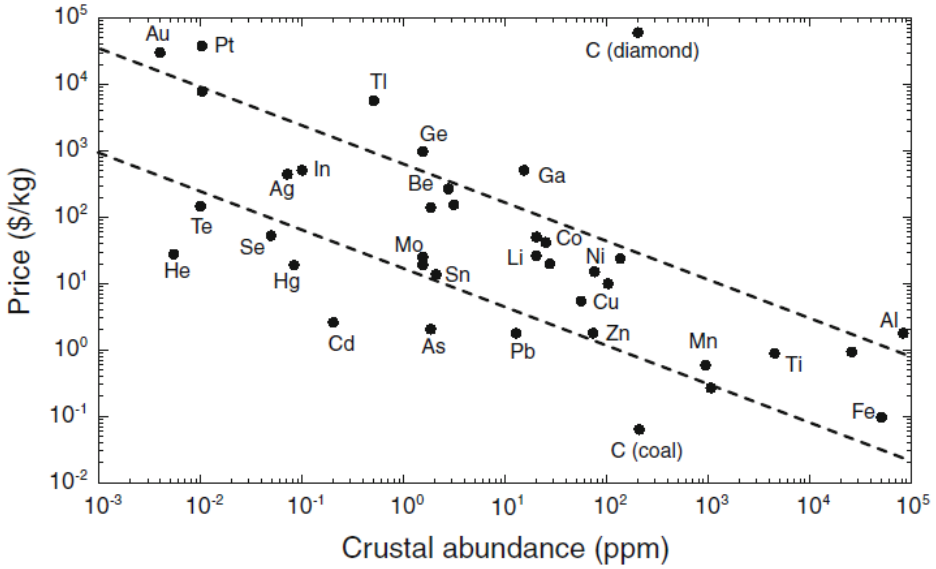

Figure 1.5: Price versus crustal abundance of some elements[28].

The x- and y-axes in Figure 1.5 above, correspond to the crustal abundance and the respective

price in dollar(s) per kilogram of an element, respectively. The diagram in Figure 1.5 reveals that the rarer the elements become, the more expensive they are. It is evidenced by key-elements of the state-of-the-art TE materials, as their abundance is low (10×10^{-2} ppm) and their prices are among the highest (few hundreds American dollars (US dollars) per kilogram). However, elements such as Fe and Al are among the most abundant elements (10×10^{3} ppm) in the Earth's crust. Their respective prize per kilogram is very economical only of few US dollars per kilogram.

In addition to being scarce, some of the key-elements of the best TE materials are toxic. For example, lead (Pb) is a toxic and harmful element which can damage the brain through seizure and can lead to coma. Figure 1.6 below compares the environmental impact of the best TE materials with other materials. Complex materials involving lead and antimony such as PbTe, Bi_2Te_3, (Bi, Sb), Zn_4Sb_3 are among the most toxic. Figure 1.6 highlights the need of finding TE oxides (or environmentally friendly) materials for thermoelectric applications.

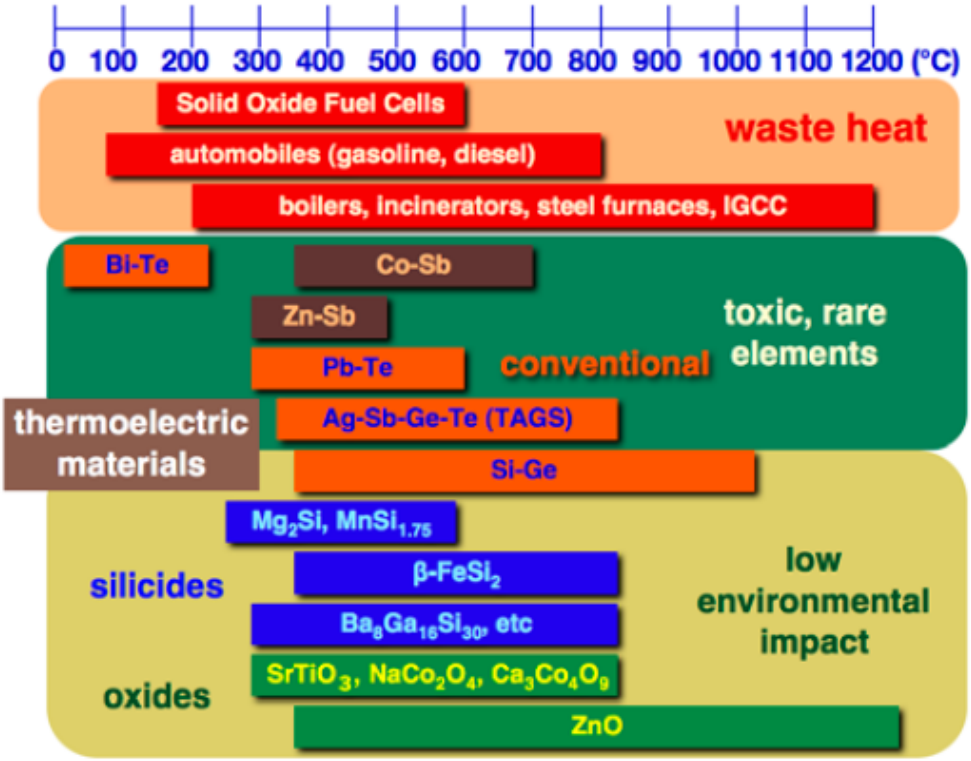

Figure 1.6: Schematic comparison of various TE materials in terms of the temperature range of operation and environmental friendliness of constituent elements. [16].

Additionally, the operating temperatures of Bi_2Te_3 and PbTe are 300 K and temperatures around 700 K, respectively. It is in agreement with Figure 1.4, which shows the figure of merit of the best TE materials. The figure of merit of both bismuth and lead telluride decreases as temperature increases. It should be noted that both bismuth and antimony telluride melt at 853 and 893 K and are therefore not suitable for high-temperature applications. In order to convert the waste heat from furnaces and manufacturing processes, materials such as $Bi_2Sr_2Co_2O_7$, $SrTiO_3$, ZnO or $CaMnO_3$ are more appropriate. Because they are stable at high temperature. These materials belong to the

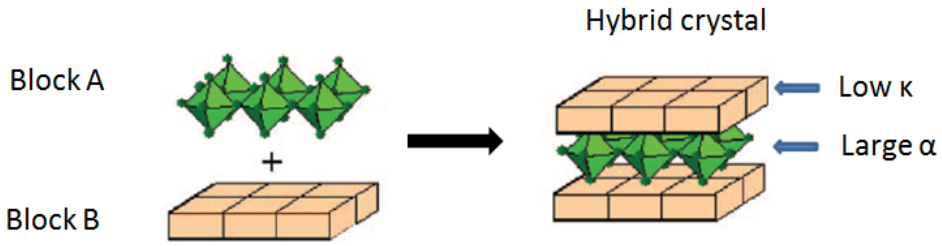

Figure 1.7: Schematic representation of hybrid crystal structure.[30]

class of materials known as the oxides.

The inability and instability of the state-of-the-art TE materials at operating at high temperatures, as well as the scarcity and toxicity of some of their key-elements, lead the thermoelectric community to search for new classes of materials abundant, environmentally friendly and stable at high temperature.

Among these new TE materials are the oxides. As oxides are abundant, non-toxic, low cost and minimal in environmental impact along their stability at high temperature indicates that they can be used to recuperate the waste heat energy for power generation, with high efficiency.

1.2.2 Review of some thermoelectric oxides

Thermoelectric oxides are ionic compounds consisting of cations and oxygen anions, alternately placed with the Coulomb interaction between them[16]. The cation can either be an alkaline (Na, Li, Ca, Ba), a transition metal (Fe, Co, Ni, Mn, Zn) or a lanthanide (Eu). This diversity of elements, thus structures, is another aspect favouring the use of oxides for TE applications. The TE properties of some of the best TE oxides are discussed below. These materials are some layered cobaltites, perovskites and a wurzite.

The layered cobaltites

Koumoto *et al.*[30] developed the concept of hybrid structure. Hybrid structured materials consist of alternated blocks with different compositions and symmetries. Each block has a specific thermoelectric function (Seebeck, electrical and thermal conductivities). Consequently, the TE properties of hybrid structured materials are decoupled and can individually be tuned to attain greatest ZT. Figure 1.7 illustrates the hybrid structured crystal of new functional oxides.

The crystal lattice in Figure 1.7 consists of blocks A and B, alternately stacked along a direction. Blocks A and B are made up of different elements (green octahedra and bricks, respectively) and their symmetry are different. On one hand, the transport of phonons (κ) can be hindered by the blocks B. On the other hand, the diffusion of the free carriers in the block A may lead to large values of the thermopower (α). Combining these two TE properties (κ and α) may give rise to high TE

performance. The system A+B is a hybrid crystal. The layered cobaltite family is an example of hybrid structured crystals. The TE properties of some the best layered cobaltites are discussed below.

a) $Na_{0.5}CoO_2$

The seminal work of Terasaki, Sasago and Uchinokura[31] on the large thermopower of $Na_{0.5}CoO_2$ single crystals, brought the attention of the thermoelectric community onto the use of oxide materials as thermoelectric materials.$Na_{0.5}CoO_2$ crystallises in an hexagonal lattice, which is associated with the symmetry space group $P6_3/mmc$ (194). Figure 1.8 on the next page depicts the 3D-view of the crystal structure of $Na_{0.5}CoO_2$.

Figure 1.8 (a) illustrates the layered structure of sodium cobalt oxide, as the Na and CoO_2 layers are alternately stacked along the *c*-axis. In the crystal structure each cobalt is surrounded by six oxygen atoms forming edge-sharing CoO_6 octahedra. $Na_{0.5}CoO_2$ is often regarded as a 2D material due to the 2D layers of CoO_2. This material exhibits a large in-plane thermopower (about $100\,\mu V\,K^{-1}$) and a low in-plane electrical resistivity ($200\,\mu\Omega\,cm$), at room temperature. The positive sign of the Seebeck coefficient of sodium cobalt oxide indicates that the majority of free-carries are holes. In other words $Na_{0.5}CoO_2$ can be regarded as a *p*-type material. This large in-plane thermopower coupled with a low in-plane resistivity suggests that $Na_{0.5}CoO_2$ is a potential thermoelectric material.

Numerous studies on $Na_{0.5}CoO_2$ demonstrate that the large thermopower is due to spin, charge and orbital degeneracy of the cobalt cations[32,33]. The crystal lattice found in Figure 1.8 (a) plays a major role in the understanding of the unexpected low TE properties of $Na_{0.5}CoO_2$. The in-plane-resistivity is much lower than that of the out-of-plane resistivity. Consequently, the electric conduction in $Na_{0.5}CoO_2$ is mainly due to the in-plane electrical conductivity. This conduction of electrons occurs in the *a*-*b* plane in the CoO_2 sheets (layers). The electrons are strongly correlated in the CoO_2 layers and are hardly affected by Na layers. As a result, $Na_{0.5}CoO_2$ exhibits a high electrical conductivity in the *a*-*b* plane. The thermal conductivity of $Na_{0.5}CoO_2$ was also investigated and was found to be low in comparison to that of traditional oxides. This low value of the thermal conductivity is explained by the scattering of phonons due to Na^+ ions. These sodium ions are distributed between the cobalt layers. Interfaces between CoO_2 layers and sodium also contribute to a reduction of κ. Mikio Ito[34] reported a $ZT = 0.7$ - 0.8 for polycrystalline $Na_{0.5}CoO_2$. $Na_{0.5}CoO_2$ is therefore a hybrid crytsal, as the CoO_2 and the Na layers mainly control the thermal and electrical conductivities, respectively.

b) $Ca_2Co_2O_5$

Another *p*-type TE oxide with outstanding thermoelectric properties is $Ca_2Co_2O_5$. It belongs to the family of calcium cobalt oxides, with the formula $[Ca_2CoO_3]_yCoO_2$. These materials are often designated by Ca-uvw, where u, v and w are integers and correspond to the indices of Co, Ca and O, respectively. For instance, Ca-349 refers to $Ca_3Co_4O_9$. $Ca_2Co_2O_5$ possesses a layered structure

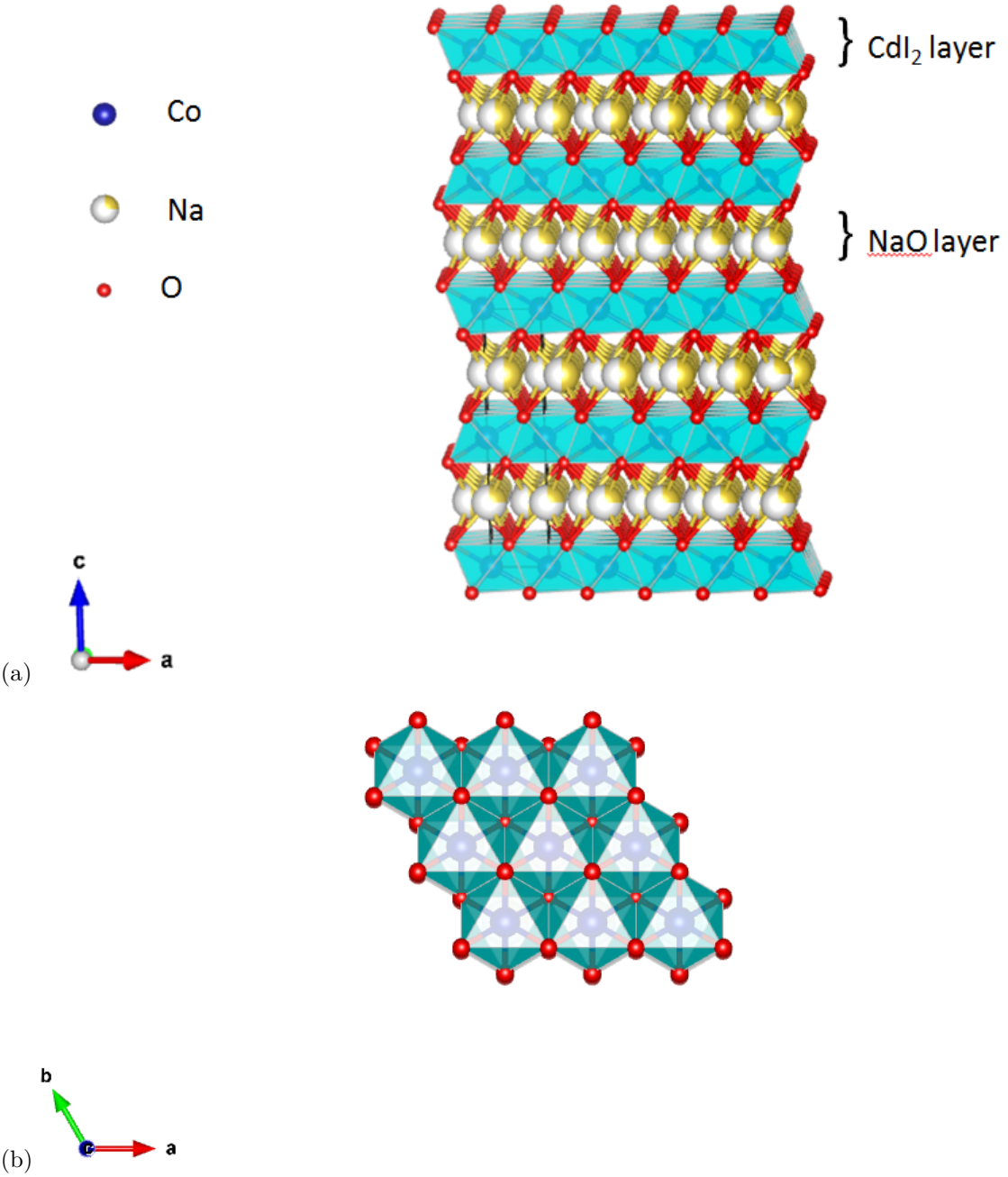

Figure 1.8: Crystal structure of the unit cell of $NaCo_2O_4$.The blue (yellow) spheres represent the Na^+ (Co^{2+})-cation; the anions, the oxygens, are represented by the red spheres. (a) Alternated layers of CoO_2 and Na along the *c*-axis. (b) 2D triangle of CoO_2 within the *a*-*b* plane.

similar to that of $Na_{0.5}CoO_2$[35]. In this superlattice, there are $CaCoO_3$ layers alternating with layers of CoO_2 along the [0 1 0] direction, as seen in Figure 1.9 below.

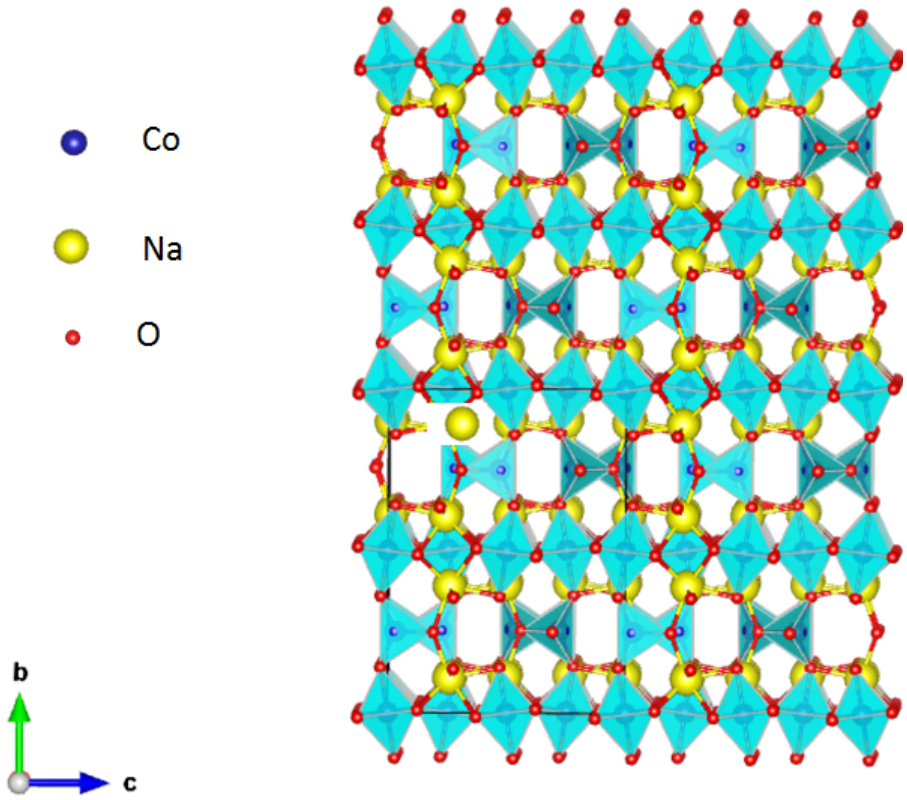

Figure 1.9: The crystal lattice of the hybrid $Ca_2Co_2O_5$, also called Ca-225.

In Figure 1.9, the yellow, blue and red spheres represent the calcium (Ca), cobalt (Co) and oxygen (O) atoms, respectively. It should be noted that Co is surrounded by six O, together they form CoO_6 octahedra as illustrated in Figure 1.9. Like in $Na_{0.5}CoO_2$, the octahedra form CoO_2 layers. These CoO_2 layers are separated by $CaCoO_3$ layers along the *b*-axis. $CaCoO_3$ layers are double rock-salt blocks made up of Ca, Co and O. Funahashi *et al.*[35] reported a thermopower of $210\,\mu V\,K^{-1}$ at 1000 K. The positive sign of the Seebeck coefficient indicates the *p*-type character of this material: the majority of carriers responsible for its electric conduction are holes. Additionally, the electrical resistivity study shows that this material behaves like a semiconductor because ρ decreases with increasing temperature. The CoO_2 crystalline sheet structures contribute to a high electrical conductivity of $714.3\,S\,cm^{-1}$ at 963 K. κ values for this material are less than $1.0\,W\,m^{-1}\,K^{-2}$ for temperatures between 473 K an 873 K. According to Funahashi *et al.*[35], the thermal conductivity is suppressed by phonon scattering at the interface between the two types of CoO_2 layers[35]. Eventually the figure of merit ZT of Co-225 whiskers is estimated to vary from 1.2 to 2.7 for temperatures above 873 K[35]. These values are greater than that of standard TE materials such as $Yb_{14}MnSb_{11}$, whose $ZT \sim 1$ at 1000 K.

c) $Bi_2Sr_2Co_2Oy$

$Bi_2Sr_2Co_2Oy$ is another layered cobaltate exhibiting low electrical resistivity and large Seebeck

coefficient for power generation applications at high temperatures and in air. Its crystal lattice is similar to that of $Ca_3Co_4O_9$; and it consists of blocks alternately stacked along the *b*-axis. These blocks are CoO_2 sheets and $Bi_2Sr_2O_4$. The $Bi_2Sr_2O_4$ blocks are in place of the $CaCoO_3$ layers, and are made of two layers of SrO sandwiching two layers of BiO. This specific arrangement of $Bi_2Sr_2O_4$ is called the quadruple rock salt structure.

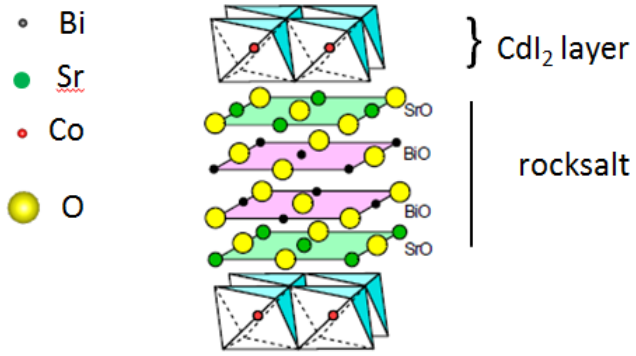

Figure 1.10: The crystal structure of the layered $Bi_2Sr_2Co_2Oy$, also called BC-222.[16]

The black, green, red and yellow spheres represent the calcium (Bi), cobalt (Sr), cobalt (Co) and oxygen (O) atoms, respectively. Like in the $[Ca_2CoO_3]_yCoO_2$ system Co atoms have an octahedral environment and form CoO_2 layers. These layers are illustrated by the white-light blue blocks in Figure 1.10 above. They are separated by a quadruple rock-salt block of Bi, Sr and O, along the *b*-axis. The two pink sheets of BiO are located between two layers of SrO in green in Figure 1.10. The Seebeck coefficient of bismuth strontium cobaltate, in air, peaks at 973 K, and reaches the value of 290 $\mu V\,K^{-1}$. The electrical and thermal resistivities of this material are low at high temperature. ρ is about 2 mΩ cm at 1000 K and κ is in the order of 2 $W\,m^{-1}\,K^{-1}$ at 800 K. Funahashi *et al.* reported a figure of merit near unity at 1000 K: $ZT \geq 1.1$[36]. This value is higher than the one of SiGe at 1000 K. ZT_{SiGe} is about 0.58 at that temperature, as seen in Figure 1.4.

1) Some perovskite oxide materials with high TE properties

The band structure of ABO_3 perovskite materials is at the origin of their large Seebeck coefficient and high electrical conductivity. The bottom of the CB consists of B *d* states and the upper valence band is composed of O*p* states. The large power factor of the perovskite-type structured materials is due to the triply degenerate t_{2g} states of the B 3*d* orbitals. Because of the symmetry of the crystal (Jahn Teller effect), these orbitals are split into a singlet (low energy) and a doublet (high energy). The states associated with the singlet near the Fermi level are degenerate and the large thermopower power is due to their very high density (Heikes formula[37]). On the other hand, the band associated with the doublet is very dispersive[38]. The electrons of the doublet states are responsible for the high electrical conductivity of the material. In other words, there are two types of conduction electrons at the bottom of the CB. The first type of conduction electrons are the light electrons[38] of the

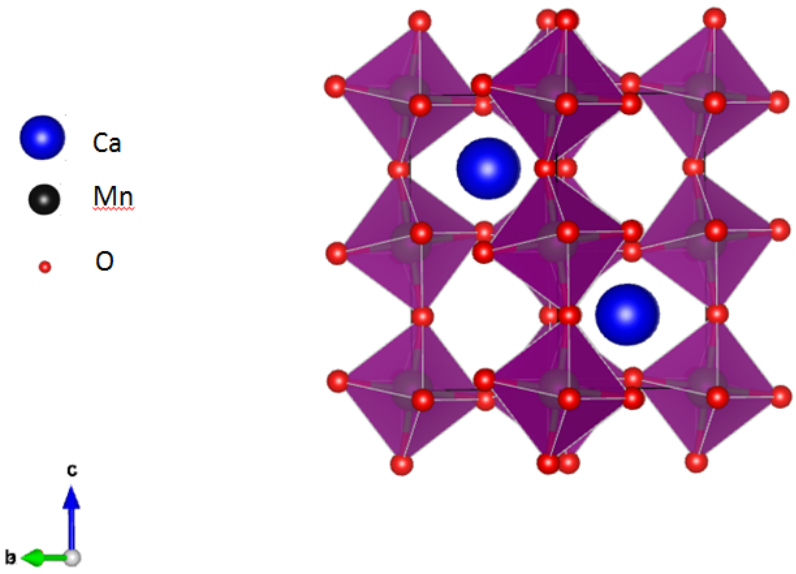

Figure 1.11: Typical unit cell of $CaMnO_3$: a perovskite compound. The blue (black) spheres represent the Ca (Mn)-cation; the anions, the oxygens, are represented by the red spheres.

dispersive bands and are responsible for the high electrical conductivity. The heavy electrons which belong to the dispersionless degenerate states are the second type of conduction electrons. These electrons greatly contribute to the large thermopower of these ABO_3 materials. The perovskite-type structure thus allows for large Seebeck an high electrical conductivity.

a) $CaMnO_3$

One of best *n*-type semiconductor oxide, utilised in TE oxide module, is $CaMnO_3$. The thermoelectric properties[39,40,41,42] of this material have been extensively investigated. This compound crystallises in a perovskite-type structure[43,44]. It is typically a cubic lattice made from a corner sharing octahedra. In general in a perovskite, the A and B cations have an oxidation number of 2+ and 4+, respectively. In the crystal structure of $CaMnO_3$, Ca^{2+} ions are surrounded by 6 anions (O^{2-}) and together they form CaO_6 octahedra, as seen in Figure 1.11 above. From room temperature to 1180 K crystallises in an orthorhombic lattice characterised by the symmetry space group Pnma (62). For temperatures higher than 1180 K a structural transition occurs at the atomic scale. $CaMnO_3$[45] crystal structure then orders in a higher symmetry space group: a cubic lattice whose space group is $Pm\bar{3}m$ (221). The cubic and orthorhombic phases differ in the angle of the $Mn-\widehat{O}-Mn$ bond. The angle value is either equal or lower than 180° for these two phases, respectively.

Figure 1.11 illustrates the orthorhombic structure of the room-temperature $CaMnO_3$. The blue, green spheres represent the Ca^{2+} and Mn^{2+} cations; the anions, O^{2-}, are represented by the red spheres. The $Mn-\widehat{O}-Mn$ bond is distorted, thereby introducing a tilt between CaO_6 octahedra. At room temperature, $CaMnO_3$[42] behaves like an insulator material and exhibits an outstanding Seebeck coefficient of about $-300\,\mu V\,K^{-1}$. The negative sign of the thermopower indicates that *n*-

type conduction occurs in this manganite perovskite: the majority of the free-carriers are electrons. Additionaly, numerous studies[46,47] have demonstrated that the electrical conductivity of $CaMnO_3$ can be enhanced by either doping the A- or B-site of this perovskite. The most common dopant on the manganese site is niobium. Bocher *et al.*[47] investigated the TE properties of polycrystalline $CaMn_{1-x}Nb_xO_3$ (with x = 0.02; 0.05 and 0.08). The figure of merit of the 2 % Nb sample is the highest. $CaMn_{0.98}Nb_{0.02}O_3$ exhibits a Seebeck coefficient and an electrical resistivity of $-251\,\mu V\,K^{-1}$ and $4.0 \times 10^{-2}\,\Omega\,cm$ at 1000 K respectively.

Taking into account its low thermal conductivity ($1.5\,W\,m^{-1}\,K^{-1}$) at the same temperature, Bocher *et al.*[47] reported a value of 0.30 for its ZT. The calcium site has been doped by rare-Earth elements like Yb, Tb, Nd, Lu and Ho; $Ca_{1-x}RE_xMnO_3$. Funahashi *et al.*[40] demonstrated that, the substitution of Ca by these elements induces a hopping conduction within $Ca_{1-x}RE_xMnO_3$ compounds,for temperatures above 400 K; it is due to the introduction of extra electrons by the high valence state of RE^{3+}. The 2 % sample, with lutetium as the doping material, behaves like a metal for temperature above 973 K. It also exhibits an electrical resistivity (ρ) of around $5\,m\Omega\,cm$. Its thermopower (α) and thermal conductivity (κ) at 973 K are $-130\,\mu V\,K^{-1}$ and $\sim 1.5\,W\,m^{-1}\,K^{-1}$, respectively. As a consequence the ZT of $Ca_{0.8}Lu_{0.2}MnO_3$ sample reaches 0.16 at 973 K.

b) $SrTiO_3$

Eventually, heavily-doped strontium titanate ($SrTiO_3$) exhibits promising thermoelectric properties at high temperature. $SrTiO_3$ has a perovskite-type structure, but unlike $CaMnO_3$ it crystallises in an isotropic cubic lattice. Figure 1.12 on the next page illustrates the unit cell of the crystal structure of $SrTiO_3$. The green, light blue and red spheres represent the Sr, Ti and O atoms, respectively. Both strontium and titanium ions have an octahedral environment of the within the lattice, as they are surrounded by six oxygens.

$SrTiO_3$ is an insulator at room temperature with a bandgap of $\sim 3.2\,eV$[48]; its band structure is characterised by Ti $3d$ orbitals at the bottom of the conduction band and O $2p$ at the top of the valence band. However, heat treatment under reduced atmosphere generates oxygen vacancies, thereby introducing electrons into the conduction band[49]. Otha *et al.*[50,51] investigated the TE properties of single crystals Nb-doped $SrTiO_3$ and La-doped $SrTiO_3$ at the Ti and Sr site, respectively. Both samples exhibit large thermopower values in the order $-0.2\,\mu V\,K^{-1}$ at 1000 K. Their σ decreases as temperature increases proportionally to T^{-2} below 750 K and $T^{-1.5}$ above 750 K. Only small changes of κ are observable after the introduction of extra electrons in the conduction band by La and Nb. κ is about 6-10 $W\,m^{-1}\,K^{-1}$ at room temperature. The thermal conductivity decreases and $2.5\,W\,m^{-1}\,K^{-1}$ at 1000 K for both La-doped and Nb-doped $SrTiO_3$. Both samples reach a figure of merit (ZT) of about 0.1-0.2 at 1000 K. Otha[51] also investigated the TE properties of polycrystalline $SrNb_{0.20}Ti_{0.80}O_3$ and reported a value of 0.35 for its ZT at 1000 K. To go further $SrTiO_3$ when appropriately doped can form a superlattice Ruddelsden-Popper structure, also known as RP-phase. Strontium titanate RP-phase[52,53] has the formula $(SrO)(SrTiO_3)_n$, with n been an integer. The

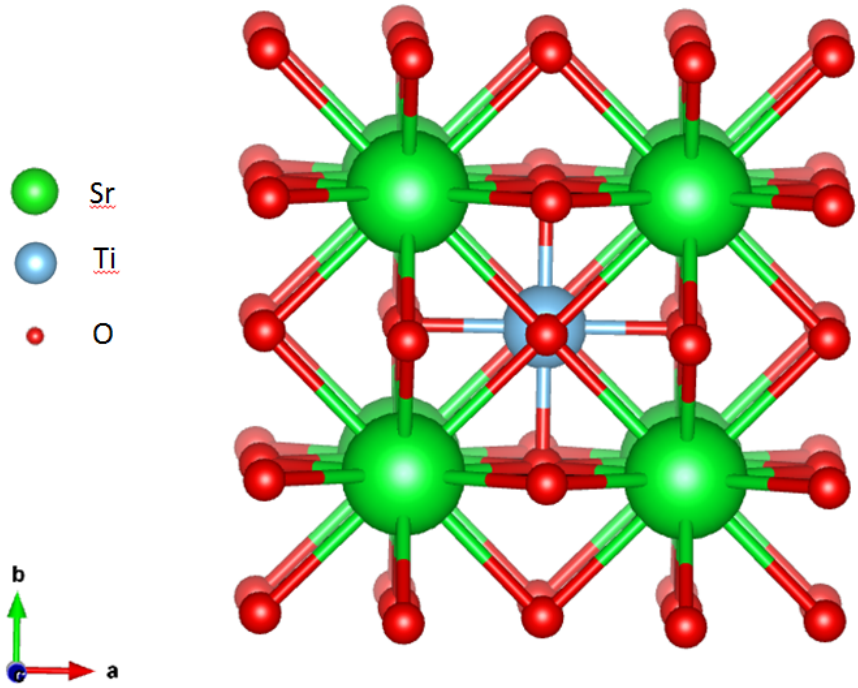

Figure 1.12: The unit cell of the crystal structure of $SrTiO_3$. The strontium atoms (in green) are surrounded by six oxygen atoms (in red). The titanium atom is located at the centre of the cube.

superlattice consists of perovskite ($SrTiO_3$) layers separated by SrO layers. The crystal lattice of $(SrO)(SrTiO_3)_n$ systems contributes to an enhancement of their ZT, as it enables the reduction of κ due to scattering of phonons at the interface of the different layers. Wang *et al.*[54] demonstrated that κ is reduced but σ is also reduced. Hence, for systems such as $(SrO)(SrTiO_3)_n$ (n = 1, 2) the ZT value (0.15) is lower than that of $SrNb_{0.20}Ti_{0.80}O_3$[51]. Eventually the major issue of SrTiO3-based oxides as TE material is the need of reducing conditions for the n-type doping. The reducing conditions limit the number of applications of this oxide to vacuum or inert atmosphere-applications.

2) A Wurtzite with high TE properties

Zinc oxide (ZnO) is one of the best *n*-type TE oxide. ZnO is well known as a transparent conductor oxide (TCO) due to its wide bandgap of 3.2-3.5 eV. This material has been highly investigated over the past 30 years as a replacement for the toxic indium tin oxide (ITO); because zinc is more abundant in the Earth's crust (70 ppm) than indium (4.61 ppm). ZnO crystallises in a Wurtzite structure: a hexagonal lattice whose unit cell has the following lattice parameters: a = 3.253 Å, c = 5.213 Å.

Figure 1.13 on the next page illustrates the layered structure of ZnO. The green and red spheres represent the zinc and oxygen atoms, respectively. There is a 4-fold coordination of O^{2-} around the Zn^{2+}. Theoretical studies[55] make evident that this material can be treated like a semiconductor, as its conductivity increases with increasing temperature. Indeed, a small doping concentration of both aluminium and gallium increases its conductivity by up to three orders of magnitude at room temperature. Thereby Zn:Al (AZO) and Zn:Ga (GZO) behave like metals. The conductivities of AZO and GZO both reach up to $1 \times 10^4\,S\,cm^{-1}$. These high conductivity values suggest that these

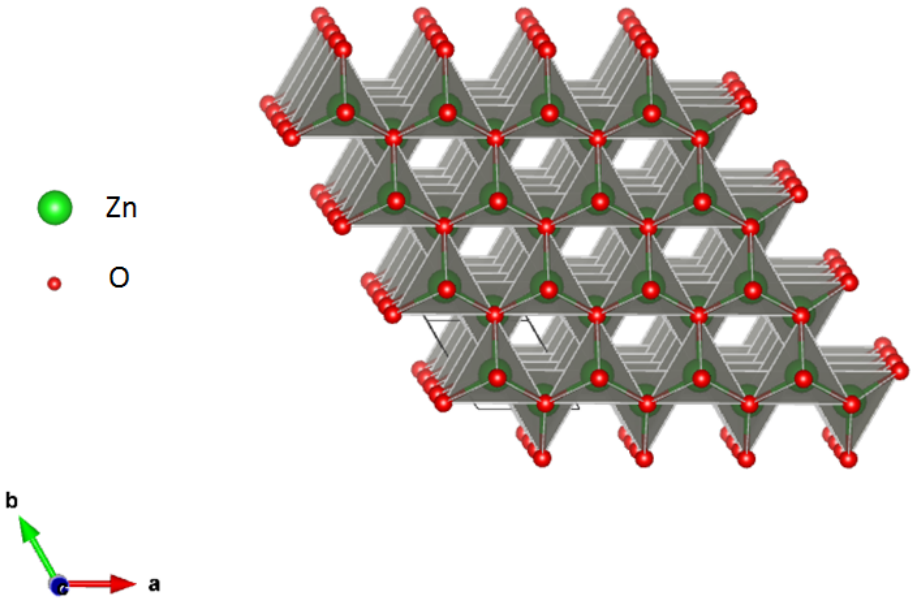

Figure 1.13: The crystal structure of zinc oxide in the ab-plane.

compounds are potential TCOs. It also demonstrates why they are excellent replacements for ITO, as transparent conducting electrodes[56,57]. Recently, studies[55,58,59] have exposed the potential of ZnO-based oxide materials for high-temperature energy conversion. Ohtaki *et al.*[58] investigated the TE properties of aluminium-doped zinc oxide ($Zn_{1-x}AlxO$) powder samples (with x = 0, 0.005, 0.01, 0.02 and 0.05). The solubility limit of Al in ZnO correspond to x = 0.02, as transmission electron microscopy images revealed the presence of secondary phase[60] ($ZnAl_2O_4$) for x $\geq$ 0.02. Nevertheless, the thermopower and electrical resistivity of $Zn_{0.98}Al_{0.02}O$ ceramic sample are optimal for high-temperature thermoelectric applications. Indeed at 1273 K α and σ are both about $-180\,\mu V\,K^{-1}$ and $1.9 \times 10^4\,S\,cm^{-1}$ respectively; the sign of the thermopower indicates that the majority of free-carriers are electrons: $Zn_{0.98}Al_{0.02}O$ can be viewed as a *n*-type semiconductor. These values are in the same order of magnitude of those found in Si-Ge alloys, which are utilised in radioactive thermoelectric generators for space applications. The ZT of this TCO, at 1273 K, is near 0.30. The large value of κ is responsible for the low value of its figure of merit ZT at high temperature. Indeed, at 1273 K, κ is about $5\,W\,m^{-1}\,K^{-1}$, which is higher than that of the state-of-the-art TE and other oxide materials. ZnO has also been doped by gallium oxide as the dopant material on the zinc site. $Zn_{1-x}Ga_xO$ show similar thermoelectric properties as $Zn_{1-x}Al_xO$. Additionally, the dually doped zinc oxide is another promising TCO with high thermoelectric performance. Indeed, Ohtaki and co-workers[59] measured the thermopower, electrical and thermal conductivities of $Zn_{1-x-y}Al_xGa_yO$. $Zn_{0.96}Al_{0.02}Ga_{0.02}O$ polycrystalline sample proved to be the best candidate for TE applications, as its ZT values were the greatest: about 0.47 at 1000 K and 0.65 at 1247 K.

To summarise, the high cost, toxicity and scarcity of traditional TE materials leads this thermoelectric research to be directed towards abundant, cheap and environmental friendly materials like the TE oxides. TE oxides have better stability than tellurides and antimonides and thus may

be suitable for high temperature applications. Most *p*-type oxides exhibit better thermoelectric properties than *n*-type oxides. Great figures of merit of both *n*- and *p*-type are needed for a high performance of a TE module. Consequently, in order to enhance the thermoelectric properties of TE oxide modules, the search for new *n*-type oxide with great ZT is of a great importance.

1.3 AB_2O_6 oxides family

Throughout the thesis thermoelectric and magnetic studies have been carried out on oxides with the chemical formula AB_2O_6, in the context of the search of new materials. The A and B elements in this formula can be a transition metal (Fe, Co, Ni, etc), an alkaline (Ba, Ca, Mg), or a lanthanide (Eu). The herein work was restricted to compounds in which the B type is one of the four following elements: V, Ta, Nb and Sb. The majority of these structures can be described as variants of a hexagonal close packing of oxygen atoms with cations distributed in different manners, in an ordered way, in the octahedral voids[61]. Such arrangements are defined by the size ratio between A and B cations. In most of these oxides, A and B are present in the form of A^{2+} and B^{5+}, respectively. The family tree of the crystallographic structures of some AB_2O_6 compounds is discussed. The AB_2O_6 compounds (with B = V, Ta, Nb and Sb) are then classified in groups using sorting maps. It is followed by a comparison of the nuclear structures of these AB_2O_6 and that of the best TE oxides. The last part of the chapter is dedicated to a literature review on the magnetic properties of some AB_2O_6 oxides.

The so-called family tree of the crystal chemistry can established for the AB_2O_6 compounds, by comparing the crystal symmetry of several structures in group-subgroup relations. Such trees have been reported by H. Bärnighausen[62] and Müller *et al.*[63], about different families of oxides. A tree consists of space groups, which are arranged vertically with arrows in between them. These arrows, as seen in Figure 1.14 on the next page, give the direction of symmetry change. There are additional informations on the type of symmetry reduction, the preservation or change of lattice translations. Some changes of origin are sometimes necessary to go from one subgroup to another subgroup. The family tree some of AB_2O_6 derived by Beck[61] is displayed in Figure 1.14.

Within Megaw's nomenclature[64] the noblest member of the tree is the member with the highest symmetry space group compounds. The type structure associated with a noblest member is known as the aristotype. The structure types and subgroups of an aristotype are called hettotypes. Their respective symmetry space groups are lower than that of the aristotype. The lowering of the symmetry space group from aristotype to hettotypes is due to:

- a lowering of the class of the parent group; it indicated by *t* in the tree.
- a loss of translational symmetry but the subgroup has the same class as the parent group, indicated by *k*. In such cases the resulting unit cell is bigger than the original one;
- a loss of translational symmetry but the subgroup has the same class as the space group type as the parent one. This structural change is also associated with an increase of the unit cell.

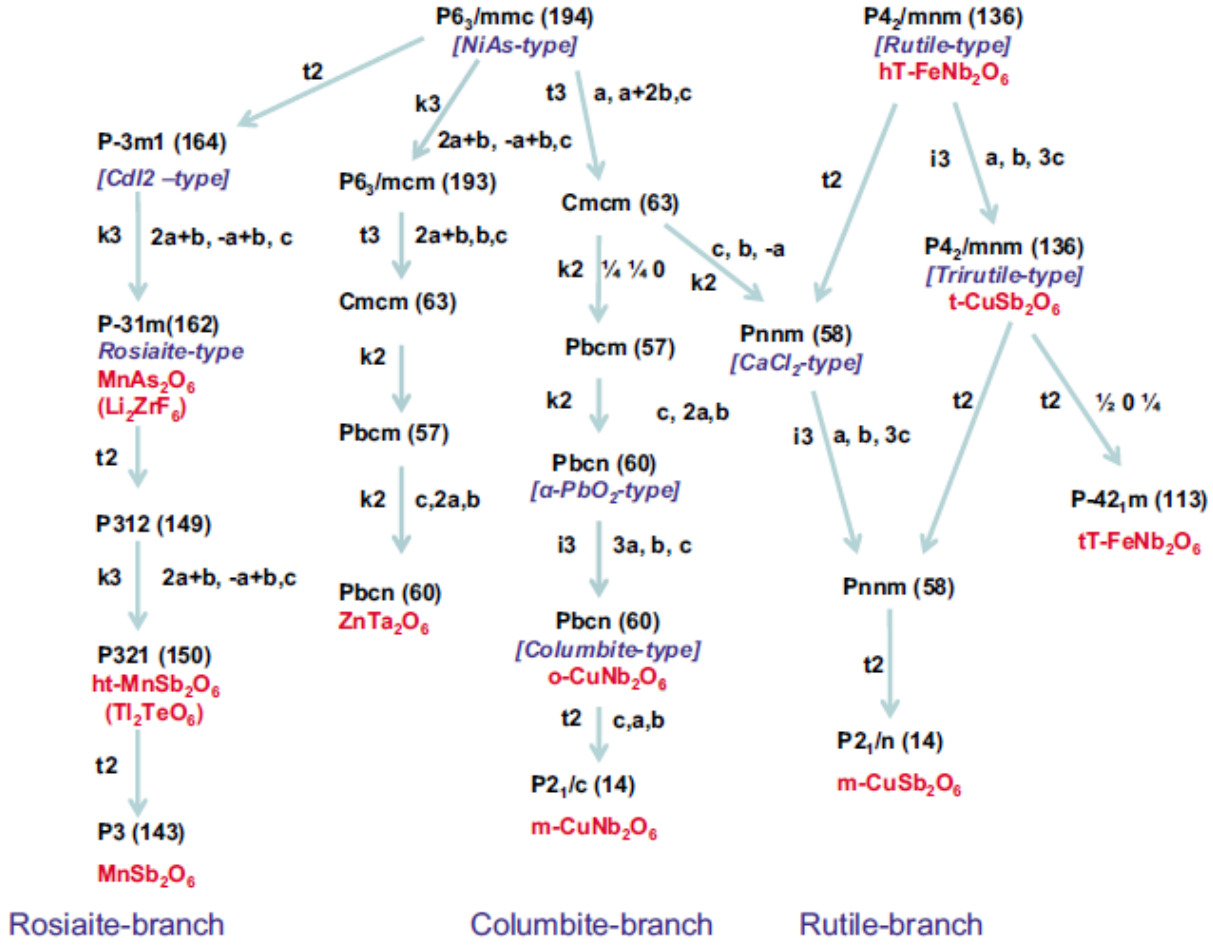

Figure 1.14: Family tree of some AB_2O_6, according to Beck[61].

Table 1.1: Crystallograhic parameters of the unit cell of the rosiaite $CdSb_2O_6$. ICSD stands for Inorganic Crystal Structures Database. Space group: $P\bar{3}1m$ (162).

Lattice parameters a = 5.2373(0) Å, b = 5.2373(0) Å, c = 4.7983(1) Å. ICSD number = 71028					
Atom	Type	Wyckoff positions	x	y	z
Cd1	Cd	1a	0.000	0.000	0.000
Sb1	Sb	2d	0.333	0.667	0.500
O1	O	6k	0.365(1)	0.000	0.282(1)

In the tree of AB_2O_6 oxides[61], the noblest members are $P6_3/mmc$ (194) and $P4_2/mnm$ (136). These structures can be found in compounds such as NiAs- and h-T $FeNb_2O_6$, respectively. "h-T" stands for high-temperature and indicates that $FeNb_2O_6$ orders in a rutile-type structure at high temperature. The tree of AB_2O_6 in Figure 1.14 consists of three branches: the rosiaite, columbite and rutile. The lattice of three structures within these branches are described in the following three subsections.

1.3.1 The rosiaite-type structure

The branch on the left of the tree in Figure 1.14 corresponds to the Rosiaite branch. There is a lowering of the symmetry space group from $P\bar{3}m1$ (164) to $P3$. The 3-fold symmetry belongs to all the intermediate subgroups of this branch. A reduction of the translation symmetry from $P\bar{3}m1$ (164) leads to the formation of a variant symmetry space group $P\bar{3}m1$ (162). A tripling of the unit cell occurs while there is lowering of symmetry of the crystal. The type-structure at this point of the tree of AB_2O_6 oxides is the rosiaite. Compounds with the rosiaite-type structure such as $MnAs_2O_6$ order in a trigonal lattice, whose symmetry space group is $P\bar{3}m1$ (162). The branch ends up with the space group P3 (143). Such phase (crystal structure with the space group P3 (143)) is realised in a low temperature modification of $MnSb_2O_6$ where subtle changes in the fine structure comply better with individual needs of the different cations[61].

Within the trigonal lattice of the rosiaite-type structure A- and B-cations are octahedrally coordinated to oxygen atoms. When viewing the structure of a rosiaite-type structured material, one finds layers where one third of the octahedra are filled with A cations alternating with the ones where B cations occupy two thirds of them according to the stoichiometric relation of the cations. The AO_6 and BO_6 octahedra form 1D chains, which are alternately stacked along the [0 0 1] direction. AO_6 octahedra are isolated from each others. The BO_6 layers are corner-linked with the AO_6 octahedra along the c-axis, as seen in Figure 1.15 on the next page. The AO_6 octahedra are located at the edges of the unit cell whereas the BO_6 octahedra are in the middle of the unit cell. Since one deals with a trigonal lattice one has $\alpha = \beta = 90°$ and $\gamma = 120°$. $CdSb_2O_6$, $SrSb_2O_6$ also crystallise in the rosiaite-type structure.

1.3.2 The columbite-type structure

The third branch of the family tree of AB_2O_6 in Figure 1.14 is the Columbite branch. It is named after an intermediate subgroup between Cmcm (63) and the lowest subgroup at the end of the branch

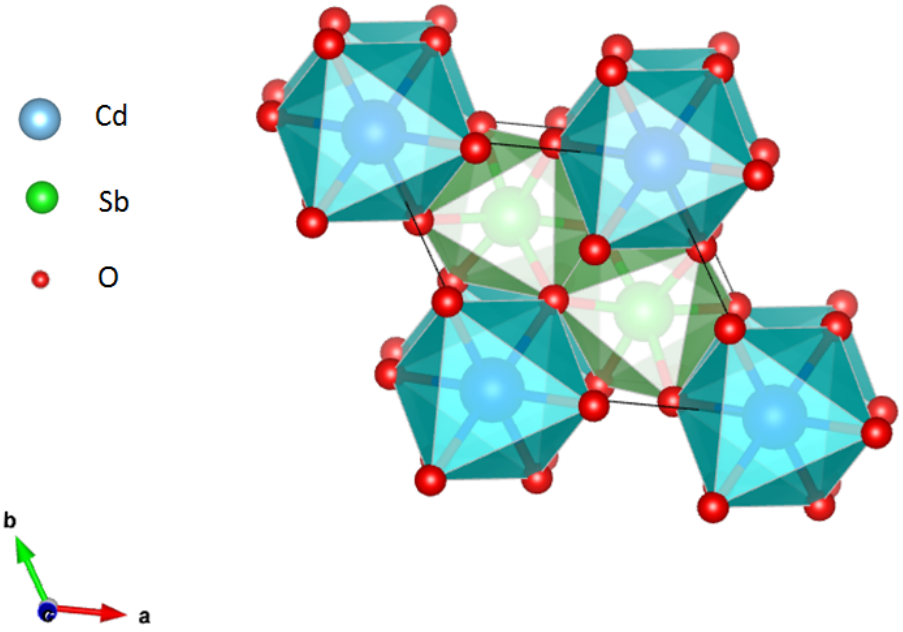

Figure 1.15: The unit cell of a rosiaite-type structure, here $CdSb_2O_6$.The blue (green) spheres represent the Cd^{2+} (Sb^{5+})-cation; the anions, the oxygens, are represented by the red spheres.

Table 1.2: Crystallograhic parameters of the unit cell of the columbite $CoNb_2O_6$. Space group: Pbcn (60).

Lattice parameters a = 14.1475(18) Å, b = 5.7120(7) Å, c = 5.0446(6) Å. ICSD number = 15854					
Atom	Type	Wyckoff positions	x	y	z
Co1	Co	4c	0.000	0.1579(4)	0.250
Nb1	Nb	8d	0.1613(1)	0.3628(2)	0.7821(2)
O1	O	8d	0.0941(4)	0.3722(1)	0.4474(1)
O2	O	8d	0.0829(1)	0.1184(2)	0.8977(3)
O2	O	8d	0.2372(2)	0.1531(4)	0.4345(2)

$P2_1/c$ (14): the columbite-type structure. In Figure 1.14, the hettotype structure which precedes the columbite-type structure in the columbite branch is found in a binary compound AB_2 (α-PbO_2-type. Similarly the rosiaite-type structure ($P\bar{3}m1$ (162)) is derived from the hettotype structure found in a binary compound (CdI_2). There is a tripling of the unit cell as one goes from α-PbO_2-type to the well-known columbite-type structure. Materials with the columbite-type structure order in an orthorhombic lattice whose symmetry space group is Pbcn (60), as depicted in Figure 1.16 on page 26. The unit cell of the orthorhombic structure consists of layers of hexagonal closed-packed oxygen octahedra AO_6 and NbO_6. These two types of octahedra with common edges are staggered in zigzag and are stacked along [1 0 0] direction, with the -A-Nb-Nb-A- sequence. It should be noted that another arrangement of the A and B cations in the triple cell is possible and it corresponds to a variant of the columbite-type structure: $ZnTa_2O_6$-type structure. The latter differs from the columbite-type structure as cations are A cations interspersed into the B layers. Thus, the A and B cations belong to the same layer in compounds with $ZnTa_2O_6$-type structure. Compounds such as $FeNb_2O_6$, $CoNb_2O_6$, $NiNb_2O_6$ crystallise in the columbite-type structure.

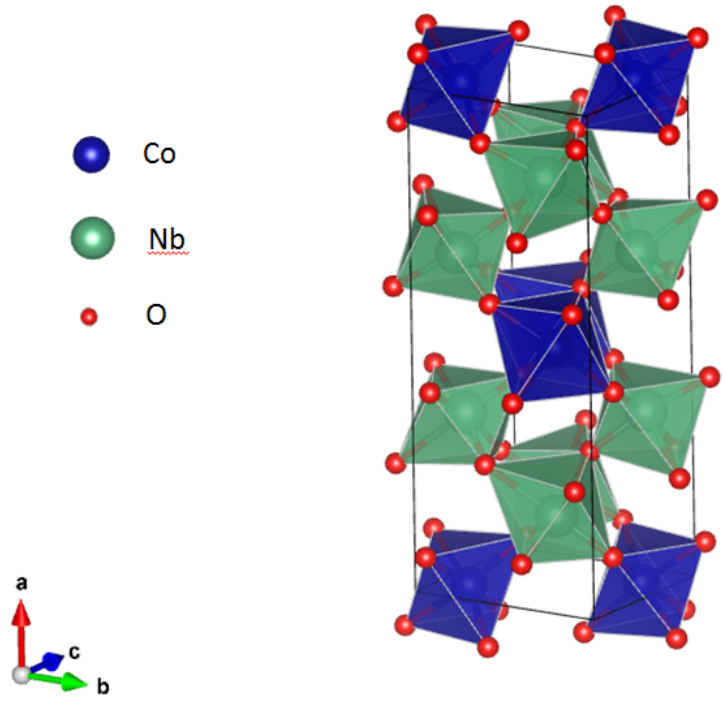

Figure 1.16: The unit cell of cobalt diniobate oxide- a typical columbite type structure.The blue (green) spheres represent the Co^{2+} (Nb^{5+})-cation; the anions, the oxygens, are represented by the red spheres.

1.3.3 The trirutile-type structure

The Rutile branch is the last branch of the tree of AB_2O_6 oxides in Figure 1.14. There is conservation of the 2-fold symmetry in this series, just as the 3-fold symmetry belongs to all the groups of the hettotype structures in the rosiaite branch. The lowest symmetry space group of the branch is $P2_1/n$ (14) and can be found in materials such as *m*-$CuSb_2O_6$. This space group is in fact a variant of the lowest subgroup of the columbite branch: $P2_1/c$ (14). One of the most encountered structure between the noblest member $P4_2/mnm$ (136) and lowest member of this branch which is the trirutile-type structure. This structure can be deduced from the rutile by a tripling of the unit cell along the [0 0 1] direction. For further details on the rutile family and its derivatives the reader is encouraged to consult the seminal work of W. Baur[65].

Like in the columbite-type structures the cations (A^{2+}, Ta^{5+}) are octahedrally coordinated to the oxygen atoms in the trirutile-type structure. However, the octahedra are slightly distorted due to a static Jahn-Teller effect[66]. The Jahn-teller effect is geometric distortion of the bonds between atoms which thus reduces the symmetry space group of the studied material. This phenomena occurs because the distortion lowers the overall energy of the compound. In the tetragonal lattice the AO_6 and BO_6 octahedra are slightly distorted due the Jahn-Teller effect. The A cations occupy a body-centered tetragonal arrangement, resulting in square-planar Ni layers stacked along the *c*-axis. Additionally, layers of A and B cations are alternately stacked along the [0 0 1] direction, as illustrated in Figure 1.17 on the next page. This alternation of layers of A nd B cations is also found within columbite structured materials but along the *a*-axis.

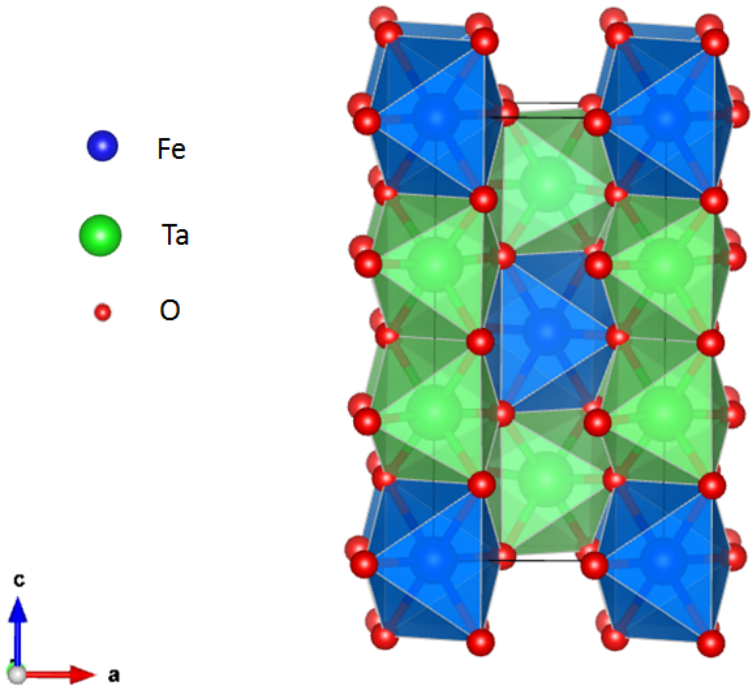

Figure 1.17: The unit cell of $FeTa_2O_6$- a typical trirutile type structure.The blue (green) spheres represent the Fe^{2+} (Ta^{5+})-cation; the anions, the oxygens, are represented by the red spheres.

Table 1.3: Crystallograhic parameters of the unit cell of the trirutile $FeTa_2O_6$. Space group: $P4_2/mnm$ (136).

Lattice parameters a = 4.7515(3) Å, b = 4.7515(3) Å, c = 9.254(1) Å. ICSD number = 79684					
Atom	Type	Wyckoff positions	x	y	z
Fe1	Fe	2a	0.000	0.000	0.000
Ta1	Ta	4e	0.000	0.000	0.333(2)
O1	O	4f	0.307(5)	0.307(5)	0.000
O2	O	8j	0.297(3)	0.297(3)	0.322(1)

Table 1.4: Crystallograhic parameters of the unit cell of a brannerite compound: ZnV_2O_6. Space group: C2 (5).

Lattice parameters a = 9.2651(9) Å, b = 3.5242(5) Å, c = 6.5889(8) Å. ICSD number = 30880					
Atom	Type	Wyckoff positions	x	y	z
Zn1	Zn	2a	0.000	0.000	0.000
V1	V	4i	0.1916(2)	0.000	0.6528(2)
O1	O	4i	0.0328(6)	0.000	0.7193(11)
O2	O	4i	0.3406(6)	0.000	0.8884(10)
O2	O	4i	0.3065(6)	0.000	0.4345(9)

1.3.4 The brannerite structure and the rossite structure

As the work done throughout the thesis focuses one AB_2O_6 systems, with B = V, Ta, Nb and Sb, two additional type-structures can be added: the brannerite and rossite.

Materials with the brannerite[67] structure crystallise in a monoclinic lattice, whose space group symmetry is C121 (5) or C2/m (12). Within the lattice on finds AO_6 and BO_6 octahedron. Brannerite such as ZnV_2O_6 consist of edge-connected ZnO_6 octahedra forming 1D chains along [0 1 0] direction. The 1D chains form bidimensional layers separated by vanadium oxide layer. The layer of VO_6 octahedra is composed of zigzag chains of edge-connected VO_6 octahedra parallel to the A chains, as depicted in Figure 1.18 on the next page. Note that the AO_6 are not directly connected to each other along the [0 0 1] direction. α-CoV_2O_6, MgV_2O_6 and MnV_2O_6 are another AB_2O_6 oxides which crystallise in a brannerite-type structure. The brannerite and the rossite both crystallise within a monoclinic crystallographic lattice. The unit cell is characterised by the following angles : $\alpha = 90\,°$; $104\,° < \beta < 112\,°$; $\gamma = 90\,°$.

The rossite-type structure[68] is a variant of the brannerite type structure, as its symmetry space group is also C 2/m (12). In crystal lattices with the rossite-type structure the B cations are no longer surrounded by octahedra but rather BO_5 trigonal bipyramids. As a consequence there is not zigzag chains of BO_6 along the a-axis. Instead the BO_5 polyhedra form two groups of three trigonal bipyramidal which are not directly connected to each to other. The AO_6 octahedra form 1D chains along [0 1 0] direction. The Wyckoff positions of atoms within the unit cell of a rossite-type structure are displayed in Table 1.5. Other AB_2O_6 oxides which order in a rossite-type structure are CaV_2O_6 and CdV_2O_6.

1.3.5 Structure and properties

A sorting map is another type of diagram used to classify the crystal structures of compounds which belong to the same family. The classification lies on a set of coordinates. These coordinates can be related to the magnetic (ferromagnetic, antiferromagnetic and paramagnetic) and electric properties (insulator, semiconductor and metal) of the studied compounds. Materials with similar properties

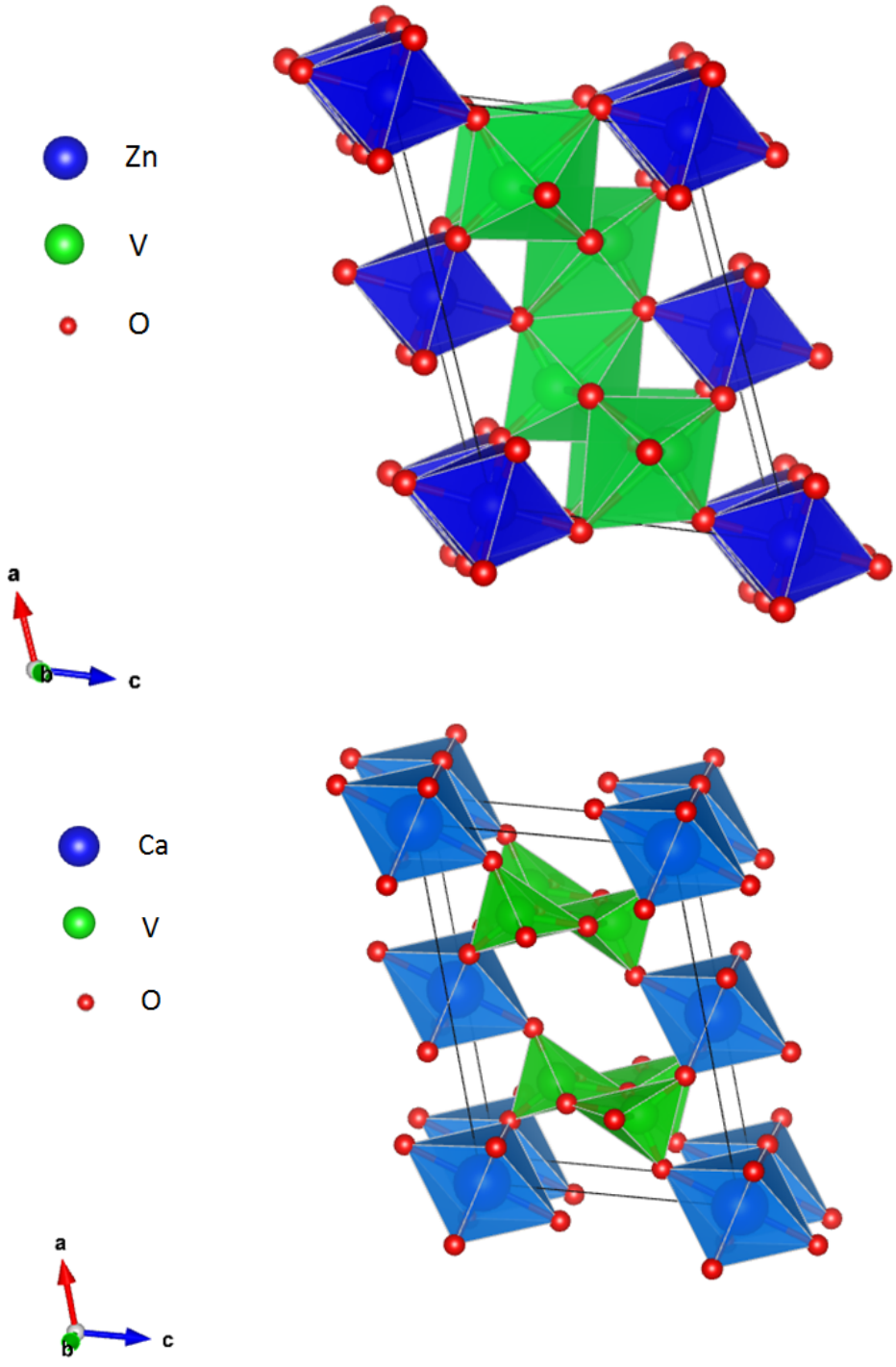

Figure 1.18: Typical unit cell of the brannerite and rossite type structures. The brannerite structure and the rossite structures are represented by the ZnV_2O_6 (top) and the CaV_2O_6 (bottom), respectively. The blue (green) spheres represent the A (B)-cation; the anions (the oxygens) are represented by the red spheres.

Table 1.5: Crystallograhic parameters of the unit cell compound: CaV_2O_6. Space group: C2/m (12).

Lattice parameters a = 9.18(1) Å, b = 3.58(3) Å, c = 6.48(1) Å. ICSD number = 21067					
Atom	Type	Wyckoff positions	x	y	z
Ca1	Ca	2a	0.000	0.000	0.000
V1	V	4i	0.2342	0.000	0.6691
O1	O	4i	0.08740	0.000	0.7219
O2	O	4i	0.1434	0.500	0.11820
O2	O	4i	0.2465	0.000	0.3934

belong to regions in a sorting map. Hence, the sorting map is a guideline to select useful materials to study. The coordinates used in establishing a sorting map of AB_2O_6 oxides are the radii of the cations A and B: r_A and r_B, respectively.

The AB_2O_6 oxides can be classified using the symmetry space group as criteria. The classifiation of the compounds of this family is synonym of the establishment of a sorting map. Such diagram (or sorting map) is useful, as the physical properties of a material are related to its atomic structure. For instance, magnetic properties such as the direct exchange coupling[66] is directly related to the distance between two magnetic ions. One thus expects the exchange coupling constants in $CoTa_2O_6$ and $NiTa_2O_6$ to be similar to that of $CoTa_2O_6$ and $CoNb_2O_6$. The exchange coupling constants in $CoTa_2O_6$ and $NiTa_2O_6$ are comparable in magnitde because these two compounds crystallise in a tetragonal lattice whereas $CoNb_2O_6$ has a orthorhombic crystal structure. The sorting map of AB_2O_6 (with B = V, Ta, Nb and Sb) is depicted in Figure 1.19 on page 30.

In Figure 1.19, x- and y-axes represent the radius of A- and B-cations of AB_2O_6 oxides, respectively. There are four rows and each of these rows appears at 0.54, 0.64, 0.60 and 0.64 Å. These values are the respective radius of V, Nb, Sb and Ta. Tantalum, antimony, vanadium and niobium are associated with 1^{rst}, 2^{nd}, 3^{rd} and 4^{th} row, respectively. AB_2O_6 oxides can therefore be classified into four groups which are the niobates, the antimonates, the tantalates and the vanadates. This Figure highlights that the crystal structure of these AB_2O_6 oxides is mainly influenced by the B-cation. In addition, there are four rectangles (regions) in the sorting map of the AB_2O_6 oxides in Figure 1.19 and they all are all associated with a specific structure type. The rosiaite, rossite, columbite, brannerite and trirutile structures are represented by the pink, black, blue, green and red regions in Figure 1.19. The red and magenta rectangles are mostly filled out with red dots and pink diamonds, respectively. Hence, tantalates and antimonates mostly crystallise in a trirutile and rosiaite structures respectively. Similarly, the brannerite and columbite structures are mostly found in vanadate and niobate AB_2O_6 oxides. Figure 1.19 is in therefore agreement with the family tree in Figure 1.14.

1.3.6 Analogy between some TE oxides and some AB_2O_6 oxides

There are similarities between some AB_2O_6 oxides and the layered cobaltites. Firstly, due their abundance, high-temperature stability and very low toxicity, AB_2O_6 oxides are promising materials for high temperature thermoelectric applications. Secondly, their crystal structures possess some traits of the crystallographic lattice of the layered cobaltites. Indeed the crystal structures of some

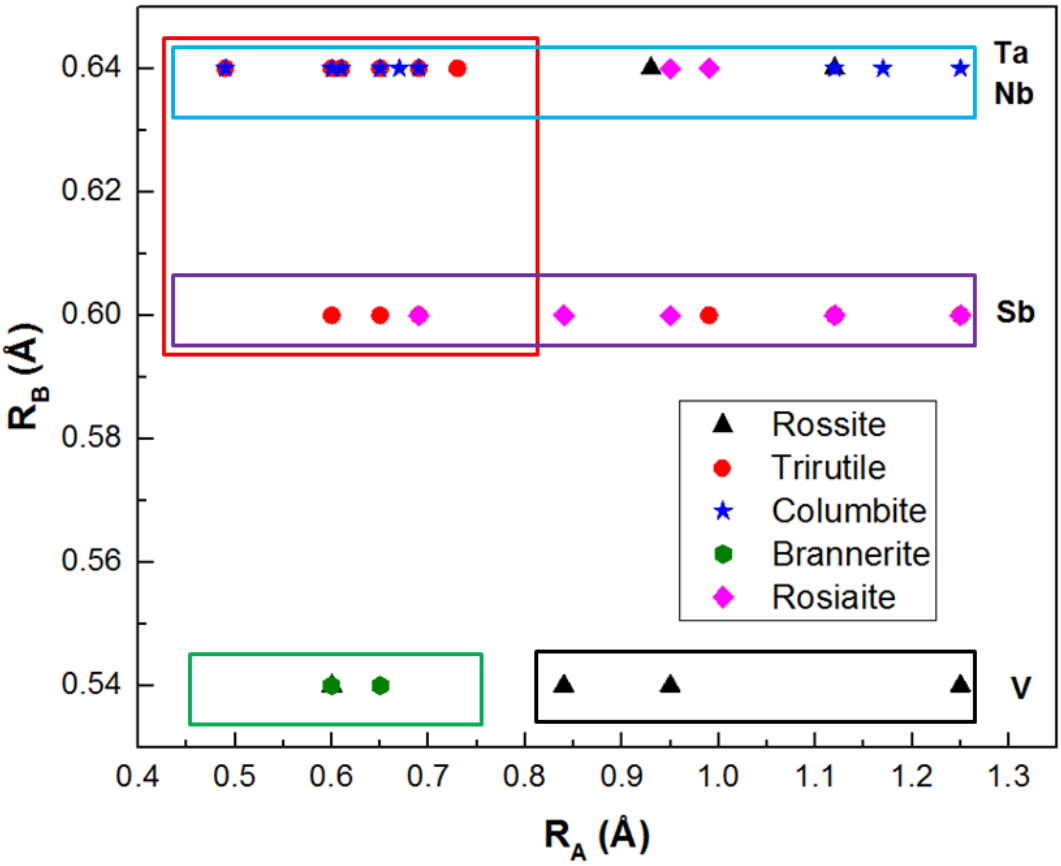

Figure 1.19: A sorting map of the AB_2O_6 oxides. The radius of different A elements is on the x-axis, whereas each row is associated with one of the four transition metal elements: V, Nb, Ta and Sb.

AB_2O_6 consist of different types of blocks (or layers) with specific compositions and symmetries. Within some AB_2O_6 oxides one finds CdI_2-type layers. Eventually, some AB_2O_6 can be viewed as high-symmetry superstructures, due to the presence of heavy elements and/or many atoms in their crystal lattices. As a consequence, AB_2O_6 fulfill some of the guidelines for the determination of good TE materials.

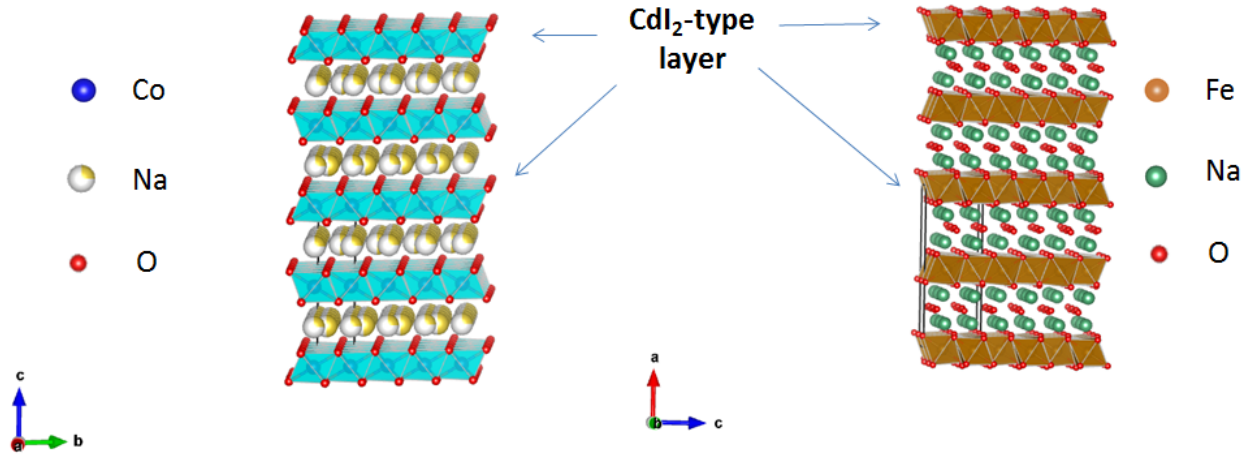

Figure 1.20: The layered structure of $NaxCo_2O_4$ (on the left) and $FeNb_2O_6$ (on the right).

Figure 1.20 above is a comparison of the atomic structure of $Na_{0.5}CoO_2$ (on the left) and $FeNb_2O_6$ (on the right). In both structures the red spheres represent the oxygen atoms. The white and blue spheres correspond the sodium and cobalt atoms, respectively. Both Co and Na are octahedrally coordinated with oxygens. In $FeNb_2O_6$, the green and brown layers are in place of Na and CoO_2 layers, respectively. The green and brown spheres represent the niobium (Nb) and iron (Fe) atoms, respectively. In $Na_{0.5}CoO_2$, the reduction of κ is due to sodium ions and the interface between yellow layer (Na) and blue layer (Co). They act as scattering centres for phonons. The conductivity of $Na_{0.5}CoO_2$ is mainly due to the in-plane conduction electrons in the CdI_2-type CoO_2 layers. As a consequence, one can independently tailor σ and κ. Similarly, the layered structure of $FeNb_2O_6$ consists of alternated FeO_6 and Nb_2O_6 layers along the c-axis. The Fe-O layers play the role of CoO_2 sheets. Additionally, there are blocks made up of heavy elements (niobium, $Z = 41$) between these CdI_2-type layers. Its TE properties may therefore be individually tuned to attain the best ZT. Finally, AB_2O_6 crystal structures can also be described as a hybrid crystal in the point of view of magnetism. For instance, the magnetism in AB_2O_6 compounds with the columbite-type structure is due to ordering of A cations, which form layers in the a-c plane. In $FeNb_2O_6$ magnetic Fe^{2+} ions form 2D layers and are separated by non-magnetic Nb layers, as seen on the right diagram in Figure 1.20.

Due to their atomic structures and stability at high temperature, AB_2O_6 are strong candidates for high temperature thermoelectric technologies. Their crystal structures made of low cost and environmental friendly elements can be viewed as superstructures which are made of different types

of blocks. The blocks are associated with the A or B cations, respectively. Each block or layer has a specific function. These functions combined together may yield high TE performances.

1.3.7 Magnetic properties of some AB_2O_6 oxides

This section is a literature review on the magnetic properties of some AB_2O_6 oxides. There is where it is available a review of the investigations on the magnetic susceptibility, the sublattice magnetisation, the magnetisation field-dependence magnetisation of some tantalates, niobates, metantimonates and vanadates.

1.3.7.1 The tantalates - ATa_2O_6

Most magnetic tantalates such as $FeTa_2O_6$, $CoTa_2O_6$ and $NiTa_2O_6$ crystallise in a trirutile-type structure. Santos *et al.*[69] developed models to describe the magnetic interactions in a class of tantalite compounds of compositions $A_xA'_{1-x}Ta_2O_6$, with A, A' = Fe, Co or Ni. These models are anisotropic Heisenberg or Ising models. Such models enable a better understanding of the various low-temperature magnetic phases observed by neutron diffraction in these compounds.

$FeTa_2O_6$

The magnetic structure of $FeTa_2O_6$ has previously been investigated using Mössbauer spectroscopy[70,71,72], and powder neutron-diffraction measurements[70,73]. These studies demonstrated that the tapiolite $FeTa_2O_6$ exhibits antiferromagnetic ordering below $T_N = 8.5\,\mathrm{K}$. The magnetic peaks in the neutron diffraction pattern can be indexed by the propagation vector $\vec{k} = (\frac{1}{2}\ ,\ 0,\ \frac{1}{2})$. These studies suggest that the spins in $FeTa_2O_6$ are constrained to the a–b plane, with each layer consisting of a collinear arrangement of moments where opposite spins are oriented along $\pm$ [1 1 0] directions. However they didn't establish an exact configuration of the 3D magnetic structure. This is due to the fact that these early reasearch were based exclusively upon the analysis of polycrystalline samples. Recently, Chung *et al.*[74] shed light on the sublattice magnetisation by performing magnetic measurements on $FeTa_2O_6$ single crystals.

Magnetic susceptibility[74,75] data ($\frac{d\chi}{dT}$) shows a maximum at T_N. It is confirmed by the presence of a sharp peak (λ anomaly) in the magnetic heat capacity data. The lambda anomaly is a signature of low dimensional 2D-systems. In addition χ vs T curve shows a broad maximum at 14 K for **H** along the [1 1 0] direction. Chung *et al.*[74] showed that this broad maximum is due to short-range correlations between the magnetic moments. The magnetic entropy (disordering of the spins due to thermal excitation) was deduced from the measured heat capacity. 73 % of the magnetic entropy of $FeTa_2O_6$ is lost above T_N due to short-range order effects. In ferromagnetic (antiferromagnetic) materials, below T_C (T_N) there is ordering of the magnetic moments. Ferromagnetic and antiferromagnetic systems exhibit a long-range order, as the ordering of the magnetic moments is repeated over infinitely great distances. This order gradually gives way to disorder, with increasing temperature. Slightly above T_C the ordering of magnetic moments does not persist over a long distance.

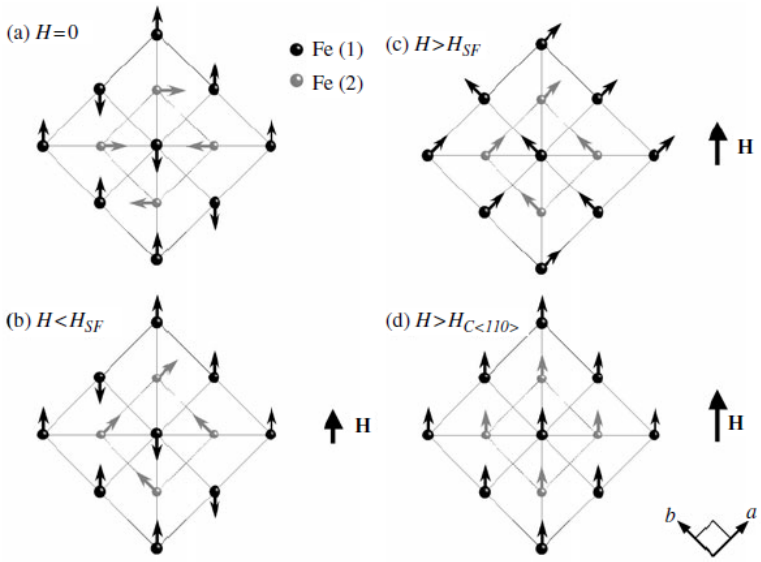

Figure 1.21: Different configurations of the magnetic structure of $FeTa_2O_6$ after the application of a magnetic field **H**. a) **H** = 0 configuration, (b) H ∥ [1 1 0] before spin-flip, (c) **H** ∥ [1 1 0] after spin-flop and (d) **H** ∥ [1 1 0] at saturation.[74]

One speaks of short-range ordering.

Chung *et al.*[74] established a model for the magnetic structure via magnetisation measurements on $FeTa_2O_6$ single crystals. The **M** vs **H** studies indicated that the ordered antiferromagnetic structure of $FeTa_2O_6$ is composed of collinear ⟨1 1 0⟩ spins lying in the *a*–*b* plane. This is in agreement with the work of Eicher *et al.*[70]. The magnetic field dependence of the magnetisation revealed that the bulk crystal contains approximately equal populations of spins along the four symmetry equivalent ⟨110⟩ directions. A spin-flip, at T = 1.6 K and H = 70 kOe, suggests the perpendicular sets of spins in the *a*–*b* plane. Figure 1.21 (a) is the model, proposed by Chung *et al.*[74], for the magnetic structure of $FeTa_2O_6$.

The square represents the lattice of $FeTa_2O_6$. The dots and small arrows are the magnetic Fe^{2+} ions and the magnetic moments they carry, respectively. There are two types of Fe: Fe (1) in black and Fe (2) in grey. The magnetic field direction is illustrated by the large black arrow pointing in the [1 1 0] direction. H_{SF} is the field for which the spin-flip occurs: 70 kOe. As the field **H** increases the magnetic moments of Fe (2) move away from their initial position (configuration (a)). The sublattice of moments that is parallel to the field gets flipped for $\mathbf{H} = H_{SF}$. Eventually for stronger magnetic fields all magnetic moments are aligned and it corresponds to the saturation (configuration (d)). The previous studies and that of Chung *et al.*[74] all agree on the refined value for the moments of Fe^{2+} ions: $\mu_{eff} = 5\,\mu_B$ per Fe^{2+}.

$FeTa_2O_6$ powder susceptibility data[4] has been modelled by Muraoka *et al.*[75] using the Padé approximated[76,77,78] high-temperature expansion of a two-dimensional anisotropic Heisenberg model with S = 2 spins placed on a square lattice. The refined values[75] of the nearest- and next-nearest neighbours exchange interactions, *J* and *J'* respectively, are given by the following relations:

- $-0.41 \leq \frac{J}{k_B} \leq -0.39\,\mathrm{K}$,
- $0.6 \leq \alpha \leq 0.9$.

α is equal to $\frac{J'}{J}$. Fan and Wu[79] established the phase diagram of $FeTa_2O_6$ and derived the phase diagram for frustrated 2D Ising model at 0 K. According to Fan and Wu the antiferromagnetic configuration, exhibited by $FeTa_2O_6$, will be realised as the ground state structure only if - $\mid J \mid >$ 2 J'. The J and J' values obtained by Muraoka *et al.*[75] fulfill this condition.

$CoTa_2O_6$

Early investigations of the magnetic properties of cobalt ditantalate oxide ($CoTa_2O_6$) consisted of neutron diffraction[80] and magnetic susceptibility[65,80,81] measurements on powder samples. These studies suggest the antiferromagnetic character of $CoTa_2O_6$. The magnetic susceptibility χ as function of temperature T is characterised by an inflection point at 6.63(5) K. It indicates that the magnetic moments are ordered below $T_N = 6.63(5)\,\mathrm{K}$. Like in the χ vs T curve of $FeTa_2O_6$, a broad maximum is observed above the Néel temperature. The broad maximum indicates the presence of enhanced short-range correlations between the magnetic moments which is characteristic of low-dimensional materials. A λ-anomaly is observed in the specific-heat data. The temperature at which this sharp peak occurs coincides with the Néel temperature $T_N = 6.63(5)\,\mathrm{K}$.

The magnetic reflections in the neutron iffraction patterns, recored at temperatures below T_N, were indexed with the propagation vector $\vec{k} = (\frac{1}{4}\ ,\ \frac{1}{4},\ \frac{1}{4})$. The smallest supercell that indexes all of the well-defined magnetic reflections is a $2\sqrt{2}$a × $2\sqrt{2}$a × 4c unit cell. Reimers[80] proposed two models to fit the magnetic reflections. The first moel has a helical spin arrangement and the second one is a model in which the two sublattices have different cone axes. The second mode was the most successful. Recently Kinast *et al.*[82] performed magnetic measurements on $CoTa_2O_6$ polycrystalline sample. Their magnetic susceptibility, heat capacity data are in agreement with those of Reimers. However unlike Reimers they used two propagation vectors to index all magnetic reflections:

- The first one is $\vec{k_1} = (\frac{1}{4},\ \frac{1}{4},\ \frac{1}{4})$ for the corner ions. Their moments are aligned along the [1 1 0] direction.
- The second one $\vec{k_2} = (\text{-}\frac{1}{4},\ \frac{1}{4},\ \frac{1}{4})$ for the center ions, with moments along the [$\bar{1}$ 1 0] direction.

The primitive cell of the magnetic structure derived from these two modulations vectors has the following dimensions: $a_{mag} = 2\sqrt{2}$a, $b_{mag} = 2\ \sqrt{2}$a and c_{mag} 4c. The magnetic structure is displayed in Figure 1.22. a and c are the lattice parameters of the nuclear structure. For a better visualization of the magnetic moments, Kinast *et al.*[82] illustrated the magnetic structure in the supercell (4a × 4a × 4c) in Figure 1.22 on the next page.

In Figure 1.22, the spheres and arrows represent the Co^{2+} ions and the magnetic moments they carry. Dark (bright) spheres represent corner (center) ions. There is a ↑↑↓↓ sequence of the magnetic moments along the three axes. All magnetic moments lie in the *a*-*b* plane, and alternate

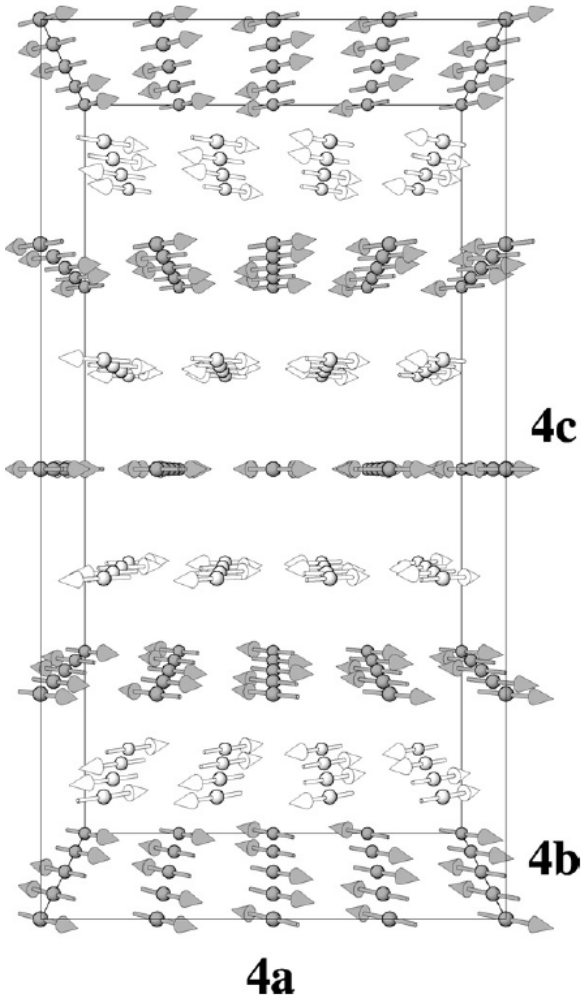

Figure 1.22: Magnetic structure of $CoTa_2O_6$ according to Kinast *et al.*[82].

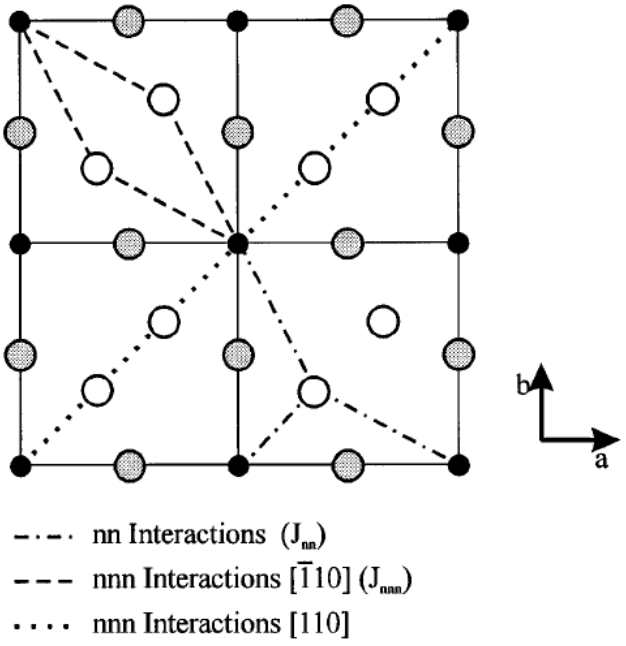

Figure 1.23: 2D view of the crystal structure of $CoTa_2O_6$[83]. The black, grey and white circles represent the cobalt (Co), tantalum (Ta) and oxygen (O) atoms. The dash lines indicate the potentisl exchange pathways associated.

their orientations between the [1 1 0] and [$\bar{}$1 1 0] directions on successive planes. In addition, Kinast *et al.*[82] measured the field-dependence of the magnetisation of polycrystalline $CoTa_2O_6$ sample. The **M** vs **H** curve enables the determination of easy-axis magnetic anisotropy which is the preferred direction for the orientation of the magnetic moments. A sudden change in the **M** vs **H** curve is synonym of spin-flip transition. Although not pronounced the low-temperature curve presents a clear change in slope around $\mathbf{H} = 70\,\mathrm{kOe}$. The easy-axis corresponds to [1 1 0] direction. This model and the second model of Remeirs[80] for the magnetic structure of $CoTa_2O_6$ both fit the neutron diffraction patterns. However, these models are based on powder neutron diffraction measurements. Neutron diffraction on $CoTa_2O_6$ single crystals is therefore necessary for a better understanding of its magnetic structure, since single crystals inform on the intrinsic properties of a material.

Eventually Kinast *et al.*[82] refined an effective magnetic moment $\mu_{eff} = 4.68\,\mu_B$ per Co^{2+}. This value of μ_{eff} corresponds to a high-spin Co^{2+} in octahedral geometry. Like Muraoka *et al.*[75], Kinast and coworkers used a Heisenberg model on a square lattice to fit magnetic susceptibility data; but Kinast's model was based on spin $S = \frac{3}{2}$ instead of $S = \frac{1}{2}$.

Figure 1.23 depicts the potential exchange pathways connecting nearest neighbours (J_{nn}) and next-nearest neighbours (J_{nnn}). The dominant interactions in the square lattice in Figure 1.23 are the in plane exchange interactions, involving a next-nearest-neighbours. They take place along the diagonals of the square lattice. Other possible interactions are the ones between nearest neighbours, involving the Co-O distance and bond angles far from 180° or 90°. These two exchange interactions are $J^{'}$ and J, respectively. Kinast *et al.*[82] refined a value of $-1.57\,\mathrm{K}$ for $\frac{J}{k_B}$ and -1.96 K for $\frac{J^{'}}{k_B}$.

1.3.7.2 The niobates - ANb_2O_6

Most magnetic niobates crystallise in the columbite-type structure, as evidenced by $FeNb_2O_6$, $CoNb_2O_6$ and $NiNb_2O_6$. These compounds have been extensively studied. Recently, Prabhakaran *et al.*[84] investigated the field dependence magnetisation (**M** vs **H**) of single crystals of ANb_2O_6 (A = Ni, Co, Fe, Mn) niobates.

$FeNb_2O_6$

Magnetic susceptibility[85,86,87] and neutron diffraction[85,88] measurements have been performed on both polycrystalline and single crystals $FeNb_2O_6$ samples. These studies demonstrate that iron diniobate oxide exhibits an antiferromagnetic order below 4.9 K. The χ vs T curves, depending on crystallographic orientation, expose that the magnetic moments lie in the *a*- *c* plane. Their orientation is close to the crystallographic *a* axis. Two modulation vectors are needed to index all magnetic peaks: $\vec{k_1} = (\frac{1}{2}, \frac{1}{2}, 0)$ and $\vec{k_2} = 0, \frac{1}{2}, 0)$. Heid *et al.*[85] performed neutron diffraction on $FeNb_2O_6$ single crystals. Heid's model for the magnetic structure of $FeNb_2O_6$ consists of two different magnetic domains, where each one results in one of the two propagation vectors. The sublattice magnetisation of $FeNb_2O_6$ according to Heid *et al.*[85] is exposed in Figure 1.24 below.

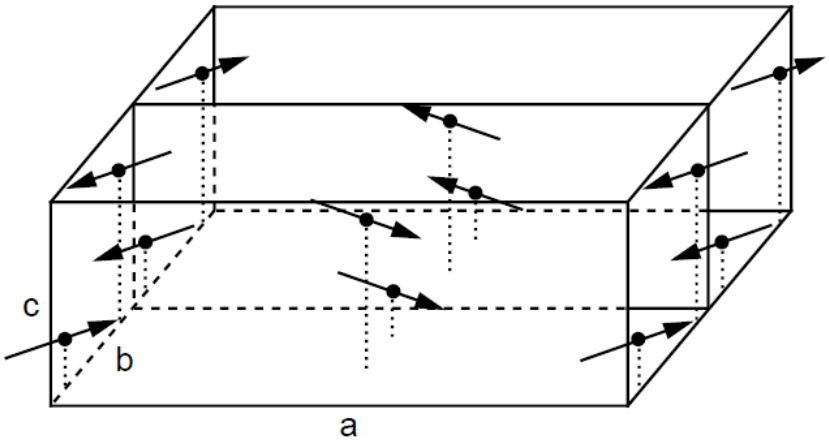

Figure 1.24: Magnetic structure of $FeNb_2O_6$ according to Heid *et al.*[85].

Figure 1.24 depicts the magnetic unit cell of $FeNb_2O_6$. It can be observed that there is a doubling the nuclear cell along the [0 1 0] direction. The black dots and arrows represent the Fe^{2+} ions and the magnetic moments they carry. Mossbauer studies[85,89] indicate that there are two magnetically nonequivalent sites of the Fe^{2+} ion a in the lattice. They are the corner ions (x = 0 or x =1) and the center ions (x = $\frac{1}{2}$). Along the *b*-axis the sequence of magnetic moments is identical to the one along the three axes in $CoTa_2O_6$: $\uparrow\uparrow\downarrow\downarrow$. The moments form a canting angle of 23° to the *a*-axis. The magnetic moments form ferromagnetic chains along the *c*-axis. Heid and coworkers refined a value of 4.5 μ_B per Fe^{2+} ion for the effective magnetic moment μ_{eff} of iron ions, in agreement with the theoretical value (4.52 μ_B).

To interpret the magnetisation measurements Heid *et al.*[85] took into account the crystal field, spin-orbit coupling, isotropic Heisenberg exchange, magnetic dipole-dipole interaction and an external field into account (Zeeman effect). Within this model for the magnetism in $FeNb_2O_6$ very good agreement between theory and experiment was obtained. This model reveals that the ferromagnetic superexchange in the chains along the [0 0 1] direction is the strongest interaction. The interchain exchange interaction was found to be smaller and antiferromagnetic.

$CoNb_2O_6$

The magnetic properties of cobalt niobate oxide have been extensively studied. Magnetic susceptibility[90,91,92], heat capacity[90,91] and neutron diffraction[91,92,93] measurements revealed two magnetic phase transitions. There is a switch from the paramagnetic state to an ordered spin structure at $T_{N1} = 2.95\,\mathrm{K}$, as evidenced by a sharp peak in the specific heat data and a broad maximum in the χ vs T curve. The second phase transition occurs at $T_{N2} = 1.97\,\mathrm{K}$. Magnetisation studies[90,91,93,94] demonstrate that below 1.97 K there is an commensurate antiferromagnetic structure. In addition, there is an intermediate state between the paramagnetic and antiferromagetic phases that changes with applied field. This intermediate state can be visualise by the presence of a $\frac{1}{3}$ magnetisation plateau[95] in the **M** vs **H** curve, for field in the *a*-*c* and *b*-*c* planes.

The crystallographic orientation dependence magnetic susceptibility from Scharf *et al.*[92] showed the magnetic moments within this antiferromagnetic structure are canted in the *a*-*c* plane. They form an angle of $\gamma = 31°$ with the *c*-axis. Like in $FeNb_2O_6$ the moments form ferromagnetic chains along the *c*-axis. The moments are arranged collinearly within *b*-*c* planes, and non collinearly between neighbouring *b*-*c* planes, as seen in Figure 1.25 below.

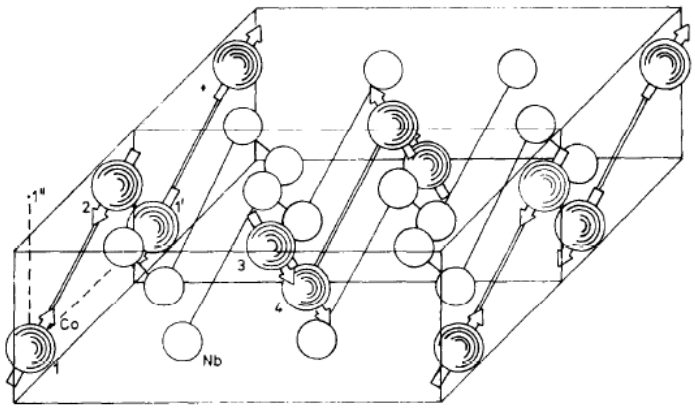

Figure 1.25: Antiferromagnetic structure of $FeNb_2O_6$ below 1.97 K according to Scharf *et al.*[92].

Figure 1.25 above exposes the non collinear magnetic antiferromagnetic structure of $CoNb_2O_6$ below 1.97 K, according to Scharf *et al.*[32]. Like for the sublattice magnetisation of $FeNb_2O_6$ there is a doubling the nuclear cell along the *y*-axis. The empty and plain spheres represent the Co^{2+} and Nb^{5+} ions, respectively. The magnetic moments are illustrated by arrows. The magnetic space

group associated with this structure is $P_b2_12_12_1$ (19). Recently Sarvezuk *et al.*[96] performed neutron diffraction on powdered $CoNb_2O_6$ sample and showed that two coexisting magnetic phases exist below 1.97 K. Two propagation vectors were needed to index all magnetic reflections: $\vec{k_1} = (0, \frac{1}{2}, 0)$ and $\vec{k_2} = (\frac{1}{2}, \pm\frac{1}{2}, 0)$. Each phase is associated with one propagation vector. The volume fraction for the $(0, \frac{1}{2}, 0)$ and $(\frac{1}{2}, \pm\frac{1}{2}, 0)$ phases are 80 and 20 %, respectively.

Several studies have been performed to understand the intermediate state between paramagnetic and antiferromagnetic states. According to Scharf *et al.*[92] it corresponds to an incommensurate magnetic structure with a propagation vector k = $(0, k_y, 0)$, $0.37 < k_y < \frac{1}{2}$. The value of k_y depends on the temperature. Scharf *et al.*[32] described the magnetic structure within this temperature range as a helical structure with the *b*-axis as the screw axis with an angle of 133°. Later, Hanawa *et al.*[91,97] investigated this helical structure through heat capacity and magnetisation measurements under applied fields on both powder and single crystals samples. Magnetic fields were applied along *a*, *b* and *c* directions. These studies revealed the antiferromagnetic character of the helical structure. Two spin-flips can be observed in the **M** vs **H** curves, for $H \parallel a$ and $H \parallel c$ for temperature between 1.97 and 2.95 K. These spin-flips indicate the existence of metamagnetic phases between T_{N1} and T_{N2}.

Mistuda *et al.*[92] performed neutron diffraction on $CoNb_2O_6$ single crystals below 3 K in order for a better understanding of the ordering of moments between 1.97 and 2.95 K. These investigations reveal strong ferromagnetic intrachain interactions in zigzag chains along the *c*-direction resulting in a quasi-one-dimensional. But magnetic order in other dimensions are expected. As temperature decreases and is near T_{N2} the magnetic structure of $CoNb_2O_6$ behaves as a 2D-system. It is evidenced by the fact that heat capacity data can be fitted by a 2D-Ising model. The restructuration of the magnetic structure for temperatures below T_{N2} highlights the presence of competing interactions such as the interchain exchange interaction and Co^{2+} single ion anisotropy.

Heid *et al.*[85,98] also investigated the magnetic structure of $CoNb_2O_6$. Field dependence magnetisation, with field in *a*-*c*, reveal the presence of three spin flip phases in the *c*-axis direction, with two of those phases sharing common boundaries when the same fields were applied to the *a*-axis. To explain all these features Heid and coworkers introduced a new model in which the dipole-dipole interactions are in the same order of magnitude than the interchain interactions.

Later Kobayashi *et al.*[99] performed neutron scattering with **H** parallel to the *c*-axis, at low fields. The results are slightly different to those of Heid and coworkers, as the new spin-flip phases comprised of ferrimagnetic ordering instead of ferromagnetic ordering. Kobayashi and coworkers used a quasi-1D Ising model to describe the different phases in $CoNb_2O_6$. According to their model, the magnetic structure of cobalt diniobate oxide consists of 1D ferromganetoc zigzag chains along the *c*-axis which are arranfged in an isoceles triangular geometry in the *a*-*b* plane. Due to the competition between interactions related to the triangle distortion one speaks of a geometrically frustrated isosceles triangular Ising antiferromagnet. This concept is discussed in details by Lee *et al.*[100] in

the 2010's paper. Lee and coworkers derived all possible magnetic structures of $CoNb_2O_6$ based on an isosceles triangular lattice. The magnetic structure of $CoNb_2O_6$ is fascinating and complex as there is interplay of quantum mechanics (interactions) and geometric frustration (triangular lattice). Eventually there is very good agreement between all these studies on the value of the refined effective magnetic moment μ_{eff} of Co^{2+}, which was found to be equal to $3\,\mu_B$ per Co^{2+}.

1.3.7.3 The antimonates ASb_2O_6

There have been few reports on the magnetic properties of antimonate oxides. This subsection summarises the seminal works on the magnetic $CoSb_2O_6$ and $NiSb_2O_6$.

$CoSb_2O_6$

Reimers *et al.*[80] performed one of the early studies of the magnetic properties of $CoSb_2O_6$. The researchers study found that $CoSb_2O_6$ exhibits a long-range antiferromagnetic order below $T_N = 13.0(2)\,K$. The heat capacity data confirmed the ordering of the magnetic moments of Co^{2+} by the presence of a λ-anomaly at T_N. It should be highlited that a broad maximum at around 35 K is observable in the susceptibility data. This broad maximum is indicative of short-range correlations, which is a signature of low-dimensional systems. The magnetic reflections can be indexed by the propagation vector $\vec{k} = (\frac{1}{2}, 0, \frac{1}{2})$. These two magnetic structures were found to be consistent with the reflection intensities. The two structures can be described in terms of two sublattices (origin and the body center) where the moments within one sublattice are antiparallel along [1 0 0] and [0 0 1] but parallel along [0 1 0]. All moments lie within the *a*-*b* plane along [1 1 0] and [1 $\bar{1}$ 0].

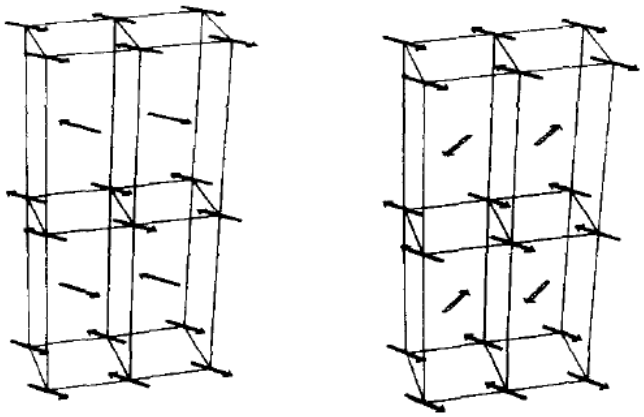

Figure 1.26: The ($2a$, a, $2c$) magnetic unit cell of $CoSb_2O_6$ according to the two models. The collinear and orthogonal models are displayed on the left and the right respectively[80].

Figure 1.26 above illustrates the two models for the magnetic structure of $CoSb_2O_6$, according to Reimers and coworkers. The arrows represent the magnetic moments. Both structural models illustrate the antiferromagnetic character of $CoSb_2O_6$. The lattice parameters of the magnetic unit cell along the *a*- and *c*-axes are the doubles of those of the nuclear structure. The structures differ in the angle of the moments between the two sublattices. Indeed for the structure shown on the left in

Figure 1.26 the two sublattices have collinear magnetic moments, whereas in the model on the right on Figure 1.26 the moments of the two sublattices are orthogonal. Because all the measurements were collected using polycrystalline samples, the two are indistinguishable. Consequently, the growth of large enough single crystals is very important for a better understanding of the magnetic properties of compounds.

Like $CoTa_2O_6$ powder magnetic susceptibility and specific heat data were modelled by an Ising model with S = $\frac{3}{2}$ spins placed on a square lattice. In such models the nearest neighbour exchange coupling J dominates the next-nearest neighbour exchange coupling $J^{'}$. Finally, Reimers *et al.*[80] refined a value of 4.62 μ_B per Co^{2+} for μ_{eff}.

$NiSb_2O_6$

Nickel metantimonate oxide $NiSb_2O_6$ is another magnetic antimonate. Magnetic susceptibility data[101]of this material demonstrate that the Ni^{2+} ions exhibit local magnetic order below ∼50 K followed by long-range antiferromagnetic order below $T_N = 6.7\,K$. Ehrenberg *et al.*[102] performed neutron diffraction on powdered $NiSb_2O_6$ samples. Like for $CoSb_2O_6$ all magnetic reflections were indexed by the modulation vector $\vec{k} = (\frac{1}{2},\ 0,\ \frac{1}{2})$. Ehrenberg and coworkers refined a magnetic structure in which the magnetic moments are collinearly aligned parallel to [1 1 0]. The magnetic moments build an arrangement of ferromagnetic and antiferromagnetic chains, which are perpendicular to each other. These chains run along the [1 0 0] and [0 1 0] directions, as seen in Figure 1.27 below.

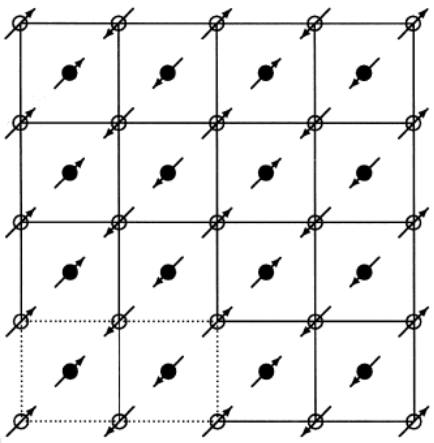

Figure 1.27: The magnetic structure of $NiSb_2O_6$ in the *a*-*b* plane, according to the Ehrenberg's model[102].

The empty and filled circles represent Ni^{2+} ions in (z = 0) and out (z = $\frac{1}{2}$) of the *a*-*b* plane, respectively. it should be noted that the magnetic moments form a "↑↑↓↓ " sequence along the *a*-axis. On the other hand ferromagnetic chains run along the *b*-axis. The dotted rectangle indicates a possible choice for the magnetic unit cell of $NiSb_2O_6$. Ehrenberg *et al.*[102] refined a value of 1.6(1) μ_B per Ni^{2+} ion as absolute value of the magnetic moments of nickel ions. This value is lower than the theoretical value of $g_o.m_s = 2\,\mu_B$, indicating that the spins are not completely ordered in this system.

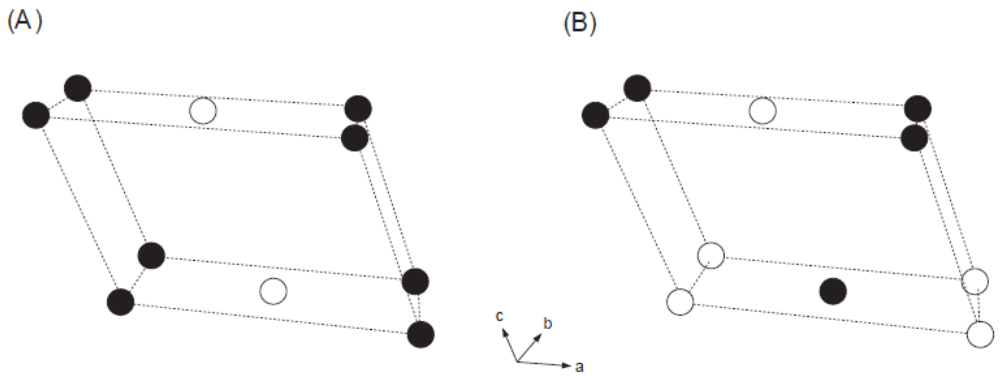

Figure 1.28: Two possible magnetic structures in α-CuV_2O_6 which produce (A) (100) and (B) $(10\frac{\bar{1}}{2})$ magnetic reflections, respectively. Only the Cu atoms are shown. $\uparrow$ and $\downarrow$ moments are represented by the open and solid circles, respectively.

1.3.7.4 The vanadates AV_2O_6

There have been few reports on the magnetic properties of vanadates. The magnetic properties of CuV_2O_6 and CoV_2O_6 are further discussed in details.

CuV_2O_6

Magnetic properties of α-CuV_2O_6 have been studied by means of susceptibility measurement, NMR and neutron diffraction on polycrystalline[103,104] and single crystals[105]. α-CuV_2O_6 crystallises in the triclinic structure of space group P $\bar{1}$ (2). Cu^{2+} spins ($S = \frac{1}{2}$) order antiferromagnetically below 22.6 K. This said one of the highlights of the susceptibility data is the presence of a broad maximum at around 48 K. This maximum is in fact indicative of low-dimensional short range correlations due to anisotropic exchange interactions between the Cu^{2+} ions in the crystal structure. A magnetic reflection appears at $2\theta = 16.3°$ and can be indexed as either (1 0 0) or (1 0 $\frac{\bar{1}}{2}$) on the basis of the original triclinic cell. Consequently Kikuchi[103] proposed two indistingishable models for the magnetic structure of this material. The non distinguishability comes from the fact that neutron diffraction was performed on powder samples. These models are illustrated in Figure 1.28.

In both magnetic structures, only the Cu atoms are shown. Up and down spins re represented by the open and solid circles, respectively. The nearest-neighbour spins align ferromagnetically. The broad maximum in susceptibility data indicates a dominant antiferromagnetic coupling between Cu^{2+} spins. Hence, the exchange coupling between the next-nearest neighbours is stronger than that between the nearest neighbours Cu^{2+} ions. The antiferromagnetic spin chains in α-CuV_2O_6 are therefore along [1 1 0] (or [1 $\bar{1}$ 0]) rather than [0 1 0]. Prokoviev[105] attempted to fit the temperature dependence of the susceptibility by a Heisenberg $S = \frac{1}{2}$ linear chain model. These attempts yielded unsatisfactory results indicating that α-CuV_2O_6 should be described as an anisotropic three-dimensional magnetic system. This is in agreement with the work of Vasilév and coworkers[104] who refined a value of -14 K and 36 K for the interchain (J') and intrachain (J) coupling constants, respectively. This relative large value of $|J'|$ compared with J confirmed then that α-CuV_2O_6 can not be described as a 1D antiferromagnet. They refined a a value of 1.6(1) μ_B per Ni^{2+} ion as absolute

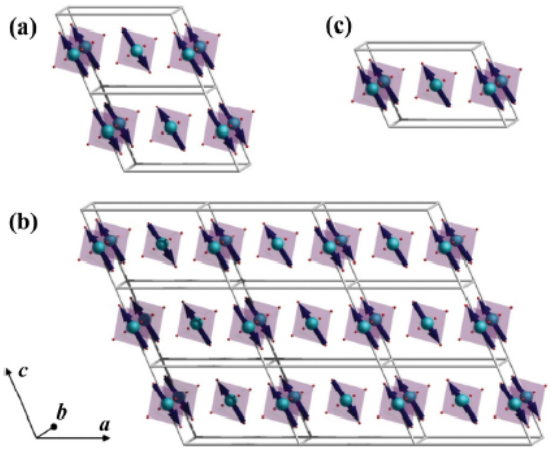

Figure 1.29: Magnetic structure ofα-CoV_2O_6 (a) in the antiferromagnetic ground state, (b) in the ferrimagnetic state , and (c) in the ferromagnetic state[106].

value of the magnetic moments of nickel ions.

CoV_2O_6

α-CoV_2O_6 crystallises in a brannerite-type structure. Magnetic susceptibility measurements were performed on flux grown α-CoV_2O_6 single crystals, with fields parallel to a, b and c axes. The χ vs T curves suggest that the moments lie in the a-c plane. The susceptibility curve for $H \parallel c$ has a higher response to temperature changes than the one for H $\parallel$ a, suggesting the c-axis is the easy axis for the Co^{2+} ions. It is an energetically favorable direction of spontaneous magnetisation. The χ vs T curves also reveal an antiferromagnetic ordering of the Co^{2+} ions below $T_N = 14\,\mathrm{K}$. Lenertz *et al.*[106] performed neutron diffraction on powdered α-CoV_2O_6 sample. The magnetic reflections were indexed by the propagation vector $\vec{k} = (1,\ 0,\ \frac{1}{2})$. Their refined subattice magentization is depicted in Figure 1.29 and corresponds to the structure on the top left (a).

In Figure 1.29 above Co and O atoms are represented by the blue and and red spheres, respectively. V and some O atoms are not shown for visibility reasons. The blue arrows indicate the direction of the magnetic moments. For the antiferromagnetic ground state (a) there is a doubling of the nuclear structure along the c-axis. One observes ferromagnetic chains along the b-axis and an antiferromagnetic arrangement in the a-c plane.

The application of a magnetic field -for temperature below T_N - creates excitations of the magnetic moments. Typically as the magnitude of the magnetic field **H** increases, the magnetic moments align themselves in the direction of the field. The state of the system in which all spins are parallel to each others and point in the direction of the field is the saturation point of the system. The moments order ferromagnetically at the saturation. The application of a magnetic field along particular directions may lead to some intermediate ordered states between the ground and the saturation states. The latter are called excited states. These excited states can be visualise via neutron diffraction measurements - under the application of a field.

In the case of α-CoV_2O_6 new magnetic peaks are generated for H = 2.5 T[106]. These magnetic reflections can be indexed with the modulation vector $\vec{k} = (\frac{2}{3}, 0, \frac{1}{3})$ in the C 1 (5) space group. Another way of presenting the sublattice magnetisation is to use a ninefold unit cell (3a, b, 3c) with no modulation vector in the P 1 (1) space group. This sublattice is shown at the bottom of Figure 1.29 (b), and it corresponds to a ferrimagnetic ordering of the spins. In the ferrimagnetic structure the chains follow an "up-up-down" sequence along the *a*- and *c*-axes. This ferrimagnetic ordering is associated with the 1/3-magnetisation plateau between 1.9 and 3.2 T in the magnetic field dependence of the magnetisation (M vs H)[106,107].

As the field reaches 5 T the magnetic moments reoder thermselves. It can be seen in the neutron diffraction patterns measured below 5 K as the peaks from both the antiferromagnetic and the ferrimagnetic superstructures are suppressed. Additionally extra reflections at the positions of nuclear reflections such as (1 1 0), (1 1 1), and (2 0 0) are observed. The latter correspond to a simple ferromagnetic order of spin chains with propagation vector (0 0 0), as shown in Figure 4.3 (c). In the anti-, ferri- and ferromagnetic states, as seen in Figure 1.29, the magnetic moments are at an angle of 9.3° with respect to the *c*-axis. This is in agreement with the susceptibility data from He *et al.*[107]. Note that co-existing magnetic phase were observed in non-aligned samples: antiferromagnetic and ferrimagnetic phases at 2.5 T; all three spin-ordered phases at 5 T.

The magnetic properties (ground state, field-induced magnetic states, the susceptibility data, puzzling steplike magnetic behavior) of $\alpha-CoV_2O_6$ can be reproduced by an Ising model[106,108,109] on a triangular lattice with frustrated antiferromagnetic couplings between neighbour pairs of sites. The magnitude of the ordered moments from 0 to 5.0 T is about 4.4(1) μ_B per Co^{2+} ion. This large value of μ_{eff} of Co^{2+} moments in monoclinic CoV_2O_6 significantly exceeds the ideal spin-only value of 3.87 μ_B, evidencing a strong orbital contribution.

Table 1.6: Magnetic properties of the antiferromagnetic ground state of some AB_2O_6. * planar = square lattice ; **triangle = isoscele triangle.

Compound	**propagation vector(s)**	**Long-range order**	**Short-range order**	**Model**	**Magnetic moment**
$FeTa_2O_6$	$\vec{k} = (\frac{1}{2}, 0, \frac{1}{2})$	$T_N = 8.5\,K$	$T_{max} = 15\,K$	planar* Heisenberg $S = \frac{1}{2}$	$5.06\,\mu_B/Fe^{2+}$
$CoTa_2O_6$	$\vec{k_1} = (\frac{1}{4}, \frac{1}{4}, \frac{1}{4})$ $\vec{k_2} = (-\frac{1}{4}, \frac{1}{4}, \frac{1}{4})$	$T_N = 6.6\,K$	$T_{max} = 15.6\,K$	planar Heisenberg $S = \frac{3}{2}$	$4.68\,\mu_B/Co^{2+}$
$FeNb_2O_6$	$\vec{k_1} = (0, \frac{1}{2}, 0)$ $\vec{k_2} = (\frac{1}{2}, \frac{1}{2}, 0)$	$T_N = 4.9\,K$		Heisenberg	$5.42\,\mu_B/Fe^{2+}$
$CoNb_2O_6$	$\vec{k_1} = (0, \frac{1}{2}, 0)$ $\vec{k_2} = (\frac{1}{2}, \pm\frac{1}{2}, 0)$	$T_N = 2.9\,K$		triangle** Ising $S = \frac{1}{2}$	$3.0\,\mu_B/Co^{2+}$
$CoSb_2O_6$	$\vec{k} = (\frac{1}{2}, 0, \frac{1}{2})$	$T_N = 13\,K$	$T_{max} = 35\,K$	Ising $S = \frac{3}{2}$	$4.62\,\mu_B/Co^{2+}$
$NiSb_2O_6$	$\vec{k} = (\frac{1}{2}, 0, \frac{1}{2})$	$T_N = 2.5\,K$			$1.6\,\mu_B/Ni^{2+}$
CuV_2O_6		$T_N = 22.6\,K$	$T_{max} = 48\,K$	Heisenberg $S = \frac{1}{2}$	$0.70\,\mu_B/Cu^{2+}$ $0.72\,\mu_B/Cu^{2+}$
CoV_2O_6	$\vec{k} = (1, 0, \frac{1}{2})$	$T_N = 14\,K$		triangle Heisenberg $S = \frac{1}{2}$	$4.4\,\mu_B/Co^{2+}$

1.4 Definition of the project

AB_2O_6 oxides are interesting materials to study, due to the wide range of compositions and crystal structures. The investigation of the structural-property relationship in these systems may lead to high temperature thermoelectric applications. This said, some AB_2O_6 exhibit exotic magnetic features, whose understanding raises questions regarding fundamental physical problems.
The thesis is organised in two parts, which consist of two chapters each. The first part discusses the thermoelectric properties of two AB_2O_6 oxides, whereas the magnetic structures of two other AB_2O_6 compounds is investigated in the second part. Prior to these two parts, Chapter 3 introduces some fundamentals on some transport properties: the Seebeck coefficient, the electrical and thermal conductivities. The projects presented in Chapter 4 and Chapter 5 are both thermoelectric applications-driven. In Chapter 4 the influence of a doping material (Y^{3+}) on the thermoelectric properties of $CdSb_2O_6$ is investigated. Polycrystallines Y-doped $CdSb_2O_6$ have been prepared by a solid-state reaction and their Seebeck coefficient, electrical conductivity have been investigated. Analysis and characterization of powdered WV_2O_6 are addressed in Chapter 4. Results of the investigations on the thermal conductivity and thermopower of this material are presented and discussed in Chapter 5. The electrical and thermal conductivity of tungsten divanadate oxide has also been measured and several models are assessed for the understanding of its behaviour. Furthermore, Chapter 6 and 7 are dedicated to the magnetic structures of $NiTa_2O_6$ and $NiNb_2O_6$. Chapter 6 is dedicated to the models for the sublattice magnetisation of nickel ditantalate oxide. The cation distribution of this material is also revisited. The last chapter of the thesis is dedicated to determination of the magnetic structure of $NiNb_2O_6$.

Chapter 2

Experimental and computational methods

This chapter is dedicated to the experimental techniques used throughout the thesis. The main techniques used for structural characterization were powder x-ray and neutron diffraction. There is an introduction to both the theoretical background and technical details about the specific instruments of these techniques. In addition, the computational methods related to these two techniques are also presented. It is then followed by a description of the ZEM-3 and the MMR instruments, utilised for thermoelectric characterization. An introduction to the principles of energy-dispersive x-ray (EDX) concludes the chapter.

2.1 Powder x-ray diffraction

2.1.1 Principles

X-ray diffraction[110,111,112] (XRD) relies on the phenomenon of diffraction, whereby x-rays encounter a periodic structure with geometrical variations of the length scale of the wavelength of the x-rays. William Lawrence Bragg and his father William Henry Bragg[113] were the first to observe particular patterns due to the interaction between x-rays and crystalline solids for specific wavelengths and incident angles. Their work was motivated by the demonstration of the wave character of x-rays by Max Von Laue[114].

A crystalline solid can be described by an ensemble of crystallographic lattice planes with distances d_{hkl}. As a set of x-rays meets the atomic planes their path is deflected and reflected. An x-ray diffraction pattern results from the interference between the scattered x-rays. Constructive interferences occur when the scattered x-rays are in phase. On the other hand destructive interferences is observed when the scattered x-rays are out of phase. Bragg derived the rule governing the diffraction pattern of crystalline solid by means of geometry. Figure 2.1 is a simple version of Bragg's model.

Two in-phase incindent waves, beam 1 and beam 2, encounter a set of atomic planes with separation d_{hkl}, at an angle θ. There is a path difference between the beam 1 which gets reflected by the plane *mm'* and the beam 2 which is transmitted then reflected by the plane *nn'*. This path difference is equal to (SQ + QT). The scattered waves 1' and 2' interfere constructively if (SQ + QT) is a

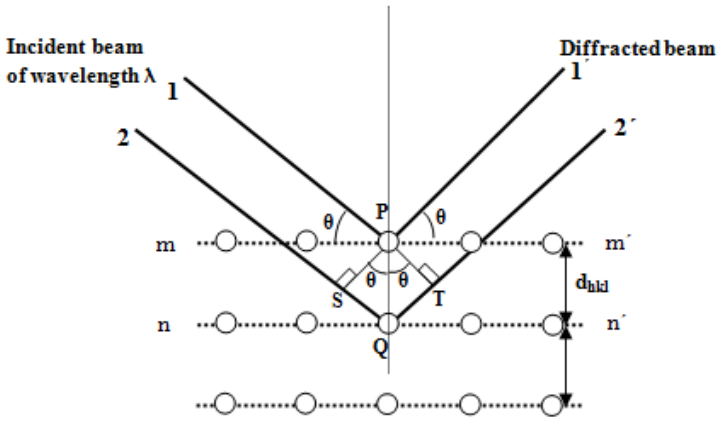

Figure 2.1: Schematic representation of diffraction by x-rays. Source: *http://nptel.ac.in/courses/*

multiple of the wavelength ($n\lambda$) of the incident x-rays. Let us derive SQ and QT from Figure 2.1.

In the rectangle triangle SPQ one has:

$$SQ = PQ.sin(\theta). \tag{2.1}$$

PQ is the interdistance between crystallographic planes, Hence, PQ = d_{hkl} = d. Similarly one has QT = d.sin(θ). Therefore the path difference is equal to the following equation

$$(SQ + QT) = 2dsin(\theta). \tag{2.2}$$

The condition for the scattered waves to be in phase can be written as:

$$2d_{hkl}sin(\theta) = n\lambda. \tag{2.3}$$

Equation (2.3) is known as the Bragg's law for x-ray diffraction. The determination of the atomic structures from x-ray diffraction was based on the fact that the detected scattered intensities were directly related to the the coordinates of the atoms. The electron density function in this case was expressed by the following formula:

$$\rho(xyz) = \frac{1}{V} \sum_{hkl=-\infty}^{+\infty} |F(hkl)|.exp[-2\pi.i.(hx + ky + lz)], \tag{2.4}$$

where x,y,z are the coordinate of an atom, h k l are the Miller indices, V represents the total volume of the material and F (h k l) is the atomic structure factor of the lattice along different planes. The structure factor F(h k l) of a diffracted x-ray along the (h k l) plane is is a mathematical function describing the amplitude and phase of the diffracted x-ray from crystal lattice planes characterised by Miller indices h,k,l. It should be noted that the scattering factor of an atom A (f_A) describes the effects of the electronic cloud of the atom on the path of an incident wave.

Figure 2.2: Experimetal set-up for x-ray diffraction. It is the PANalytical X'pert instrument, which was extensively used during the course of this work for powder x-ray diffraction.

2.1.2 Instrumentation

A simple experimental set-up for XRD involves an anode tube, also known as source, sending a flux of x-rays with a particular energy $\frac{hc}{\lambda}$ on a sample. The emitted photons interact with the atoms of various atomic planes within the sample, are reflected at different angles by the crystallographic planes and then are collected by a detector. Figure 2.2 presents a simplest set up for XRD.

Figure 2.2 illustrates the Bragg-Brentano configuration with a θ - θ geometry. In this diffractometer x-rays are produced from a monochromated cobalt anode and have a wavelength of 1.789 Å. The powder samples were sprinkled on a glass slide and fixed with a drop of ethanol. The glass slide was then placed in the centre of the spinner sample stage. This sample stage was chosen to minimize preferred orientation, which can lead to a misinterpretation of the x-ray diffraction pattern. An X'Celerator detector was used to detect the scattered x-rays. Eventually the optics of the PANalyitcal were kept the same for all measurements: programmable divergence slits of 4° and a beam mask of 15 mm.

2.1.3 Structure refinement

The refinement of the crystal structures of the studied AB_2O_6 from powder XRD was performed using the *Fullprof*[115] program. This software is based on the Rietveld method, which is a least-square fitting of the peaks profile Rietveld[116,117]. Several mathematical functions can be used to fit the peaks. Gaussian, Lorentzian and a Pseudo-Voigt are among these functions. A pseudo-Voigt is a linear combination of a Gaussian and a Lorentzian functions. Throughout the thesis, the pseudo-Voigt was chosen as model to fit the x-rays diffraction (XRD) patterns, as it best fitted the peaks within

the different XRD patterns. In order to fully fit an XRD pattern, an additional function is added as it takes into account the anisotropy of peaks. The combination of a pseudo-Voigt and this extra function is the Thompson-Cox-Hastings function. Consequently, the Thompson-Cox-Hastings [118] with axial divergence is the profile used to fully fit the AB_2O_6 oxides powder x-ray diffractograms.

Additionally, some fitting parameters indicate the agreement between the calculated pattern from the Thompson-Cox-Hastings function and the measured XRD pattern. The first agreement factor is R_B or R_{Bragg} is defined by equation (2.4):

$$R_B = \frac{\sum_{h,k,l} |I_{obs(h,k,l)} - I_{calc(h,k,l)}|}{\sum_{h,k,l} |I_{obs(h,k,l)}|} \tag{2.5}$$

R_{Bragg} indicates whether or not the model chosen was appropriate. However, this fitting parameter does not take into account peaks due to the presence of spurious phases. Another agreement factors are responsible for this task: the conventional R_p and weighted R_{wp} profiles. R_p and R_{wp} are defined by the following formulas, respectively:

$$R_p = \frac{\sum_i |y_{i,obs} - y_{i,calc}|}{\sum_i |y_{i,obs}|} \tag{2.6}$$

$$R_{wp} = \frac{\sum_i w_i.|I_{i,obs} - I_{i,calc}|^2}{\sum_i w_i.y_{i,obs}^2} \tag{2.7}$$

Where w_i is the statistical weight. The agreement factors are calculated at each iteration of the calculations and stored in a file. An alternative approach to access a structural refinement is to judge the quality of the residual line: the difference between observed and calculated profile. Low values of R_B, R_p nd R_{wp} are associated with a good fit: the residual is almost a straight line.

2.2 Powder neutron diffraction

2.2.1 Principles

Powder neutron diffraction is another structural characterization method used during the thesis. It follows the same principle (Bragg's law) as x-ray diffraction. The main difference is that the neutrons replace the x-rays. Neutrons are particles with no charge. The penetration depth of neutrons is therefore more important than that of x-rays. To go further, a neutron carries a spin $\frac{1}{2}$ and can thus interact with other spins. These are typically the spins of unpaired electrons within a material. Hence, neutron diffraction is the optimal method to investigate the magnetic structure of materials.

2.2.2 Instrumentation

Unlike x-ray diffractometers which are commonly found in laboratories neutron powder spectrometers are rare and they are found in reactor centres or spallation sources. This is due to their large size and the fact that their production of neutrons involve radioactive elements [119,120]. In spallation sources negatively charged hydrogen H^- are first accelerated to very high speed. Their electrons

are stripped off by a foil, leaving the H^- anions with only protons. The protons accumulate in bunches and are released as constitute a beam at specific rate. The beam of protons hit a target (tungsten W) thereby ejecting thermal neutrons of the target. Eventually, these neutrons are slowed down in a moderator and guided through beam lines to areas containing specific instruments where they are used in a wide variety of experiments. ISIS [121], in Didcot in the United Kingdom, is one of world-leading centre for neutron scattering experiments, using a spallation source. On the other hand, in Saclay in France neutron scattering experiments are performed with neutrons produced from a reactor source. At the LLB, neutrons are produced in the Orphée nuclear reactor with a nominal power of 14 W. Both diffractometers 3T2 and G4.1 were utilised for the structural and physical characterization of both $NiNb_2O_6$ and $NiTa_2O_6$. A description and comparison of both spectrometer is presented below.

G4.1

The medium resolution G4.1 is a two-axis diffractometer using cold neutrons with a wavelength of 2.428 338 Å. The neutrons are selected with a pyrolytic graphite (002) monochromator. The sample is placed in the cryostat configuration as pictured on Figure 2.3. 3 g of each nickel samples ($NiNb_2O_6$ and $NiTa_2O_6$) were placed in a vanadium tube. Scattered neutrons are detected by a multidetector: 800 (BF_3) cells with 0.1° of separation. One of the main advantages of this instrument is its high acquisition time - the lowest recording time is of the order of one minute. In addition to that the resolution of G4.1 is optimal at low angles as depicted in Figure 2.4 on page 52. As a consequence, G4.1 was utilised to determine the magnetic structure of both $NiTa_2O_6$ and $NiNb_2O_6$, and also to study the evolution of the magnetic moment value of the nickel ions within these materials as function of temperature. The magnetic structures crystallize in high symmetry space groups. The high symmetry planes which fulfill the Bragg's law are thus more intense at low angles ($2\theta < 60°$). The sublattice magnetisation can then be extracted from the magnetic reflections.

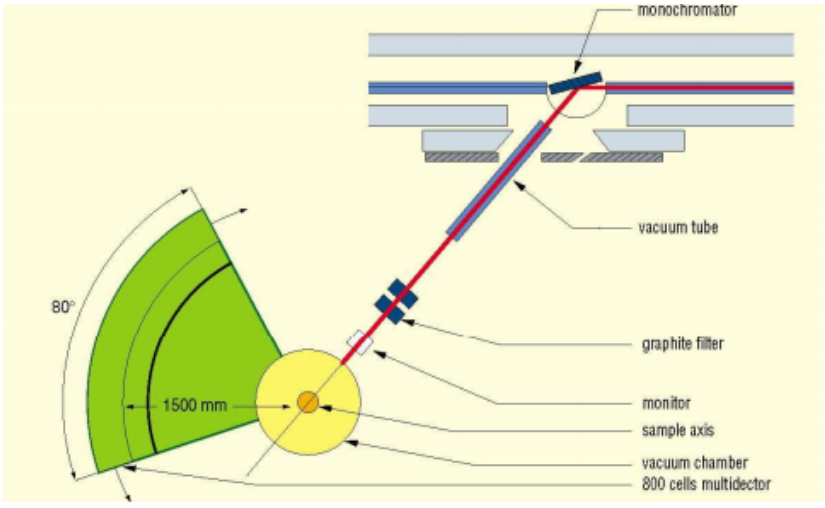

Figure 2.3: Schematic representation of G4.1 diffractomter. Source *http://www-llb.cea.fr/en/fr-en/pdf/g41-llb.pdf.*

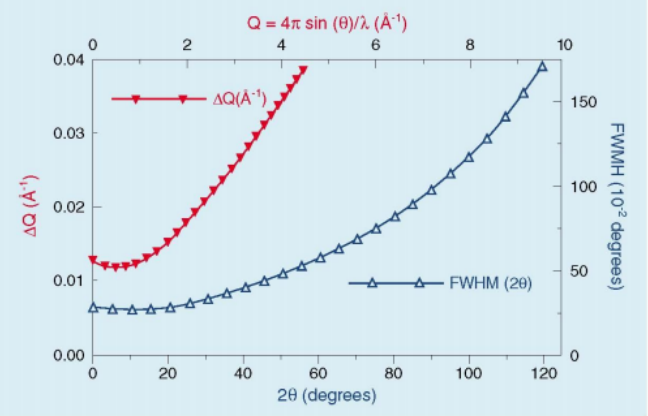

Figure 2.4: Resolution curve of the two-axis G4.1 diffractometer. Source *http://www-llb.cea.fr/en/fr-en/pdf/g41-llb.pdf.*

3T2

The 3T2 diffractometer is also a two-axis diffractometer, with a similar geometry as G4.1, as seen in Figure 2.5 below. In this spectrometer cold neutrons with a wavelength of 1.227 634 Å are selected with *Ge* (355) monochromator, instead of the pyrolytic graphite (002) in the G4.1 instrument. The sample is placed in vanadium tube, which is then introduced in cryofurnace configuration. On the other hand the scattered neutrons are collected by a detector bank constituted of *50* ^{3}*He* tubes spaced 2.4° apart. Another striking difference with the G4.1 system is the collection time on this apparatus. In fact the typical time on the 3T2 are between 12 h and 24 h. Consequently this spectrometer is often called the high-resolution 3T2 diffractometer. Its resolution curve is presented in Figure 2.6 on the next page. This accuracy allows one to accurately determine the positions and temperature factors of atoms within the crystallographic lattice. The neutron diffraction pattern of both nickel compounds was recorded with the same acquisition time: 24 h.

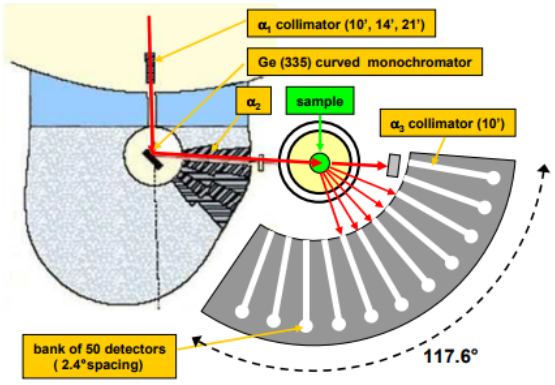

Figure 2.5: Schematic representation of the high-resolution 3T2 diffractometer. Source *http://www-llb.cea.fr/spectros/pdf/3t2-llb.pdf.*

The G4.1 and the 3T2 diffractometers complement each other: the atomic positions and thermal factors determined with 3T2 will be used to refine the magnitude of the magnetic moments evaluated from G4.1 data.

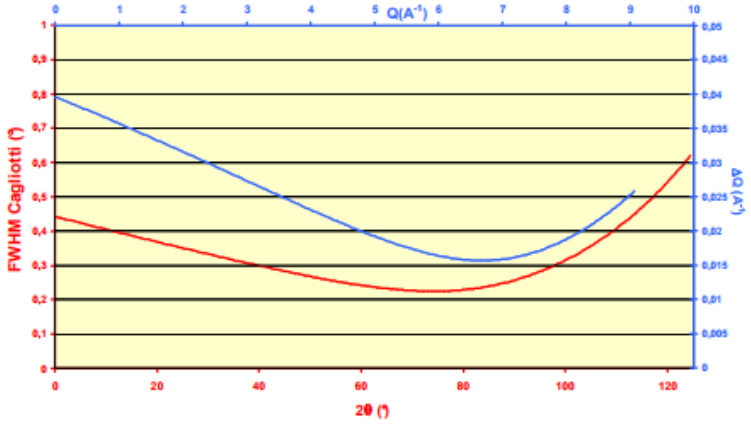

Figure 2.6: Resolution curve of the two-axis 3T2 diffractometer. Source *http://www-llb.cea.fr/spectros/pdf/3t2-llb.pdf*.

2.2.3 Structure refinement

The lattice parameters, Wyckoff positions were determined in the same fashion as for the powder x-ray diffraction data. Only the magnetic structure determination is described in this subsection.

In the paramagnetic regime, above the Néel (or Curie) temperature, the magnetic moments of the magnetic atoms are randomly orientated and only the coherent scattering due to the nuclear structure is observed. Below the ordering temperature (T_N or T_C) the magnetic moments ordered over a long distance: one observes extra reflections or magnetic reflections on the NDPs associated with these temperatures. More details on the origin of the ordering of the magnetic moments belowT_N or T_C are given in section B of the Appendix. The magnetic structure and other magnetic properties are extracted from the refinement of these magnetic reflections. Note that the refinement factor, R_{mag}, related to the fitting of the magnetic reflections is given by:

$$R_{mag} = \frac{\sum_{h,k,l} |I_{obs,m(h,k,l)} - I_{calc,m(h,k,l)}|}{\sum_{h,k,l} |I_{obs,m(h,k,l)}|}. \tag{2.8}$$

This is similar to R_B or R_{Bragg} except that the intensities are those of the magnetic peaks. There are two methods to determine the magnetic structure of a material from powder neutron diffraction. They are the magnetic symmetry and the representation analysis. The mathematical calculations of these two methods are implemented in the programs *Jana* and *Fullprof*, respectively.

***Fullprof*: A computational approach of the representation analysis method**

In this method the magnetic structure is described by the nuclear structure and a propagation vector $\vec{k}$. The different steps to determine the magnetic structure are the following:

- The derivation of the modulation vector $\vec{k}$ by the tool *k_search*. One first identifies the magnetic reflections, by subtracting a neutron diffractogram measured below T_N from a neutron diffraction pattern measured above. One then evaluates the d spacing associated with all the

different planes orientations. By combining all these d spacing values one can identify the crystal system (orthorhombic, cubic, etc) of the magnetic lattice. The propagation or modulation vector $\vec{k}$ is the ratio between the basis of nuclear and magnetic lattices.

- The derivation of the little group $G_{\vec{k}}$. $G_{\vec{k}}$ contains the symmetry operations of the nuclear space which leave the propagation vector invariant.
- The derivation of the irreducible representations (IRs) of the little group $G_{\vec{k}}$ by BasIreps. The periodicity of a primary IR agrees with the nuclear structure's periodicity. The active IRs and their combination are potential models for the magnetic structure of the studied material.
- The refinement of the magnitude and phase of magnetic moments, within the different models, is the last step of the refinement.

The tool FP_Studio enables the visualization of the magnetic structure. One of the advantages of the representation analysis method (thus *Fullprof*) is the reduction of number of possible models for a magnetic structure: one only focuses on the IRs of the little group $G_{\vec{k}}$ and their superposition. This is due to the Landau theorem on second order phase transition[122,123]. However it is not yet possible to refine $2\vec{k}$-magnetic structure. *Fullprof* does not yet handle magnetic space groups. As a consequence *Fullprof* can not differentiate between the subgroups of a representation.

***Jana*: A computational approach of the magnetic symmetry analysis method**

The magnetic structure can be described by one of the Shubnikov groups[124,125]. The refinement of the magnetic structure of a material from powder neutron diffraction with *Jana* has the following organization:

- The derivation of little group $G_{\vec{k}}$.
- The derivation of the IRs of the little group associated with the propagation vector $\vec{k}$.*Jana* is connected with ISODISTORT (Bilbao Crystallographer Server), which enables the derivation of the magnetic space groups related to an irreducible representation.
- The selection of a magnetic space group of the chosen representation. The Shubnikov group and its subgroups are the potential models for the sublattice magnetisation of the material.
- The final step is to refine the magnitude and phase of magnetic moments within the magnetic structure, according to the chosen Shubnikov group.

The program VESTA enables the visualisation of the refined magnetic structure. *Jana* is versatile program as it is possible to choose the different subgroups of the same representation. In addition*Jana* interacts with ISODISTORT, one can then combines IRs and select an the different magnetic subgroups associated with the combination of the chosen IRs. However, one of the disadvantages is the large number of potential models for a magnetic structure. In addition the

nomenclature of the representations is not straightforward in *Jana*.

The pros and cons of *Fullprof* and *Jana* have been discussed. The magnetic symmetry refinement (*Jana*) and the representation analysis (*Fullprof*) are complementary for magnetic structure determination. Both software were utilised to shed light on the discrepancies between the magnetic structure models of $NiTa_2O_6$ and to determine the magnetic sublattice magnetisation of $NiNb_2O_6$.

2.3 Thermoelectric measurements on the ZEM-3

The ZEM-3 instrument, in Figure 2.7 on page 56, enables the simultaneous measurement of the electrical conductivity (σ) and Seebeck coefficient (α) of bulk or thin films materials within the temperature range from 25 °C up to 1000 °C. The instrument is connected to computer program which controls the measurement and collects the data. A bottle of He gas and a vacuum pump are connected to the apparatus in order to cool and evacuate the furnace, respectively. The sample is situated in the furnace. The sample can either be a rectangular bar or a rod, which is clamped between two electrodes. The difference of temperature between these two electrodes must be less than 50 °C. Two probes 3 mm apart are placed in contact with the rectangular bar. These probes are also thermocouples of type K (Type M8 & L). Figure 2.8 on page 57 is a schematic representation of the furnace.

As illustrated in Figure 2.8 a current is constantly supplied to the sample. For the measurement of the conductivity, a potential difference is measured between the two side probes. Knowing the width of the sample the software program calculates the conductivity (σ) of the sample. Regarding the thermopower, the bottom electrode plays the role of hot end whereas the top electrode is the cold end. The difference of temperature between the side electrodes generates a difference of potential. The Seebeck coefficient (α) is given by the ratio between the created voltage and the applied temperature difference.

2.3.1 Sample preparation

The sample shape for the ZEM system can either be a rectangular bar or a cylinder. An ideal sample should have the following dimensions: from 6 mm up to 22 mm long and between 2 to 4 mm wide. For this work the rectangular bar shape was chosen. This was done in order to insure a good electrical contact between the side probes and the rectangular column. A rectangular bar is prepared in the following manner.

- The powder is pressed between two die within a pellet press instrument. This process leads to the formation of a pellet.
- The pellet is pressurised at 30 psi for 10 mins using the cold isostatic pressure - also known as CIP.
- This pressurised pellet is then sintered at a higher temperature than the one used for the synthesis.

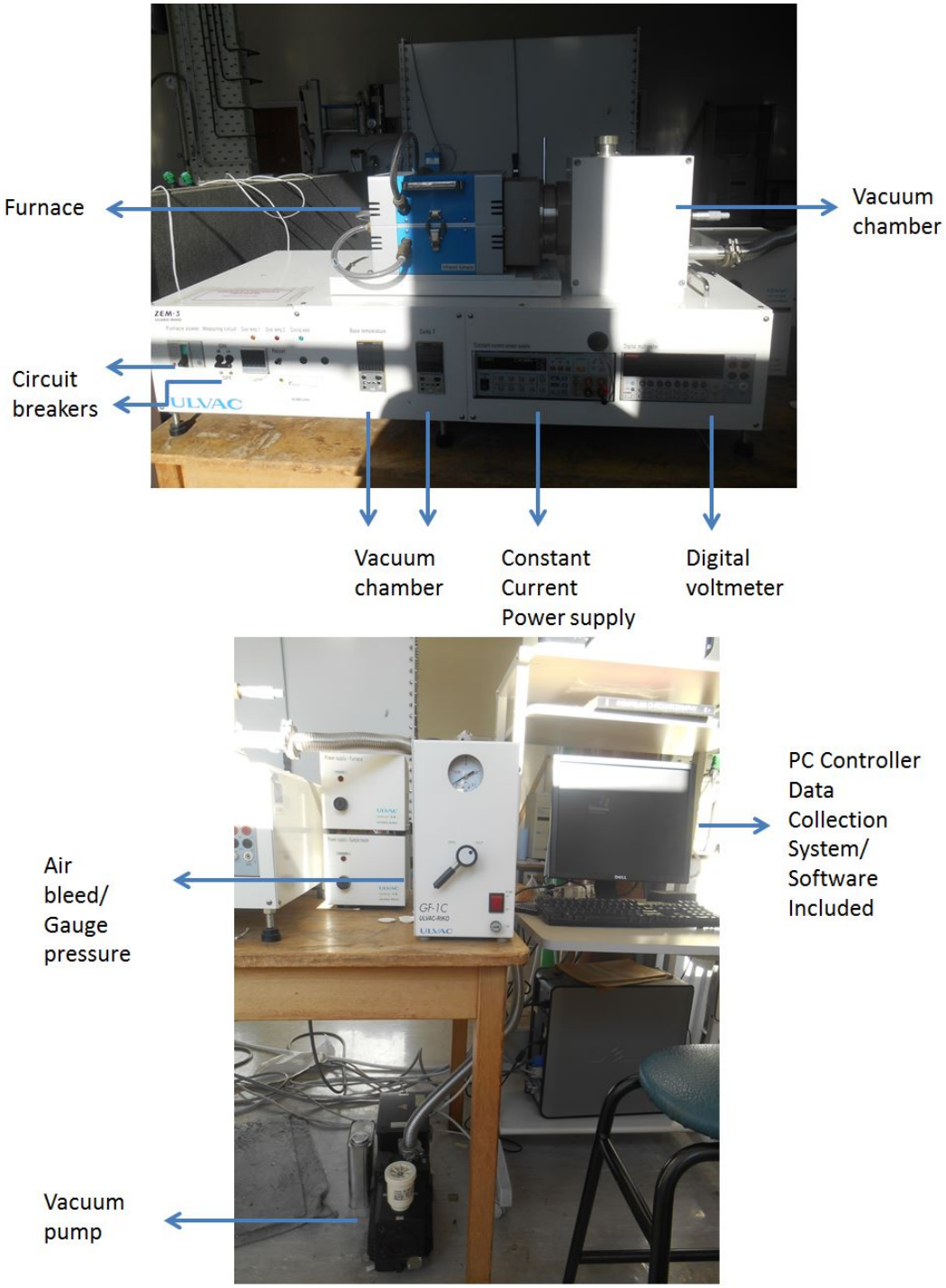

Figure 2.7: The ZEM-3 instrument utlised for the measurement of conductivity and thermopower of Y-doped $CdSbO_6$ and WV_2O_6.

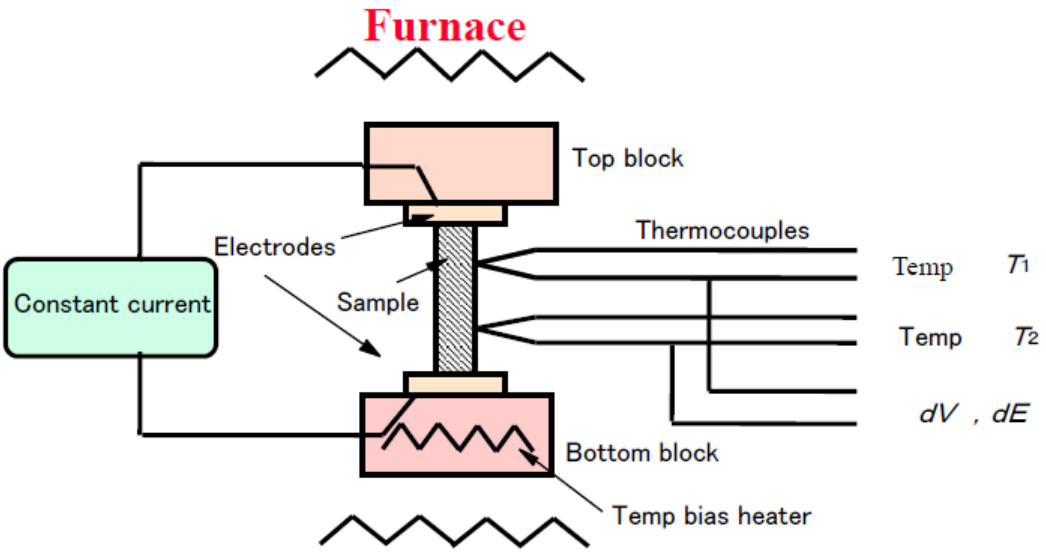

Figure 2.8: Schematic representation of a furnace within a ZEM-3 instrument.

- Eventually using wax and a diamond cutter rectangular bars are prepared.

To ensure good electrical contact all surfaces of the rectangular bars are polished. Rectangular bars of WV_2O_6 and Y-doped $CdSb_2O_6$ have been prepared throughout the thesis with this method. To calculate the density of a pellet two methods were utilised: the Archimede's method and the standard method. The standard method is simply the ratio of the mass by the volume. The former method, established by Archimede, gives an indication of the porosity of an object by use of a liquid. The principle of this method states that the apparent weight of an object immersed in a liquid decreases by an amount equal to the weight of the volume of the liquid that it displaces[126]. The presence of pores within the object creates an important decrease of the density of the object. This principle is summed up by the following formula:

$$d_o = d_s . \frac{m_1}{m_3 - m_2}, \tag{2.9}$$

where m_1 and m_2 represent the mass of the object before immersion in the liquid and when the object is completely submerged by the liquid, respectively. After been taking out of the container, typically a beaker, the object is dried with non absorbing materials. One then measures its mass m_3. d_o and d_s are the density of the object and the solvent used for the experiment, respectively.

2.3.2 A measurement at a specific temperature

The first step in the process for the measurement of the Seebeck at a specific temperature is the insertion of the rectangular bar between the two electrodes. The probes and electrodes are tightened around the sample to insure a good ohmic contact. It is followed by a rapid test of the ohmic character of the bar. The *V-I* plot is a straight line in the ideal case, otherwise polishing may be needed. The furnace is then closed. It is then evacuated (via the vacuum pump) and filled with helium several times. The dimensions of the bar are entered in a program which controls the measurements and

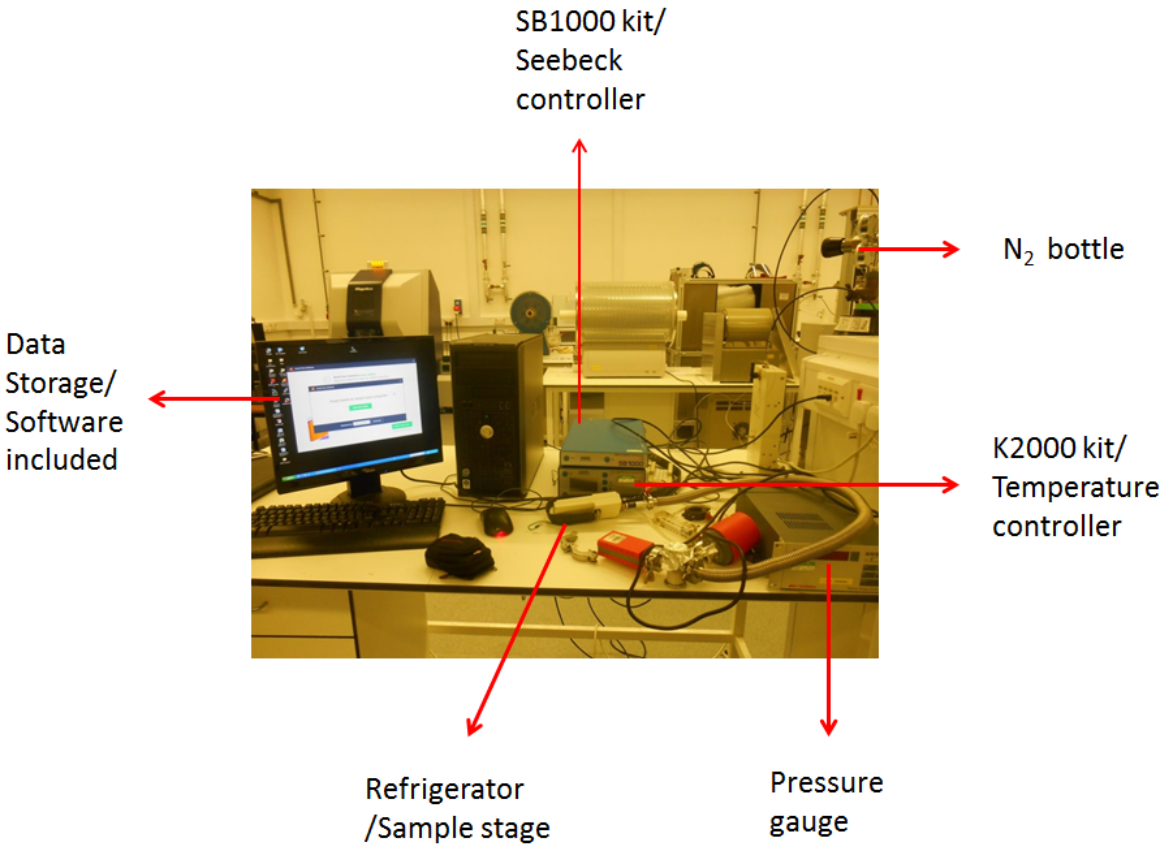

Figure 2.9: A MMR instrument. This apparatus measures the thermopower of metals and semiconductors.

stores the data. Furthermore, the furnace is heated up to the set temperature. Once this set temperature does not fluctuate the system creates three ΔT between two electrodes. The plot α vs ΔT gives a line and the slope of this line corresponds the thermopower of the bar. At a specific temperature the thermopower is measured several times (ΔT), in order to have a better statistics, thus a better accuracy on data.

2.4 Thermoelectric measurements on the MMR

The MMR system is an instrument which measures the Seebeck coefficient of metals and semiconductors for temperatures between 80 K and 300 K. The instrument is made up of various kits: a SB1000 which evaluates the thermopower, a K2000 which controls the temperature of the system and a chamber where the sample is mounted on a sample stage. Similarly to the ZEM-3 instrument, the MMR can be connected to a vacuum pump to evacuate the chamber. The chamber can thus be filled with (N_2) gas, which enables a cooling of the sample stage. The instrument is connected to a computer program, which controls the measurement and stores the data. Figure 2.9 at the top of the page illustrates the MMR system utilised throughout the thesis.

The sample stage in the MMR instrument is different to that of the ZEM-3. There are two pairs of thermocouples: one of copper and a metal with known properties, and the other pair of copper and a the material whose thermopower needs to be determined. Each pair of thermocouples form two junctions. One of the junctions is considered a reference junction, and the other the

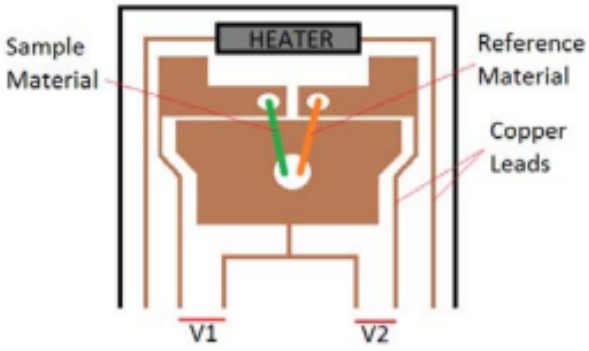

Figure 2.10: Sample stage in the MMR system. The orange and green bars represent the fference and sample materials, respectively. Source: *www.semimetrics.com/*

working junction. The working junction is near the heater and the latter is controlled by the MMR Programmable Seebeck Controller SB1000. The refrigerator is placed underneath the sample stage near the reference junction and is controlled by the K2000 temperature controller. The Seebeck stage has two outputs: one for the reference material V2 and one for the material with properties to be determined V1.

2.4.1 Sample preparation

For the SB1000 instrument a small bar is designed, but with smaller dimensions in comparison to that of the rectangular bar for the ZEM. One of the main requirements on the sample dimension is that its length needs to be similar to that of the reference wire: from 4 up to 6 mm. In addition to that, the the bar's thickness has to be of the order of magnitude of the wire's thickness. It is typically 0.002 up to 0.032 mm. Successive polishing are needed to design bars for the MMR system. Silver paint is used to mount the sample and the reference wire on the sample stage in order to insure a good ohmic contact. Throughout the thesis the reference wire used for the measurements of the thermopower of AB_2O_6 oxides was constantan.

2.4.2 A measurement at a specific temperature

The heater and the refrigerator play the role of the hot and cold ends, respectively. If power is applied to the heater a temperature difference will be created between the working and reference junction. This is due to their respective distance from the heater. As a consequence, differences of potential will be generated in each pair, giving non zero values to V1 and V2. These two voltages can be expressed by the following formulas:

$$V1 = \alpha_1.\Delta T, \tag{2.10}$$

$$V2 = \alpha_2.\Delta T. \tag{2.11}$$

α_1 and α_2 are the Seebeck coefficient of the material with unknown properties and the reference

wire, respectively. Therefore, the Seebeck coefficient of the material is given by:

$$\alpha_1 = \alpha_2 . \frac{V1}{V2} \tag{2.12}$$

Like in the ZEM-3, for a better accuracy on the value of the sample's thermopower three different ΔT are created at a specific temperature. It is also common to perform measurements at different power settings as the power controls the temperature difference: the greater the power the greater the ΔT. The difference of temperature varies from 0.01 to 2 K.

2.5 EDX analysis

Energy-dispersive x-ray (EDX) is another structural characterization technique. This technique enables the calculations of atomic and mass percentage for each element within a studied compound from SEM images. The principles of this technique are presented below.

An incident beam of electrons is focused onto the studied material. These electrons have a specific energy and therefore excite some electrons of the inner shells (K, L,M,etc) of the studied sample. The excited electrons will be ejected from the atom into the vacuum - thereby leaving holes in the inner shells. Some electrons of the higher energy levels will fill the holes of the energy levels of the inner shells, thereby there will be emission of an x-ray. The energy of this x-ray is characteristic of the difference in energy between higher- and lower-energy levels. However, only the transitions for which the difference of quantum number of orbital angular momentum $\Delta l = \pm 1$ are allowed. The emitted x-rays are detected and the result of this process is a pattern constituted of peaks. The x- and y-axes of this diagram correspond the energy and the intensity of the x-rays, respectively. The detected x-rays have different energies. These energies correspond to the different states of an element X: X^+, X^{2+}, etc. By combining the peak position (energy) and its intensity one can determine the content of each element within the studied material. For more details on energy-dispersive x-ray the reader is encoruaged to consult the book of Shindo *et al.*[127]. Another description is proposed by Goldstein[128].

Chapter 3

Transport properties fundamentals

In this chapter fundamentals on some transport properties are introduced. The three physical quantities (thermopower, electrical and thermal conductivities) related to the Figure of merit of a material are successively derived.

3.1 The thermopower

3.1.1 Mechanisms of Seebeck effect

The Seebeck effect (or thermopower) involves two principal physical phenomena, which are the charge-carrier diffusion and the phonon drag. The former is often referred as the entropy per carrier. As a material is exposed to a temperature gradient, there is unbalance of free-carrier concentration at the two ends of a conductor. The free-carriers tend to diffuse from the hot end to the cooler one to reach a steady state. The charge-carrier diffusion builds up a net charge at the cold end. It gives rise to an electrostatic potential counteracting the chemical potential of the diffusion and brings the system to equilibrium.

The second effect related to the Seebeck effect is the phonon drag. Its contribution to the thermopower is more important at low temperature than at high temperature. Electrons have a very long relaxation time at low temperature, hence transfer their momentum to phonons in the direction of the electric current. This energy transport contributes to the Peltier heat which may be much larger than the charge-carrier diffusion effect. The temperatures for which the phonon drag is important are those which fulfill the following relation:

$$T \sim \frac{1}{5}\Theta_D \tag{3.1}$$

where Θ_D is the Debye temperature. The phonon drag vanishes as temperature increases.

3.1.2 Generalised description of the Seebeck coefficient

In his 1971's paper [129], Fritzsche derived a general expression of the thermopower α without reference to a specific conduction process. He writes the Seebeck coefficient as an integral over one electron energy states. From this generalised formula of α one can derive Mott's thermopower formula for metallic conduction around of the Fermi level and also the familiar thermopower formula for crys-

talline semiconductors. However Fritzsche also added that his expression is valid if one does not take into account correlation effects.

The starting point of his derivation is to express the electric conduction or conductivity as

$$\sigma = \int \sigma(E) dE. \tag{3.2}$$

$\sigma(E)$ is the differential conductivity and a measure of the fractional contribution of electrons with an energy E to the total conductivity. At a finite temperature only electrons near the Fermi surface contribute to the conduction process. Hence, equation (3.2) can be written as

$$\sigma \equiv \int \sigma(E)(-\frac{\partial f_{eq}}{\partial E}) dE. \tag{3.3}$$

The second term in the integral is a bell-shaped function centered at E = E_F, where f is the Fermi-Dirac distribution and E_F is the Fermi energy. At any temperature T, f is given by

$$f(E) = \frac{1}{e^{\frac{(E-E_F)}{k_B T}} + 1} \tag{3.4}$$

Fritzsche then derives the Peltier coefficient Π as a function of the conductivity. Π corresponds to the energy transported per unit charge. Every electron above the Fermi level contributes to Π in proportion to its contribution to σ. Mathematically it corresponds to $\frac{\sigma(E)}{\sigma}$. The Peltier coefficient is given by the formula formula:

$$\Pi = -\frac{1}{e} \int (E - E_F) \frac{\sigma(E)}{\sigma} dE. \tag{3.5}$$

The Thomson relation[10] relates Seebeck and Peltier coefficients:

$$\Pi = T\alpha \tag{3.6}$$

where T is the temperature. One then gets Fritzsche's generalised expression for the thermopower:

$$\alpha = -\frac{k_B}{e} \int \frac{(E - E_F)}{k_B T} \frac{\sigma(E)}{\sigma} dE. \tag{3.7}$$

3.1.3 The Seebeck coefficient for *n*- and *p*-type semiconductors

From equation (3.7) one can derive the familiar expressions of the thermopower for *n*- and *p*-type semiconductors. One of the assumption made for such cases is that the conduction take place only in a single band, located at the density of states edge. For a *n*-type semiconductor, this edge is the bottom of the conduction band (CB). One arrives at the following well known expression for the thermopower :

$$\alpha = -\frac{k_B}{e}.(\frac{(E_C - E_F)}{k_B T} + A_C). \tag{3.8}$$

It is due to the fact that the integral in equation (4.10) can be viewed as a weighted average. The term $\frac{\sigma(E)}{\sigma}$ indicates the contribution of the electron of energy E to the electric conduction. For a *n*-type semiconductor only carries whose energy E > E_F participate at the electrical conduction. As a consequence the major part of the integral is equal to $\frac{(E-E_F)}{k_B T}$. The term A_C is a constant and it accounts for the carriers distributed beyond E_C; it is equal to

$$A_C = \int_0^\infty \frac{\epsilon}{k_B T}\sigma(\epsilon)d\epsilon / \int_0^\infty \sigma(\epsilon)d\epsilon \tag{3.9}$$

with ϵ= E - E_C. In a similar way, one can derive the thermopower of *p*-type semiconductor, should conduction take place only in a single band located at the top of the valence band. α in this case is given by

$$\alpha = \frac{k_B}{e}.(\frac{(E_F - E_V)}{k_B T} + A_V). \tag{3.10}$$

The weight average A_V is equal to

$$A_V = \int_{-\infty}^0 \frac{\epsilon}{k_B T}\sigma(\epsilon)d\epsilon / \int_{-\infty}^0 \sigma(\epsilon)d\epsilon, \tag{3.11}$$

and $\epsilon = E_V$ - E.

3.1.4 The Seebeck coefficient for metals and degenerate semiconductors

It is possible to derive the thermopower's expression of metals and heavily doped semiconductors from the generalised expression of α. This derivation is done by Mott in his book entitled *The theory of the properties of metals and alloys*[130]. Mott established that in metals and degenerate semiconductors in which conduction occurs in multiple bands, the Seebeck coefficient is expressed as

$$\alpha = \frac{(\pi k_B)^2 T}{3q}\frac{\partial ln[\sigma(E)]}{\partial E}\|_{E_F} \tag{3.12}$$

q and k_B are the free-carrier's charge and the Boltzmann's constant, respectively. equation (3.12) is the well known Mott formula, which relates the Seebeck coefficient to the derivative of the differential conductivity. This formula can also be derived from Boltzmann equations[131,132]. Mott formula can be simplified under the following approximations: (i) conduction occur in a single parabolic band, (ii) the scattering effects are neglected. For such cases equation (3.12) becomes:

$$\alpha = \frac{8(\pi k_B)^2 T}{3eh^2} m^* T(\frac{\pi}{3n})^{2/3}. \tag{3.13}$$

m^*, h and n represent the effective mass of the free-carrier, the Planck's constant and the carrier concentration, respectively. This formula indicates that the Seebeck coefficient of metals and heavily doped semiconductors is linearly proportional to temperature.

3.1.5 The Seebeck coefficient for metal oxides

In transition-metal oxides (TMOs) the correlation between electrons plays a major role in the material properties[133]. This correlation can no longer be neglected in the derivation of α. After the report of Terasaki on the large thermopower of $Na_{0.5}CoO_2$ single crystals[31], numerous investigations (theoretical and experimental) were carried out in order to comprehend the anomaly large values of α in this metal oxide. Taking into account the electron transport properties of semiconductor oxides and the theory of irreversible thermodynamics the Seebeck coefficient in metal oxides can be expressed as

$$\alpha = -\frac{k_B}{e}(\frac{H}{T} - \frac{\mu}{T}) \tag{3.14}$$

where μ is the chemical potential and H is the heat transport per particle[134]. In the high-temperature limit, Koshibae and Maekawa[133] demonstrated that H becomes negligibly small, as the heat transfer integrals become much lower than k_BT. Mathematically, the term $\frac{H}{T}$ goes to zero as $T \to \infty$. The thermopower becomes proportional to the chemical potential

$$\alpha = \frac{\mu}{eT}. \tag{3.15}$$

According to thermodynamics, the chemical potential and entropy of a system are tied by the following relation:

$$\frac{\mu}{T} = -(\frac{\partial s}{\partial n})_{E,V} \tag{3.16}$$

where s is the entropy, E and and V are the internal energy and the volume of the system, respectively. n is the concentration of the charge carriers. It follows that

$$\alpha = -\frac{1}{e}(\frac{\partial s}{\partial n})_{E,V}. \tag{3.17}$$

The above equation clearly demonstrates that the thermopower can be defined as the entropy per charge carrier in a material.

In strongly correlated systems[33,37,135] such as TMOs the spin and orbital degrees of freedom of the charge carrier must be considered to evaluate the thermopower. Beside for high temperature limit the entropy can be written as $s = k_B\ln(g)$, where g represents the degeneracy of the system. g represents the number of ways of rearranging the charge carriers in the different energy levels N, taking into account the spin, charge and orbital degeneracy. Therefore, in the high temperature limit, the thermopower in strongly correlated transition-metal oxides is given by

$$\alpha = -\frac{k_B}{e}(\frac{\partial ln(g)}{\partial n})_{E,V}. \tag{3.18}$$

This equation is the so-called Heikes[37] formula for thermopower. In order to simplify this expression one needs to determine the degeneracy. For instance, for a system of spinless fermions no two particles can occupy the same site because of the Pauli's principle (Figure 3.1A). g is therefore

$$g = \frac{N!}{(N-n)!n!}. \tag{3.19}$$

Using Stirling's approximation, ln $(n!) \simeq n$ ln (n) - n, and differentiating with respect to n, the thermopower can be rewritten as

$$\alpha = -\frac{k_B}{e} ln[\frac{1-\rho}{\rho}] \tag{3.20}$$

where$\rho = n$ / N is the carrier density, the ratio of charge carriers to available sites (N). This formula is the generalised Heikes formula. This situation is physically applicable to a system in enormous magnetic fields or electron-paired with strong binding energy[134].

For a system of electrons with spin, an electron can either be in the spin-up or spin down configuration. Two parameters control the degeneracy: the Coulomb repulsion between two electrons and the overall temperature of the system. The former parameter can be seen as a kinetic energy, as it allows electrons to hop between sites. If the thermal energy (k_BT) is greater than the one-site Coulomb repulsion (U_o two electrons can occupy the same site, see Figure 3.1B. The degeneracy then represents the number of ways of distributing independently the $N_\uparrow$ and the $N_\downarrow$ among the N sites. g can be expressed as

$$g = \frac{2N!}{(2N-n)!n!}. \tag{3.21}$$

Consequently, the thermopower is expressed as

$$\alpha = -\frac{k_B}{e} ln[\frac{2-\rho}{\rho}]. \tag{3.22}$$

Furthermore, for a system of fermions with spin, where the electron–electron repulsion (U_o) is greater than the thermal energy (k_BT), there is forbidden double occupancy as shown in Figure 3.1C. The electronic degeneracy and the Seebeck coefficient are the respective following relations:

$$g = 2^n \frac{N!}{(N-n)!n!}. \tag{3.23}$$

$$\alpha = -\frac{k_B}{e} ln(2[\frac{1-\rho}{\rho}]). \tag{3.24}$$

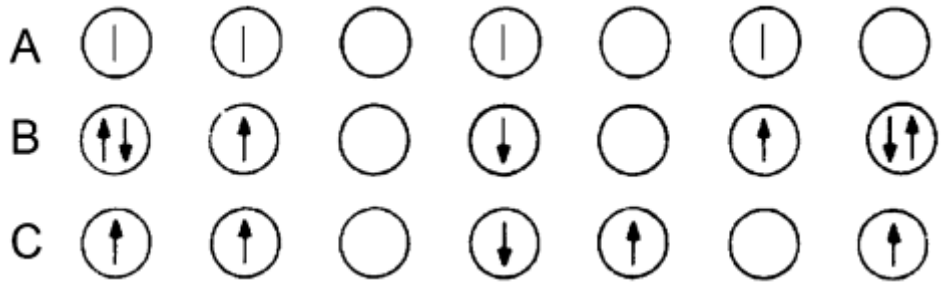

Figure 3.1: Possible high-temperature site configuration of (A) spinless fermions, (B) fermions with spin without coulombic interaction, and (C) fermions with spin with large electronic interactions.[134]

One can rewrite the last equation as

$$\alpha = -\frac{k_B}{e} ln(2) + -\frac{k_B}{e} ln[\frac{1-\rho}{\rho}]. \tag{3.25}$$

This equation demonstrates that thermopower for such systems is greater than that of spinless fermions. Consequently the spin degrees of freedom can enhance the Seebeck coefficient of some TMOs. Figure 3.1 illustrates the three different configurations discussed above. The first one (A) corresponds to a system of spinless fermions. On the contrary for (B) and (C) one deals with fermions with spins. These configurations are associated with $k_B\mathrm{T} \gg U_o$ and $k_B\mathrm{T} \ll U_o$, respectively.

Eventually, one considers systems in which one cation - whose electrons are responsible for the electric conduction - is present with mixed valency or two different electronic configurations. This is typically the case of Co^{3+}/Co^{4+} in $Ca_3Co_4O_9$ or Mn^{3+}/Mn^{4+} in doped $CaMnO_3$[133,134,135]. Therefore, if g_I and g_{II} are the electronic degeneracies of sites I (Co^{3+}) and II (ceCo^{4+}), the thermopower[33] can be expressed as a function of $\frac{n}{N}$

$$\alpha = -\frac{k_B}{e} ln\{\frac{g_I}{g_{II}}\{\frac{1-\rho}{\rho}\}\}. \tag{3.26}$$

This equation shows that the electronic degeneracies ($\frac{g_I}{g_{II}}$) of the ions involved play an important role in defining the magnitude and sign of the thermopower for oxide thermoelectric materials. Koshibae and Maekawa[33] investigated the impact of spin, charge and orbital degeneracy on the thermopower in cobalt oxide materials such as $NaxCoO_2$ and $La_{1-x}Sr_xCoO_3$. They demonstrated that in such compounds the three states of Co^{3+} and Co^{4+} sites, i.e., low-spin, intermediate spin and high-spin states, are considered to be close in energy. The large degeneracies of spin, charge and orbital in Co^{3+} and Co^{4+} sites, but also the ratio between them are important for the enhancement of thermopower.

3.2 The Electrical conductivity of semiconductor oxides

3.2.1 The broad band model

The band model is based on the molecular orbital theory[136]. A solid can be described as aggregations of an almost infinite number of atoms in a periodic lattice. The interaction between atoms lead to an overlap of the atomic orbitals which are closely spaced in energy and spread over the whole crystal.

The narrowly spaced energy states form energy bands. The electronic structure of the solid thus does not consist of discrete energy levels but consists of bands. There are three types of materials: metal, semiconductor and insulator. The electronic structure of semiconductors is marked by a gap between two bands. This gap is called the bandgap E_g. The bands below the bandpap form the valence band (VB) in which all energy states are occupied by electrons. The conduction band (CB) consists of unoccupied bands which are located above the band gap. For metals there is no bandgap, the bottom of the CB and the VB are overlapped. Insulators are characterised by large bandgap (higher than 3 eV), so that no electrons from the VB can reach the CB. An important concept in band theory is the Fermi level. It is the highest occupied state at T = 0 K and the energy associated with this state is called the Fermi energy E_F. The discussion below is restricted to semiconductors.

3.2.1.1 Conduction in intrinsic semiconductor

In an intrinsic semiconductor the free-carriers belong to some atoms of the studied material. The conduction in these materials occur when the electrons are excited, thereby they leave the top of the VB and thus populate the bottom of the CB. The minimum energy required for introduce free delocalized electrons in the CB is called the activation energy E_A. This excitation typically occurs via an increase of the solid temperature.

3.2.1.2 Conduction in extrinsic semiconductor

Extrinsic semiconductors are intrinsic semiconductor which are doped. The introduction of substitutional atoms (with higher or lower valence state) in the lattice is called a doping process. The substitutional element is the dopant or doping element. For a *n*-type doping process, the dopant has a higher valence state than the host atom. The filled donor band is commonly near the empty conduction band. For conduction to occur there needs to be an excitement of electrons of the donor band, also called donor electrons. The energy requires to supply the donor electrons to the CB is the activation energy E_A of the system. It is also the difference between the bottom of the CB and the donor band. For a *p*-type doping, the dopant element has a lower valence state than the host element. Doping atoms form an empty acceptor band lying above the fully occupied valence band of the host material. The thermally excited electrons of the top of VB will populate the acceptor levels, thereby releasing holes in the VB. Electric conduction occurs because of the migration of free delocalised holes in the valence band.

In practice, one often uses an Arrehnius plot to assess whether or not the band conduction occurs in a material. In other words, a fit of the electrical conductivity data with the band model is required. The logarithm of the electrical conductivity [log (σ)] is plotted against the inverse of the temperature [$\frac{1}{T}$], in an Arrehnius plot. If the band model holds true for the studied material, the electrical conductivity of the material (σ) and the activation energy (E_A) are tied by

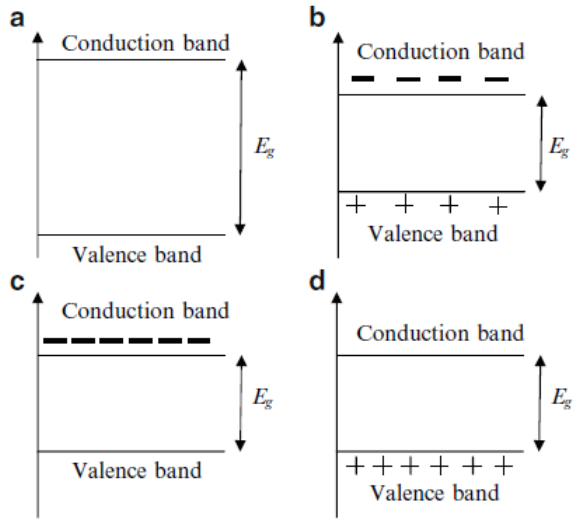

Figure 3.2: Simple energy band diagrams for (a) an insulator, (b) an intrinsic semiconductor, (c) an n-type semiconductor, and (d) a p-type semiconductor. [10]

$$\sigma \propto exp(\frac{-E_A}{k_B T}), \tag{3.27}$$

where k_B is the Boltzmann constant. The band conduction model predicts a linear dependence between log (σ) and $\frac{1}{T}$, in the Arrhenius plot. The activation energy of the material is thus deduced from the slope of the line in the Arrenhius plot. The diagram below is a simple version of an energy band diagram for an insulator, intrinsic semiconductor, n-type and p-type semiconductors.

3.2.2 The hopping models

The electrical conductivity in semiconductor oxide materials is best explained through the polaron hopping model. A generalised expression of σ based on this model is derived. Prior to that there is an introduction of the concept of polaron followed by a brief history of the hopping conduction. The Mott model for conductivity will also be discussed.

3.2.2.1 Mechanisms

In semiconductor oxide materials, and particularly those with large ionic bonding between cations and anions, fluctuations of the electric potential associated with each ion become too large. In order to explain their electric conduction's behaviour one needs to take into account the coupling between the electrons of the narrow band type semiconductor and the lattice ions (virtual phonons). Indeed as an electron moves through the lattice it influences the dynamics of the surrounding lattice. The electron pulls nearby positive ions towards it and pushes nearby negative ions away. The electron and its virtual phonons taken together can be treated as a new composite particle, called a polaron. This concept was introduced by Landau in his 1933's paper [137]. When the electron–phonon interaction is weak the overlap of neighbouring orbitals is larger thus resulting in the creation of large

polarons. On the other hand in systems in which the electron–phonon interaction is strong, electrons push negative ions further away, and the overlap of neighbouring orbitals becomes narrower until electrons fall into localised states. This phenomenon is defined as a small polaron.

3.2.2.2 History of hopping conduction

The concept of hopping conduction was first introduced by Conwell[138] and Mott[139] under the name of phonon assisted hopping. They proposed a model for a "new" process of conduction in which charge carriers conduct the electric current by thermally activated tunnelling from an occupied site to an empty site. The model was then developed by Miller and Abrahams[140] in the 60's. It would be the inspiration source of the variable-range hopping (vrh) theory of Mott[141]. In the early 70's, Ambegaokar[142] and Pollak[143] developed a more sophisticated treatment, which is based on the percolation theory[143,144,145,146]. In such model the hopping conduction is equivalent to the conduction process of a random network of small conductances that link sites. These localised sites, typically electronic states, are spatially close to each others and their corresponding energies are also in the same order of magnitude. Such an approach is still considered today as the most reliable theory for the evaluation of the electrical conductivity of semiconductor metal oxides but also of non-crystalline semiconductors at low temperature.

3.2.2.3 Electrical conductivity in polaron hopping model

For the polaron hopping conduction electrons hop to localised neighbouring[147] sites near the Fermi level, as seen in Figure 3.3. The electronic states are represented by dashes and the electrons by black dots. The y-axis represents the energy of an electron. The density-of-states is shown on the right. The shaded region corresponds to the valence band in which all energy levels are occupied.

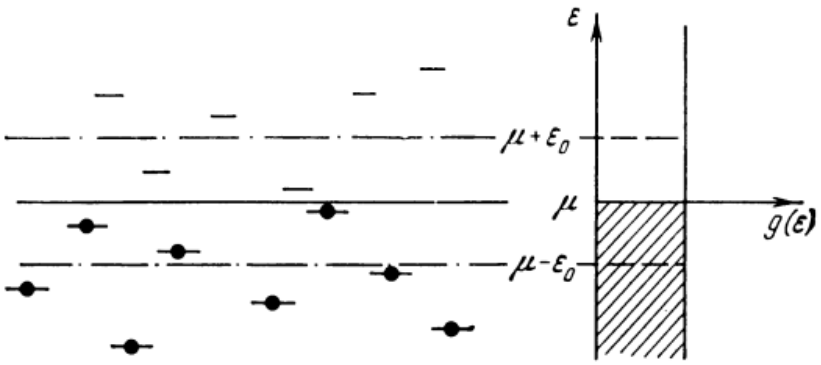

Figure 3.3: Band structure made of localised states, whose energies are separated from the Fermi level by less than ϵ_o. The density-of-states diagram is shown on the right; the range of occupied states is shaded[147].

Th hopping probability of a carrier tunneling from a localised state i with energy E_i to an empty

state j with energy E_j is given by

$$P_{ij} \sim exp(-2.\alpha.R_{ij} - \frac{E_j - E_i}{k_B T}), \tag{3.28}$$

with α the localization parameter of these states, R_{ij} the physical distance separating the two localised states. For the sake of simplificaton one introduces the parameter W, such that W = E_j - E_i. Equation (3.28) illustrates that the hopping probability at a given temperature depends on two parameters: (i) R_{ij} the spatial separation of the sites, and W, their energy separation. Apsley and Hughes[148,149] noted that the two variables were independent and so they combined them into a single parameter, the range $\mathcal{R}$ between two sites which determines the probability of hopping between them. So one had $\mathcal{R} = 2.\alpha.R_{ij}$ -$\frac{E_j - E_i}{k_B T}$, Hence, the hopping probability becomes:

$$P_{ij} \sim exp(-\mathcal{R}). \tag{3.29}$$

The states can be regarded as "points" in a four-dimensional hopping space made of the three spatial coordinates and one energy coordinate. $\mathcal{R}$ is the "distance" between two points of the four-dimensional hopping space.

The probability distribution function of all hops originating from one site is dominated by the hop to the nearest neighbouring site in the four-dimensional hopping space. It corresponds to two configurations:

- The first one describes hopping to empty spatially nearest neighbour sites. In other words the first term on the right hand site of equation (3.28) is dominant. Typically one must have $\alpha R_0 \gg 1$, with R_0 the average spatial distance to the nearest neighbouring empty localised state.
- The second configuration describes hopping to empty nearest neighbour sites whose energy is close to that of the charge-carrier's state. Here the second term on the right hand side of equation (3.28) contributes significantly to the hopping probability.

In the second configuration electrons preferably hop to sites that are further away in space but closer in energy. This is the variable-range hopping (vrh) process which is also known as the Mott's model[141,150] for hopping conduction. Details on this hopping conduction are discussed futher below.

Since the probability distribution function of all hops originating from one site is dominated by the hop to the site at closest range, the average hopping probability from this site i is approximated by

$$P_i \approx exp(-R_{i,nn}). \tag{3.30}$$

One can then derive the electrical conductivity from the hopping propability. The electric conductivity consists of a series of hops while the net electric conduction depends on an average of the

probabilities of the different hops. The appropriate average over the probabilities is the geometric mean, i.e.

$$\sigma \sim \langle P \rangle = \lim_{n\to\infty} [\prod_{i}^{n} P_i]^{1/n} \tag{3.31}$$

$$= exp[\lim_{n\to\infty} \frac{1}{n} \sum_{i}^{n} ln(P_i)] \tag{3.32}$$

$$= exp(-\bar{\mathcal{R}}_{nn}). \tag{3.33}$$

Combining this equation and the density of states *g(E)* of the charge-carriers can enable the electrical conductivity to be represented as

$$\sigma = \frac{\sigma_o}{T} exp\{\frac{-W}{k_B T}\}. \tag{3.34}$$

This equation represents the generalised expression of the electric conduction in the small polaron hopping model[151,152]. W is the activation energy E_A, the energy required for the electron to hop from its original site *i* to an empty localised site *j*. The pre-factor σ_o is given by the following relation:

$$\sigma_o = \frac{g_d e^2 \nu_o}{a k_B}, \tag{3.35}$$

where g_d is a factor which depends on lattice geometry. *a* is the polaron jump distance, such that the charge carriers can not hop to sites located at distances beyond *a*. ν_o is characteristic frequency. One can therefore rewrite equation (3.34) as

$$\sigma = \frac{g_d e^2 \nu_o}{a k_B T} exp\{\frac{-E_A}{k_B T}\}. \tag{3.36}$$

3.2.2.4 The Mott's model or variable-range hopping model

In Mott's formalism[141,150] the dominant contribution to the hopping current is through states within k_BT of the chemical potential μ. In order to evaluate $R_{i,nn}$ Mott makes the following assumptions: the carrier hops to a empty site within a sphere of radius r(T) and the density of states *g(E)* is constant over the energy range of hopping μ. The average distance $\bar{R}$ between the original site and the empty site is about $\frac{3}{4}r$. The average energy difference between an energetically closest site within this sphere and the original site is given by

$$\bar{W} = \frac{3}{4\pi r^3 g(\mu)}. \tag{3.37}$$

$g(\mu)$ represents the density of states around μ. Replacing r by $\frac{4}{3}\bar{R}$ in the above equation gives

$$\bar{W} = \frac{3^4}{4^4 \pi \bar{R}^3 g(\mu)}. \tag{3.38}$$

Therefore the average close range $\bar{\mathcal{R}}^{'}$ can be expressed as

$$\bar{\mathcal{R}}^{'} = 2.\alpha.\bar{R} + \frac{\bar{W}}{k_B T} \tag{3.39}$$

$$= 2.\alpha.\bar{R} + \frac{3^4}{4^4 \pi \bar{R}^3 g(\mu) k_B T}. \tag{3.40}$$

There is an optimal average distance $\bar{R}^{'}$ which minimizes the range $\bar{\mathcal{R}}^{'}$. One differentiates the latter with respect to $\bar{R}$. This critical distance is given by the following formula

$$\bar{R}^{'} = \frac{3}{4}\{\frac{3}{2.\pi.\alpha.g(\mu).k_B.T}\}^{1/4} \tag{3.41}$$

This expression is characteristic for the vrh conduction. At low temperature carriers can hop to sites which are further away spatially, but close in energy. As a consequence the average nearest hopping range is given by

$$\bar{\mathcal{R}}^{'}_{nn} = (\frac{T_o}{T})^{1/4}, \tag{3.42}$$

with

$$T_o = (\frac{3}{4})^4 \frac{3}{2\pi.\alpha^3.k_B.g(\mu)}. \tag{3.43}$$

Combining equation (4.38) and equation (4.47) one can write the conductivity as

$$\sigma = \sigma_o exp\{-(\frac{T_o}{T})^{1/4}\}. \tag{3.44}$$

This equation is the electrical conductivity in the variable-range hopping model of Mott. The parameter σ_o is a constant which is to be determined experimentally. The conductivity is dominated by the { - $(\frac{T_o}{T})^{1/4}$ } term, thus log σ has $T^{1/4}$ temperature dependence. However eq.(4.46) describes the vrh mechanism for a 3D system. For a *d*-dimensional system it can be shown that the Mott's variable-range becomes:

$$\sigma = \sigma_o exp\{-(\frac{T_o}{T})^{1/d+1}\}. \tag{3.45}$$

3.3 Thermal conductivity fundamentals

3.3.1 Mimimum thermal conductivity κ_{min}

The thermal conductivity, κ, is a physical quantity which measures the ability of a material at transferring heat. The heat is channeled via the free-carriers (electronic contribution) and the

lattice (lattice contribution). These two contributions are represented by the symbols κ_e and κ_l, respectively. The relation between κ, κ_e and κ_l is summed up in equation (4.51):

$$\kappa = \kappa_e + \kappa_l \tag{3.46}$$

One of the requirements to achieve high figure of merit is that of a low thermal conductivity. Although very poor electrical conductors glasses[153,154,155] exhibit some of the lowest lattice thermal conductivities. In such materials thermal conductivity is viewed as a random walk of energy through a lattice. The investigation of the thermal properties of glasses by Slack[153,154] lead to the concept of minimium thermal conductivity.

In 1992 Cahill *et al.*[156,157,158] proposed a model to estimate the minimum thermal conductivity of non perfect crystals. This model is based on the seminal work of Debye and Einstein. Einstein[159] described the atomic vibrations of a solid as harmonic oscillators that all vibrate at the same frequency ν. Hence, for thermal transport to occur the oscillators must be coupled. He made the assumption that each atom was connected to its neighbours by harmonic forces. Due to this crude approximation Einstein's model failed to reproduce not only the temperature dependence, but also the absolute magnitude of the thermal conductivity of crystals. Debye improved Einstein's model by taking into account the periodicity of a crystal. Indeed the repetition of atoms within lattice produces coherence between the atomic oscillators. Using this idea Cahill *et al.*[160,161] demonstrated that the thermal conductivity of a material is given by:

$$\kappa_{min} = (\frac{\pi}{6})^{1/3}.k_B.n_a^{2/3}.\sum_i[\nu_i(\frac{T}{\Theta_i})^2\int_0^{\Theta_i/T}\frac{x^3e^x}{(e^x-1)^2}dx], \tag{3.47}$$

where ω is the frequency of the phonon and $x = \frac{\hbar\omega}{k_BT}$; n_a corresponds to the number of atoms per unit volume, ν_i represents the sound velocity, and Θ_i is the cut-off frequency in the unit of K for polarisation mode i. The cut-off frequency for a mode i is a critical frequency, above which the oscillators resonate anharmonically. Θ_i is given by

$$\Theta_i = \frac{\hbar.\nu_i}{k_B}.[6\pi^2n_a]^{\frac{1}{3}}. \tag{3.48}$$

In Cahill's model the thermal conductivity can be viewed as a random walk of heat between localized oscillators of varying sizes and frequencies and the dominant heat transport is between nearest neighbours.

3.3.2 The Callaway-Debye model

The Callaway-Debye model[160,161] is the model commonly used to fit the lattice contribution of the thermal conductivity of a crystal. In this model, the lattice is also represented by a series of chains of atoms of mass M held together by springs of force constant k. The conduction of heat occurs when two neighbouring atoms move in phase with one another. There is a critical frequency for

the phonons or modes of vibrations of the oscillators. It is known as the Debye frequency, ω_D. ω_D is defined as the maximum vibrational frequency of a given mode i in a crystal. This frequency is associated with a temperature known as the Debye temperature (Θ_D). Θ_D is the temperature above which all vibrational modes in a crystal are excited. The Debye temperature is given by:

$$\Theta_D = \frac{\hbar\omega_D}{k_B}, \tag{3.49}$$

where $\hbar$ is the Planck constant and k_B is the Boltzmann constant. Note that the vibrational modes below ω_D are called *N*-processes.

With increasing temperature numerous processes develop and hinder to the conduction of the heat by the lattice. This decay of κ corresponds to an enhancement of the anharmonicity of the oscillators; it is due to scattering mechanisms, which increase with increasing temperature. These scattering mechanisms are: Umklapp phonon-phonon scattering (U), phonon-defect scattering (d), phonon-electron scattering, and phonon-boundary scattering (b). The scattering rate of each scattering process is associated with a relation time τ. The combined relaxation time τ_c can be calculated from the individual relaxation time τ_i, using the Matthiessen's rule[162],

$$\frac{1}{\tau_c} = \sum_i \frac{1}{\tau_i} \tag{3.50}$$

$$= \frac{1}{\tau_U} + \frac{1}{\tau_b} + \frac{1}{\tau_d} + \frac{1}{\tau_e}. \tag{3.51}$$

τ_U, τ_b, τ_d and τ_e are the relaxation times of Umklapp-, grain boundary-, defect- and electron-phonon scattering, respectively.

Umklapp processes Phonon-phonon scatterings become increasingly anharmonic as the temperature increases, causing a deterioration of heat conduction. *U*-processes become dominantly important in controlling the thermal conductivity of a crystal, with increasing temperature. The relaxation time τ_U is given by:

$$\tau_U^{-1} = B.\omega^2 = 2\gamma^2 \frac{k_B T}{\mu V_o} \frac{\omega^2}{\omega_D}.\omega^2, \tag{3.52}$$

where γ is the Gruneisen anharmonicity parameter, V_o is the volume per atom and ω is the frequency of a phonon.

Phonon-grain boundary scattering The main source of this type of scattering is the sample size, namely the size of the particulates at the microscopic scale. Phonon-grain boundary scatterings is independent of temperature and frequency. τ_b is given by:

$$\tau_b^{-1} = \frac{\nu_s}{l}, \tag{3.53}$$

with ν_s as the velocity of sound, l as the effective length or characteristic length of the sample. The latter is usually determined experimentally from SEM images. Note that it is possible to determine the sound velocity from the Debye temperature, and vice-versa.

Phonon-defect scattering There are multiple defects or impurities within the lattice. They are for instance, isotopes, substitutional impurities with different masses, vacancies and so forth. Defects are considered as a point-defect if their size is smaller than the wavelength of the phonon. This scattering by the defect can strongly scatter phonons and is due to the difference in mass and bonding between the atoms. The scattering rate τ_d^{-1} is given by:

$$\tau_d = A.\omega^4 = \frac{V_o \Gamma (\frac{k_B T}{\hbar})^4}{4\pi\nu_s^3}.\omega^4, \tag{3.54}$$

where Γ is the mass-fluctuation-scattering[158,163] parameter.

Phonon-electron scattering When dealing with highly doped materials, the scattering of phonons by electrons needs to be taken into account. The contribution to the thermal conductivity by phonon-electron scattering is often assumed to be negligible. τ_e is given by:

$$\tau_e^{-1} = \frac{n\epsilon^2\omega}{\rho V^2 k_B T}\sqrt{\frac{\pi m^* V^2}{2k_B T}} exp(\frac{m^* V^2}{2k_B T}), \tag{3.55}$$

where n is free-carriers (electron) concentration, ϵ is deformation potential, ρ is mass density of the material; m^* is effective electron mass of the electron.

It should be noted that Umklapp processes are also called intrinsic relaxation time processes, whereas point defects, grain boundary and electron-phonon are extrinsic relaxation time processes. Taking into account the scattering of the phonons by the above processes, Callaway[160,161] demonstrated that the lattice contribution of a material is given by:

$$\kappa = \kappa_1 + \kappa_2. \tag{3.56}$$

According to this model κ_1 and κ_1 are respectively given by:

$$\kappa_1 = \frac{k_B}{2\pi^2\nu_s}.(\frac{k_B T}{\hbar})^3 \int_0^{\frac{\Theta_D}{T}} \tau_c \frac{x^4 e^x}{(e^x - 1)^2} dx \tag{3.57}$$

and

$$\kappa_2 = \frac{k_B}{2\pi^2\nu_s}.(\frac{k_BT}{\hbar})^3 \frac{[\int_0^{\frac{\Theta_D}{T}} \frac{\tau_t(x)x^4e^x}{\tau_N(x)(e^x-1)^2}dx]^2}{\int_0^{\frac{\Theta_D}{T}} \frac{\tau_t(x)x^4e^x}{\tau_N(x)\tau_c(x)(e^x-1)^2}dx} \tag{3.58}$$

where Θ_D is the Debye temperature, $x = \frac{\hbar\omega}{k_BT}$ is a dimensionless variable. ω and ν_s represent the phonon frequency and the average sound velocity in the material, respectively. τ_N represent the scattering time due to normal phonon processes. τ_t^{-1} is the combined scattering rate and is given by:

$$\tau_t^{-1} = \tau_c^{-1} + \tau_R^{-1}. \tag{3.59}$$

κ_2 is large for pure crystals but decreases rapidly in presence of defects with the lattice, which is the case of impure crystals. Most crystal compounds have intrinsic defects (grain boundary, vacancies, point defects, etc), thus are impure crystals. Consequently for these materials κ_2 is negligible; one has:

$$\kappa \sim \kappa_1. \tag{3.60}$$

Chapter 4

Thermoelectric properties of Y-doped $CdSb_2O_6$

4.1 Motivation

Transparent conducting oxides[56,57,164] (TCO) have been highly investigated and are utilised in the industry of flat panel displays such as high-definition televisions (HDTVs), mobile phones and other devices. A transparent conducting oxide is a material which combines the high electrical conductivity of metals with a high transmittance in the visible range. Typically TCO materials[57] have an average transmittance above 80% for wavelength between 400 nm and 800 nm, an electrical conductivity of the order of $10^4\,\mathrm{S\,cm^{-1}}$. TCOs are wide bandgap semiconductors with a direct bandgap above 3.1 eV.

Transparent conducting oxides are potential TE materials due to their bandgap E_g in the order of $\sim 10k_B\mathrm{T}$. This wide bandgap would prevent the bipolar effect observed in narrow semiconductors. The bipolar conduction is observed when the carrier concentrations and mobilities of the electrons are comparable to that of holes. As a consequence at high temperature the Seebeck coefficient should be very small, as observed in Bi_2Te_3[165]. For wide bandgap semiconductors the bipolar effect is practically suppressed as only one type of the carriers is responsible for the electric conduction. An example of transparent conducting oxide material with high TE properties is ZnO. Zinc oxide is one of the best *n*-type TCOs[57,166] but also is one of best TE oxides[58,59].
When doped with a small quantity of Y^{3+}, cadmium metantimonate oxide ($CdSb_2O_6$) has the characteristics of a TCO[167]. $CdSb_2O_6$ crystallises in a rosiaite-type structure, the space group symmetry of its trigonal lattice is $P\bar{3}1m$ (162). Mizoguchi *et al.*[168] refined the crystal structure of $CdSb_2O_6$ by means of x-ray diffraction. The positions of the cadmium, antimony and oxygen atoms are displayed in Table 4.1 on the next page. The Wyckoff positions were refined using a unit cell with the following characteristics: a = 5.2373(0) Å, c = 4.7983(1) Å and $Z = 1$. The unit cell of rosiaite-type structured lattice is displayed in Figure 4.1 on the next page.

In Figure 4.1 the blue, green and red spheres represent the cadmium, antimony and oxygen atoms, respectively. One notes a 6-fold coordination of O^{2-} around the Sb^{5+} and Cd^{2+} ions. The crystal structure of the cadmium metantimonate consists of two-dimensional layers of edge-sharing CdO_6 octahedra in the *a*-*b* plane.

Table 4.1: Crystallographic parameters of $CdSb_2O_6$ samples after structural refinement of a room temperature powder x-ray diffraction pattern[168]. Space group: $P\bar{3}1m$ (162).

atom	**site**	**x**	**y**	**z**	$B_{iso}(\AA^2)$
Cd	1a	0	0	0	0.0036(3)
Sb	2d	1/3	2/3	1/2	0.0003(2)
O	6k	0.365(1)	0	0.282(1)	0.005(2)

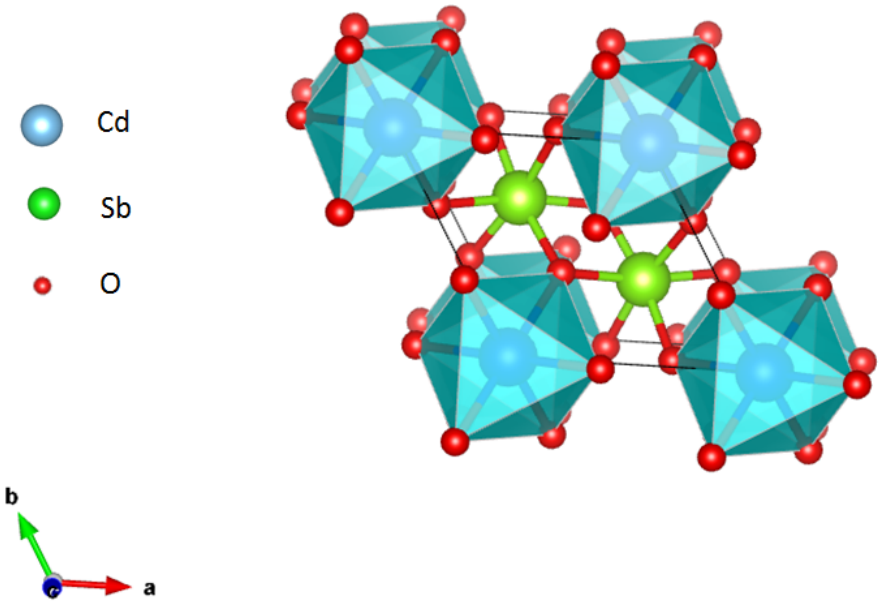

Figure 4.1: Unit cell of the trigonal lattice of $CdSb_2O_6$.

The TCO character of $Cd_{1-x}Y_xSb_2O_6$ polycrystalline sample was recently reported by Yanagawa *et al.*[167], with a room-temperature electrical conductivity of at least $1 \times 10^2\,S\,cm^{-1}$ and a bandgap of 4.1 eV. However, the thermoelectric properties of this AB_2O_6 oxide have not yet been investigated. As far as we are concerned this work is therefore a first characterization of the thermoelectric properties of yttrium-doped $CdSb_2O_6$ polycrystalline samples. In order to investigate the TE properties of impurity-doped $CdSb_2O_6$, solid solutions of $Cd_{1-x}Y_xSb_2O_6$ (x= 0.03; 0.05; 0.08; 0.1) have been prepared by standard solid state reaction. There is a discussion on the temperature dependence of their thermopower. It is followed by an analysis of their electrical conductivity data and their power factor.

4.2 A literature review of $CdSb_2O_6$

4.2.1 Methods of synthesis

Solid state reaction is by far the most utilised technique to prepare cadmium metantimonate samples. The early studies[15,169] on polycrystalline samples were dedicated to the establishment of the crystal structure. Castro *et al*[169] explored the trigonal systems of $CdSb_2O_6$ by means of standard X-ray diffraction. They reported the atomic positions of Cd, Sb and O within the crystal lattice with $P\bar{3}1m$ (162) as symmetry space group. Besisdes powders, thin films of cadmium metantimonate were prepared by sputtering method by Yanagawa *et al.*[167].

4.2.2 Electronic structure

Band structure calculations were performed using the Linear Muffin-Tin Orbital (LMTO) approximation method[170] for the determination of the electronic structure of $CdSb_2O_6$. Mizuguchi and coworker[168] derived Molecular Orbital (MO) diagram of ${Sb_2O_6}^{2-}$ in order to identify the nature of the chemical bonding between Cd^{2+} and ${Sb_2O_6}^{2-}$. The MO diagrams of ${Sb_2O_6}^{2-}$ are mixtures between the Sb 5*s*, Sb 5*p* and O 2*p* orbitals. The highest occupied molecular orbital (HOMO) is made up of nonbonding O 2*p* orbitals whereas the lowest unoccupied molecular orbital (LUMO) is an antibonding orbital resulting from the interaction between the Sb 5*s* and O 2*p* orbitals. Due to a spatial and energetic proximity of the latter orbitals an overlap between these two orbitals occurs. This overlap strengthens the cation-anion bond. Andersen described the chemical bond Sb -O as a covalent bond[168].

Mizugushi and coworkers then performed band structure calculations with Linear Muffin-Tin Orbital approximation (LMTO). The valence and conduction bands correspond to HOMO and LUMO energy levels, respectively. The plots in Figure 4.2b) at the top of the next page illustrate the variation of the energy of states (Energy / ev) as function of the position in the reciprocal space (**k**). The letters Γ, K, M, A and H are high symmetrical points in the unit cell of the reciprocal space or Brillouin zone, as seen in Figure 4.2a). For example, Γ is a point in the centre of the Brillouin zone, A is the middle of facets perpendicular to $\vec{b_3}$. $\vec{b_1}$, $\vec{b_2}$ and $\vec{b_3}$ are the unitary vectors of the reciprocal space and are given by

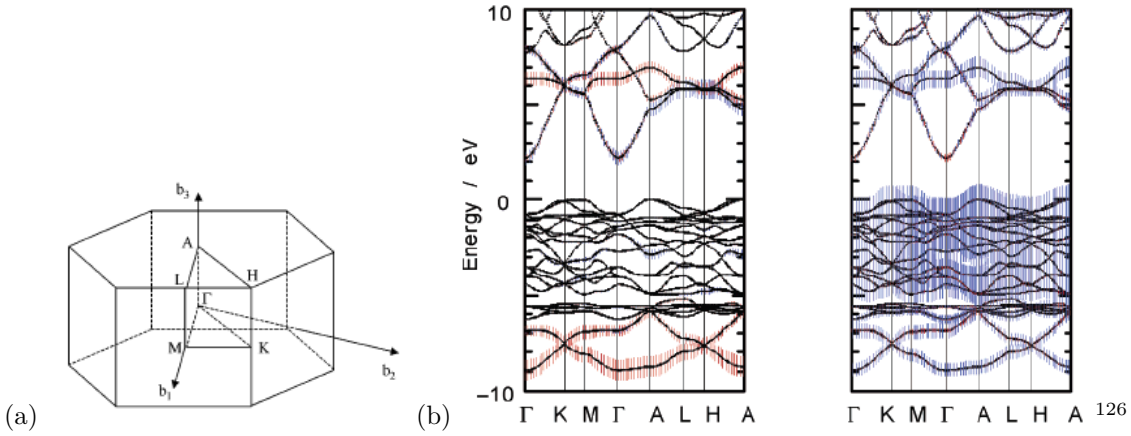

Figure 4.2: (a)The Brillouin zone for a primitive hexagonal lattice[168]. (b) The band structure of $CdSb_2O_6$ derived from the LMTO approach. The fatbands on the left-hand side show the Sb $5s$ orbital contribution in red and the Cd $5s$ orbital contribution in blue. The O $2s$ orbital contribution in red and the O $2p$ orbital contribution in blue are shown by the fatbands on the right-hand side .

$$\vec{b_1} = 2\pi \frac{\vec{b} \times \vec{c}}{\vec{a}.(\vec{b} \times \vec{c})}, \tag{4.1}$$

$$\vec{b_2} = 2\pi \frac{\vec{c} \times \vec{a}}{\vec{a}.(\vec{b} \times \vec{c})}, \tag{4.2}$$

$$\vec{b_3} = 2\pi \frac{\vec{a} \times \vec{b}}{\vec{a}.(\vec{b} \times \vec{c})}, \tag{4.3}$$

where $\vec{a}$, $\vec{b}$ and $\vec{c}$ are the unitary vectors of the real space. In Figure 4.2 above, the bands whose energies are lower than 0 eV form the valence band (VB), whereas the conduction band (CB) consists of bands with energies higher than 2 eV. The minimum of the conduction band is located at the Γ point and the top of the valence band is located at the A point. For the calculations of the band structure, energies are evaluated for all k points between the high symmetry points. The calculations are run along the paths bewteen the high symmetry points, illustrated by the letters on the top of the electronic structure: Γ, K, M, Γ, A, L, H and A. The top of the valence band of this material is dominated by Cd $4d$ and O $2p$ orbitals. The lowest energy states of the conduction band mainly consists of Cd $5d$ and Sb $5s$ orbitals. The lowering of the conduction band, at Γ point, is due to a bonding overlap between the Cd $5s$ orbitals with the O $2p$ orbitals involved in an antibonding interaction with two Sb $5s$ orbitals across a shared octahedral edge. The bottom of the CB at the Γ point has a parabolic shape. This dispersive band is similar to that of a free electrons gas. The large bandgap (3.8 eV) and the dispersive band at the Γ point indicate that $CdSb_2O_6$ is suitable for n-type doping. Note that the bandgap is indirect as the lowest point of the CB and the highest point of the VB are not directly aligned.

4.2.3 Physical properties

Yanagawa *et al.*[167] reported optical properties on polycrystalline samples of $CdSb_2O_6$ and Yttrium-doped $CdSb_2O_6$ ($Cd_{1-x}Y_xSb_2O_6$). Diffuse reflectance on these samples was measured in the near

ultraviolet and visible region. Since cadmium metantimonate powder has a yellowish colour, MgO (white powder) was used as reference material as it has no optical absorption in the measured wavelength region. The absorption edge of $Cd_{1-x}Y_xSb_2O_6$ (with x = 0; 0.01; 0.05) samples appear below 300 nm. The absorption edge is defined as the transition between absorbing and non-absorbing regions in the diffuse reflectance spectrum of a solid. Light with lower energy photons (long wavelength) is not absorbed whereas light with higher energy photons (short wavelength) is absorbed. The absorption edge therefore determines the energy separation between the valence band (long wavelength) and conduction band (short wavelength) of the studied material. The optical bandgap of the Y-doped $CdSb_2O_6$ samples is thus larger than 4.1 eV. This bandgap value is in agreement with that of Mizoguchi *et al.*[168], who estimated a value of ∼3.8 eV by means of band structure calculations. In addition, samples with higher yttrium content have a lower bandgap than those with low yttrium content.

Yanagawa *et al.*[167] also measured DC electrical conductivity of $Cd_{1-x}Y_xSb_2O_6$ samples in a temperature range between 77 and 300 K by means of four-point probe technique. At room temperature the electrical conductivity of the two doped samples (x = 0.01 and x = 0.05) and $CdSb_2O_6$ reach $1.4 \times 10^{-1}\,S\,cm^{-1}$ and $2.7\,S\,cm^{-1}$ and $5.6 \times 10^{-6}\,S\,cm^{-1}$, respectively. The conductivity of cadmium metantimonate increases by 4 or 5 orders of magnitude when doped with Y_2O_3. This behaviour is supported by diffuse reflectance measurement in the wavelength region higher than 470 nm, as the reflectance of Y-doped $CdSb_2O_6$ samples is lower than that of the nonsubstituted sample. In this region the conduction electrons are responsible for the optical absorption. As a conclusion, the substitution of Cd^{2+} by a cation with a higher valence Y^{3+} introduces extra electrons in the conduction band, thus reducing the bandgap of the material.

4.2.4 Devices and applications

Due to their wide bandgap, good electrical conductivity and high transmittance in the visible region, $Cd_{1-x}Y_xSb_2O_6$ systems can be treated as transparent conductor oxides. It can therefore be used as electrodes in the photovoltaic field. Elsewhere, when doped with Eu^{3+} (0.5%) and Tb^{3+} (1.5%) $CdSb_2O_6$ behaves as an efficient material for photocatalysis reactions and as a white light emitter[171].

4.3 Synthesis

$CdSb_2O_6$ (with x = 0.03; 0.05; 0.08 and 0.10) polycrystalline samples have been prepared by a solid state reaction. A solid state reaction is a direct reaction between reagents at high temperature under specific atmosphere (air, argon, vacuum,etc), whose feasibility depends on thermodynamic and kinetic parameters. It is the standard route for solid state scientists. The synthesis, in accordance with Yanagawa *et al.*[167], has been carried out by mixing appropriate amounts of CdO (99.9%) and Sb_2O_3 (99.99%) and $Y(NO_3)_3.6H_2O$ (99.98%). The two first precursors or reagents (cadmium oxide and antimony trioxide) are brown and white powders respectively; while the third one, yttrium nitrite hexahydrate, is a salt. The solid state reaction is described by the following equation

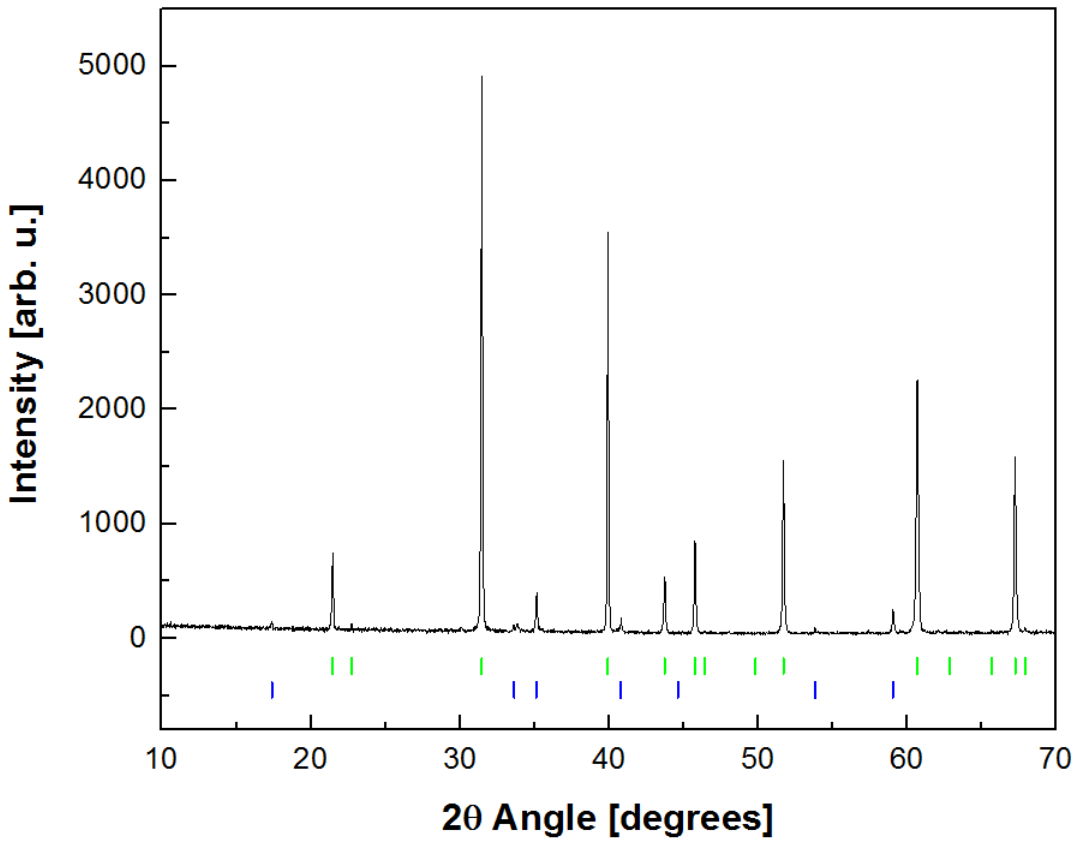

Figure 4.3: Room-temperature x-ray diffraction patterns of $Cd_{0.98}Y_{0.02}Sb_2O_6$ samples sintered at 1423 K.

$$(1-x)\mathrm{CdO} + \mathrm{Sb_2O_3} + (x)\mathrm{Y(NO_3)_3.6H_2O} \xrightarrow{air} \mathrm{CdSb_2O_6}, \tag{4.4}$$

where x represents the content on yttrium. The reagents were mixed with a pestle in an agate mortar under acetone. The mixture was then placed in an aluminium crucible and the furnace used to carry the reaction had the following heating program: calcination at 853 K for 24 h, followed by 1173 K for 24 h, then 1223 K for 12 h, and finally 1273 Kfor 48 h. In order to reach phase purity a second re-grinding and a repetition of the annealing process was performed. The mixing ratios of the starting materials are displayed in Table 4.2 on page 83. These contents of yttrium were chosen as the introduction of Y^{3+} in the lattice do not change the crystal structure of the material. This was illustrated by the x-ray diffraction patterns of $Cd_{1-x}Y_xSb_2O_6$. The positions and relative intensities of the reflections of the doped samples are very similar to that of undoped sample. In other words, these values of x are below the solubility of $CdSb_2O_6$. The obtained powder samples have a similar colour to that described by Yanagawa and coworkers, a yellow-green colour. The excess of Sb_2O_3 is due to his partially volatility at high temperature which initiate the formation of $Cd_2Sb_2O_7$, as seen in Figure 4.3 above.

Figure 4.3 above depicts the room temperature x-ray diffraction pattern of a $Cd_{0.98}Y_{0.02}Sb_2O_6$. The green ticks correspond to the Bragg peak positions of the trigonal phase $P\bar{3}1m$ whereas the reflections indexed by the blue ticks are the expected reflections for the $Cd_2Sb_2O_7$ compound. To avoid the formation of this phase 15% excess of antimony trioxide were added during the synthesis

as indicated by "1.15" in the third column of Table 4.2. The lattice associated with these reflections has $Fd\bar{3}mz$ as symmetry space group.

Table 4.2: The molar quantities for the synthesis of $Cd_{1-x}Y_xSb_2O_6$.

Sample	**CdO (mol)**	**Sb_2O_3 (mol)**	**$Y(NO_3)_3.6H_2O$ (mol)**
a	1.00	1.15	0
b	0.97	1.15	0.03
c	0.95	1.15	0.05
d	0.92	1.15	0.08
e	0.90	1.15	0.10

4.4 Powder x-ray diffraction

Powder x-ray diffraction (XRD) is by far the most used technique by solid-state scientists to assess the phase purity of a prepared polycrystalline sample. It is considered to be "the eyes" of the solid state scientist. The phase purity of each sample has thus been examined through x-ray powder diffraction (XRD), obtained with a PANalytical diffractometer. Details on this instrument are given in section 2.1.2 of Chapter 2. The powder diffractograms of the five samples are shown in Figure 4.4 on the next page.

The profiles of the five XRD patterns are similar as indicated by the positions and the relative intensities of the Bragg peaks. The diffraction pattern suggests that the Y^{3+} are integrated within the lattice and substitute some Cd^{2+} without changing the trigonal lattice structure. Refinements of the crystal structures from the diffractograms have been performed utilising the *Fullprof* program. The Rietveld method[115] was implemented to extract the main crystallographic parameters of the samples structure. This method is based on a least-squares fitting of the observed intensities and comparison with a chosen structural model. All reflections in the patterns in Figure 4.4 were indexed by the a trigonal cell with the symmetry space group $P\bar{3}1m$ (162) as illustrated in Figure 4.5 on page 85. The experimental data in Figure 4.5 correspond to the red dots. The calculated profile is represented by the continuous black line; the blue line at the bottom of the diagram corresponds to a difference curve (observed-calculated). The green tick marks indicate the Bragg peak positions. A good level of agreement between the observed and calculated XRD patterns was obtained for all samples. The agreement between measured and calculated XRD patterns is indicated by the low values of the refinement factors coefficients: $\chi^2 = 3.61\,\%$, $R_B = 6.982\,\%$ and $R_F = 5.514\,\%$. The fitting parameters are defined in the section 2.1 of Chapter 2.

The lattice parameters, the atoms positions (Wyckoff positions) and the fitting parameters are presented in Table 4.3.

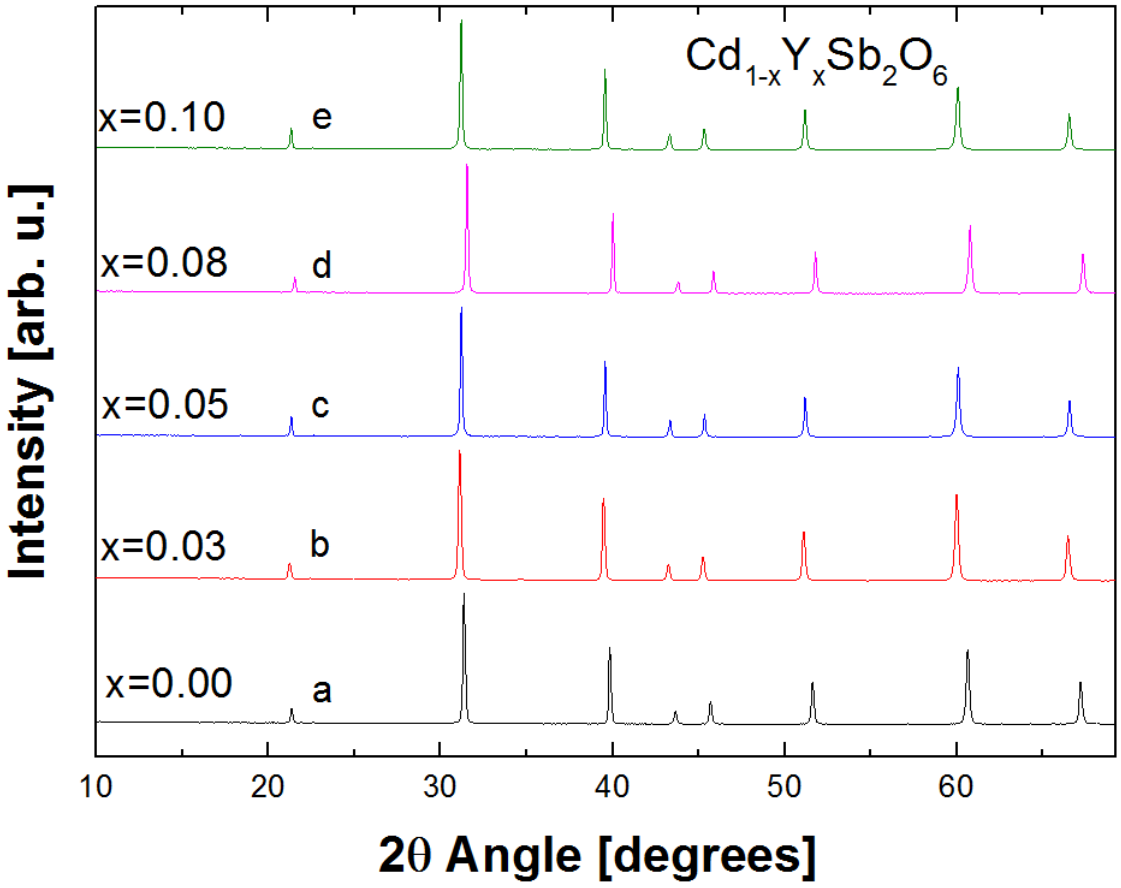

Figure 4.4: The x-ray diffraction pattern of $CdSb_2O_6$ and of four Y-doped $CdSb_2O_6$ with the doping concentration x equal to 0.03; 0.05; 0.08 and 0.10.

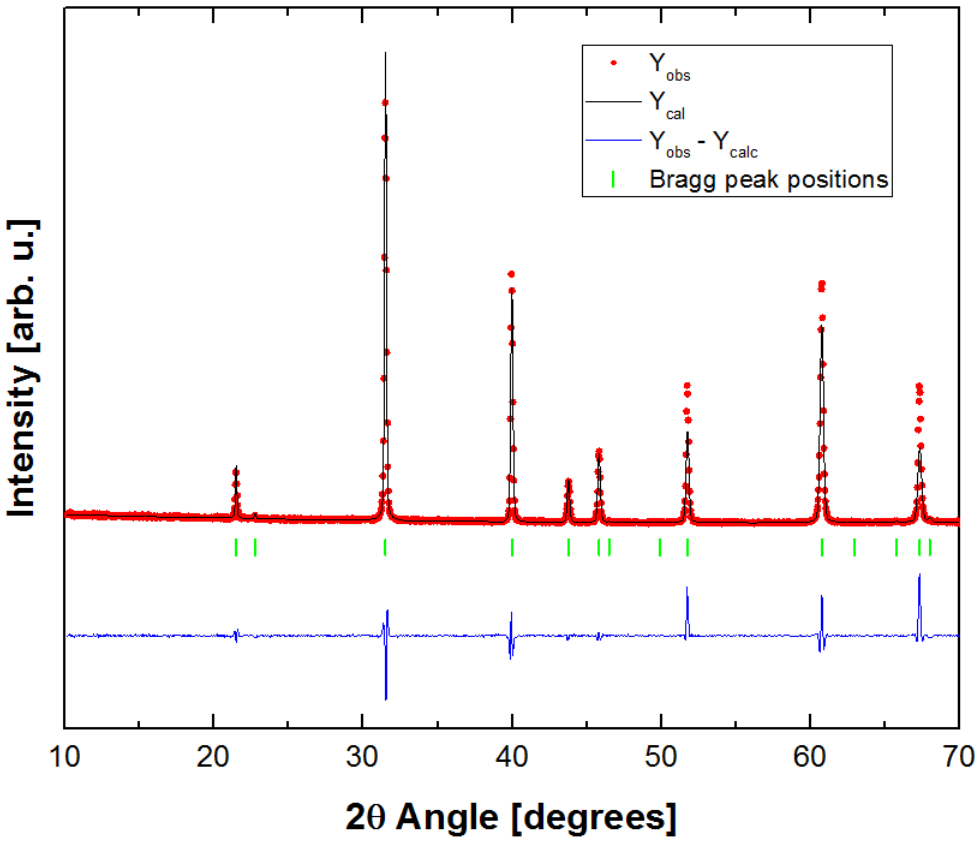

Figure 4.5: Rietveld refinement result for $Cd_{0.95}Y_{0.05}Sb_2O_6$.

Table 4.3: Crystallographic parameters of of $Cd_{1-x}Y_xSb_2O_6$ samples after structural refinement of the room temperature powders x-ray diffraction patterns. Space group: $P\bar{3}1m$ (162)

Sample	**atom**	**site**	**x**	**y**	**z**
$CdSb_2O_6$	Cd	1a	0.000	0.000	0.000
a = 5.239 46(10) Å	Sb	2d	0.333	0.667	0.500
b = 5.239 46(10) Å	O	6k	0.37575(4)	0.000	0.21484(3)
c = 4.801 42(11) Å					
$V = 114.149(4)$ Å^3			$R_{wp} = 14\%$	$R_B = 6.35\%$	$R_F = 5.22\%$
$Cd_{0.97}Y_{0.03}Sb_2O_6$	Cd/Y	1a	0.000	0.000	0.000
a = 5.240 14(13) Å	Sb	2d	0.333	0.667	0.500
b = 5.240 14(13) Å	O	6k	0.38278(6)	0.000	0.23189(3)
c = 4.801 43(15) Å					
$V = 114.244(5)$ Å^3			$R_{wp} = 14.8\%$	$R_B = 10.30\%$	$R_F = 6.59\%$
$Cd_{0.95}Y_{0.05}Sb_2O_6$	Cd/Y	1a	0.000	0.000	0.000
a = 5.240 22(14) Å	Sb	2d	0.333	0.667	0.500
b = 5.240 22(14) Å	O	6k	0.34201(1)	0.000	0.23379(4)
c = 4.804 19(15) Å					
$V = 114.249(6)$ Å^3			$R_{wp} = 17.0\%$	$R_B = 8.31\%$	$R_F = 6.45\%$
$Cd_{0.92}Y_{0.08}Sb_2O_6$	Cd/Y	1a	0.000	0.000	0.000
a = 5.240 77(13) Å	Sb	2d	0.333	0.667	0.500
b = 5.240 77(13) Å	O	6k	0.37730(5)	0.000	0.22030(3)
c = 4.8072(13) Å					
$V = 114.343(5)$ Å^3			$R_{wp} = 10.8\%$	$R_B = 4.40\%$	$R_F = 3.73\%$
$Cd_{0.90}Y_{0.10}Sb_2O_6$	Cd/Y	1a	0.000	0.000	0.000
a = 5.240 89(12) Å	Sb	2d	0.333	0.667	0.500
b = 5.240 89(12) Å	O	6k	0.304090(8)	0.000	0.24701(3)
c = 4.8066(14) Å					
V = 114.335(5) Å^3			$R_{wp} = 14.3\%$	$R_B = 7.48\%$	$R_F = 5.28\%$

4.4.1 The Vegard's law

Figure 4.6 on page 88 shows the Y^{3+}-dependence of the lattice. All three lattice parameters a and c increase as the doping concentration of Y^{3+} increases. As a consequence the volume V increases from 114.149(4) Å^3 to 114.343(5) Å^3; a(x), and c(x) follow the Vegard's law as there is a linear relationship between Y^{3+} content and the expansion the lattice. The rate of the lattice expansion was extracted from the slopes of the lines in Figure 4.6 and can be estimated at 0.0194 Å^3 per 0.01 Y^{3+} introduced within the system. The increase of the volume of the unit cell with increasing substitution ratio is in disagreement with the work of Yanagawa and coworkers[165] who reported a decrease of the lattice parameters with increasing substitution ratio. The value of ionic radius of 6-coordinated Cd^{2+}, Y^{3+} are 0.95 and 0.90 Å, respectively. As a consequence the unit cell is expected to shrink as Y^{3+} ions substitute Cd^{2+} ions. The oxygen ions link up the cations together. Each cation is surounded by six oxygens and together they form octahedra. The oxygens are considered to be free within the lattice. Although there is been replacement of up to 10% of the Cd^{2+} by Y^{3+} the solubility limit was not achieved, as confirmed by the x-ray diffraction pattern in Figure 4.5. The diffractograms do not present reflections of some spurious phases. The fairly low values of R_{wp}, R_B and R_F indicate that the five prepared samples are all single phase. The refininement of the crystal structure of the powdered Y- doped $CdSb_2O_6$ samples from XRD patterns is the first step of structural characterization.

4.4.2 Energy-dispersive x-ray (EDX) analysis

The atomic composition of the yttrium-doped cadmium metantimonate polycrystalline samples was then investigated by means of energy-dispersive x-ray (EDX) technique. Details on this technique are given in section 2.5 of Chapter 2. Series of images on the rectangular bars were taken on a scanning electron microscope (SEM)[30,34,170]. SEM images give an indication on the particles size, the porosity of the material, the presence of defect, and so forth. In addition to that, one can perform energy-dispersive analysis on a SEM image. EDX informs on the composition of a compound as it enables the calculations of atomic and mass percentage for each element within the studied compound. Hence, EDX analysis was carried out to investigate the yttrium content on each of the $Cd_{1-x}Y_xSb_2O_6$ samples. Some of the images taken on the pellets of Y-doped $CdSb_2O_6$ are displayed in Figure 4.7 on page 89. For each sample, different regions were imaged in order to have a better statistics on the physical quantities such as the grain size and the atomic percentage of each element.

The images in Figure 4.7 were taken at a voltage of 30 kV and a magnification of 10kX. The white ruler below each image corresponds to 1 μm. The first, second and third rows correspond to the images of the samples x = 3, 5 and 10 %, respectively. These images illustrate a decrease of the particle size with an increasing substitution ratio x. Indeed, most of the agglomerates in the top row images have a size (diameter) larger than 1 μm. However, the average particle size rapidly decreases and reaches down do 0.4 μm as one goes from the top to the bottom in Figure 4.7. This set of SEM images suggest that the decrease of the particles size within the $Cd_{1-x}Y_xSb_2O_6$ samples is related

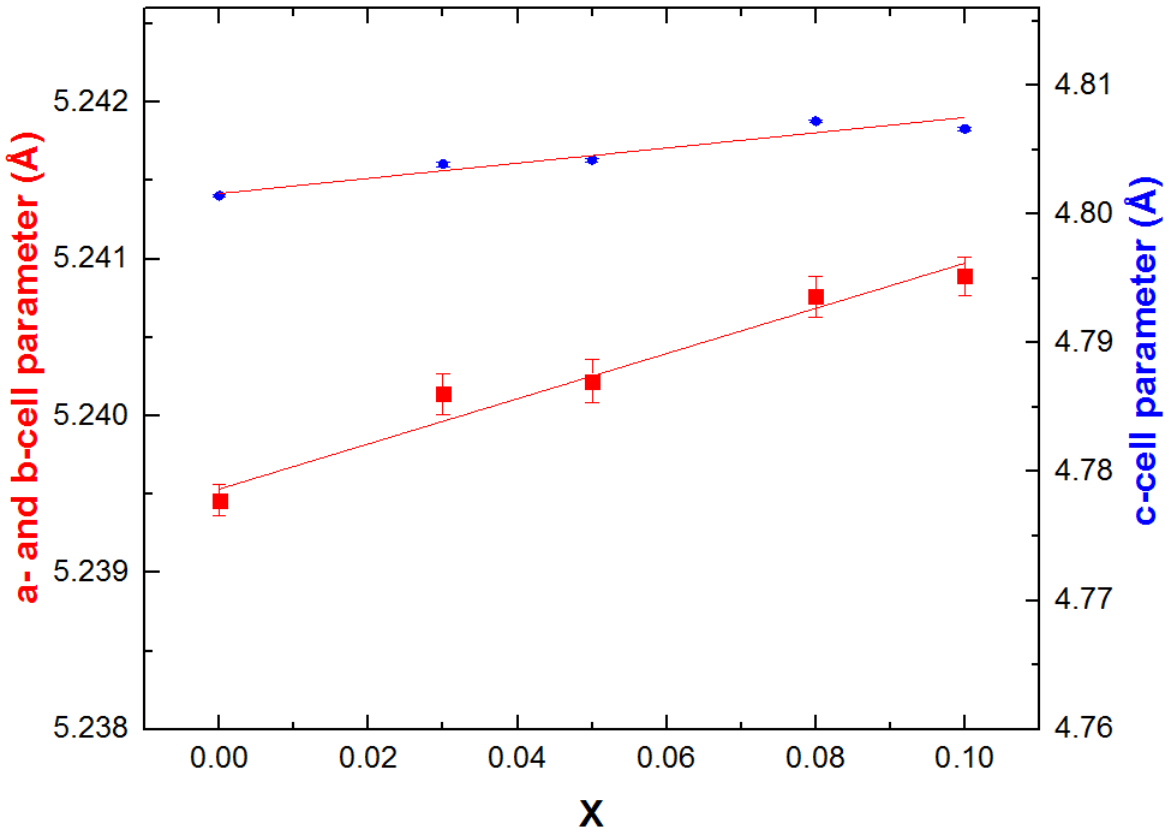

(a)

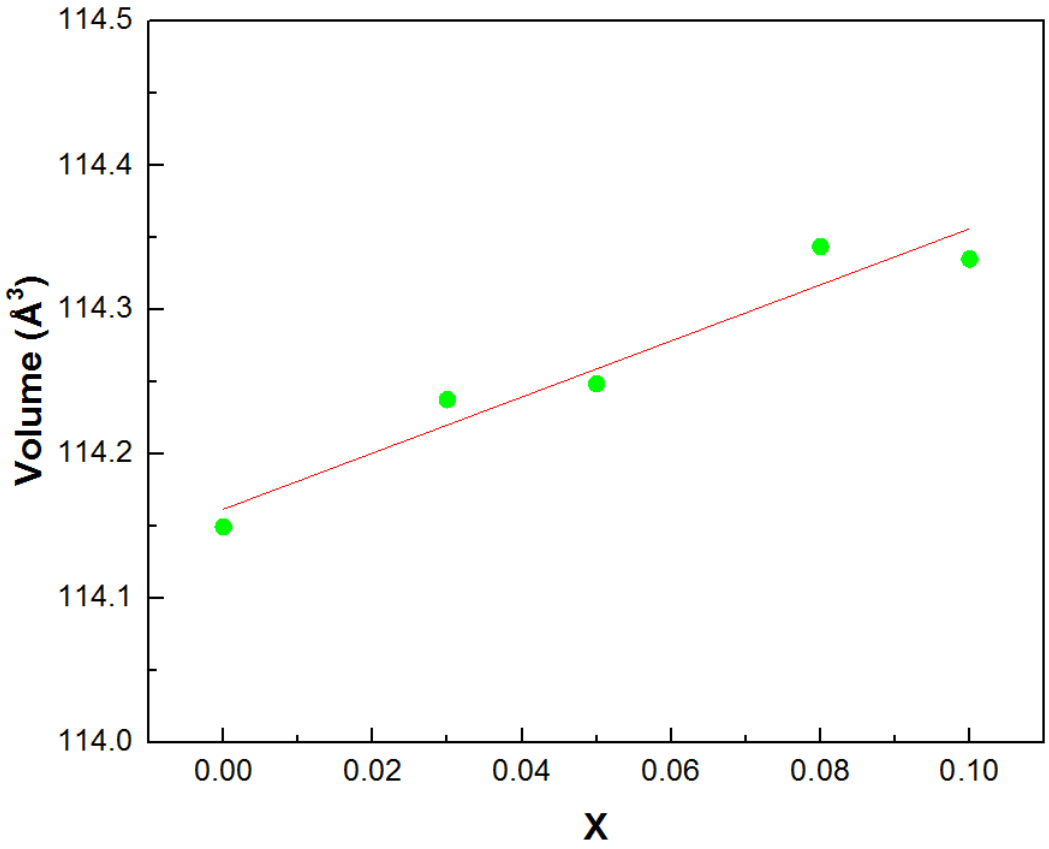

(b)

Figure 4.6: (a) Cell parameters of $Cd_{1-x}Y_xSb_2O_6$ (x $<$ 0.10) plotted versus x (Y content. (b) The relationship between the doping concentration x and volume of the unit cell.

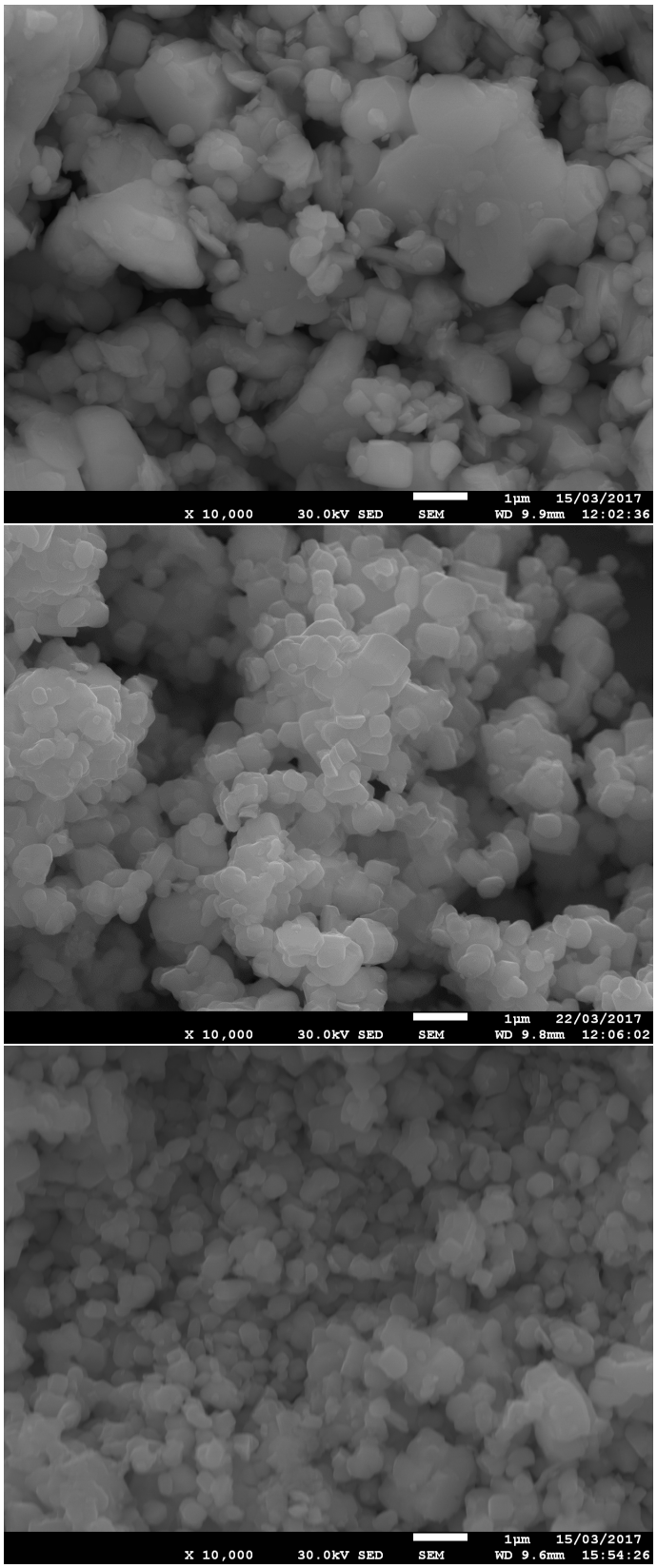

Figure 4.7: SEM images of $Cd_{1-x}Y_xSb_2O_6$ rectangular bars with x = 0.03 (1^{rst} row); 0.05 (2^{nd} row) and 0.10 (3^{rd} row). These images were taken at a voltage of 30 kV and a magnification of 10kX. The white ruler below each image corresponds to 1 μm.

the yttrium concentration within the lattice. It may be due to the fact the ionic radius of yttrium ions is smaller than that of cadmium ions. The SEM images also indicate that the $Cd_{1-x}Y_xSb_2O_6$ samples become more porous with increasing substitution ratio. It is confirmed by the density measurements of the samples. The relative densities of samples $Cd_{0.97}Y_{0.03}Sb_2O_6$ and $Cd_{0.95}Y_{0.05}Sb_2O_6$ are 69 and 63.5 %, respectively. Therefore, the more Y^{3+} substitute Cd^{2+}, the more the particles size decreases and the less dense the material becomes.

EDX measurements have been performed on three images of Y-doped $CdSb_2O_6$ (with x = 3; 5; 10 %) and of the parent material $CdSb_2O_6$. Note that the atomic percentage of oxygen (O) does not appear in Table 4.4 as this element is light (small molar mass). Hence, oxygen can not be appropriately quantify. Elements with a Z number less than 11 emit low-energy x-rays, thus the emitted x-rays are mostly absorbed by the sample and only a weak signal is detected. Table 4.4 below presents the results of the EDX analysis.

Table 4.4: Ratio of the atomic percentages of elements (Cd, Y, Sb) within $Cd_{1-x}Y_xSb_2O_6$ polycrystalline samples. These data are extracted from EDX measurements. * All experimental values normalised using Sb as a known reference.

		Samples			
Ratio	**Atomic percentage (%)**	**x = 0**	**x = 0.03**	**x = 0.05**	**x = 0.10**
Cd/Sb	theoretical	0.5	0.486	0.477	0.450
	experimental*	0.480 ± 0.014	0.482 ± 0.003	0.473 ± 0.004	0.428 ± 0.002
Y/Sb	theoretical	-	0.015	0.025	0.05
	experimental	-	0.015 ± 0.003	0.025 ± 0.007	0.049 ± 0.004

The atomic percentage of antimony is constant within all four compositions therefore this element was used as a reference element to explore the atomic percentage ratio between cadmium and yttrium. The atomic percentages of antimony (Sb) were normalised to 22.222 %. The experimental atomic percentages for the ratios Cd/Sb and Y/Sb correspond to the averages of the measured values for three images which are then normalised with respect to the antimony atomic percentage. For each sample, the experimental and theoretical (nominal) atomic percentages are in good agreement as the errors on these values is lower than 3σ. σ is the error on an atomic percentage. For instance, the experimental and nominal values of the atomic percentage ratio (Cd/Sb) in $Cd_{0.97}Y_{0.03}Sb_2O_6$ sample are both equal to 0.480 (014) and 0.5 respectively. The atomic percentage ratio Cd/Sb, Y/Sb are within good agreement for the other samples as indicated in Table 4.4 above.

X-ray diffraction confirmed the phase purity of the different samples as the positions and relative intensities of the observed reflections are those of the a lattice with the space group $P\bar{3}1m$ (162). The EDX measurement confirmed that the quantities of yttrium in each sample was similar to that of the respective theoretical values. The phase purity of these materials were confirmed by the 1:2 ratio between the atomic percentages of the ensemble (Cd, Y) and the ones of Sb. These two structural characterisation techniques confirmed that the prepared $Cd_{1-x}Y_xSb_2O_6$ samples are all single phase. The thermoelectric properties of these polycrystalline samples have then been investigated.

4.5 Thermoelectric properties

The electrical conductivity and the thermopower of the $Cd_{1-x}Y_xSb_2O_6$ samples have been measured simultaneously on the ZEM instrument. Rectangular bars have been designed for this system. The $Cd_{1-x}Y_xSb_2O_6$ rectangular bars are displayed in Figure 4.8 below. Details on the ZEM machine and the preparation method of the rectangular bars are given in sections 2.3.1 and 2.3.2 of Chapter 2. The electrical conductivity data is discussed followed by analysis of the temperature dependence of the different Seebeck coefficients. The final part of this section is dedicated to the power factors of the yttrium-doped $CdSb_2O_6$ samples. The crystal structure of the Y-doped $CdSb_2O_6$ is assumed to be constant from room temperature to 1000 K.

a)  b) 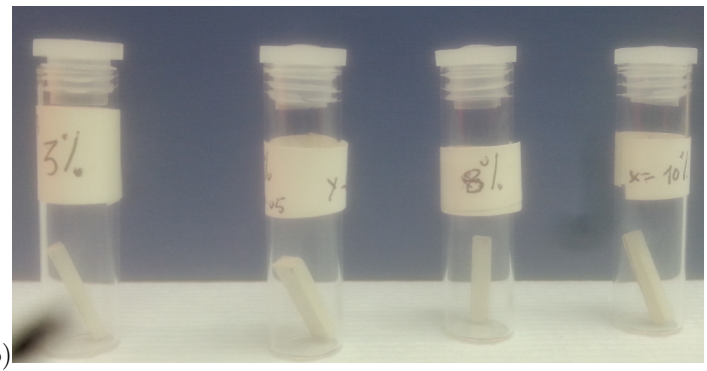

Figure 4.8: a) A $CdSb_2O_6$ pellet. b) Four vials, each containing a rectangular bar of $Cd_{1-x}Y_xSb_2O_6$ sample with x = 0.03; 0.05; 0.08 and 0.10. All these materials have a green-yellow colour.

4.5.1 The electrical conductivity

The electrical conductivity (σ) as function of the temperature (T) has been measured for all four yttrium-doped cadmium metantimonate samples. $CdSb_2O_6$ is an insulator[167] at room temperature, as its resistivity is near $1 \times 10^6\,\Omega$cm. The ZEM instrument cannot measure highly resistive materials and as a result no measurements were perform on $CdSb_2O_6$. The electrical conductivity data of the three other samples are illustrated in Figure 4.9 on the next page.

The introduction of yttrium within the lattice of $CdSb_2O_6$ has enhanced the conductivity by five orders of magnitude. For instance, the $Cd_{0.97}Y_{0.03}Sb_2O_6$ sample exhibits an electric conduction of $50\,S\,cm^{-1}$ at 950 K. This value differs from the one reported by Yanagawa and coworkers[167] ($1 \times 10^2\,S\,cm^{-1}$). This discrepancy may be due to the poor density of the current polycrystalline materials. Additionally, it appears that at room temperature $Cd_{0.97}Y_{0.03}Sb_2O_6$ polycrystalline sample is the best conductor. Its conductivity is one order of magnitude higher than that of $Cd_{0.95}Y_{0.05}Sb_2O_6$ and $Cd_{0.90}Y_{0.10}Sb_2O_6$: $\sim 29\,S\,cm^{-1}$ and $\sim 7\,S\,cm^{-1}$, respectively. Data mining[19] was used to compare the current electrical conductivities data with some established TE materials. The conductivity values of the yttrium-doped cadmium metantimonate ceramics are comparable to that of Ni-doped $CuNd_2O_4$[172]. $Cu_{0.98}Ni_{0.02}Nd_2O_4$ exhibits an electrical conductivity of about $43\,S\,cm^{-1}$ at 1000 K.

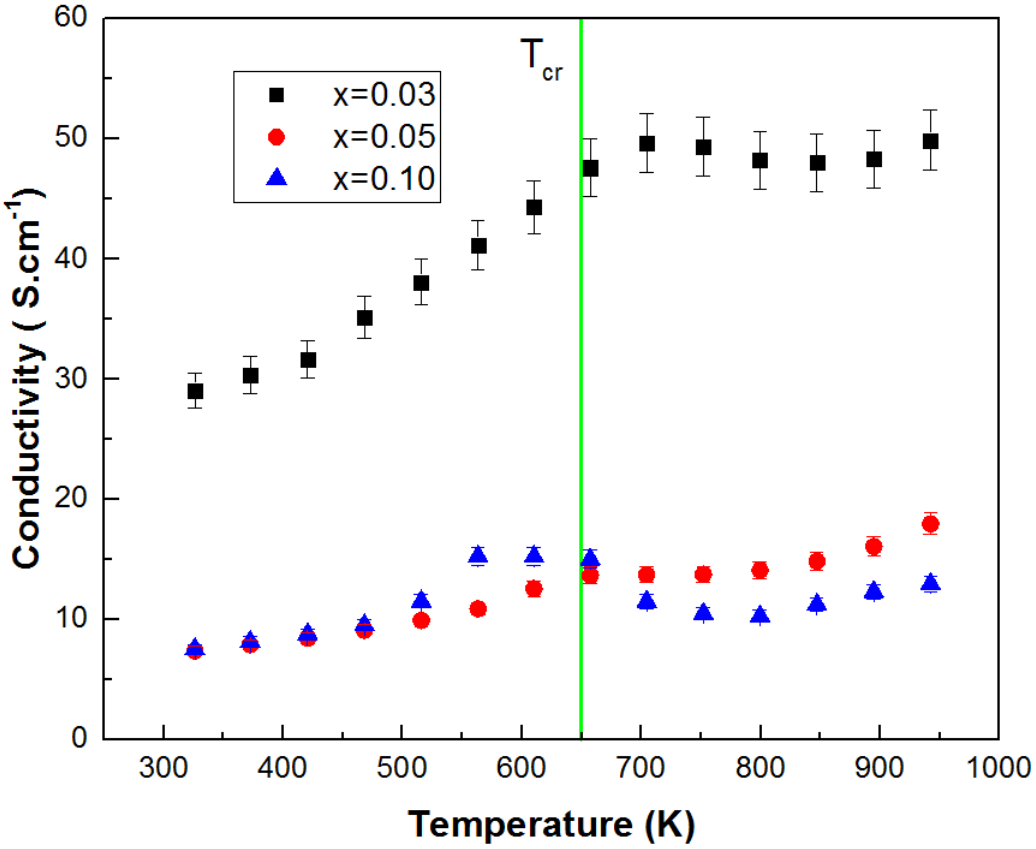

Figure 4.9: Electrical conductivity σ of $Cd_{1-x}Y_xSb_2O_6$ samples. The black squares represents $Cd_{0.97}Y_{0.03}Sb_2O_6$. The samples with 5 % and 10 % of yttrium are shown by the red triangles and blue dots, respectively.

4.5.1.1 Analysis

The three profiles in Figure 4.9 suggest that the electric conduction of $Cd_{0.95}Y_{0.05}Sb_2O_6$ behaves similarly as $Cd_{0.90}Y_{0.10}Sb_2O_6$, as temperature increases. The range of their conductivities values vary between $7\,S\,cm^{-1}$ at 300 K and $19\,S\,cm^{-1}$ at 950 K. The conductivity of the sample x = 0.03 almost doubles in the same temperature range. The slopes of the the three conductivities profiles change at 650 K and this is well pronounced for samples for which x is equal to 0.05 and 0.10. From room temperature to 650 K, $Cd_{0.95}Y_{0.05}Sb_2O_6$ has a higher resistivity than that of $Cd_{0.90}Y_{0.10}Sb_2O_6$. However, for temperatures above 650 K the sample x = 0.05 becomes a better conductor than the sample x =0.10. Indeed at 950 K the samples for which x = 0.05 and 0.10 exhibit the following respective conductivity values: $18\,S\,cm^{-1}$ and $13\,S\,cm^{-1}$.

The curves also indicate that from 650 K to 950 K the fewer Y^{3+} atoms are contained within the lattice, the better the conductivity of the material. It is also the case at 950 K where the three samples have the following respective conductivity values: $50\,S\,cm^{-1}$, $18\,S\,cm^{-1}$, $13\,S\,cm^{-1}$. Optical and electrical measurements from Yanagawa *et al.*[167] demonstrated that the free-carriers or conduction electrons are the Cd^{2+} electrons. Y^{3+} has a higher valence state that Cd^{2+}. One thus expects the free-carriers concentration to increase as the yttrium content increases. Therefore there should be an increase of the electrical conductivity. The behaviour of σ at high temperatures with respect to the doping concentration, does not follow this trend. Figure 4.9 suggests that there is a critical doping carrier concentration $n_{Y,cri}$ such that an increase of the Y^{3+} content contributes to a deterioration of the conduction of free-carriers. This concept is illustrated by the diagram at the top in Figure 4.10.

This behaviour of the electrical conductivity with respect to the doping concentration also occurs in Sn-doped CdO. Yan *et al.*[173] studied the electrical properties of CdO thin films. The thin films were doped withSn: 1; 2.5; 5.2; 6.2 and 11.4 %. Yan and coworkers emphasised that there is a critical doping carrier concentration of tin, in fact 2.5%, beyond which there is deterioration of the electrical properties (μ, σ) of the $Cd_{1-x}Sn_xO$ films. The electrical conductivity increases from $1 \times 10^3\,S\,cm^{-1}$ for x = 0% to $4.2 \times 10^4\,S\,cm^{-1}$ for x = 2.5%, it then decreases down to $8 \times 10^3\,S\,cm^{-1}$ as x increases up to 11.4%. According to Yan and co-workers the decrease of the mobility of the free-carriers with increasing doping concentration plays a major role in the reduction of the electrical properties of $Cd_{1-x}Sn_xO$ samples. The crystalline defects such as oxygen vacancies and grain boundaries also contribute to a deterioration of the electrical conductivity at high temperature. The current study on $Cd_{1-x}Y_xSb_2O_6$ systems present similar features with the work of Yan *et al.*[173]. There is thus an optimal doping concentration x between 0 and 0.05, for which σ reaches its maximum as depicted by the diagram at the bottom in Figure 4.10. The decrease of the free-carriers mobility with increasing doping concentration may be responsible for the decrease of the electric conduction in Y-doped $CdSb_2O_6$ samples. Additionally, the decrease of density of the $Cd_{1-x}Y_xSb_2O_6$ with increasing Y^{3+} concentration may play role in the previous studies results. As it is well known that a decrease in relative density may contribute in a decrease their electrical conductivity.

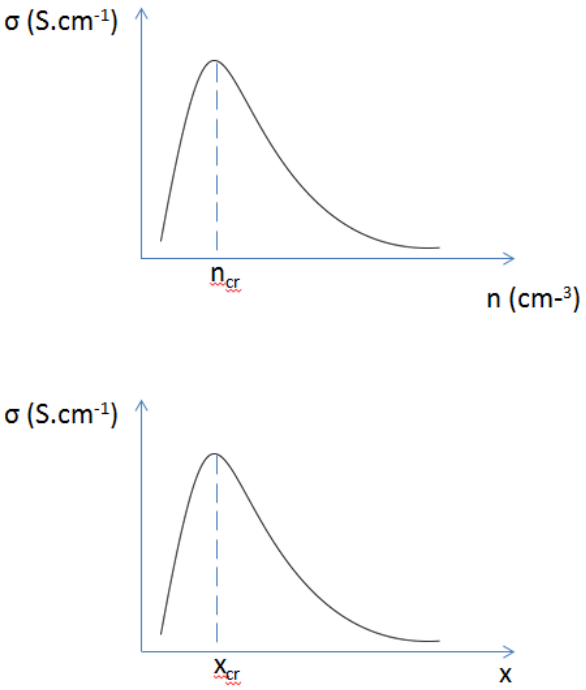

Figure 4.10: Schematic representations of the electrical conductivity of Y-doped $CdSb_2O_6$ samples with respect to carrier concentration (top) and doping concentration (bottom).

4.5.1.2 A model for the electrical conductivity of $Cd_{1-x}Y_xSb_2O_6$ samples from 300 to 650 K

The conductivity of Y-doped $CdSb_2O_6$ samples increases with increasing temperature from room temperature to 650 K, as seen in Figure 4.9. These materials can therefore be viewed as *n*-type semiconductors. Several models were tested to fit the experimental data. The broad band model was ruled out, as the trend of the data points in the Arrhenius plot ($\ln[\sigma]$ vs $\frac{1}{T}$) was not a straight line. There were also discrepancies between the profile calculated from the variable range hopping and the experimental data. On the other hand, there was good agreement (low χ^2) between the measured conductivities values and those predicted by the small polaron hopping model. In this model, for electric conduction to occur, electrons hop between localised states near the Fermi level. If the behaviour of σ within $Cd_{1-x}Y_xSb_2O_6$ ceramics is welll explained by the small polaron hopping, the plot $\ln[\sigma.T]$ vs $\frac{1}{T}$ should be a straight line. The slope and intercept of the line are equal to - $\frac{\Delta}{k_B}$ and $\ln(A)$, respectively. Δ corresponds to the activation energy E_A. Figure 4.11 on the next page illustrates the evolution of $\ln(\sigma.T)$ as function of $\frac{1}{T}$ for $Cd_{0.97}Y_{0.03}Sb_2O_6$.

The lowest values on the *x*-axis in Figure 4.11 correspond to high temperature whereas those near 0.021 K^{-1} are related to low-temperature values. For instance, 0.0015 K^{-1} and 0.021 K^{-1} correspond to 667 K and 48 K respectively. Figure 4.11 demonstrates the linear response of the $\ln(\sigma T)$ as $\frac{1}{T}$ varies from 0.0016 to 0.0027 K^{-1}. The respective temperatures for these two values of $\frac{1}{T}$ are 625 and 370 K. It was therefore possible to fit the black squares with the small polaron hopping model in equation (3.36) of Chapter 3. The fitting curve is represented by the green line in Figure 4.11. The activation energy E_A was deduced from the slope and it is about 0.073 $\pm$ 0.004 eV. The electrical conductivity data of $Cd_{0.95}Y_{0.05}Sb_2O_6$ and $Cd_{0.90}Y_{0.10}Sb_2O_6$ also fitted within the small polaron

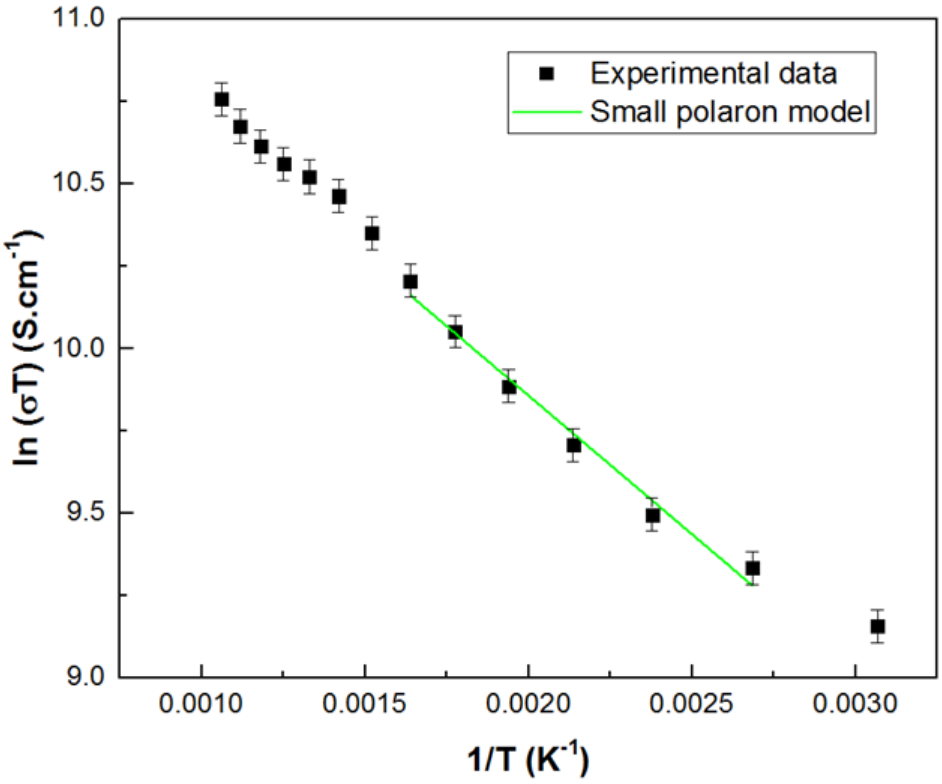

Figure 4.11: Fitting of electrical conductivity data with small polaron model. The black diamonds represent the experimental data and the red line stands for the theoretical model.

model, and the results are presented in Figure 4.12. The respective activation energies for these two samples are 0.069 ± 0.005 eV and 0.055 ± 0.003 eV. As expected the difference in energy between the bottom of the conduction and the donor states decreases as more Y^{3+} are introduced in the CB.

4.5.2 The Seebeck coefficient

The thermopower α of $Cd_{1-x}Y_xSb_2O_6$ rectangular bars has also been measured on the ZEM instrument. Figure 4.13 on page 97 exposes the temperature dependence of their thermopower. The negative sign of the Seebeck of these materials indicates that the free-carriers responsible for the electric conduction in these materials are electrons. It is in agreement with the band structure calculations which indicates that $CdSb_2O_6$ is suitable for *n*-type doping. For example, at 326 K the value of thermopower of $Cd_{0.97}Y_{0.03}Sb_2O_6$, $Cd_{0.95}Y_{0.05}Sb_2O_6$ and $Cd_{0.90}Y_{0.10}Sb_2O_6$ are −50.01, −59.32 and −61.34 $\mu V\,K^{-1}$, respectively. Within all three samples $|\alpha|$ increases with increasing temperature. The absolute value of the thermopower is the relevant parameter because the power factor is proportional to α^2. The magnitude of $|\alpha|$ has practically doubled as T increases from room temperature to 950 K. For instance, at 300 and 950 K temperatures the absolute value of the thermopower of $Cd_{0.97}Y_{0.03}Sb_2O_6$ takes the respective values of about 50 and 100 $\mu V\,K^{-1}$. Besides the Seebeck coefficients of $Cd_{0.95}Y_{0.05}Sb_2O_6$ (green triangles) and and $Cd_{0.90}Y_{0.10}Sb_2O_6$ (red squares) are similar at any given temperature. The high-temperature thermopower values of the prepared samples are in the same order of magnitude of that of $Cu_{0.98}Ni_{0.02}Nd_2O_4$ which exhibits a thermopower of about 83 $\mu V\,K^{-1}$ at 1000 K.[172]

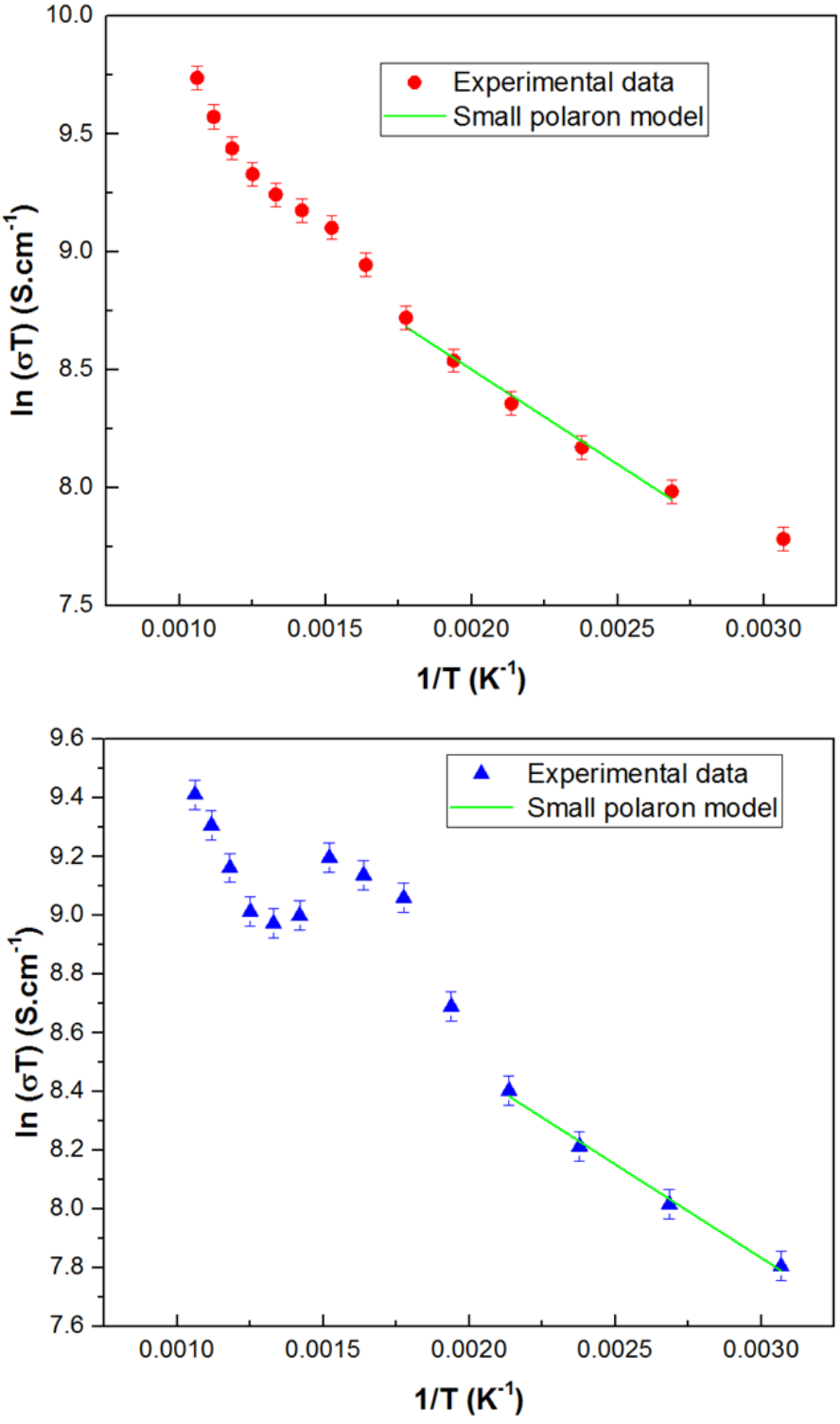

Figure 4.12: Fitting of electrical conductivity data with small polaron model for $Cd_{0.95}Y_{0.05}Sb_2O_6$ (top) and $Cd_{0.90}Y_{0.10}Sb_2O_6$ (bottom). The black diamonds represent the experimental data and the green line stands for the theoretical model.

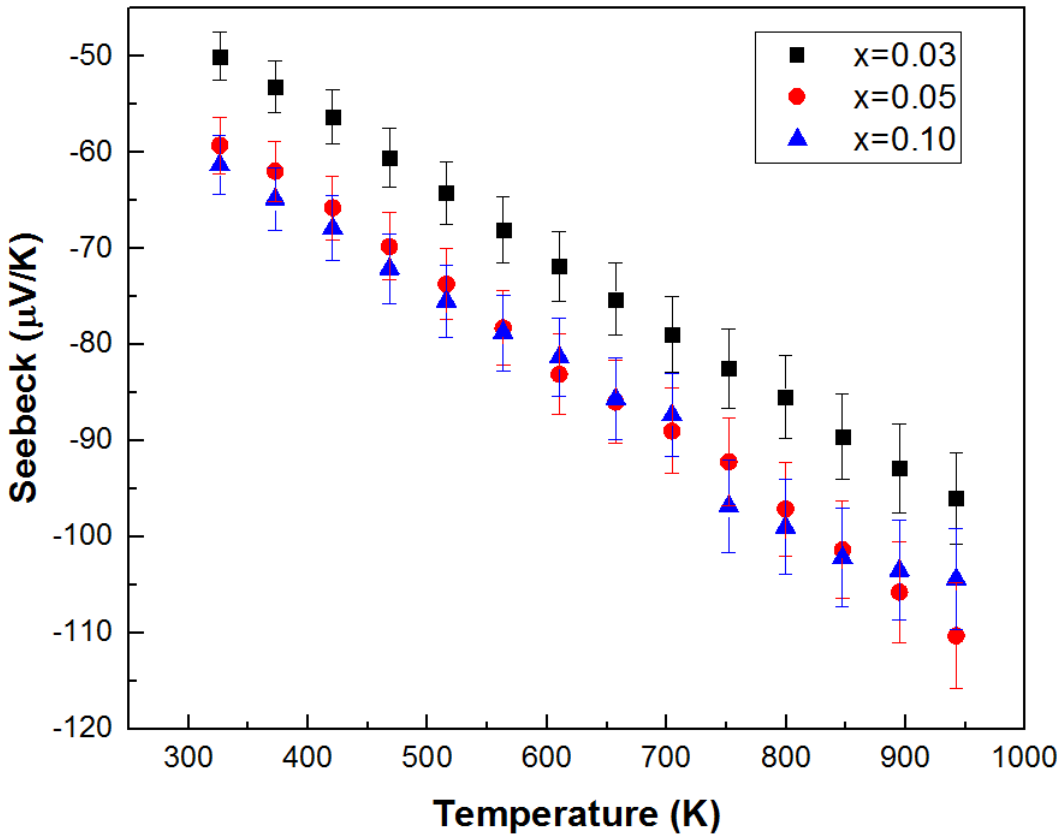

Figure 4.13: Thermopower (α) of $Cd_{1-x}Y_xSb_2O_6$ samples. The blue dots represent the sample x = 0.03; the two other samples $Cd_{0.95}Y_{0.05}Sb_2O_6$ and $Cd_{0.90}Y_{0.10}Sb_2O_6$ are shown by the green triangles and red squares, respectively.

The Y-doped $CdSb_2O_6$ systems behave as *n*-type semiconductors as their electric conduction increases with increasing temperature. As a consequence, the model used to fit the experimental data of the three samples is given by

$$\alpha(T) = \frac{k_B}{e}.(\frac{E_A}{k_B T} + A_c), \tag{4.5}$$

where k_B and e are the Boltzmann constant and the charge of the electron, respectively. The term A_c is a dimensionless parameter. Figure 4.14 illustrates the fitting of the experimental data of $Cd_{0.97}Y_{0.03}Sb_2O_6$. In this figure, the experimental data and the fitting curve are indicated by the black squares and the violet line, respectively. The low values of the x-axis correspond to high temperature values whereas low temperatures are associated with high values on the x-axis. There is good level of agreement between the measured and calculated Seebeck coefficient for temperatures between 600 and 950 K. The absence of data for temperatures below room temperature contributes to the poor fit at temperatures below 600 K. Thermopower data measured at temperatures below 300 K should improve the agreement between the experimental data and the profile derived from the model.

The thermopower of the $Cd_{0.95}Y_{0.05}Sb_2O_6$ and $Cd_{0.90}Y_{0.10}Sb_2O_6$ samples were fitted with the

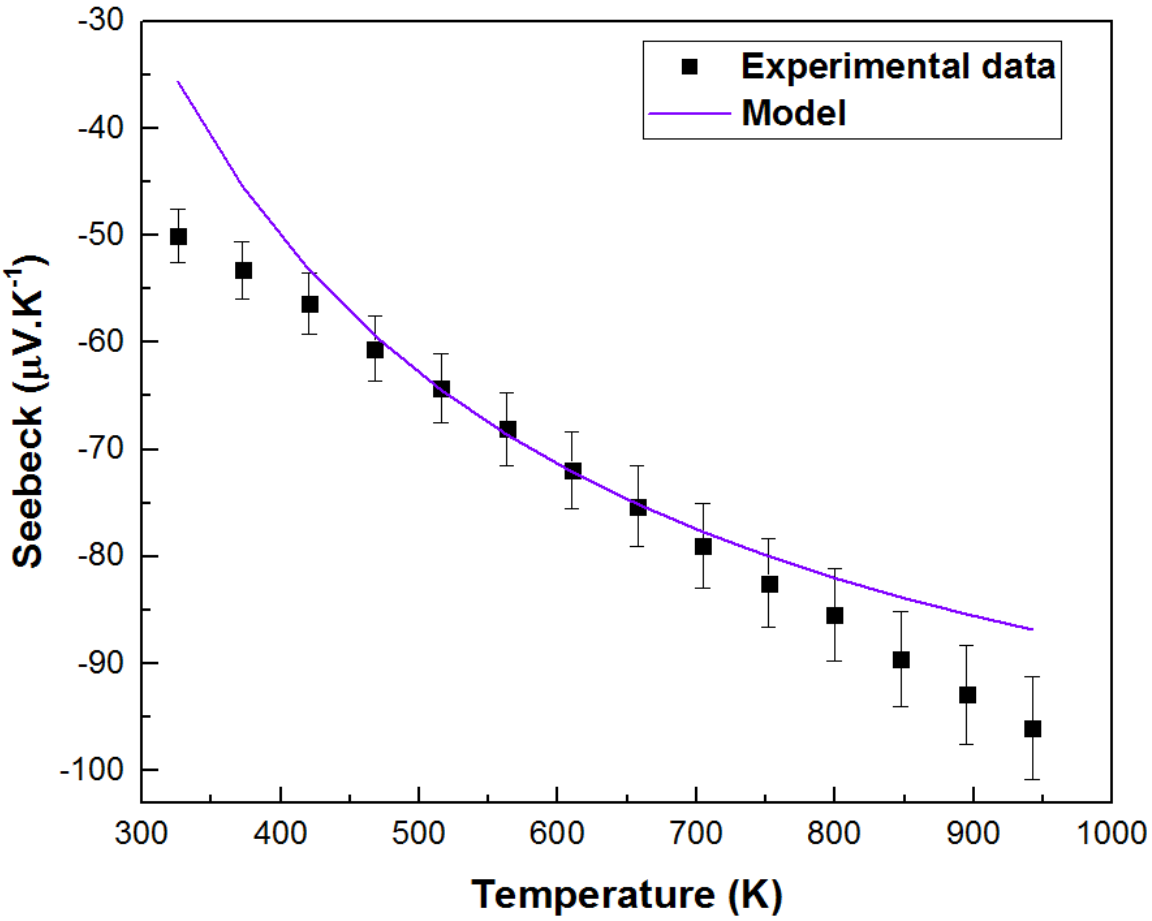

Figure 4.14: Fitting of the Seebeck coefficient of $Cd_{0.97}Y_{0.03}Sb_2O_6$. The experimental and theoretical curves are shown by the black squares and the violet line, respectively.

model in equation (4.5), as seen in Figure 4.15. The Mott formula describes the temperature dependence of the thermopower of all three materials as the values of χ^2 are low. The discrepancies between measured and calculated thermopower for these samples are more pronounced for these two samples than in $Cd_{0.97}Y_{0.03}Sb_2O_6$. Indeed at about 950 K $Cd_{0.90}Y_{0.10}Sb_2O_6$ exhibits a Seebeck coefficient of about 110.31 $\mu V\,K^{-1}$ whereas the model predicts a value of 55.15 $\mu V\,K^{-1}$. The low density of these two samples may play a important role in the shift between experimental and theoretical thermopower values. The activation energies E_A extracted from the fitting of the thermopower curves for $Cd_{0.97}Y_{0.03}Sb_2O_6$, $Cd_{0.95}Y_{0.05}Sb_2O_6$ and ce$Cd_{0.90}Y_{0.10}Sb_2O_6$ were found to be about 0.026 ± 0.004 eV , 0.028 ± 0.005 eV and 0.026 ± 0.003 eV, respectively. These values are smaller than the activation energies extracted from the electrical conductivity as expected for a material in which electric conduction occurs via thermally excited hopping of small polarons.

4.5.3 The power factor

Knowing both the electrical conductivity ρ and the Seebeck coefficient α of the different samples one then computes their respective power factor, *PF*, for temperatures between 300 K and 950 K. The power factor in Figure 4.16 on page 101 is obtained from equation (4.6):

$$PF = \frac{S^2}{\rho} = S^2.\sigma. \tag{4.6}$$

The *PF* vs T plots in Figure 4.16 indicate that the $Cd_{1-x}Y_xSb_2O_6$ samples exhibit a power factor of the other of few microwatts per meter per kelvin square. The *PF* of each material increases with increasing temperature. The *PF* of $Cd_{0.97}Y_{0.03}Sb_2O_6$ is greater than that of the two other samples. At 942 K the power factor of $Cd_{0.97}Y_{0.03}Sb_2O_6$ sample is more than the double of the values of $Cd_{0.95}Y_{0.05}Sb_2O_6$ and $Cd_{0.90}Y_{0.10}Sb_2O_6$: 45.98, 21.85 and 15.77 $\mu W\,m^{-1}\,K^2$. respectively. The trends of curves in Figure 4.16 are similar to those in Figure 4.9. It is due to the fact that the electrical conductivity is few orders of magnitude greater than the Seebeck coefficient. In other words σ dictates the behaviour of the temperature dependence of the power factor of these materials. The $Cd_{0.97}Y_{0.03}Sb_2O_6$ sample seems to be the best candidate for high-temperature thermoelectric applications, as it exhibits the highest *PF* (45.98 $\mu W\,m^{-1}\,K^{-2}$) at high temperature. The power factor of this AB_2O_6 oxide is higher than that of $Cu_{0.98}Ni_{0.02}Nd_2O_4$, which exhibits a power factor of 30.04 $\mu W\,m^{-1}\,K^{-2}$.

4.6 On the density of yttrium-doped cadmium metantimonate

This section presents the methods which were utilised to increase the density of the yttrium-doped cadmium metantimonate samples in order to improve the electrical conductivity of Y-doped $CdSb_2O_6$. The methods used herein this work are the sintering[174,175] and the ball-milling[126] techniques.

The formula in equation (2.8) in the section 2.3 of Chapter 2 was utilised for the determination of the density *d* of the prepared samples. Distilled water was used as the solvent.

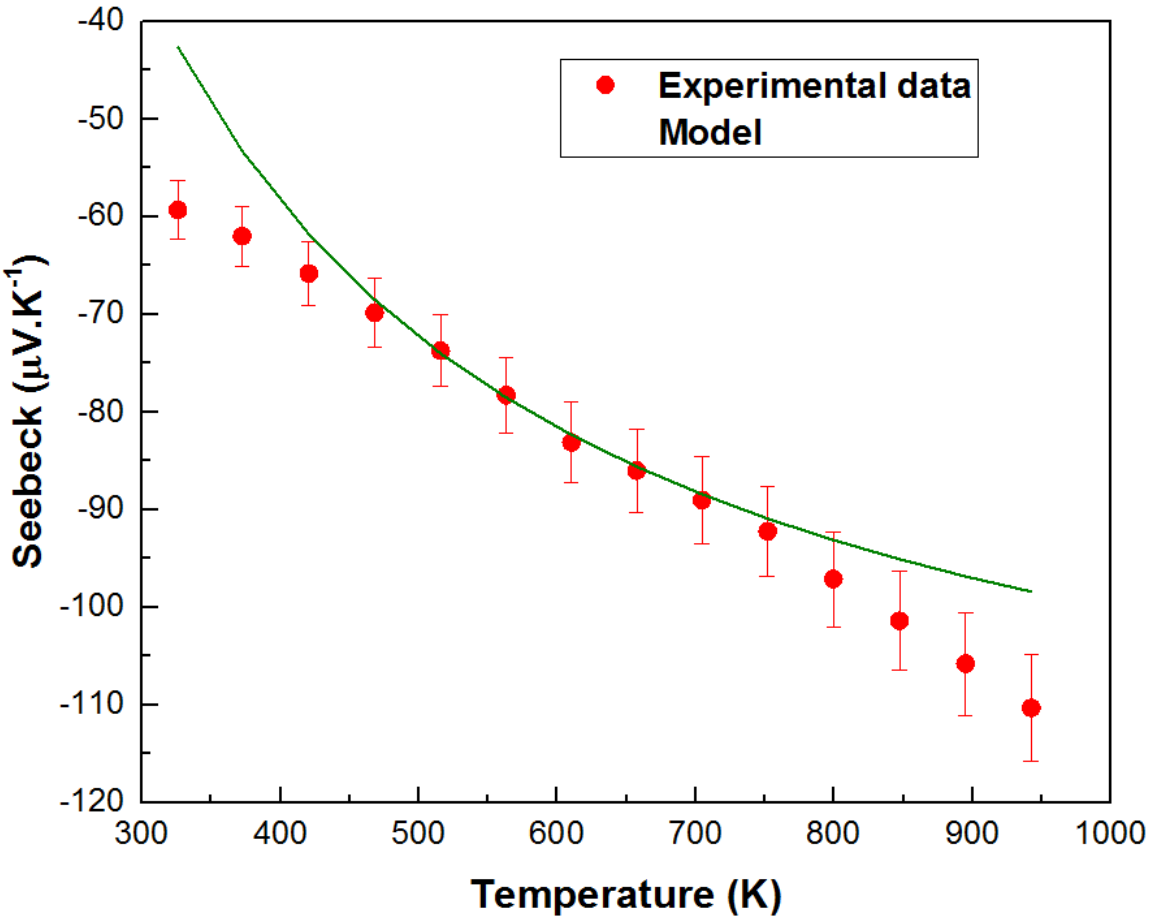

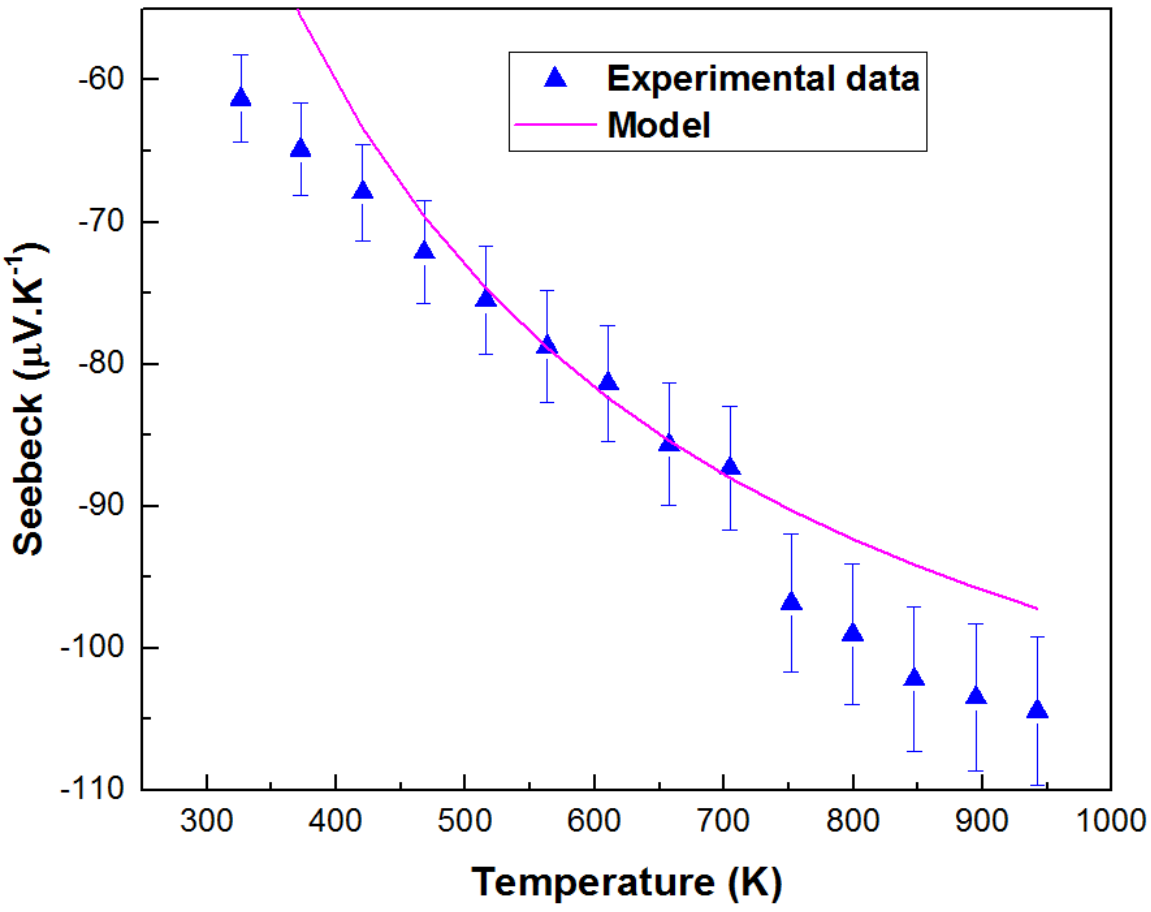

Figure 4.15: Fitting of the thermopower (α) of $Cd_{0.95}Y_{0.03}Sb_2O_6$ (top) and $Cd_{0.90}Y_{0.10}Sb_2O_6$ (bottom). The straight lines in each graph are the fitting curves. The red dots and blue triangles correspond to the experimental data.

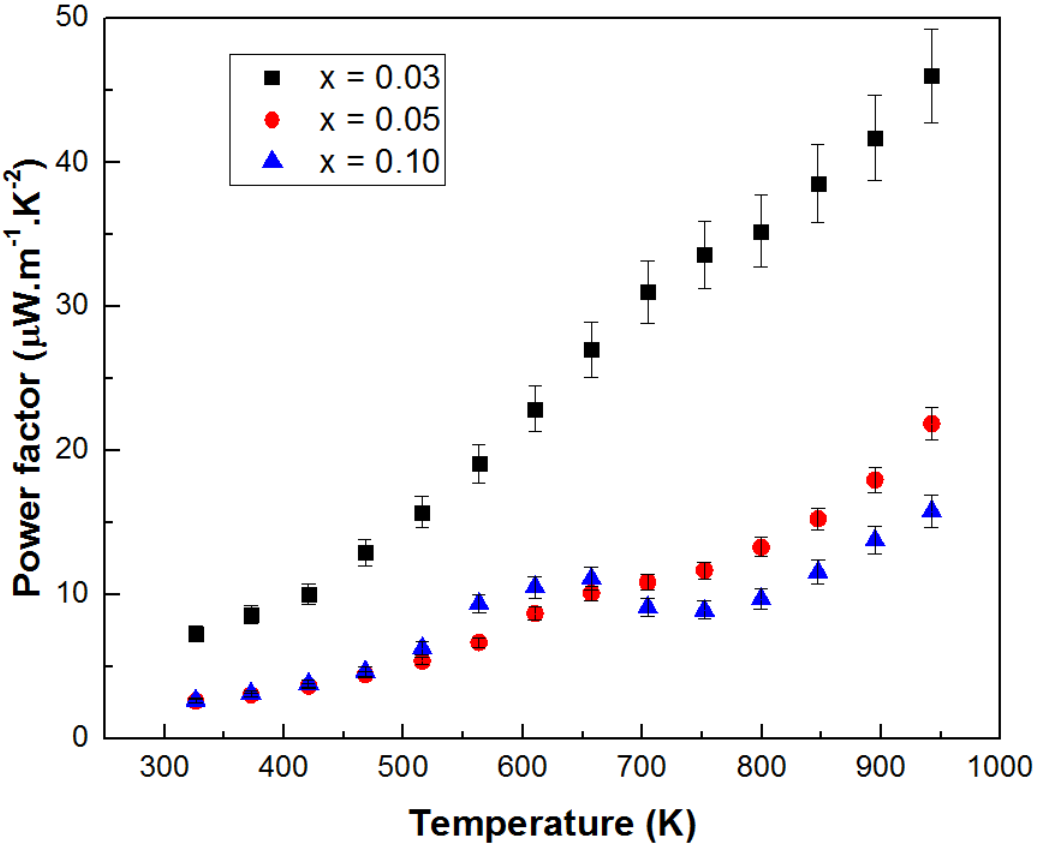

Figure 4.16: Power factor (*PF*) of $Cd_{1-x}Y_xSb_2O_6$ samples. The two samples for which x = 0.05 and 0.10 are shown by the black and blue dots, respectively. Reds dots correspond to $Cd_{0.97}Y_{0.03}Sb_2O_6$ sample.

For instance, for $Cd_{0.97}Y_{0.03}Sb_2O_6$ sample the masses m_1, m_2 and m_3 take the respective following values 3.2246 g, 2.6433 g and3.3487 g. Applying the relation in equation (2.8) one can write:

$$d = 0.99823 * \frac{3.2246}{3.3487 - 2.6433} \tag{4.7}$$

where is d is the density of the $Cd_{0.95}Y_{0.05}Sb_2O_6$ pellet, $0.998\,23\,g\,cm^{-3}$ is the density of water at room temperature. The density of this yttrium-doped cadmium metantimonate is equal to $\sim 4.56\,g\,cm^{-3}$ whereas the theoretical value is $6.58\,g\,cm^{-3}$ and it corresponds to 69 % as relative density. The low value of d suggests the presence of pores within the material. This porosity is illustrated by the voids between the particulates in Figure 4.7. The concentration of voids seems to increase as one goes from x = 3% (top image in Figure 4.7) to x = 10% (bottom image in Figure 4.7).These pores are potential defects for the electric conduction of the material.

One of the popular method of solid-state chemists to increase the density of a material is the sintering. The material is heated up to a higher temperature than that of its synthesis temperature, but below the melting point of the material[174,175]. An increment of the reaction's temperature causes an agglomeration the grains particles close to each other therefore it reduces the volume of pores within the material. Ball-milling is another process which enables the synthesis of highly dense ceramics. A ball-mill is a grinding device with a cylindrical shape. By constantly rotating clockwise or anti-clockwise around a horizontal axis the ball-mill converts material into fine powders via the presence of a grinding material. Ball-milling is a technique which favours a better inter-mixing of the reagents materials[126]. Consequently, the resulting mixture consists of fine particles with high surface area thereby there will be an increase of the reaction rate between the precursors at high temperature. Zirconium balls were utilised as grinding materials in this work.

Investigations on the effects of sintering and ball-milling on $Cd_{0.98}Y_{0.02}Sb_2O_6$ pellets were carried out with the following sequence:

- A mixture of CdO, Sb_2O_3 and $Y(NO_3)_3$,$6H_2O$ was ball-milled for 16 h; parallely to that a mixture of the three precursors was also prepared with a pestle and mortar.
- Three pellets have been prepared from the ball-mill mixture and one pellet was prepared from the pestle and mortar mixture.
- The latter pellet and one of the three prepared from the ball-mill mixture have both been sintered at 1323 K for 48 h.
- The other two pellets were fired up fro 48 h at 1373 K and 1423 K, respectively.

After sintering the phase purity of the samples was assessed. X-ray diffraction has been performed to check the phase purity of the prepared samples. The recorded diffractograms are displayed in Figure 4.17 on the next page.

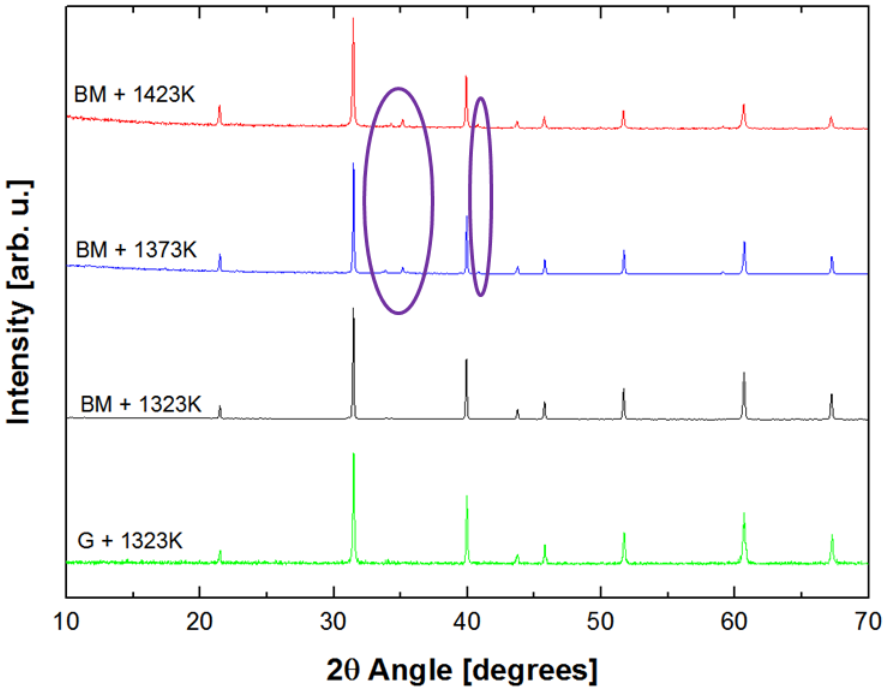

Figure 4.17: Power x-ray diffraction patterns of $Cd_{0.98}Y_{0.02}Sb_2O_6$ samples prepared under different conditions.

Table 4.5: Positions and relative intensities of reflections of $Cd_2Sb_2O_7$.

	Five reflections				
Number	1	2	3	4	5
2θ **angle** (deg)	17.381	33.654	35.118	40.787	59.055
Relative intensity (arb u)	7.29766 118	7.10619 228	6.74471 374	6.23355 144	5.56841 139

The initials "G" and "BM" stand for grinding and ball-milling, respectively. The numbers beside these two initials correspond to the sintering temperatures. The powder x-ray diffraction patterns in green and black are similar to the diffractogram in Figure 4.5 apart from the poor background of the first one. These XRD patterns are associated with powders which have been sintered at 1323 K. It suggests that the formation of $CdSb_2O_6$ is not affected by the method of preparation - grinding or ball-milling. The two other diffractograms, in blue and red, differ from the green and black diffractograms by the presence of extra peaks. The magenta ellipses indicate the the reflections an additional phase. The positions (angles) of these extra reflections correspond to some of the Bragg peak positions of $Cd_2Sb_2O_7$. The angle and intensity of some of the Bragg peak of the spurious phase are displayed in Table 4.5 above.

The intensity of the reflections of the $Cd_2Sb_2O_7$ phase are higher in the x-ray diffraction pattern in red (1423 K) than in the one in blue (1373 K). The diffractograms of powders sintered at temperature higher than 1323 K are similar to that of Figure 4.3. One deduces that by increasing the sintering temperature one increases the formation rate of the spurious phase.

Table 4.6: Investigations on the density $Cd_{0.98}Y_{0.02}Sb_2O_6$ pellets. The theoretical density for these four pellets is $6.58\,g\,cm^{-3}$.

	Samples			
	Sample A	**Sample B**	**Sample C**	**Sample D**
Temperature (°C)	1050	1050	1100	1150
Method	G	BM	BM	BM
Mass (g)	0.7964	0.6757	0.5938	0.4916
Radius (cm)	0.500	0.500	0.500	0.500
Height (cm)	0.240	0.215	0.210	0.270
Density ($g\,cm^{-3}$)	4.23	4.00	3.60	2.32
Relative density (%)	64	61	55	35

The relative density of all four powders are displayed in Table 4.6. The relative density of an object is a comparison between its measured density and its theoretical value. The relative density of a material is given by:

$$d_r = 100 * (1 - \frac{d_{th} - d_a}{d_{th}}). \tag{4.8}$$

In equation (4.8) d_{th}, d_a and d_r are the respective theoretical, actual and relative densities.

Table 4.6 demonstrates that the density of the pellet decreases with increasing sintering temperature as the ceramics become more and more porous. The density of sample B ($4.00\,g\,cm^{-3}$) is far greater than the one of sample D ($2.32\,g\,cm^{-3}$). This table confirms that preparing samples via grinding or via ball-milling lead the similar polycrystalline samples. The respective relative densities of samples B and D are 64 and 61 %.

The low density of the yttrium-doped cadmium metantimonate samples can be attributed to two main factors: the volatility of Sb_2O_3 [167] and the presence of yttrium. At high temperature the loss of the Sb_2O_3 creates re-organization of the atoms within the lattice, this restructuring of the atoms within the lattice may lead to the formation of secondary phase. The material becomes cadmium rich and there is formation of oxygen vacancies. The loss of antimony oxide results in the decrease of the density of the material as the sintering temperature increases, as seen in Table 4.6. Although the temperature of the synthesis has been optimised, for an improvement of the density of Y-doped $CdSb_2O_6$, other parameters need to be addressed. These variables are for instance the sintering time, the use a binder or the time used to increase the density of the pellets on the cold isostatic press (CIP) instrument and. The role of a binder material is to glue to the ceramics particles together thereby closing voids between the particles.

4.7 Conclusion

As a conclusion, some thermoelectric properties of transparent conducting oxides Y-doped $CdSb_2O_6$ have been investigated. The temperature dependence of σ and α suggests that these materials can be treated as n-type semiconductors. The $Cd_{0.97}Y_{0.03}Sb_2O_6$ sample proved to the best candidate for thermoelectric applications due its high power factor. At 950 K its PF reaches up to 50 $\mu W\,m^{-1}\,K^{-2}$. However, this value is two orders of magnitude lower than that of state of the art oxide thermoelectric materials such as ZnO[176]. The values indicate that there is room for improvements. The use of a binder is envisaged for an improvement of the density of the $Cd_{1-x}Y_xSb_2O_6$ pellets. Hall measurements are considered as they will enable the determination of the carriers concentration of the materials. For a complete characterization of the thermoelectric properties of these systems their respective thermal conductivity κ needs to be measured thereby enabling the determination of their figure of merit (ZT). Finally this study suggests to investigate the temperature dependence of σ, α and κ as function of the content on Y^{3+} from 0 to 5 %. A n-type doping of $CdSb_2O_6$ is envisaged with La_2O_3 as the doping material. This is due to the fact that the size (1.032 Å) and coordination state (6) of La^{3+} are similar to that of Cd^{2+} (0.95 Å and 6). The higher valence state of silver (3+) suggests that the introduction of La^{3+} in the lattice may contribute to an increase of the free-carriers concentration thereby an increase of the electrical conductivity of $Cd_{1-x}La_xSb_2O_6$.

Chapter 5

Thermoelectric properties of tungsten divanadate oxide (WV_2O_6)

5.1 Motivation

WV_2O_6 crystallizes in a trirutile-type structure. W^{6+}, V^{3+} and O^{2-} ions order in a tetragonal lattice whose symmetry space group is $P4_2/mnm$ (136). The crystal lattice of WV_2O_6 is displayed in Figure 5.1 on the next page. W^{6+} and V^{3+} cations occupy the $2a$ and $4e$ Wyckoff sites within the lattice. The light blue octahedra in this Figure represent the WO_6 octahedra which form sheets in the a-b plane. The sheets are separated by blocks made of V and O atoms. Thus, the crystal structure of WV_2O_6 is constituted of alternated sheets of edge-shared octahedra (WO_6 and VO_6) along the c-axis. The crystal structure is made up of heavy elements (W and V) and with many atoms per unit cell: two tungsten, four vanadium and sixteen oxygens atoms. Hence, WV_2O_6 can be viewed as a superstructure and thereby fulfills two of the guidelines necessary to achieve high Figure of merit ZT. Indeed the high symmetry structure may contribute to minimize the scattering of charge carriers by optical phonons. For instance, the presence of heavy elements and many atoms per unit cell within this trirutile may contribute to a reduction of the thermal conductivity κ of WV_2O_6. In addition electrical studies[177] demonstrates that WV_2O_6 conducts electrically at room temperature and behaves like a semiconductor for temperatures between 300 and 620 K; its electrical conductivity ,σ, increases with increasing temperature. These aspects of WV_2O_6 suggest its potential for thermoelectric applications. The absence of reports on the thermoelectric properties of WV_2O_6 in the literature was the motivation of the investigations carried out within this material. This chapter is organised as follows: the structural and physical properties of this trirutile are first reviewed. It is followed by a structural characterization of the prepared polycrystalline samples. The thermoelectric properties (α, σ and κ)of WV_2O_6 are presented and analysed. Prior to these sections the electronic structure of this trirutile is discussed.

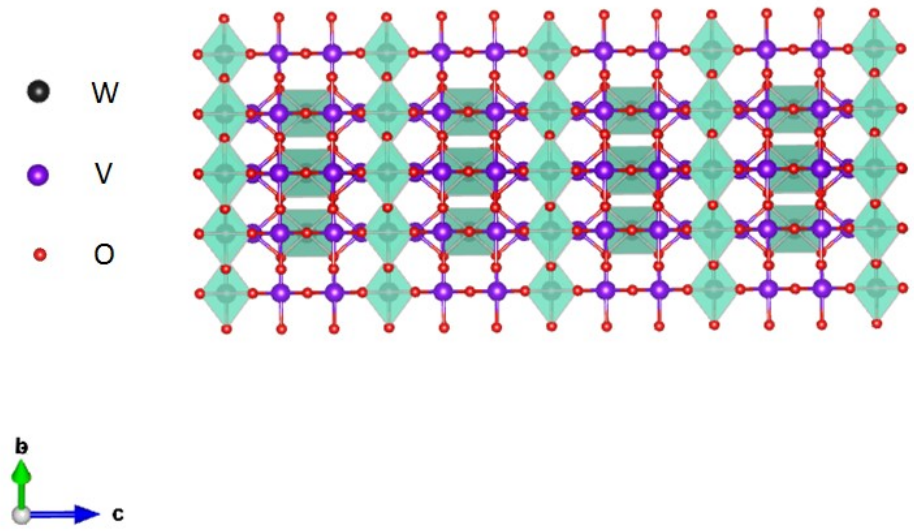

Figure 5.1: The crystal lattice of the trirutile WV_2O_6. W, V and O are represented by the black, magenta and red spheres, respectively. The light blue octahedra represent WO_6 octahedra.

5.2 A literature review of WV_2O_6

5.2.1 Methods of synthesis

Bernier and Poix[178] were the first to study the crystal structure of tungsten divanadate. They prepared powdered WV_2O_6 samples by mixing stoichiometric amount of WO_3 and V_2O_3. The mixture was heated at 950° under vacuum. Successive grindings and firings enable the formation of single phase WV_2O_6. X-ray diffraction analysis illustrates that WV_2O_6 crystallizes in a trirutile-type structure with the space group symmetry of the lattice is $P4_2/mnm$ (136). Hodeau *et al.*[177] prepared WV_2O_6 single crystals by chemical vapour transport[179,180] where $TeCl_4$ was used as transport agent for this single crystals growth. Their demonstrated that WV_2O_6 can either be trirutile or rutile. For a rutile WV_2O_6 there is disorder in the packing of magnetic cations (V^{3+}) and non-magnetic ones (W^{6+}). A regular packing is observed in WV_2O_6 tritutiles.

5.2.2 Physical properties

The magnetic properties of tungsten divanadate have been thoroughly investigated. Fruchart *et al.*[181] measured the susceptibility of polycrystalline WV_2O_6 samples. Susceptibility data of a trirutile WV_2O_6 at high temperature follows a Curie-Weiss profile of an antiferromagnetic material. There is maximum at 117 K. The Néel transition is confirmed by the study of the evolution of the intensity of a magnetic reflection (0 0 1) as function of temperature. The intersection of M(T) with the temperature axe corresponds to Néel temperature $T_N = 117 \pm 2$ K. The inverse magnetic susceptibility of an ordered WV_2O_6 shows a broad minimum whereas the one of a rutile WV_2O_6 is a straight line. Fruchart and coworkers refined the magnetic structure of the antiferromagnet WV_2O_6 from the neutron diffractograms recorded below T_N. The magnetic reflections follow the rule in equation (5.1)

$$h + k + l = 2n + 1, \tag{5.1}$$

whe h, k and l are integers and $l \neq 3$ n. The **A** configuration is their model for the sublattice magnetization of WV_2O_6. This model is given by:

$$\mathbf{A} = \mathbf{S_1} - \mathbf{S_2} - \mathbf{S_3} + \mathbf{S_4}. \tag{5.2}$$

The indexes from 1 to 4 are related to the positions of the magnetic ions (V^{3+}) within the magnetic unit cell. The magnetic structure of WV_2O_6 is similar to the collinear magnetic structure of WCr_2O_6 [182,183]. The positions of magnetic ions in the magnetic unit cell are presented in Table 5.1.

Table 5.1: Wyckoff positions of magnetic atoms within magnetic unit cell of WV_2O_6. Space group: $P4_2/mnm$ (136).

site	x	y	z
1	0	0	z
2	0	0	1 - z
3	$\frac{1}{2}$	$\frac{1}{2}$	$\frac{1}{2}$ + z
4	$\frac{1}{2}$	$\frac{1}{2}$	$\frac{1}{2}$ - z

Refining the neutron diffraction patterns below T_N only with the A_{xy} mode lead to an average magnetic moment of $0.9 \pm 0.2\,\mu_B/V^{3+}$. This value is lower than the expected value of $\mu_{eff} = 2.83\,\mu_B$. This discrepancy between measured and theoretical magnetic moment value is due to the superposition of magnetic and nuclear reflections.

Hodeau *et al.* [177] investigated the electrical properties of tungsten divanadate. Using two electrodes, made of platinum, they measured the resistance of WV_2O_6 single crystals from room temperature to 1000 K. The plot log (R) = f (1/T) was fitted by a straight line indicating that the tungsten divanadate behaves like a broad band semiconductor. Using the data from 249 K up to 625 K Hodeau *et al.* [177] deduced the activation energy, E_A, from the slope of the fitting line: E_A = 0.20 eV. This is in agreement with previous work by Rfidorff and Kornelson (1969) who refined a value of 0.24 eV for E_A.

5.3 Synthesis

Powdered WV_2O_6 samples have been prepared by a solid state reaction. The synthesis, in accordance with Bernier and Poix (1968), was carried out by mixing appropriate amounts of WO_3 (99.9%) and V_2O_3 (99.99%). Tungsten oxide is a powder with light green color whereas vanadium oxide (III) is a black powder. The solid state reaction is described by the following reaction:

$$WO_3 + V_2O_3 \xrightarrow{vacuum} WV_2O_6 \tag{5.3}$$

The precursors have been mixed with a pestle in an agate mortar under acetone. The mixture was placed under vacuum in an quartz tube and then sealed. The quartz tube was finally placed

Table 5.2: Wyckoff positions of atoms within the tetragonal unit cell of WV_2O_6. Space group: $P4_2/mnm$ (136).

atom label	**atom type**	**site**	**x**	**y**	**z**
W	W	2a	0	0	0
V	V	4e	0	0	0.33540(4)
$\mathbf{O_1}$	O	4f	0.33422 (3)	0.33422 (3)	0
$\mathbf{O_2}$	O	8j	0.29288 (4)	0.29288 (4)	0.33387 (2)

Table 5.3: Wyckoff positions of atoms within the tetragonal unit cell of WV_2O_6 by Fruchart *et al.*[181]. Space group: $P4_2/mnm$ (136).

W	W	2a	0	0	0
V	V	4e	0	0	0.334
$\mathbf{O_1}$	O	4f	0.290	0.290	0
$\mathbf{O_2}$	O	8j	0.308	0.308	0.334

in a furnace. The reaction has been carried at 1273 Kfor 48 h in order to form WV_2O_6. Note this synthesis of WV_2O_6 differs from that of Bernier and Poix[178], and Hodeau *et al.*[177], as they fired the quartz tube at 1223 K. It is due to the fact that powder diffraction of powders sintered at 1223 K reveal the presence of the reactants phase. Multiple grindings and annealing processes have been performed in order to reach phase purity. The resulting powder has a black colour and this is in agreement with the result of Hodeau and coworkers.

5.4 Powder x-ray diffraction

X-ray diffraction was performed on the prepared samples in order to assess their phase purity. Once again the PANalytical diffractometer was the instrument used for this purpose. Figure 5.2 on the next page presents the Rietveld refinement of a room-temperature x-ray diffraction pattern of WV_2O_6. The *Fullprof Suite* program was utilized this task. In Figure 5.2 the experimental data and calculated profile are shown as red dots and the continuous black line, respectively. The blue line at the bottom of the diagram corresponds to a difference curve (observed-calculated). All reflections in Figure 5.2 are those of a tetragonal lattice, whose space group symmetry is $P4_2/mnm$ (136). The Bragg peak positions associated with these reflections are indicated by the green tick marks. There is a good level of agreement between the observed and calculated profile as indicated by the low values of the refinements factors: $\chi^2 = 1.29$, $R_B = 5.26\,\%$ and $R_F = 5.09\,\%$.

From the Rietveld analysis one extracts the following lattice parameters: a = 4.633 11(1) Å, c = 8.899 78(2) Å. These results are in good agreement with those reported by Fruchart *et al.*[181].

Although the lattice parameters of the current are in good agreement with those reported in the literature, the calculated Wyckoff positions are different to those previously reported by Fruchart *et al.*[181] and Hodeau *et al.*[177]. This discrepancy is well pronounced for the oxygens on site *4f*. There is a complete ordering of the cations on *2a* and *4e* sites as none if these sites is shared by both

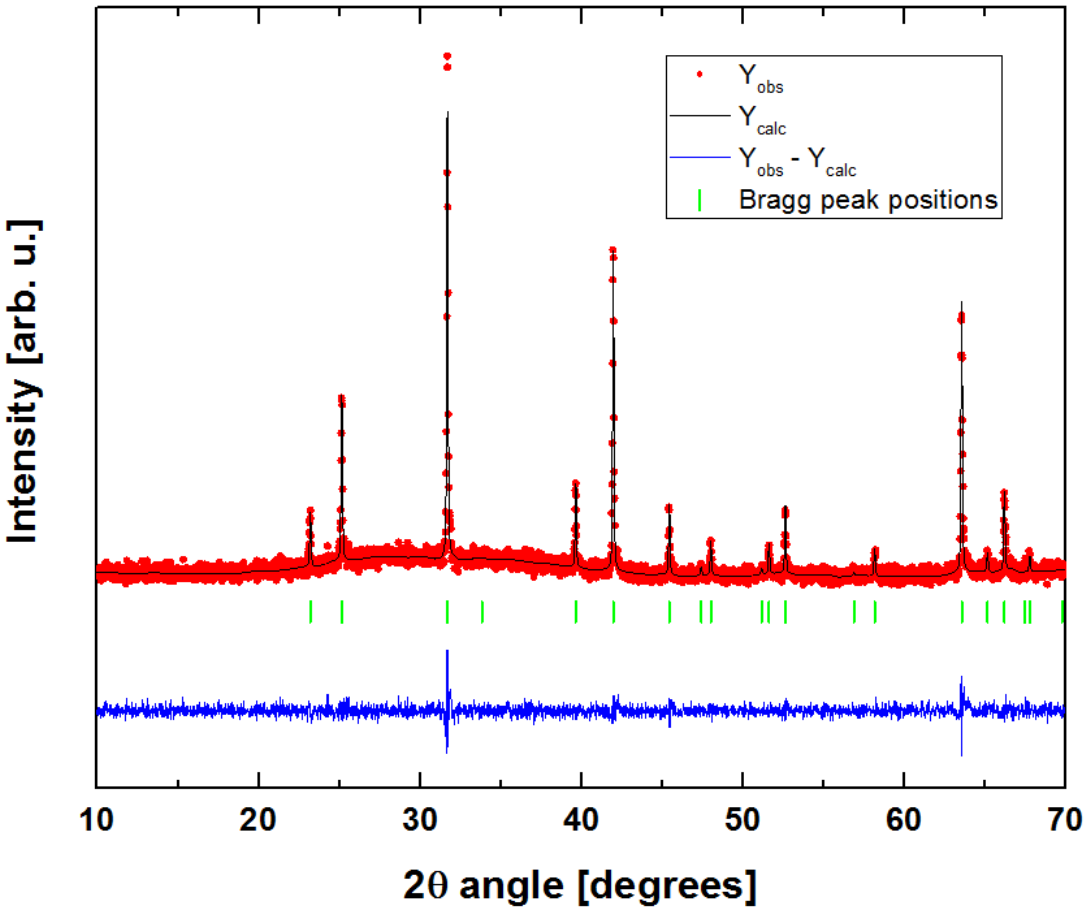

Figure 5.2: Rietveld refinement of a room-temperature x-ray diffraction pattern of WV_2O_6. The experimental data and calculated profile are shown as red dots and the continuous black line, respectively; the blue line at the bottom of the diagram corresponds to a difference curve (observed-calculated). The green ticks indicate the Bragg peak positions.

Table 5.4: Wyckoff positions of atoms within the tetragonal unit cell ofWV_2O_6 by Hodeau *et al.*[177].Space group: $P4_2/mnm$ (136).

W	W	2a	0	0	0
V	V	4e	0	0	0.33472 (3)
$\mathbf{O_1}$	O	4f	0.2943 (8)	0.2943 (8)	0
$\mathbf{O_2}$	O	8j	0.3018 (6)	0.3018 (6)	0.334

cations. Table 5.4 strongly suggests that the prepared powder of WV_2O_6 is a fully ordered trirutile. However, a trirutile is a modulated rutile. This modulation can give rise to homometric structures: two distinguishable atomic structures, for which the distance between atoms are identical but the distributions of the atoms within the lattice differs. This topic is extensively discussed in Chapter 6 on $NiTa_2O_6$. Joint x-ray and neutron refinement [184] is needed to confirm or refute the ordering of the cations within this trirutile. This says the Rietveld refinement indicates the absence of spurious phases. As consequence single phase trirutile WV_2O_6 has been prepared and the material is optimal for the characterization of its physical properties.

5.5 Electronic structure

The section is dedicated to the band structure and the density of states (DOS) of WV_2O_6. Both the electronic structure and the DOS are displayed in Figure 5.3 below. The hybrid functional [185], HSE06, was the model utilized for the band structure calculations. For these calculations the Fermi level (E_F) was chosen to be in the middle of the bandgap.

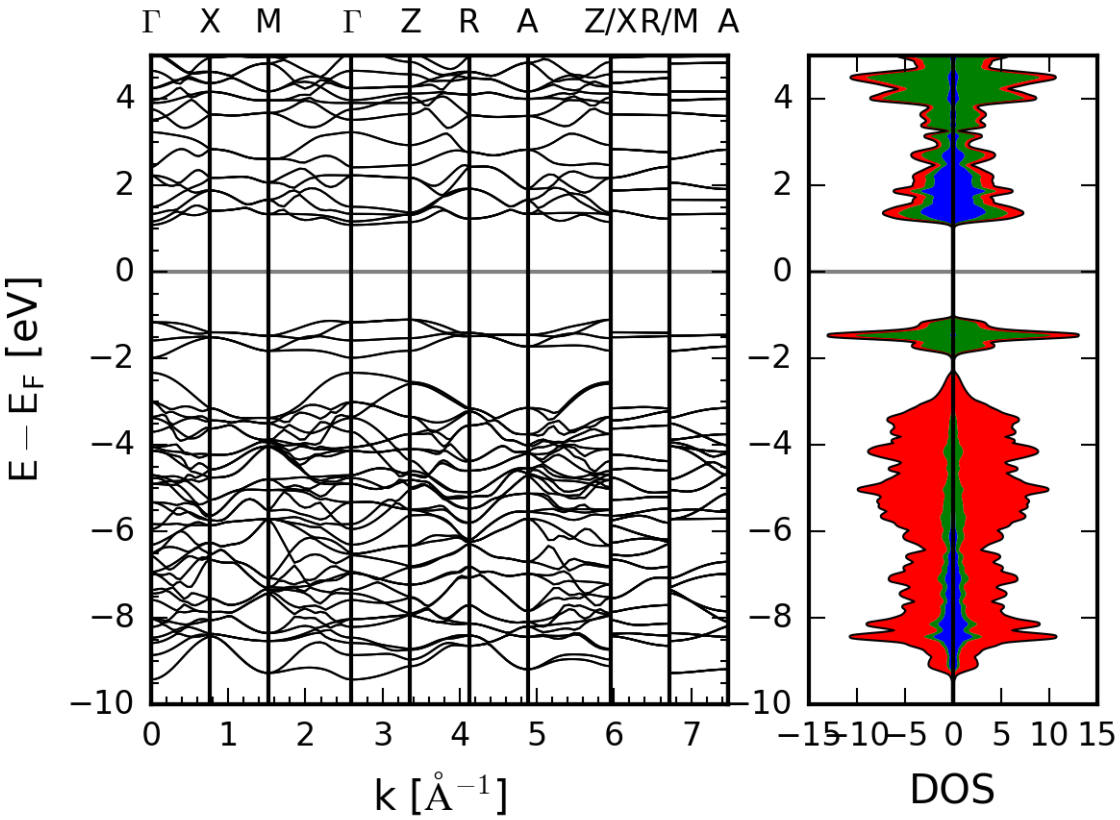

Figure 5.3: On the left, the density of states (DOS) of WV_2O_6. A detailed description of the bands is giving on the right hand side. The blue, green and red colours indicate the bands related to tungsten, vanadium and oxygen, respectively.

The diagram on the left in Figure 5.3 corresponds to the calculations of the band structure of WV_2O_6 in reciprocal space or **k**-space ($Å^{-1}$). This plot shows the variation of the energy of states (E - E_F) as function of position in the reciprocal space (**k**). The letters Γ, M, X, Z, R and A represent high symmetry points in the unit cell of this reciprocal lattice. This unit cell is also known as the

Brillouin zone and is depicted as the black parallelepiped in Figure 5.4. Γ is at the origin of the Brillouin zone. Z and X points are in the middle of the facets perpendicular to $\vec{b_3}$ and $\vec{b_2}$ vectors, respectively. A is located at one of the eight edges o the Brillouin zone. M and R correspond to the middle of the vertices parallel to $\vec{b_3}$ and $\vec{b_1}$ vectors, respectively. $\vec{b_1}$, $\vec{b_2}$ and $\vec{b_3}$ are the unitary vectors of the reciprocal space and are given by

$$\vec{b_1} = 2\pi \frac{\vec{b} \times \vec{c}}{\vec{a}.(\vec{b} \times \vec{c})}, \tag{5.4}$$

$$\vec{b_2} = 2\pi \frac{\vec{c} \times \vec{a}}{\vec{a}.(\vec{b} \times \vec{c})}, \tag{5.5}$$

$$\vec{b_3} = 2\pi \frac{\vec{a} \times \vec{b}}{\vec{a}.(\vec{b} \times \vec{c})}, \tag{5.6}$$

where $\vec{a}$, $\vec{b}$ and $\vec{c}$ are the unitary vectors of the real space. The minimum of the conduction band is loated at the Γ point, whereas the top of the valence band is located at the Z point.

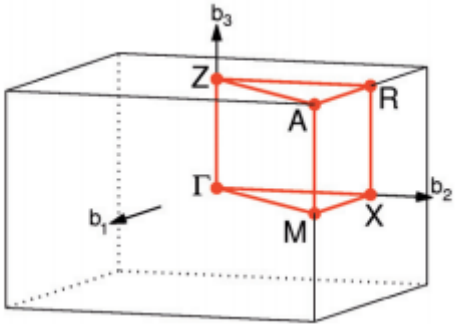

Figure 5.4: Brillouin zone of a tetragonal lattice.[186]

In order to calculate the band structure of the system, energies are evaluated for all k points between the high symmetry points. The calculations are run along the paths between the high symmetry points, illustrated by the red parallelepiped in Figure 5.4. The path chosen for the calculations is indicated by the letters on the top of the electronic structure. The higher the number of $\vec{k}$ points between two high symmetry points, the smoother is the band structure. In Figure 5.3 the bands whose energies are lower than −1 eV form the valence band (VB), whereas the conduction band (CB) consists of bands with energies higher than 1 eV. The direct bandgap is the difference in energy between the top of VB and bottom of CB, which are aligned. If these two band edges are not aligned, the bandgap is said to be indirect. In WV_2O_6 the direct and indirect bandgap are about 2.3 and 2.2 eV, respectively; if the valence (conduction) band is near the Fermi level (0 eV in this case) a p-type (n-type) doping is expected for the material.

In order to obtain the density of states (DOS), one calculates the energies across the Brillouin zone, not just the special directions. In other words **k** samples the whole Brillouin zone. The DOS is the plot on the right in Figure 5.3. The red, blue and green indicate the orbitals related

to oxygen (O), vanadium (V) and tungsten (W) atoms, respectively. The oxygens link up the V and W atoms and therefore their orbitals are located at the bottom ($-9.5 <$ E - $E_F < -2.5$ eV) of the valence band (red). The top of the valence band (VB) mainly consists of occupied V *d*-states, whereas the unoccupied W *d*-states (blue) form the bottom of the conduction band (CB). A *n*-type doping consists of introducing electrons near the bottom of the CB, thereby involving W *d*-orbitals. According to Fruchart *et al.*[181] and Hodeau *et al.*[177] the difference between the energy of such electrons and the CB is estimated to be about 0.24 eV. This energy is known as the activation energy.

5.6 Thermoelectric properties of WV_2O_6

Rectangular bars of WV_2O_6 have been prepared with the method discussed in section 2.3.1 of Chapter 2 dedicated to the ZEM instrument. The density of this bar was calculated using the Archimede method and is estimated to be equal to 3.86 g cm^{-3} and it corresponds to a relative density of 42 %. This poor value of the density is not ideal to measure the thermoelectric properties of WV_2O_6. Two sets of measurements have been performed for the determination of the thermoelectric properties of tungsten divanadate oxide. High-temperature data (300 K - 950 K) were collected on the ZEM instrument. The electrical conductivity σ, the thermal conductivity κ and the thermopower α have also been investigated at low-temperature (14 K - 260 K) using the Dynacool. The temperature dependence of the thermopower of WV_2O_6 is discussed. It is followed by a discussion on the mechanisms responsible for its electrical conductivity. The end of this chapter is dedicated to the analysis of the thermal conductivity data, the power factor and figure of merit of WV_2O_6. The crystal structure of WV_2O_6 is assumed to be constant from room temperature to 1000 K.

5.6.1 The Seebeck coefficent α of WV_2O_6

The temperature dependence of the thermopower of WV_2O_6, α, is presented in Figure 5.5. There is a gap between the blue hexagonal points between 256 and 327 K. These two temperatures are the highest and lowest temperature recorded on the Dynacool and ZEM instruments, respectively. The thermopower values at these two temperatures have the same order of magnitude: -19.90 and $-35.90\,\mu$V K^{-1}, respectively. From 100 up to 200 K the thermopower takes positive values. It is due to the fact that the material becomes insulating with decreasing temperature. The positive sign of the Seebeck coefficient indicates that most of the free-carriers responsible of the electrical properties of WV_2O_6 are holes. Hence, WV_2O_6 behaves as a *p*-type material within this temperature range.

For temperatures higher than 200 K the thermopower decreases and takes negative values. The majority of the free-carriers are electrons, thus WV_2O_6 behaves like a *n*-type semiconductor. From 600 to 1000 K the WV_2O_6 bar exhibits a thermopower of about $-59.55\,\mu$V K^{-1}. This Seebeck coefficient value is rather small with respect to the state-of-the-art thermoelectric oxide materials, as the latter exhibit a thermopower power of order of few hundreds microvolts per kelvin. The semiconductor behaviour[177] of WV_2O_6 and the negative sign of its Seebeck coefficient indicate that this material can be treated like a *n*-type semiconductor. Hence, the thermopower data from 174 to

1000 K were fitted with the model described in equation (5.7)

$$\alpha(T) = \frac{k_B}{e}.(\frac{E_A}{k_B T} + A_c) \tag{5.7}$$

where k_B, E_F and E_C correspond to the Boltzmann constant, the Fermi energy and the lowest energy of conduction band, respectively. U is a unitless fitting parameter. Figure 5.5 presents a comparison between measured and theoretical thermopower of the WV_2O_6 bar.

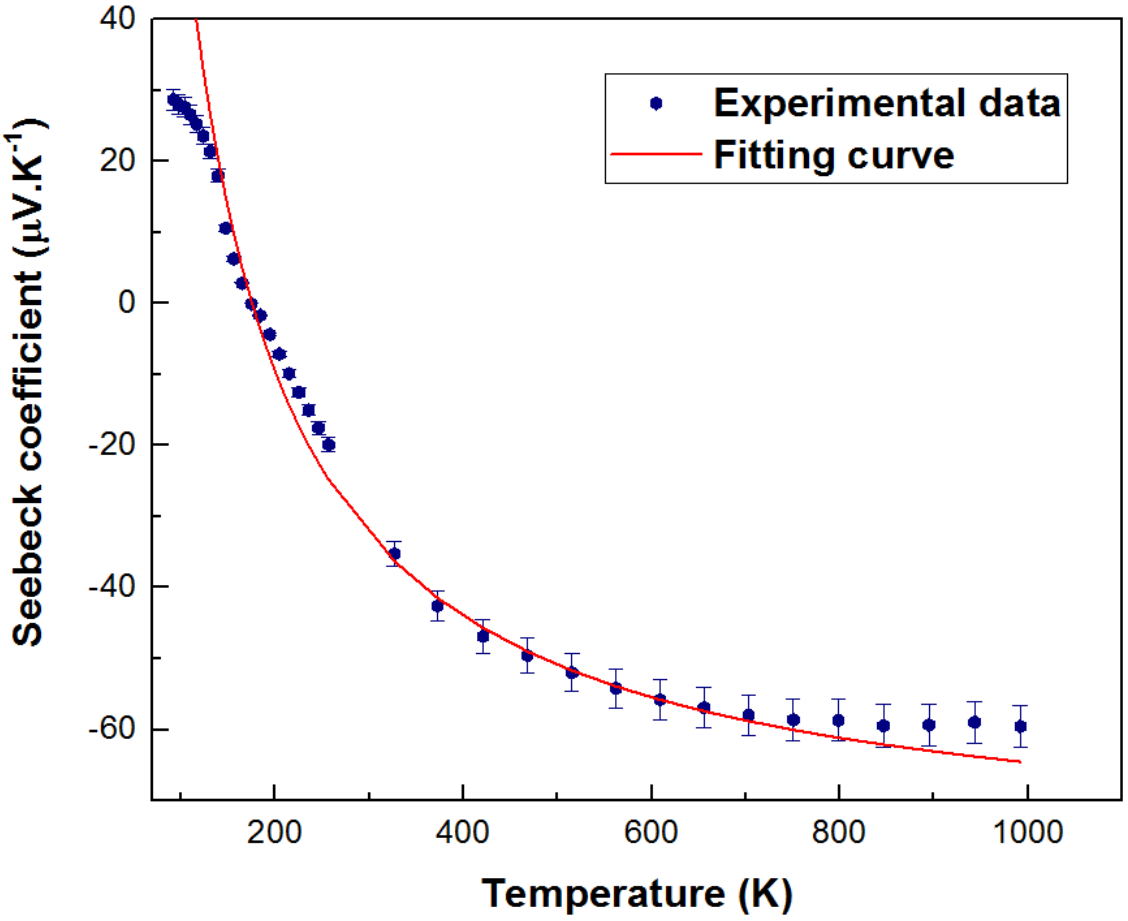

Figure 5.5: Fitting of the Seebeck coefficient data of WV_2O_6. The red curve represents the fitting curve whereas the blue dots are to the experimental data.

In Figure 5.5 the blue dots represent the experimental data whereas the model used to fit this data points corresponds to the red line. The experimental and the fitting line are within agreement as the values of the blue dots are very similar to those of the red line, from 400 to 800 K. The unitless parameter U is equal to -0.910. From 800 K onward there are discrepancies between the model and the experimental data. Indeed, at 850 and 950 K the thermopower of the WV_2O_6 bars is equal to -59.45 and $-58.96\,\mu V\,K^{-1}$, respectively. On the other hand, the respective values of α according to the red line at these temperatures are: -60.69 and $-62.10\,\mu V\,K^{-1}$. The scattering of electrons by defects within the lattice, at high temperature, may be responsible for the discrepancy between the model (red line) and the experiment data (blue hexagons). Indeed, more defects are thermally

generated within the lattice with increasing temperature. Consequently, these point defects and grain boundaries may alter the free-carriers properties such as their mobility, thus the thermopower of WV_2O_6. The term E_F - E_C in equation (4.67) corresponds to the thermopower activation energy E_A. The value of E_A which best fitted the experimental data was $0.014 \pm 0\,eV$. This value is one order of magnitude lower than the activation energy reported by Hodeau (0.20 eV).

5.6.2 The electrical conductivity σ of WV_2O_6

The ZEM measures simultaneously the thermopower and the electrical conductivity, σ, of a sample at any temperature. Hence, σ was measured within the same temperature as the Seebeck coefficient and the experimental data are presented in Figure 5.6 below.

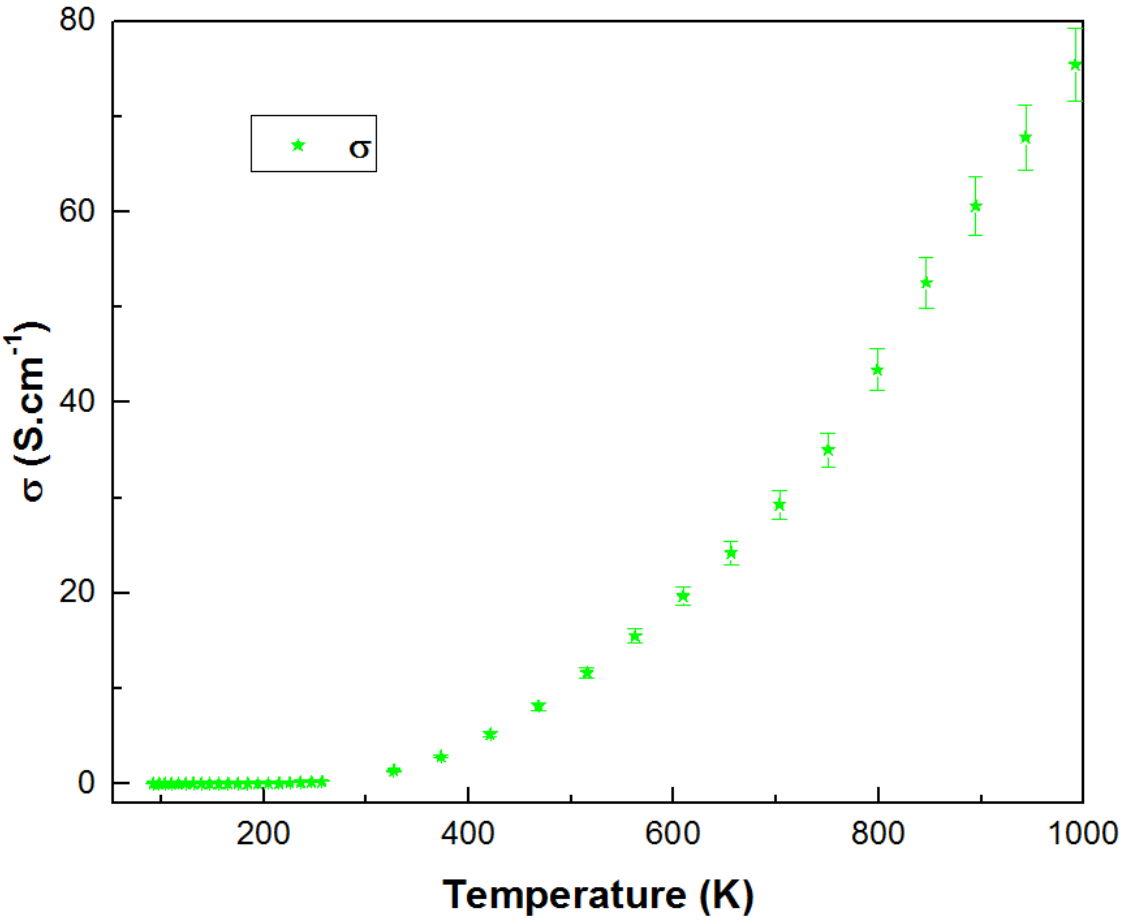

Figure 5.6: The evolution of the electrical conductivity, σ, of WV_2O_6 sample as function of the temperature.

The green stars in Figure 5.6 represent the experimental data recorded on the ZEM instrument. One notes that as the temperature increases the electrical conductivity exponentially increases. The WV_2O_6 bar exhibits an electrical conductivity of few Siemens per centimeter ($1\,S\,cm^{-1}$) at room temperature. The values of σ increases by almost two orders of magnitude as the temperature increases. At 1000 K tungsten divanadate oxide exhibits an electrical conductivity of $75\,S\,cm^{-1}$. The electrical conductivity data was compared to that of established TE materials in the data mining chart[19]. At high temperatures, WV_2O_6 exhibits an electrical conductivity which is in the same

order of magnitude than that of $CuNd_2O_4$ [172]. This material exhibits an electrical conductivity of $41\,S\,cm^{-1}$ at 700 K. In order to fit the electrical conductivity data different models are successively tested. These models are two hopping models (small polaron and variable range) and the band model.

The variable range hopping model

The first model used to fit the experimental data is the variable range hopping model for a 3D material. In the variable range hopping (vrh), derived by Mott [141], electrons jump (hop) now and then to other energy levels, which are localized around the Fermi energy. The hopping probability mainly depends on the energy separation W between two states. In order to determine whether or not the variable range hopping regime is the appropriate model to explain the electric conduction in WV_2O_6, the plot $\ln(\sigma)$ vs $\frac{1}{T}^{\frac{1}{4}}$ was tested. The result is depicted in Figure 5.7.

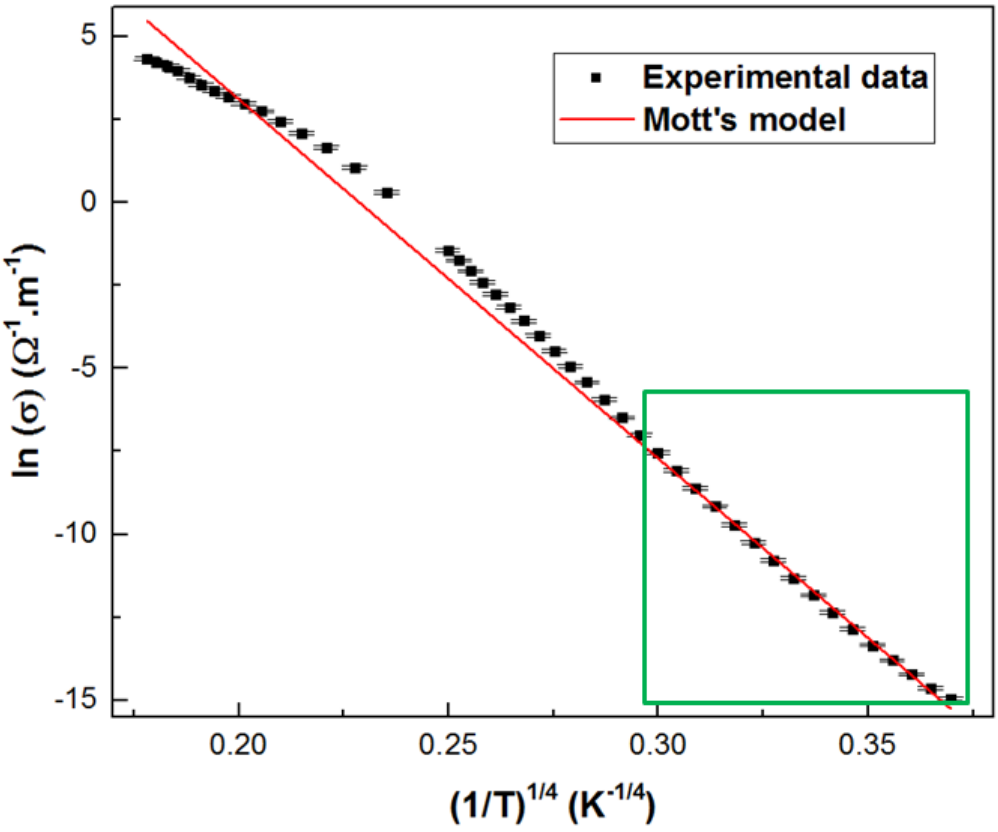

Figure 5.7: Fitting of the electrical conductivity with the variable range hopping model. The black squares represent the experimental data and the red line corresponds to the theoretical model.

In Figure 5.7 the lowest values on the x-axis correspond to high temperatures, whereas low temperatures are associated with the highest values on the x-axis. The black squares in Figure 5.7 are the experimental data and the red line corresponds the theoretical profile of the electrical conductivity according to the variable range hopping model. There is good agreement between the vrh model and experimental values for temperatures below 102 K, indicated by the green box in Figure 5.7. For instance, the values of $\ln(\sigma)$ for both the experiment and the vrh model at 82 K are equal to -7 and $-7\,S\,m^{-1}$, respectively. The shift between the black squares and the

red line increases with increasing temperature. Indeed at 515 K the logarithm of the electrical conductivity is equal to $7\,S\,m^{-1}$ experimentally whereas the variable range hopping model predicts $6\,S\,m^{-1}$. Therefore the hopping mechanism may be suitable to describe the electric conduction of tungsten divanadate oxide for temperatures below 102 K. One can thus extract the values of σ_o and T_o in the following manner. One first starts by rewriting equation.(3.45) in Chapter 3 as

$$g(T) = ln(\sigma(T)) = ln(\sigma_o) - (\frac{T_o}{T})^{\frac{1}{4}}. \tag{5.8}$$

The next step is a change of variable as one is interested in $\frac{1}{T}^{\frac{1}{4}}$:

$$X = (\frac{1}{T})^{\frac{1}{4}}, \tag{5.9}$$

$$g(X) = -D.X + B, \tag{5.10}$$

where D = $T_o^{1/4}$ and B = ln(σ_o). The values of D and B for this model are 103.558 ± 2 K and 27 ± 0 $S\,m^{-1}$, respectively.The respective values of the parameter T_o and the pre-factor σ_o are: 1.150×10^8 K ± 9 K and 1×10^{12} ± 0 $S\,m^{-1}$.

The small polaron hopping model

The small polaron hopping model was then considered as model for the electrical conductivity data of WV_2O_6. The mechanism of the small polaron hopping[187] relies on the strong interaction of electron-phonon system. In fact electrons push negative ions further away and the overlap of neighbouring orbitals becomes narrower until electrons fall into localised states. If the behaviour of σ within WV_2O_6 is welll explained by the small polaron hopping, the plot ln(σ.T) vs $\frac{1}{T}$ is thus a straight line. The slope and intercept of the line are equal to - $\frac{\Delta}{k_B}$ and ln(A), respectively. Δ corresponds to the activation energy E_A. Figure 5.8 illustrates the evolution of ln(σ.T) as function of the inverse of the temperature.

Similarly to Figure 5.7, the lowest values on the x-axis in Figure 5.8 correspond to high temperature whereas those near 0.021 K^{-1} are related to low-temperature values. For instance, 0.0015 K^{-1} and 0.021 K^{-1} correspond to 667 K and 48 K, respectively. Figure 5.8 demonstrates that ln(σ.T) vs $\frac{1}{T}$ follows and exponential decay, as indicted by the trend of the black diamonds. However, the linear response of the ln(σT) as $\frac{1}{T}$ varies from 0.005 to 0.001 K^{-1}. The respective temperatures for these two values of $\frac{1}{T}$ are 214 and 1000 K. It is therefore possible to fit the black diamonds within that temperature range with the model in equation (1.5). The fitting curve is represented by the red line in Figure 5.8. $\frac{\Delta}{k_B}$ and ln(A) are equal to -2336.82 ± 22 K and 178 ± 0 $S\,m^{-1}\,K^2$, respectively. A was found to be equal to 18 ± 0 $S\,m^{-1}$ K. Eventually, the activation energy Δ was deduced from the slope. Δ is equal to 0.204 ± 0.003 eV. The activation energy value is within good agreement with the value reported by Hodeau and coworkers:0.202 eV. Nevertheless, the small polaron model

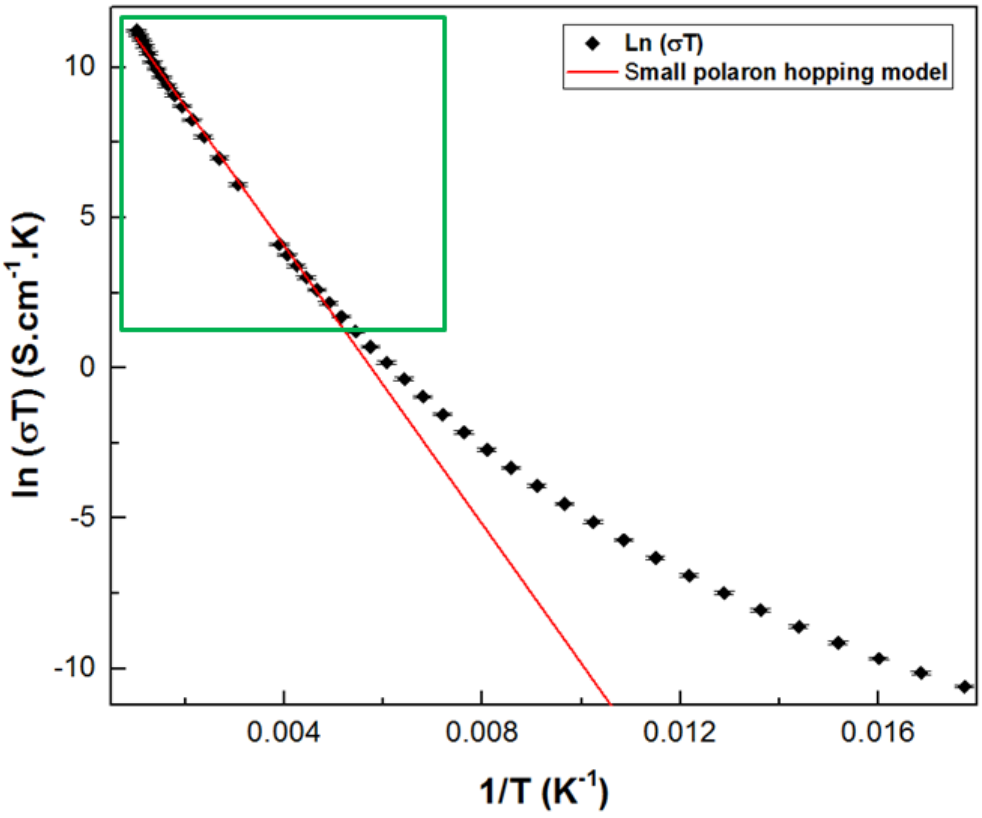

Figure 5.8: Fitting of the electrical conductivity data with the small polaron hopping model. The black diamonds represent the experimental data and the red line stands for the theoretical model.

fails to explain the behaviour of the electrical conductivity of WV_2O_6 for temperatures below 215 K.

The band model

The last model considered to explain the electrical conductivity data of WV_2O_6 was the band model. One of the striking differences between this model and the two previous ones is the delocalisation of the energy states near the Fermi level. The energy levels are closely stacked at different positions: one speaks of bands. For the band model to be valid as model for the electrical conductivity data of WV_2O_6, the plot $\ln(\sigma)$ vs $\frac{1}{T}$ should be a straight line. The slope of this line is proportional to the activation energy E_A.

The plot in Figure 5.9 is similar to that in Figure 5.8. $\ln(\sigma)$ follows an exponential decay as the temperature decreases. On the x-axis $0.004\,K^{-1}$ is equivalent 250 K, whereas 62.5 K corresponds to $0.016\,K^{-1}$. The black squares and the red line represent the experimental data and the theoretical model, respectively. For temperature below 220 K there is discrepancy between the black squares and the red line. At 118 K the theoretical model predicts a value of $-5\,S\,m^{-1}$ for $\ln(\sigma)$ whereas the value of the black square at that temperature is equal to $-3\,S\,m^{-1}$. The shift between the red line and the black squares increases with decreasing temperature. Nevertheless the band regime model (red line) well fits the experimental data (black squares) for temperatures above 215 K. At 800 K

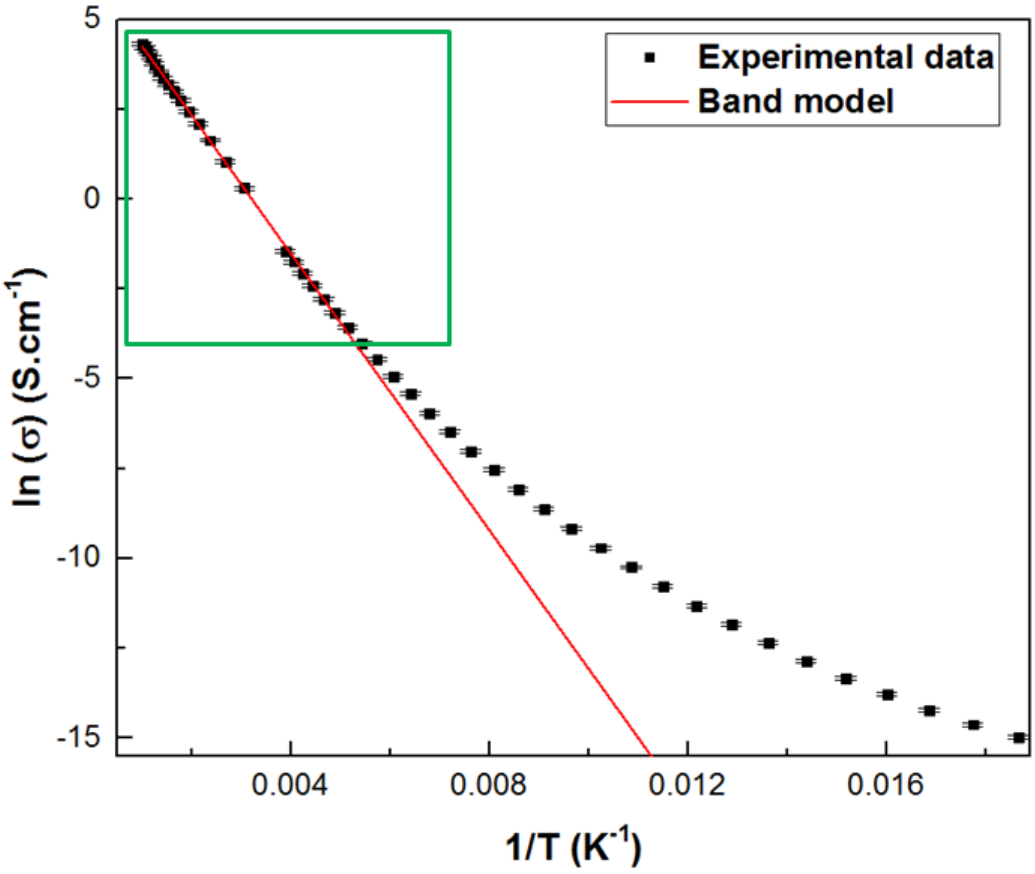

Figure 5.9: Fitting of the electrical conducitivity of WV_2O_6 with the broad band model. The black squares represent the experimental data and the theoretical model is illustrated via the red line.

the value of $\ln(\sigma)$ according to the theoretical model and the experimental data is equal to 8 and $8\,S\,m^{-1}$, respectively. Eventually the activation energy was extracted from the slope of the red line via the relation: slope $= \frac{E_A}{k_B}$. The analysis lead to a value of 0.169 ± 0.001 eV for the activation energy E_A. This value of E_A is in the same order of magnitude than the value reported by Hodeau and coworkers[177]: 0.202 eV .

The small polaron model in Figure 5.8 and the band model in Figure 5.9 both describe well the temperature dependence of the electrical conductivity of the WV_2O_6 bar, for temperatures above 215 K. The Pearson's r coefficient of the band model is higher than that of the small polaron model. The Pearson coefficient measures how linearly correlated are two variables X and Y. For a perfect negative linear correlation the Pearson's r is equal to 1 or -1. r takes the values of -0.999 11 and -0.999 55 for the small polaron and band model, respectively. Hence, the band model is the suitable model to describe the high temperature data. Table 5.5 summarizes the relationship between regimes (models) and the electrical conductivity of WV_2O_6.

Table 5.5: Relationship between regimes and electrical conductivity of WV_2O_6. E_A correspods to the activation energy, and Temp stands for temperature.

Criteria	**Models**		
Model	**Variable range hopping**	**Small polaron hopping**	**Band**
Temp. range (K)	0 - 105	215 - 1000	215 - 1000
Activation energy (eV)		0.204 ± 0.003	0.169 ± 0.001 eV
Pearson's *r*	-0.998 53	-0.999 11	-0.999 55

5.6.3 The power factor *PF* of WV_2O_6

The power factor was deduced from α and σ from the relation in equation (5.11):

$$PF = S^2.\sigma. \tag{5.11}$$

The evolution of the value of PF as function of the temperature is shown in Figure 5.10. The exponential-type profile of the power factor is similar to that σ. Indeed the power factor of the WV_2O_6 bar increases, with increasing; PF varies from 1.69 up to $26.76\,\mu W\,m^{-1}\,K^{-2}$. These values are those of κ at 300 and 1000 K, respectively. This is due to proportionality between σ and PF present in equation (5.11) and the fact that the electrical conductivity is higher than the thermopower by more than 4 orders of magnitude. The power factor of $CuNd_2O_4$ is about $41.10\,\mu W\,m^{-1}\,K^{-2}$ at 700 K. It suggests there are opportunities for improvement of the PF of WV_2O_6.

5.6.4 The thermal conductivity κ of WV_2O_6

In this section the conduction of heat in WV_2O_6 is discussed. First, the temperature dependence of electronic (κ_e) and thermal (κ_l) conductivities are discussed. The experimental data is then com-

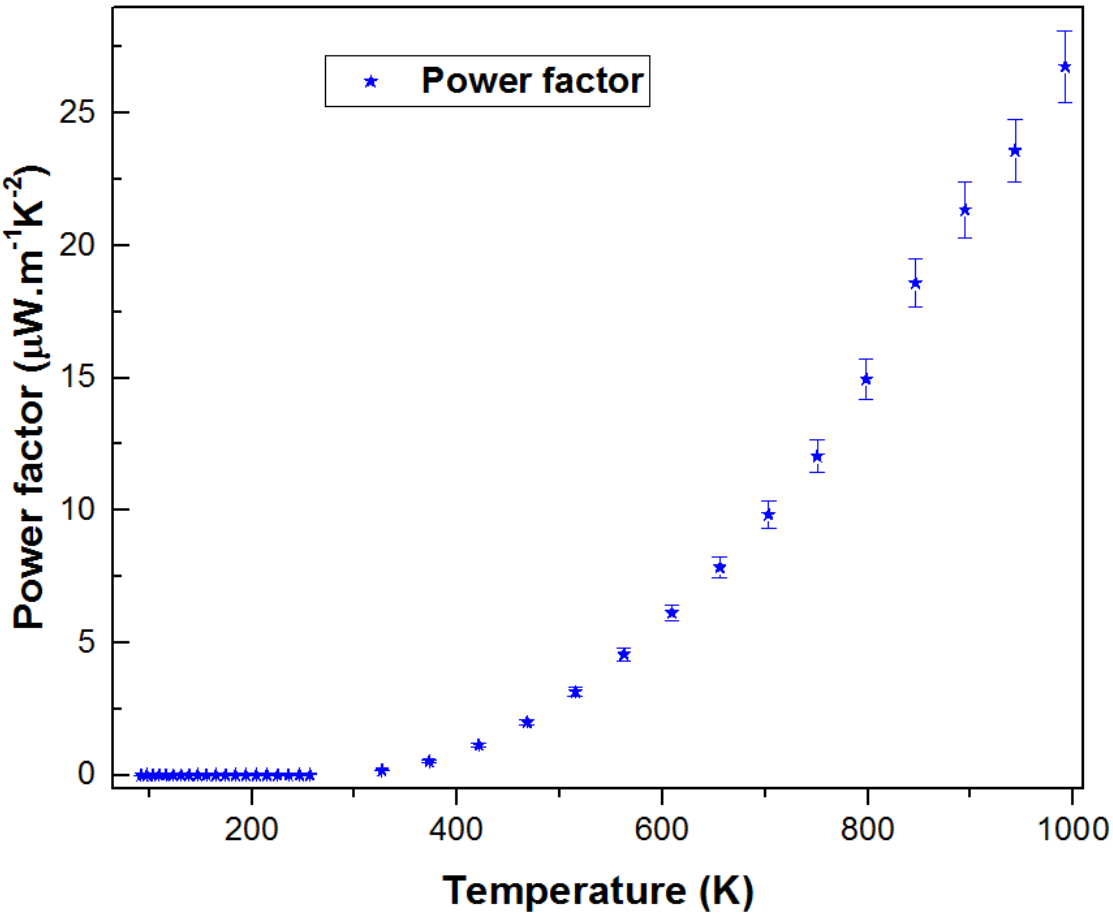

Figure 5.10: The evolution of the power factor PF of the WV_2O_6 bar as function of the temperature.

pared to the theoretical minimum conductivity which is derived from the Cahill's model.

The thermal conductivity of the WV_2O_6 bar was simultaneously measured with σ and α on the Dynacool. The data recorded from 54 to 257 K are presented in Figure 5.11. The white dots are the measured values of κ. The thermal conductivity data for temperatures above 150 K are not reliable, due to the radiation losses. From 0 to 62 K the thermal conductivity sharply increases from 0.032 to 0.800 $W\,m^{-1}\,K^{-1}$. κ decreases from temperatures above 62 K, then stabilises around 0.782 $W\,m^{-1}\,K^{-1}$. The thermal conductivity value exhibited by WV_2O_6 is in the same order of magnitude of the best TE oxides, such as the layered cobaltite $CaCo_2O_5$ [35] which exhibits a thermal conductivity of around 1 $W\,m^{-1}\,K^{-1}$ for temperatures between 473K an 873K.

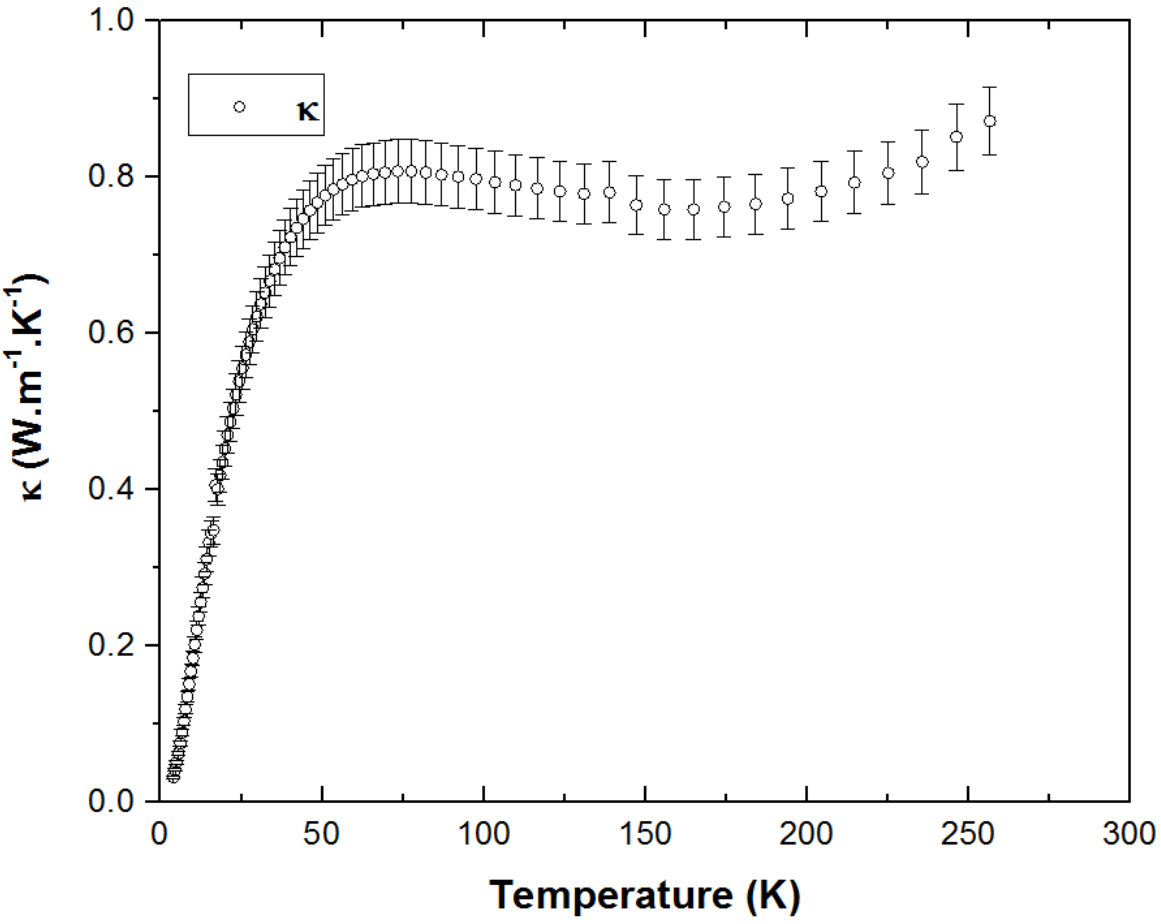

Figure 5.11: The evolution of the thermal conductivity κ of the WV_2O_6 bar as function of the temperature. The white dots represent the experimental data.

The electronic contribution κ_e

κ_e is the summation over all heat transferred within lattice due to the motion of free-carriers. Since σ is also governed by the free-carriers, it inevitably follows that the electronic contribution of the thermal conductivity is directly related to the electrical conductivity. That relationship is expressed in the following equation:

$$\frac{\kappa_e}{\sigma} = (\frac{\pi^2 k_B^2}{3e^2}).T \tag{5.12}$$

Equation (5.13) is the Wiedemann-Franz law which states that the ratio between κ_e and σ at a given temperature is equal to a constant. That constant is the Lorenz constant, which is equal to $2.44 \times 10^{-8}\,\mathrm{W\,\Omega\,K^{-2}}$. In other words κ_e is proportional to σ. The temperature-dependence of the electronic contribution of κ is presented in Figure 5.12 by the red dots.

The red dots are deduced from the electrical conductivity measured on the Dynacool; the deduction was done using the relation in equation (5.13). κ_e has the same exponential profile as the electrical conductivity, as seen in Figure 5.6. As the temperature increases from 50 and 257 K κ_e increases 0 up to $148.443\,\mu\mathrm{W\,m^{-1}\,K^{-1}}$. The red dots, blue triangles and the black squares in Figure 5.12 illustrates the electrical, lattice and total thermal conductivity, respectively. κ_e is six orders of magnitude lower than the measured thermal conductivity κ. As a consequence, Figure 5.12 highlights that the heat transfer within WV_2O_6 is mainly due to the lattice. This dominance of κ by κ_l indicates that it may be possible to tailor the electrical properties of WV_2O_6 without deteriorating its thermal properties, and vice-versa. The lattice contribution of κ was then deduced by subtracting κ_e from κ, and its temperature-dependence is discussed on the next paragraph.

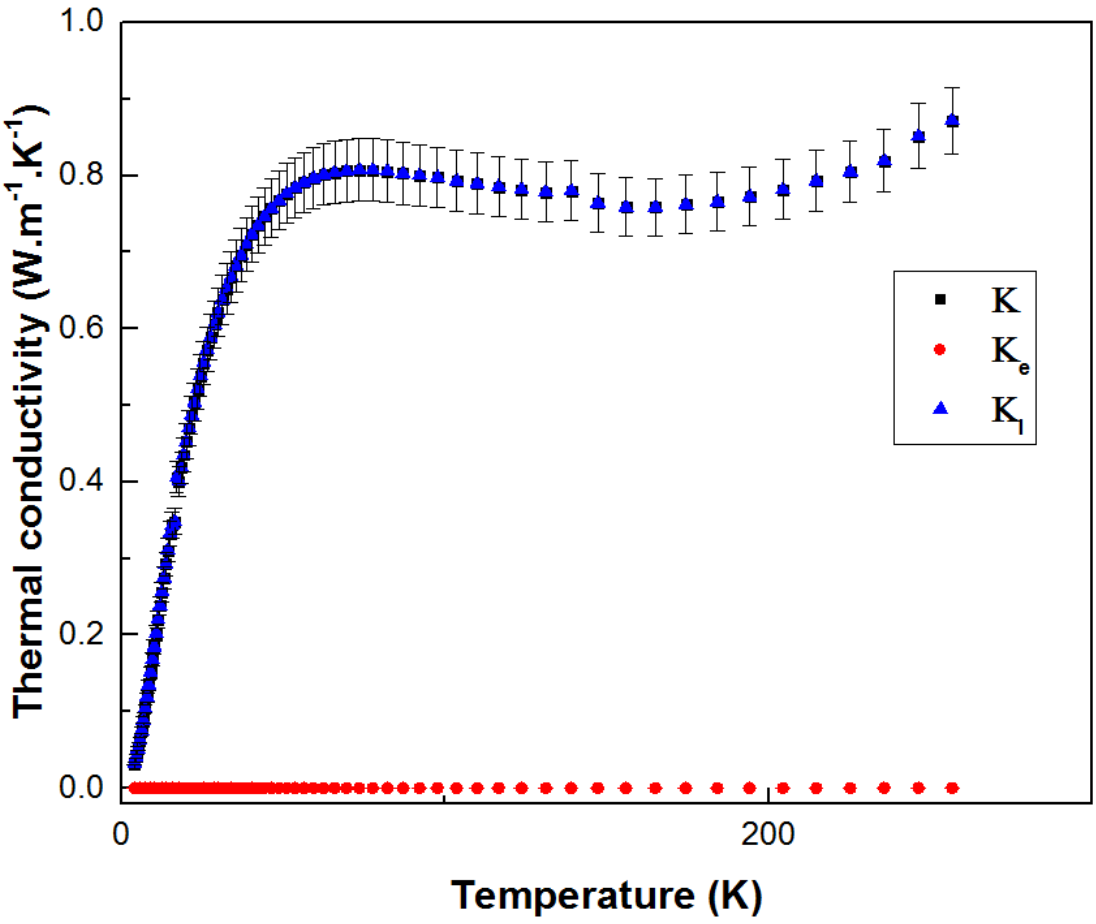

Figure 5.12: Temperature-dependence of κ, κ_e and κ_l of the WV_2O_6 bar.

The lattice contribution κ_l

The lattice contribution of the thermal conductivity, κ_l is the summation over all heat transferred within the material due to coherent lattice vibrations, also known as phonons. κ_l was estimated by subtracting the electronic part from the total thermal conductivity κ. The temperature dependence of κ_l has the profile of a thermal conductivity of a material in which different scattering mechanisms limit the thermal conductivity, at low and high temperatures, as discussed in Section 4.6.5. SEM images ware taken on a WV_2O_6 bar. These images were taken at a voltage of 30 kV and a magnification of 10kX. The presence of gaps and non-uniformity of particles in the SEM images evidence that the prepared sample is not a perfect crystal. The Callaway model was therefore taken to be equal to κ_1:

$$\kappa_1 = \frac{k_B}{2\pi^2\nu_s}.(\frac{k_BT}{\hbar})^3\int_0^{\frac{\Theta_D}{T}}\tau_c\frac{x^4e^x}{(e^x-1)^2}dx. \tag{5.13}$$

The combined relaxation time τ_c used in equation (5.55) is given by:

$$\tau_c^{-1} = \frac{\nu_s}{l} + A\omega^4 + [B_1exp(-\frac{\Theta}{3T}) + B_2].\omega^2T, \tag{5.14}$$

where $\frac{\nu_s}{l}$ is the phonon-boundary scattering rate, $A\omega^4$ accounts for the point defects scattering rate; the third and last term ω^2T describes the phonon–phonon scattering rate. The phonon-electron scattering was considered to be negligible. The characteristic length of the material l corresponds to the (average) size of particulates in Figure 5.13 and is estimated to be about 3.7 μm.

Figure 5.14 illustrates the fitting of the experimental data of κ_l (red dots) with the Callaway-Debye model (black line). Four parameters were refined for the fitting of the lattice thermal conductivity data. These parameters are ν_s, A, B_1 and B_2. B_1 and B_2 influence the tail of the fitting curve. Their determination is challenging because κ_l was not measured at high temperature. Changes in the mass-fluctuation parameter A and the sound veloctity affects the low-temperature values of the theoretical profile of κ_l. There is good agreement between the profile predicted by the Callaway-Debye model and the experimental data, for temperatures between 15 and 75 K. However, as temperature increases the the black line deviates from the red dots. This discrepancy is well pronounced for temperatures between 80 and 150 K. Several factors need to be taken into account to address the disagreement between the experimental and theoretical profiles. The low density of the prepared sample contributes to the poor fit observed in Figure 5.13. Besides, the model chosen for the scattering rates in equation (5.14) needs to be reconsidered. For instance the electron-phonon needs to be taken into account. Nevertheless, the relaxation time parameters A, B_1 and B_2 which best fit the lattice thermal conductivity of WV_2O_6 are $1.050 \times 10^{-41}\,s^3$, $1.5120 \times 10^{-15}\,s\,K^{-1}$ and $8.600 \times 10^{-17}\,s^3$, respectively. In addition, the value of ν_s and Θ_D are $5550\,m\,s^{-1}$ and 752 K, respectively. It should be noted that the sound velocity and the Debye temperature fulfill equation (3.48) in Chapter 3.

The minimal conductivity of κ_l

The Cahill's model was used to estimate the minimum thermal conductivity (κ_{min}) of WV_2O_6. The minimum thermal conductivity is given by

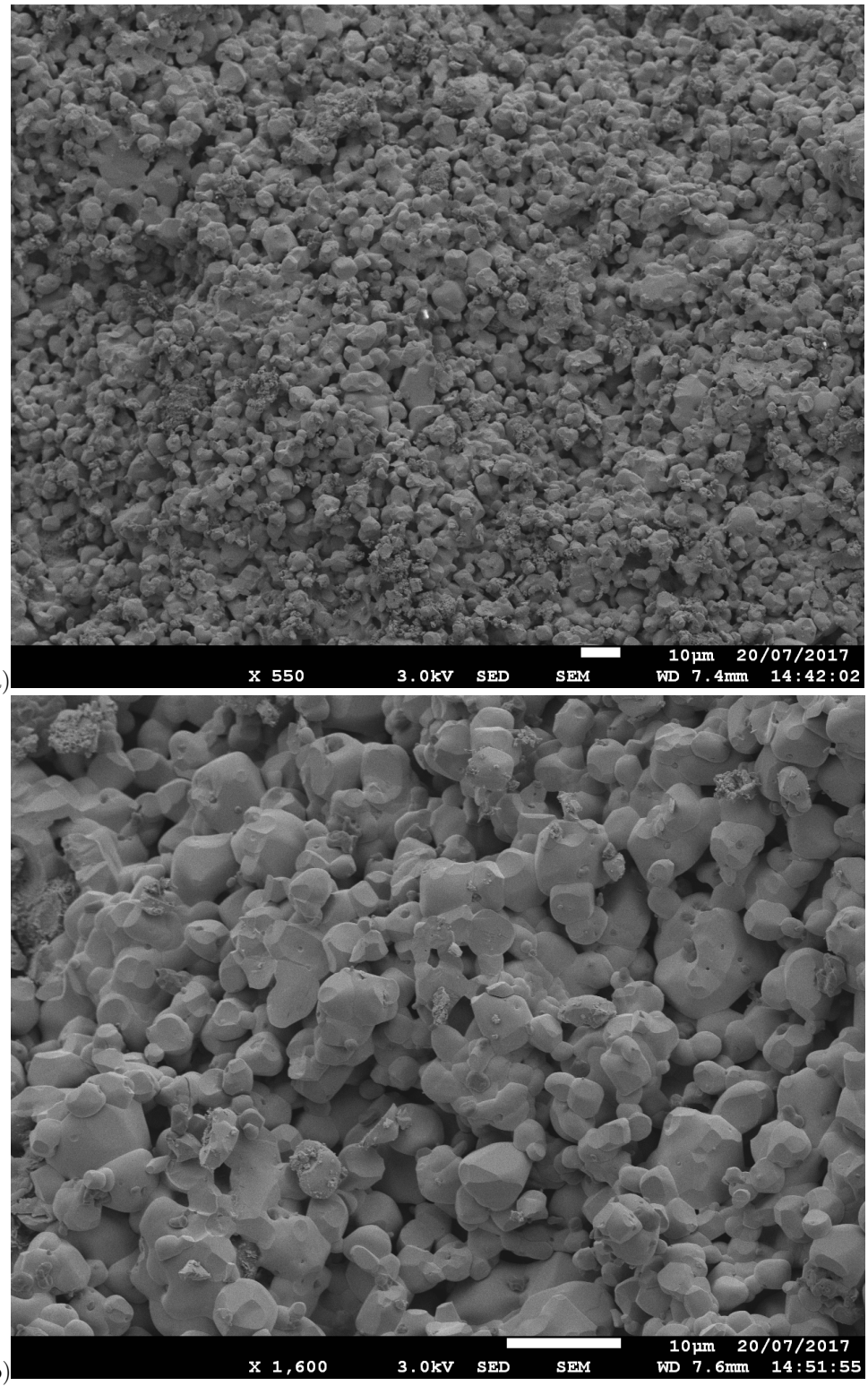

Figure 5.13: SEM images of WV_2O_6 bar. These images were taken at a voltage of 30 kV and a magnification of 10kX. The white ruler below both images corresponds to 10 μm.

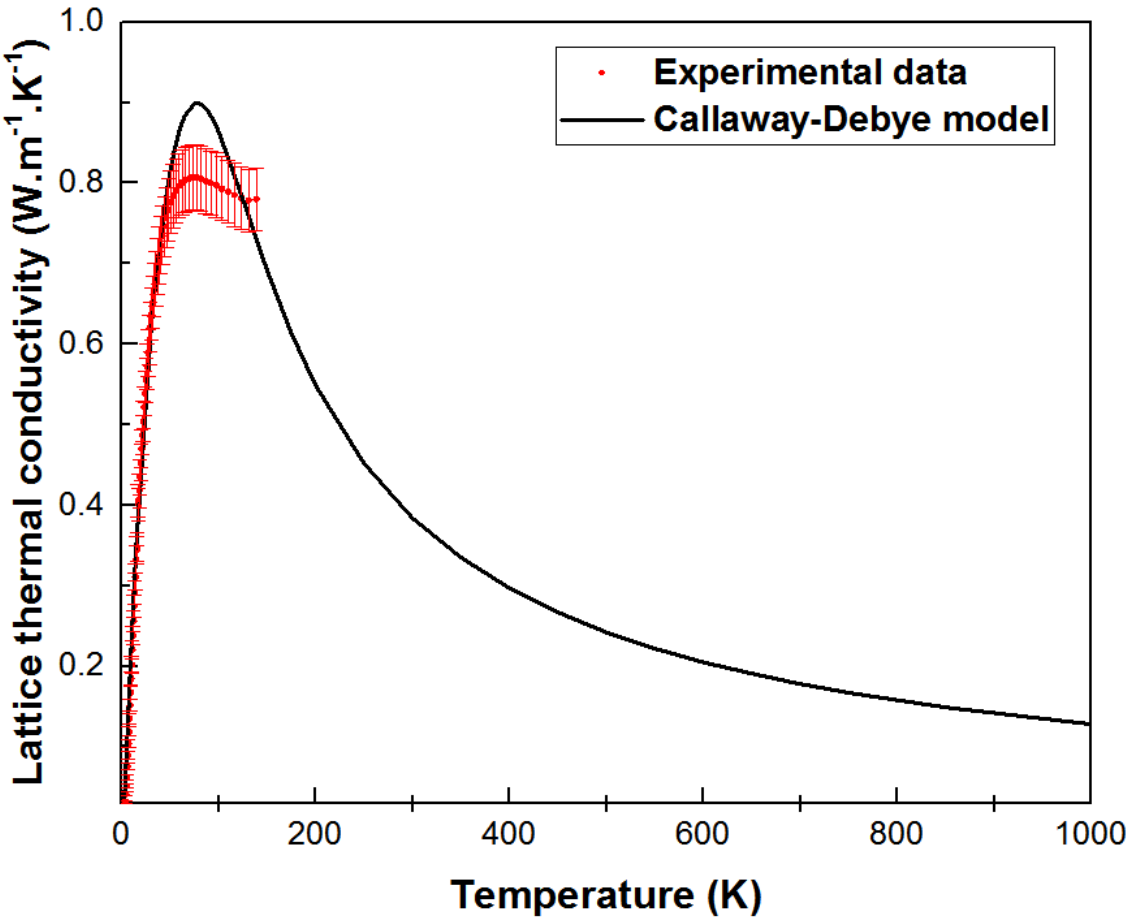

Figure 5.14: Observed (red dots) and calculated (black line) lattice thermal conductivity κ_l as function of the temperature.

$$\kappa_{min} = (\frac{\pi}{6})^{1/3}.k_B.n_a^{2/3}.\sum_i[\nu_i(\frac{T}{\Theta_i})^2\int_0^{\Theta_i/T}\frac{x^3e^x}{(e^x-1)^2}dx], \tag{5.15}$$

where ω is the frequency of the phonon and $x = \frac{\hbar\omega}{k_BT}$; n_a corresponds to the number of atoms per unit volume ($9.428 \times 10^{22}\,\mathrm{cm}^{-3}$), ν_i represents the sound velocity ($5550\,\mathrm{m\,s}^{-1}$), and Θ_i is the Debye temperature (752 K). The calculated profile is illustrated in Figure 5.15. κ_{min} increases towards a saturation value of $1.875\,\mathrm{W\,m}^{-1}\,\mathrm{K}^{-1}$ at 1000K. This value will be used for the calculation of the Figure of merit. It is due to the fact that values of the total thermal conductivity κ converge to κ_{min} at high temperature.

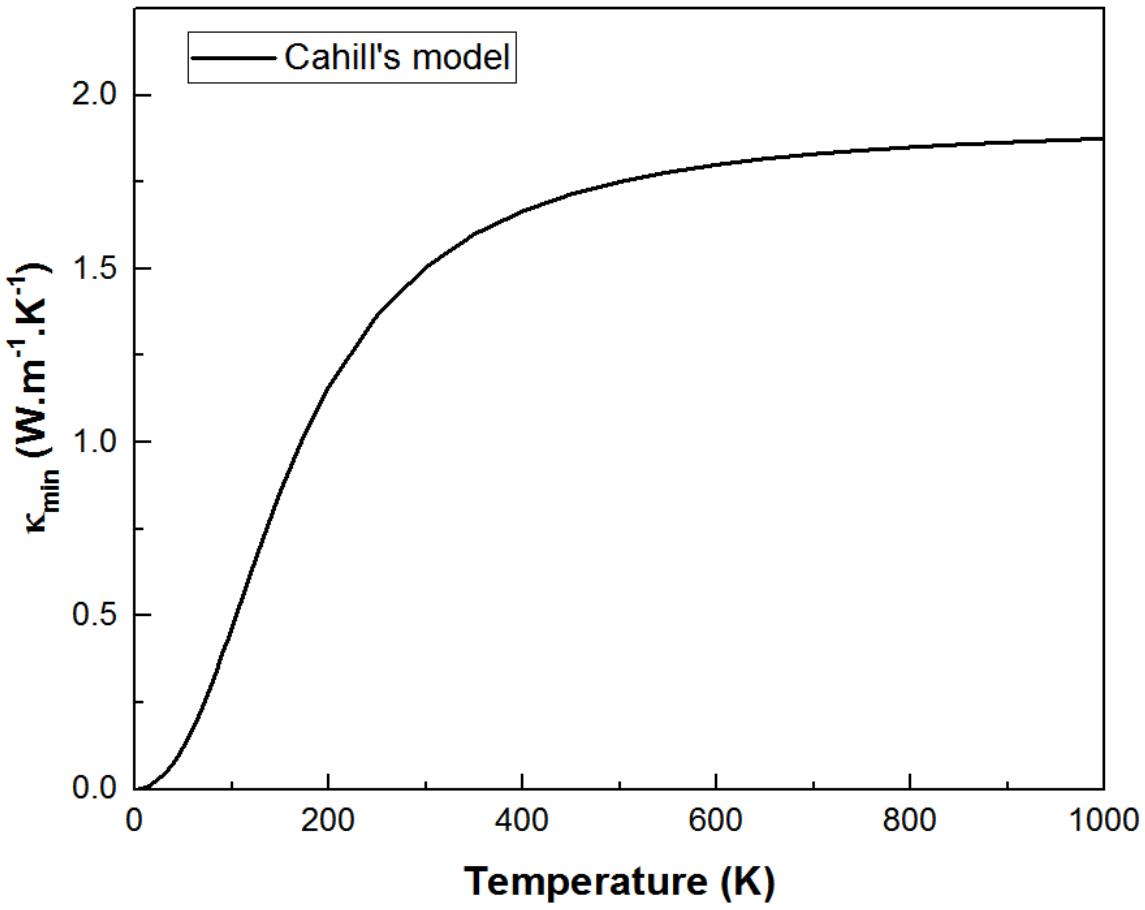

Figure 5.15: Calculated mimimum thermal conductivity from the Cahill's model.

5.6.5 The figure of merit *ZT* of WV_2O_6

The figure of merit of the WV_2O_6 was derived from the measured Seebeck coefficient (S), electrical (σ) and thermal conductivity (κ) via the relation in equation (5.15):

$$ZT = (\frac{S^2\sigma}{\kappa})T. \tag{5.16}$$

ZT is dimensionless and its value indicates the potential of material for thermoelectric applications: A material with a large ZT is a good TE material. The figure of merits of the state-of-the-art

n-type TE oxides are within the following range $0.3 \leq ZT \leq 1$. For instance $Zn_{0.98}Al_{0.02}O$[188] exhibits a ZT of 0.30 at 1279 K. Since the thermal conductivity was not measured at high temperature, κ was assumed to be equal to a constant for the calculations of the Figure of merit. This constant is the minimum thermal conductivity κ_{min} determined with the Cahill's model. The temperature dependence of the figure of merit of tungsten divanadate oxide is depicted in Figure 5.16.

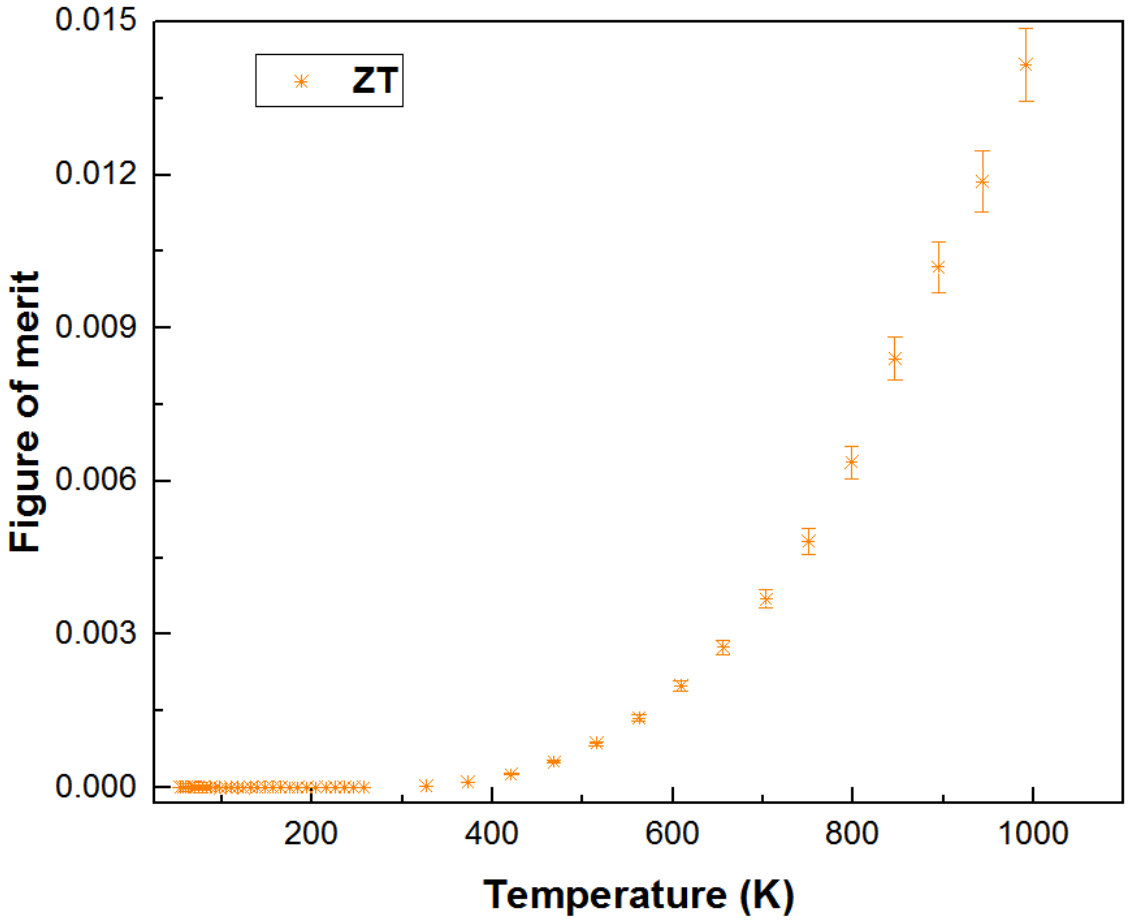

Figure 5.16: Temperature-dependence of the figure of merit ZT of WV_2O_6.

The orange asterisks in Figure 5.16 are the values of the figure of merit which are derived from the experimental data. The figure of merit of WV_2O_6 increases with increasing temperature. The highest value of ZT is observed at 1000 K and it is equal to 1.416×10^{-2}. The exponential profile of the figure of merit results from the fact that PF is much greater than κ, which is in the order of the unity. In other words, the power factor dictates the profile of ZT.WV_2O_6 exhibits a figure of merit which is one order of magnitude lower than that the standard Al-doped ZnO. However, tungsten divanadate oxide is undoped. Appropriate dopings of this material may therefore result in enhancements of its power factor thus figure of merit. For instance, increasing its PF by a factor 10 yields a figure of merit of about 0.142 at 1000 K.

5.7 Conclusion

To conclude, the thermoelectric properties of WV_2O_6 was investigated. This *n*-type semiconductor exhibits a figure of ZT of 3.395×10^{-2} at 1000 K. This value is one order of magnitude lower than that of typical *n*-type TE oxide such as ZnO [58,188]. Several strategies are envisaged for an enhancement of the TE properties of this trirutile. Due to modulated nature of WV_2O_6, the sample prepared in this work corresponds to a specific composition of the trirutile $V_xW_{3-x}O_6$ (with 1.7 $<$ x $<$ 2.1). The synthesis of several compositions of this trirutile is considered for a study of the relationship between electrical conductivity and the atomic structure of different compositions. Measurements on singles crystals reveal the intrinsic properties of a material. Single crystals growth of this homogeneous range of trirutile systems by chemical vapor transport [177] is envisaged. Joint x-ray and neutron diffraction on these single crystals will shed light on the packing of V^{3+} and W^{6+}. The effects of the crystal structure (different compositions) on the TE properties of tungsten divanadate oxide will then be investigated.

Chapter 6

$NiTa_2O_6$: revisiting the magnetic structure of a trirutile compound

6.1 The cation ordering wave in trirutile $NiTa_2O_6$

Symmetry is certainly one of the most important concepts in physics, especially in condensed matter physics[189]. Symmetry manifests itself in the crystal structures of materials. A crystal structure is a specific arrangement of atoms within a Bravais lattice[189,190]. The crystal structure of a material (hence crystallography) plays a major role in the understanding of its physical properties. For instance, phase transitions are mostly related to a change in symmetry of the crystal structure.

X-ray diffraction is one of the methods for the determination of crystal structures. The x-ray/crystal structure relationship started with the groundbreaking discovery of Max Von Laue[191]. A regular diffraction pattern is observed, when x-rays were diffracted by single crystals. William Lawrence Bragg and his father William Henry Bragg[113,191] then demonstrated, by means of geometry, that such phenomena was possible if the wavelength of the x-rays were in the same order of magnitude as the interatomic distances of the solids. This condition is known as the Bragg's law for x-ray diffraction. A fundamental assumption in x-ray diffraction is that once a well refined crystal structure has been established there is no need to consider the possibility of a different arrangement of the same atoms that produces an identical diffraction pattern[184,191], i.e, there is one-to-one relationship between a nuclear structure and a x-ray diffraction pattern.

6.1.1 Homometric structures

The determination of the atomic structures from x-ray diffraction was based on the fact that the detected scattered intensities were directly related to the the coordinates of the atoms. The electron density function in this case was expressed by the following formula:

$$\rho(xyz) = \frac{1}{V} \sum_{hkl=-\infty}^{+\infty} |F(hkl)|.exp[-2\pi.i.(hx + ky + lz)], \tag{6.1}$$

where x,y,z are the coordinate of an atom, h k l are the Miller indices, V represents the total

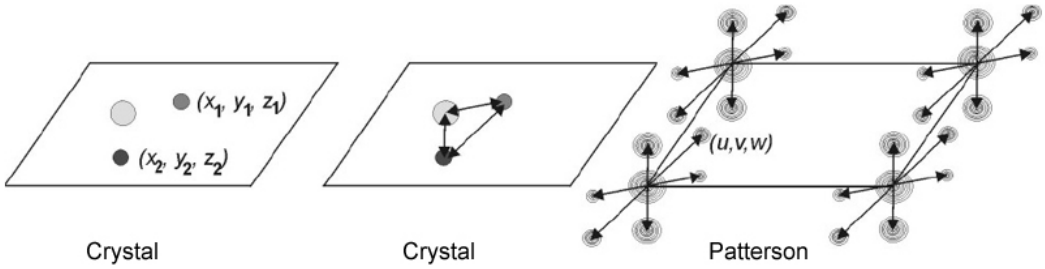

Figure 6.1: Scheme of a Patterson function derived from a crystal containing three atoms in the unit cell (left) . All possible interatomic vectors are plotted (center figure). These vectors are then moved parallel to themselves to the origin of the Patterson unit cell (right figure). Source: *http://www.xtal.iqfr.csic.es*

volume of the material and F (h k l) is the atomic structure factor of the lattice along different planes. The structure factor F(h k l) of a diffracted x-ray along the (h k l) plane is is a mathematical function describing the amplitude and phase of the diffracted x-ray from crystal lattice planes characterised by Miller indices h,k,l.

However, in his 1933's paper [192] Patterson proved that the one-to-one relationship between nuclear structure and x-ray diffraction pattern is not valid for some structures. Patterson demonstrated that two or more distinguishable arrangements of atoms can give rise to the same XRD diffraction pattern. In other words, the intensities of the x-ray reflections from the different crystal structures are the same. For Patterson the relevant parameter to determine crystal structures is the vector distance set between atoms in the crystal lattice. A new electron density function, named after him, was thus introduced. This function is given by:

$$\rho(uvw) = \frac{1}{V} \sum_{hkl=-\infty}^{+\infty} |F(hkl)|^2 . \cos[2\pi.(h\mathbf{u} + k\mathbf{v} + l\mathbf{w})], \tag{6.2}$$

where $\mathbf{u} = x_1$ - x_2, $\mathbf{v} = y_1$ - y_2 and $\mathbf{w} = z_1$ - z_2. The Patterson function provides a map of interatomic vectors between the atoms positions, as seen on the right figure in Figure 6.1.

Using the function in equation (6.2) one can demonstrate that several structures with different atomic arrangements - but same distance between the atoms - can lead to the same electron density function. Consequently these distinguishable atomic structures will exhibit the same x-ray diffractogram [184,193]. Such structures are known as homometric structures.

6.1.2 The trirutile structure as commensurately modulated rutile

A modulated structure consists of a basic structure plus an occupancy and/or a displacive wave [184,194,195]. The wave is made commensurate when the resulting lattice is a multiple of the original lattice. The trirutile-type structure derives from the rutile type as a consequence of the chemical ordering of the divalent and the pentavalent cations, leading to a tetragonal structure with the *c*-axis being tripled as compared to *a*- and *b*-axes. A trirutile is therefore a commensurate modulated rutile. All fully ordered AB_2O_6 trirutiles can be described as commensurately modulated by a scattering density wave of the form :

$$f(z) =< f > -\frac{2}{3} * g * \Delta f * \cos(2\pi z), \tag{6.3}$$

where *f(z)* describes the scattering power in position 0, 0, z along the [0 0 1] direction. <*f*> and Δf refer to the average scattering power and the difference of scattering power, respectively. They are both expressed in terms of the scattering factors of A (f_A) and B (f_B). g is the fraction amplitude, i.e. the ratio of the amplitudes of the waves generated by the two cations. Equation (6.3) exposes that the modulation is a scattering wave function which runs along the two cations along the [0 0 1] direction[184]. Note that the scattering factor of an atom A (f_A) describes the effects of the electronic cloud of the atom on the path of an incident wave. The scattering wave function therefore describes how a unit cell (cations and anions) deviates the path of an incident wave. The Unit cell of TiO_2 and $FeTa_2O_6$ are illustrated in Figure 6.2. The cations (Fe^{2+}, Ta^{5+}, Ti^{4+}) are octahedrally coordinated with the oxygens (O^{2-}). Figure 6.2 demonstrates the trirutile is commensurate modulated rutile as its unit cell is the triple of the latter along the *c*-axis.

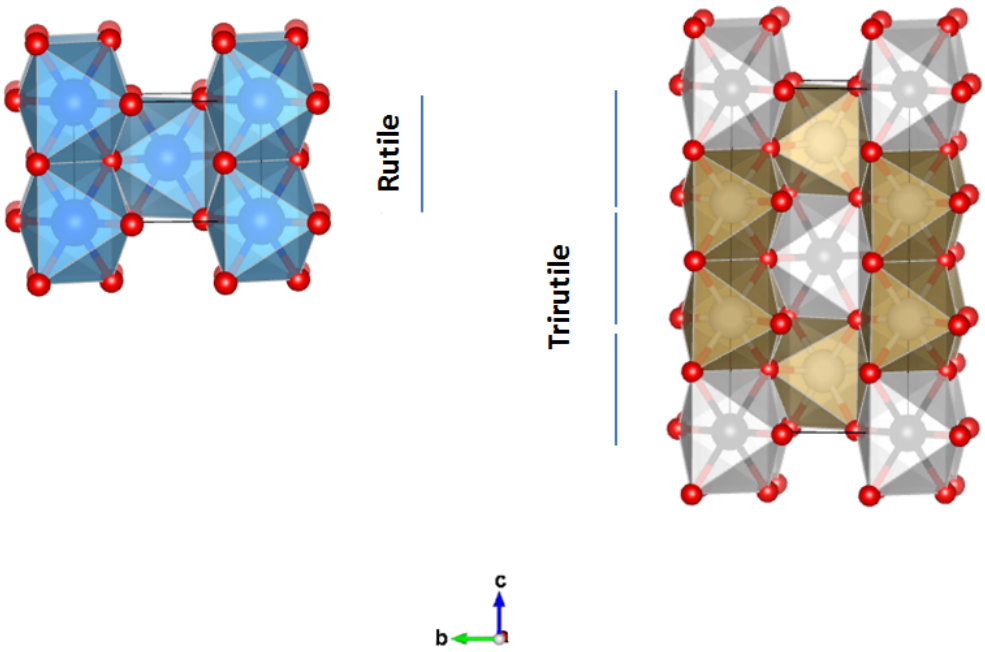

Figure 6.2: The unit cells of a rutile (left) and a trirutile (right). The black, grey and blue spheres represent the iron (Fe), tantalum (Ta) and titanium (Ti) atoms, respectively. These atoms are linked through shared oxygens atoms (O), illustrated by the red spheres.

Hansen *et al.*[184] studied the homometric character of trirutiles in the tapiolite $FeTa_2O_6$. In the fully ordered trirutile Fe^{2+} and Ta^{5+} are distributed on the *2a* and *4e* Wyckoff sites. Figure 6.3 below is a plot of the scattering density wave as function of the cation position along the *c*-axis. One thus expects each of the functions in Figure 6.3 to be associated with a unique cations distribution, i.e. distinguishable arrangements of the cations within the sites.

In Figure 6.3 f varies like a cosine function. f takes the same value for z = $\frac{1}{3}$ and z = $\frac{2}{3}$ for all g values. The functions for g = x and g = -x are antisymmetrical, where x $\in \mathbb{R}$; the black dashed

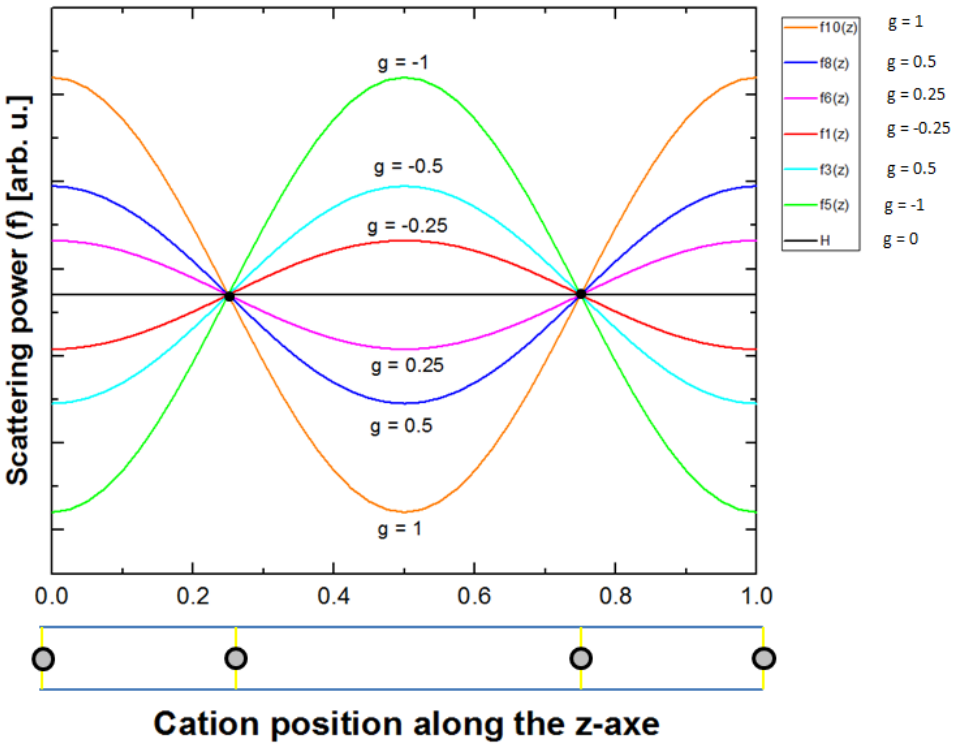

Figure 6.3: Scattering power f as a function of z coordinate within the trirutile structure. f_6, f_8 and f_{10} are the scattering wave functions for g equal to 0.25, 0.5 and 1, respectively. Likewise the red (f_1), blue cyan (f_3) and green (f_5) curves are the respective functions for g equal to -0.25, -0.5 and -1.

line represents *f(z)* for $g = 0$, in other words the average scattering power <*f*>. At the two black dots on the function *f(z)* = <*f*> the scattering functions of two different structures are identical. Consequently, the diffraction patterns of the two structures will be identical and the two atomic structures are said to be homometric.

In a fully ordered tapiolite the *2a* and *4e* Wyckoff sites are only occupied by the Fe and Ta, respectively. On the other hand a trirutile characterised by 67 % Ta in *2a* corresponds to a fully disordered trirutile, i.e. a rutile. Between these two extreme configurations there are intermediate structures for which iron and tantalum atoms can both occupied the sites *2a* and/or *4e*. This is chemically possible due to the fact that Fe^{2+} and Ta^{5+} both have the same coordination number (6) and their atomic radius is similar: 0.61 and 0.64 Å, respectively. Hansen *et al.*[184] identified two different crystal structures of $FeTa_2O_6$, thus two different *f* functions, which gave rise to the same x-ray diffraction pattern. The two crystal structures are therefore homometric. These functions are f3(z) and f8(z) in Figure 6.3 and are associated with $g = \pm 0.5$.

Hansen and coworkers showed that the scattering functions f3(z) and f8(z) are associated with the respective cation distributions:

- for $g = 0.5$ one deals with 66.7% of Fe and 33.3% of Ta at the *2a* site; the *4e* site is occupied by 16.7% of Fe and 83.3% of Ta.

- For $g = -0.5$ the site *2a* is only occupied by Ta. The site *4e* is evenly shared by both metals: 50% of Fe and 50% of Ta.

For these two homometric $FeTa_2O_6$ crystal structures there is no longer one-to-one relationship between crystal structure and x-ray diffraction pattern but rather two-to-one relationship.

6.1.3 Joint refinement: a solution to the Patterson's problem

The joint x-ray and neutron diffraction is one of the methods used to differentiate two or more-homometric structures. One performs separately both x-ray and neutrons diffraction on the studied material. X-rays and neutron have different scattering factors. The interplay between their scattering factors is essential to solve the problem outlined by Patterson. The x-ray scattering factor of an atom results from scattering by the electron cloud of an atom while neutron (non-magnetic) diffraction is due to scattering from the nucleus of an atom. During a joint x-ray and neutron diffraction, there is collection of information on the nuclei and the electrons clouds of the atoms within the structure. Hence, by combining both sets of data there is a unique arrangement of the atoms within the lattice, which fulfills both structure factors individually obtained from x-ray and neutrons diffraction. A system of two simultaneous equations is a good analogy to joint x-ray and neutron refinement. Consider the following two simultaneous equations:

$$\begin{cases} 2x + 1y = 5 \\ -1x + 1y = 2 \end{cases} \tag{6.4}$$

The first equation - (2 , 1) - can be associated with the scattering by x-rays. In the same manner the parameters (−1 , 1) are associated with neutron scattering factors. The variables (x,y) play the role of the set of vectors distance of the unknown crystal structure. There is an infinite number of solutions for the first equation, and also for the second one. But there is only one set (x,y) which fulfills both equation at the same time: (1, 3). Therefore the joint x-ray and neutron diffraction solves the problem of homometric structures.

Investigations on the atomic structure of $NiTa_2O_6$ were motivated by the work of Hansen who reported two homometric structures of the trirutile $FeTa_2O_6$. Since $NiTa_2O_6$ also crystallises in the trirutile structure, it can be viewed as a commensurately modulated structure. Hence, there is possibility of dealing with different arrangements of atoms which give rise to the same x-ray diffraction pattern. Joint x-ray and neutron diffraction was thus performed to determine the ordering of the cations (Ni^{2+} and Ta^{5+}) within the prepared powdered $NiTa_2O_6$ sample. As the establishment of the atomic structure is essential for the understanding of the properties (thermoelectric, optical and magnetic) of a material such as the magnetic structure.

6.1.4 Synthesis

A solid state reaction has been used to prepare powdered $NiTa_2O_6$ samples. Following Takano *et al.*[72], the synthesis has been carried out by mixing stoichiometric quantities of NiO (99.9%) and

Ta_2O_5 (99.99%). The NiO and Ta_2O_5 powders have a green and a white color, respectively; the solid state reaction is given by the following equation:

$$NiO + Ta_2O_5 \xrightarrow{air} NiTa_2O_6 \tag{6.5}$$

The reagents have been mixed with a pestle in an agate mortar under acetone; the mixture has been placed in an aluminium crucible and then heated at 1400 °C in a furnace for 48 hours at a rate of 5 °C/min. After two days the reaction's products had been cooled at a rate of 5 °C/min to room temperature. A second grinding and a repetition of the annealing process have been performed in order to ensure phase purity. The synthesis temperature differed from Takano and coworkers [72], who heated the NiO-Ta_2O_5 mixture at 1200 °C. This is due to the fact spurious phases (NiO, Ta_2O_5) were found in the x-ray diffraction pattern of a sample prepared at 1200 °C. The resulting powder has a light yellow colour, as seen Figure 6.4a.

6.1.5 Powder x-ray diffraction

Prior to any physical characterization, the phase purity of the prepared sample needs to be assessed. The sample quality was examined through powder x-ray diffraction, by comparing the observed diffractograms with those recorded in a database. The PANalytical instrument was utilised to measure the x-ray diffraction patterns of the prepared samples. Details on this instrument are given in section 2.1 of Chapter 2. Rietveld refinement of the diffraction pattern was then performed in order to extract the main crystallographic parameter of the crystal structure of $NiTa_2O_6$. The *Fullprof* program was utilised for this task. The resulting Rietveld refinement of a room temperature powder x-ray diffraction pattern (XRD) is shown in Figure 6.4b.

In Figure 6.4b, the measured and calculated profiles correspond to the red dots and a black line, respectively. The blue line is obtained by subtracting the observed data from the data of the calculated profile. The tick marks indicate the nuclear Bragg peak positions. All peaks correspond the nuclear reflections of a lattice whose space group is $P4_2/mnm$ (136). The crystallographic parameters of the lattice are displayed in Table 6.1 and are in good agreement with those reported in the literature. The refinement factors are defined in the appendix. The small values of the fitting and structural parameters - $\chi^2 = 2.19$, $R_B = 5.76\,\%$, $R_F = 6.15\,\%$ - and the absence of spurious reflections on the diffractogram are strong indications that a well crystallised single-phase sample has been prepared.

6.1.6 The joint x-ray and neutron diffraction on powdered $NiTa_2O_6$ sample

Joint refinement of the x-ray and neutron diffraction patterns was then performed to investigate the catiosn distribution on the *2a* and *4e* Wyckoff sites. Both diffractograms were recorded at room temperature. The 3T2 high resolution powder diffractometer was utilised to record zero-field neutron powder diffraction data on $NiTa_2O_6$ polycrystalline samples at Laboratoire Léon Brillouin

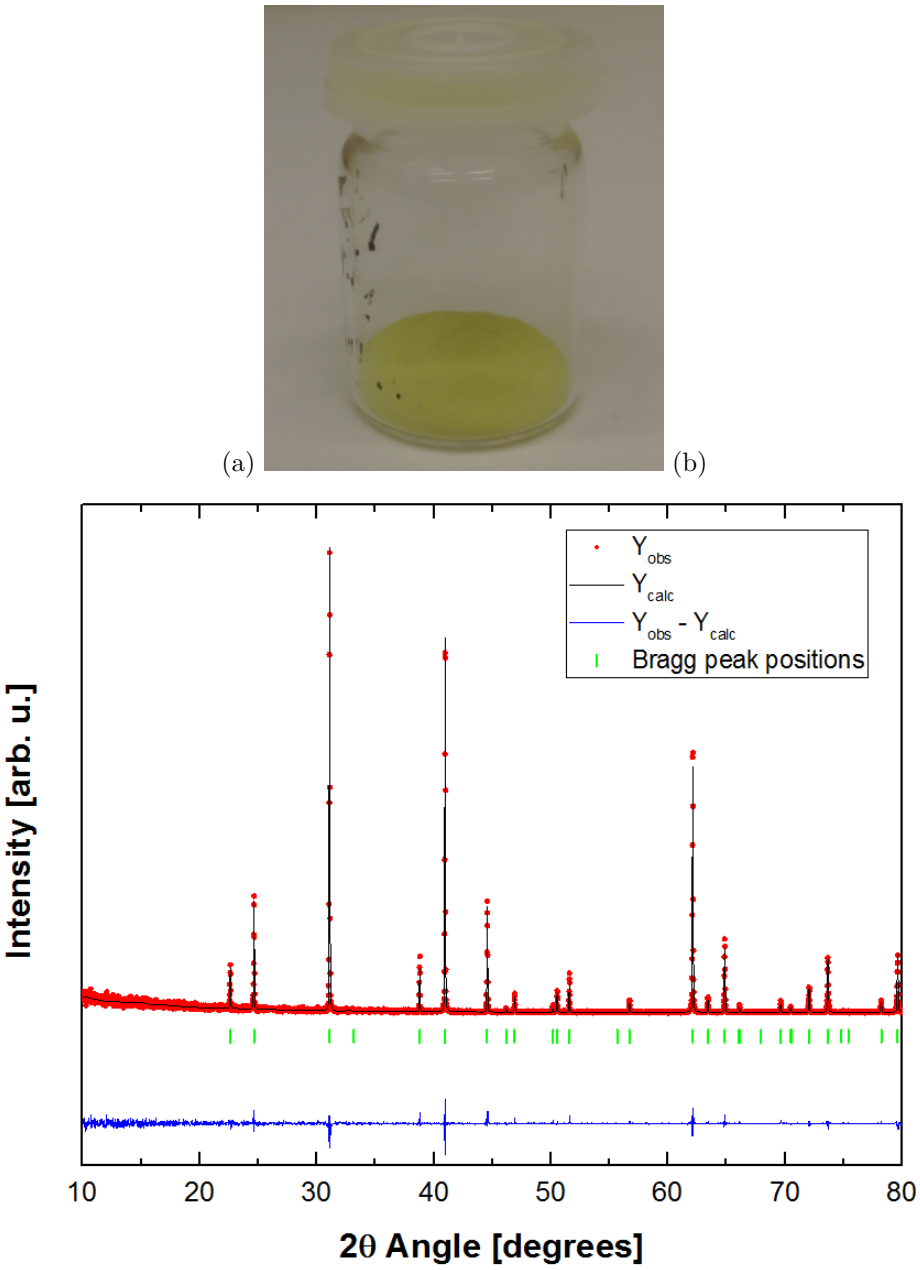

Figure 6.4: (a) Yellow $NiTa_2O_6$ polycrystalline samples. (b) Rietveld refinement of a room temperature x-ray powder diffraction pattern for $NiTa_2O_6$.

Table 6.1: Crystallographic parameters of $NiTa_2O_6$ after Rietveld refinement of the above room-temperature x-ray powder diffraction pattern. Z corresponds to the number of nickel per unit cell. The R-coefficients give an indication on the goodness of the fit.

Space group	**a**[Å]	**c**[Å]	**Z**
$P4_2/mnm$	4.7190(4)	9.1248(1)	2
	x	**y**	**z**
Ni	0	0	0
Ta	0	0	0.3312(4)
O(1)	0.3051(6)	0.3051(6)	0
O(2)	0.2920(4)	0.2920(4)	0.3322(3)
R_B (%)	5.76		
R_F (%)	6.15		

(LLB), Saclay (France). Details on this instrument are given in section 2.2.2 of Chapter 2. The software *Fullprof* was utilised to perform the joint refinement. The joint refinement was carried in the following manner: (i) the positions of both Ni^{2+} and Ta^{5+} were refined. (ii) In addition to that the occupancy of both cations was distributed on both $2a$ and $4e$ sites and refined, (iii) and the refinement factors of the different models were compared in order to determine the best model for the atomic structure of nickel ditantalate oxide.

The cation distribution on the Wyckoff sites *2a* and *4e* was explored, like in the case of $FeTa_2O_6$ [184]. One is interested in g values associated with the prepared sample, for which homometry occurs. A g-value corresponds to a specific way of arranging the Ni^{2+} and Ta^{5+} in the *2a* and *4e* sites. Instead of directly assessing the value of g one can also study the configurations in which both cations are distributed in both sites. The total occupation number of each cation is the sum of the occupancy one site *2a* and the occupancy site *4e*. The occupancy is defined as the ratio of site multiplicity and the general multiplicity.

There are four occupancy numbers to refine, as both nickel and tantalum can occupy *2a* and *4e* sites. These four occupancy numbers are given initial values. This specific configuration of the Ni^{2+} and Ta^{5+} in the Wyckoff sites is a potential model for the crystal structure. Various models were tested and here are some examples: (*) all *4e* sites are fully occupied by Ta. Ta and Ni both share the *2a* sites; (**) the reverse configuration corresponds to another model. For the "general" model both sites are occupied by both transition metal ions. This configuration is displayed in Table 6.2. During the joint x-ray and neutron calculations the occupation values are released, varied and converged towards some values. The resulting configuration associated with the lowest refinement factors is the best model for the crystal structure of $NiTa_2O_6$. It should be noted that the constraints have been added to the occupation number of the cations, in order to insure the stoichiometry of the compound. Indeed the sum of the occupation numbers of Ni^{2+} must be equal to 0.125. Similarly those of Ta^{5+} are equal to 0.250 throughout the refinement.

Table 6.2: Crystallographic parameters of the unit cell of $NiTa_2O_6$. Ni^{2+} and Ta^{5+} ions both fully occupy the *2(a)* and *4(e)* Wyckoff sites, respectively.

		Wyckoff positions				
Atom	**Type**	**x**	**y**	**z**	**Biso**	**Occ**
$Ni1$	Ni	0	0	0	0.000	0.127(1)
		0.00	0.00	0.00	0.00	241.00
$Ta1$	Ta	0	0	0	0.000	−0.002(1)
		0.00	0.00	0.00	0.00	-
						241.00
$Ni2$	Ni	0	0	0.33152	0.000	0.009(2)
				(3)		
		0.00	0.00	231.00	0.00	-
						251.00
$Ta2$	Ta	0	0	0.33152	0.000	0.241(2)
				(3)		
		0.00	0.00	231.00	0.00	251.00
O1	O	0.31051	0.31051	0	0.000	0.250
		(5)	(5)			(0)
		221.0	0.00	221.00	0.00	0.00
O2	O	0.29707	0.29707	0.3267	0.000	0.500(0)
		(3)	(3)	(2)		
		211.0	0.00	211.00	0.00	0.00

Table 6.2 is the "general" model used to perform the joint x-ray and neutron powder diffraction. The last column represents the occupancy of the atoms on the crystallographic sites. The occupation values of Ta_1 (blue font) and Ni_2 (green font) are very low- 0.002 (1) and 0.009 (2) in comparison to those of Ni_1 (blue font) and Ta_2 (green font), respectively. The occupancy values of the latter atoms are 0.127 (1) and 0.241 (2), respectively. One deduces that the Wyckoff sites (*2a* and *4e*) in the prepared $NiTa_2O_6$ sample are only occupied by Ni and Ta, respectively. This is different to the tapiolite $FeTa_2O_6$ [184] for which the iron and the tantalum both occupy the two Wyckoff positions.

The Rietveld method was utilised to perform the joint x-ray and neutron refinement. The diffractogram (a) in Figure 6.5 corresponds to the x-ray contribution of the refinement. Similarly the neutron contribution is illustrated by the diffractogram (b). The red dots and black line correspond to experimental and theoretical profiles, respectively. The green tick marks indicate the nuclear Bragg peak positions. The observed reflections are those of the lattice with the space group $P4_2/mnm$ (136). The low values of R_B and R_F indicate that agreement between the observed and calculated profiles. The lattice and fitting parameters of the joint refinement are shown in Table 6.3. The phase 1 and 2 represent the x-ray and neutron contributions, respectively. The R_B and R_F were the lowest refinement factors in the series, suggesting that the model in Table 6.3 is the most appropriate one for the crystal structure of $NiTa_2O_6$. The prepared nicked ditantalate oxide is therefore a fully ordered trirutile.

The 3D crystal structure of $NiTa_2O_6$ is shown Figure 6.6. Atoms are drawn as large spheres and the unit cell is outlined. The green spheres represent the Ta atoms whereas the Ni atoms appear

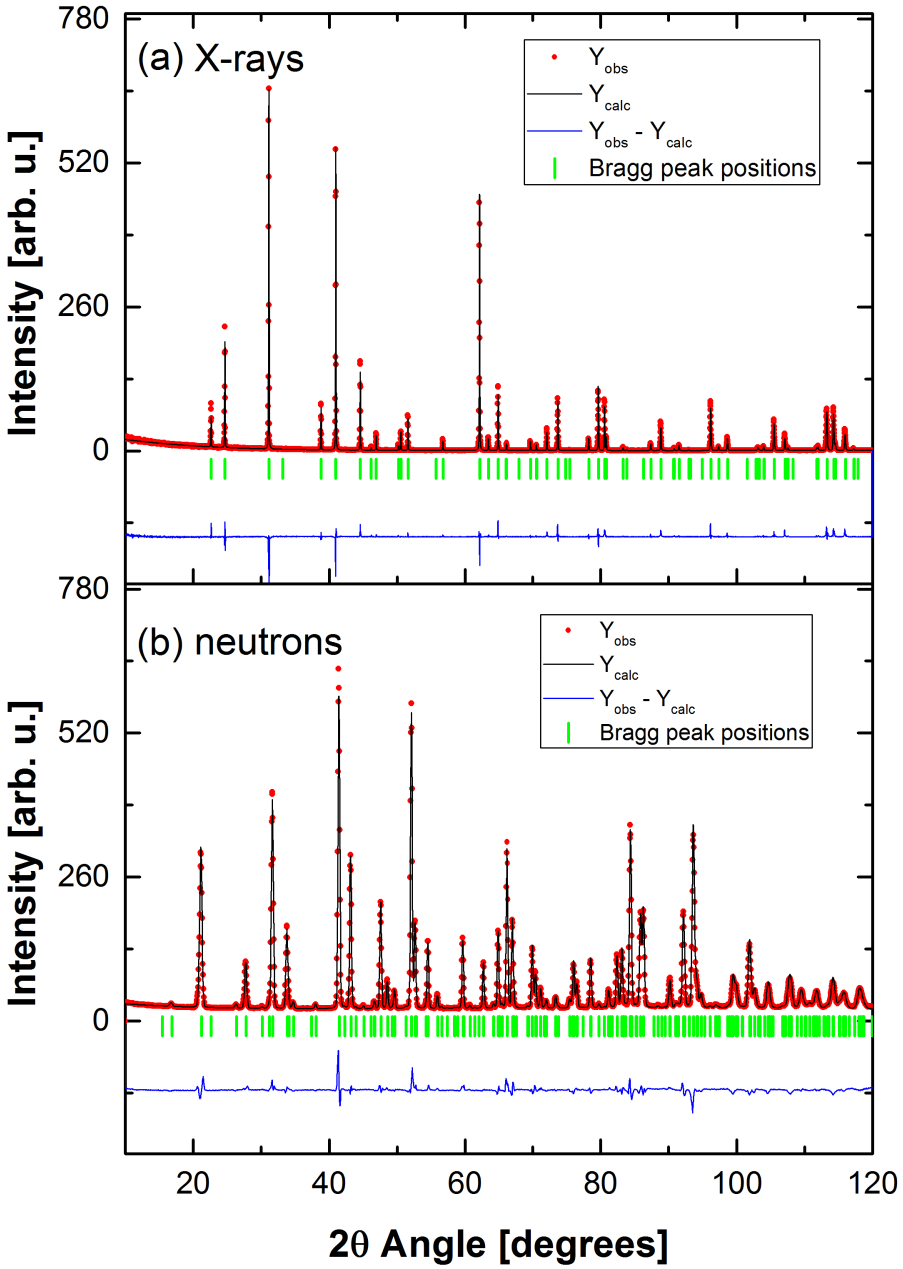

Figure 6.5: Results of the Rietveld joint x-ray and neutron powder diffraction refinement. The red dots and black line correspond to experimental and theoretical profiles, respectively. The green tick marks indicate the nuclear Bragg peak positions.

Table 6.3: Some parameters of the joint x-ray and neutron powder diffraction refinement of the crystal structure of $NiTa_2O_6$.

Phase	λ[Å]	**a**[Å]	**c**[Å]	R_B	R_F
Phase 1	1.78919	4.71769(4)	9.12340(8)	11.6	8.85
Phase 2	1.22763	4.71769(4)	9.12340(8)	5.95	4.41

Table 6.4: Wyckoff positions of atoms within the orthorhombic unit cell of $NiNb_2O_6$, obtained from Rietveld refinement of room-temperature joint x-ray and neutrondiffraction patterns. Site occupancy (site occu.) is the ratio between the site multiplicity and the general multiplicity. Space group: $P4_2/mnm$ (136).

atom label	**atom type**	**Wyckoff symbol**	**x**	**y**	**z**	**site occu.**
Ni	Ni	2a	0	0	0	1/8
Ta	Ta	4e	0	0	0	1/4
O_1	O	4f	0.31051(5)	0.31051(5)	0	1/4
O_2	O	8j	0.29707(3)	0.29707(6)	0.3267(8)	1/2

as the blue spheres. The latter are surrounded by six oxygens (red spheres) and together they form NiO_6 octahedra. The tantalum atoms also have an octahedral environment.

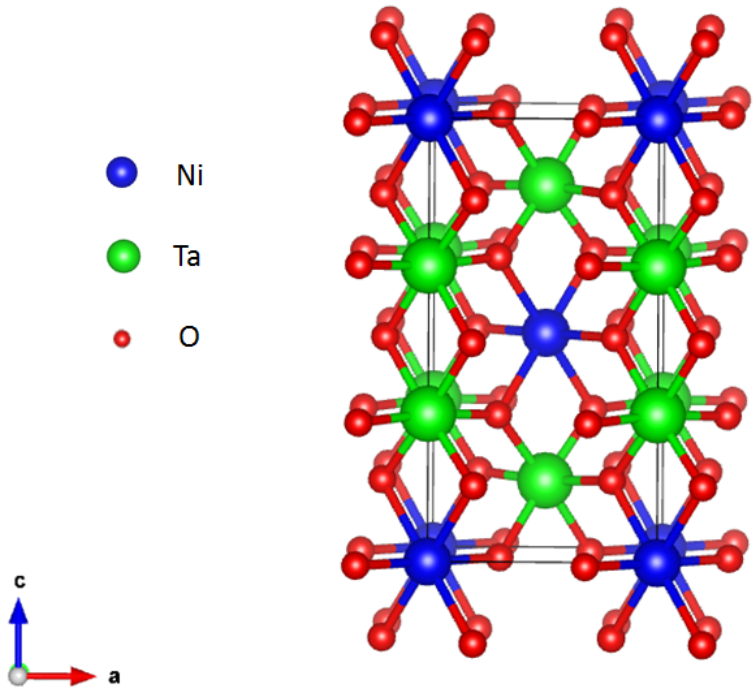

Figure 6.6: Unit cell of $NiTa_2O_6$ obtained room temperature joint x-ray and neutron powder diffraction refinement.

To summarise this section, the crystal structure of $NiTa_2O_6$ were investigated by means of a joint x-ray and neutron diffraction. This compound crystallises in a trirutile structure, which is a commensurately modulated rutile. This modulation may give rise to homometric structures. Patterson demonstrated that such structures give rise to the same x-ray diffraction pattern. By combining x-ray and neutron data one can distinguish the homometric structures. The positions and occupation numbers of the cations on the *2a* and *4e* sites were refined, under several constraints. Comparison between the refinement factors of the different models enables the identification of the appropriate model for the cations distribution in the lattice. In the prepared $NiTa_2O_6$sample the *2a* and *4e* Wyckoff sites are only occupied by Ni and Ta, respectively. Hence, the prepared nickel ditantalate oxide is a fully ordered trirutile. The lowest value of the refinement factors are strong indicators

that a well-crystallised single phase purity has been prepared, as required for the investigation of physical properties. The physical property investigated in the next section of the chapter is the magnetic structure of $NiTa_2O_6$.

6.2 Magnetic structure determination

The determination of magnetic structure is crucial for understanding the properties of magnetic materials, particularly those with technological applications such as spin electronics and permanent magnets. Magnetic structures are either commensurate and incommensurate:

- a commensurate structure has a structure periodicity which is a multiple of that of the nuclear crystal structure. This is typically the case in ferromagnets, antiferromagnets and ferrimagnet materials. For instance, for ferromagnetic materials the nuclear and magnetic crystallographic lattice are identical.
- for incommensurate structures, the magnetic unit cell is non-integer multiple of the nuclear unit cell.

Magnetic structures can be predicted theoretically[196,197]. After writing the Hamiltonian of the system one can solve the relevant eigenstates and eigenvalues. The establishment of the Hamiltonian and the eigenstates calculations are very complex, partly because it is difficult to predict which magnetic interactions are important and which ones can be neglected. This is why it is common to determine magnetic structures experimentally. There are many ways to explore magnetic structures experimentally, but neutron diffraction[120,198,199] is by far the most common technique. This method uses a beam of thermal neutrons (having a spin $\frac{1}{2}$) which then interact with any unpaired electrons in magnetic ions in the sample. Neutron diffraction patterns (NDPs) reveal information on the magnitude and orientation of electron spins within crystals. Further details on neutron diffraction are given in the section 2.2 of Chapter 2. In addition the reader is encouraged to consult, for example, the authoritative reference works of Willis and Carlie[120] or Chatterji[119].

Magnetic structures are determined by neutron diffraction via two methods. The first is the method of magnetic symmetry refinement discussed further in section 4.3 in which a magnetic model is derived from the nuclear structure of the parent material, using symmetry elements and time reversal. The end product is a magnetic space group (also called Shubnikov group[31,124,200]) which describes the symmetry relations between magnetic ions within a crystal system. All allowed magnetic space groups are subgroups of the space group of the nuclear structure. The range of possible magnetic structures is reduced by choosing one (with a particular magnetic space group) which best fits the neutron diffraction pattern. This method provides an efficient and systematic way to characterize the symmetry of the magnetic lattice from the nuclear lattice, and yields and classifies all degrees of freedom of the system. However, one of the disadvantages of the method is the large number of potential magnetic structures. The second approach, known as the representation analysis[7,8,201], combines a propagation vector $\overrightarrow{k}$ and the space group of the crystal. The propagation vector $\overrightarrow{k}$ relates equivalent magnetic atoms in different unit cells of the magnetic lattice. The irreducible representations (IRs) of the group associated with the propagation vector $\vec{k}$ are then derived. The IRs physically represent some functions which describe the symmetry operations between the magnetic ions positions and spins orientaton. Some IRs are magnetically active as

they transform the magnetic ions without changing the symmetry relations between the magnetic ions. The rest of IRs are said to be magnetically inactive, as their corresponding functions do not preserve the magnetic structure symmetry. The magnetically active IRs and their combinations are the potential models for the magnetic structure. It turns out there are fewer models to refine within this method. On the other hand different magnetic structures can be associated with the same representation, and are therefore indistinguishable from with this method. Representation analysis and magnetic symmetry refinement methods are discussed in some detail in the following sections.

6.3 Representation analysis

This section introduces the formalism of the representation analysis method. The concepts of representation and reducible representations are briefly reviewed. The little group, the cornerstone of the representation analysis approach, is then discussed. The application of representation theory to the determination of magnetic structure concludes the section.

6.3.1 Representations of groups

When dealing with physical properties (vibration spectroscopy, crystal field calculations, etc) related to crystallographic structures solid state physicists take advantage of another aspect of group theory: the representation. Representation theory facilitates the understanding of a complex structure by describing its elements in linear algebra, which is well understood. For instance, the symmetry elements of a group are represented as matrices. For an exhaustive mathematical description of representation theory the reader should consult books by Dresselhaus[202] and Fulton[203], elsewhere Kamp *et al.*[204] wrote an outstanding book introducing the concepts of representation theory.

Definition A representation of an abstract group is a substitution group such that the substitution group is homomorphic (or isomorphic) to the abstract group[202].

Typically one assigns a square matrix D (g) to a symmetry element (g) of a group G. This set of matrices form a particular representation Γ of G. It can be shown that these matrices themselves form a group. Consequently there is a unit element within these matrices. Hence, representation is a linear map from a group of symmetry elements to a group of matrices. An isomorphism corresponds to a one-to-one relationship between the representation matrices and the symmetry operations. On the other hand for a homomorphic mapping there is a many-to-one correspondence. The matrices of a representation[205] are related to the group symmetry elements as follows:

$$D(g_i)D(g_j) = D(g_i g_j) \tag{6.6}$$

$$D(e) = 1 \tag{6.7}$$

Where g_i, g_j and the identity element e are elements of G. These equations indicate that the set of matrices forming a representation have identical multiplication relations within to those of the

group symmetry elements.

Each element of the representation is defined by a matrix with respect to some chosen vectors forming basis. The matrices of a representation can be diagonalized using the application of appropriate transformations. Another picture of diagonalisation is as a change of the basis. The end product is a matrix with square blocks on the diagonal and zeros everywhere else[205]. The following equation represents the change of basis via a rotation whose matrix is U:

$$\Gamma^{'}(g) = U\Gamma(g)U^{-1}. \tag{6.8}$$

The matrix $\Gamma^{'}$ below illustrates the diagonalisation process, as it consists of square blocks:

$$\Gamma^{'}(g) = \begin{bmatrix} A_{11} & A_{12} & 0 & 0 & 0 & 0 & 0 \\ A_{21} & A_{22} & 0 & 0 & 0 & 0 & 0 \\ 0 & 0 & B_{11} & B_{12} & 0 & 0 & 0 \\ 0 & 0 & B_{21} & B_{22} & 0 & 0 & 0 \\ 0 & 0 & 0 & 0 & B_{11} & B_{12} & 0 \\ 0 & 0 & 0 & 0 & B_{21} & B_{22} & 0 \\ 0 & 0 & 0 & 0 & 0 & 0 & C_{11} \end{bmatrix} = U\Gamma(g)U^{-1}. \tag{6.9}$$

6.3.2 Irreducible representations

Definition If by one and the same equivalence transformation, all the matrices in the representation of a group can be made to acquire the same block form, then the representation is said to be reducible; otherwise the representation is irreducible.[202]

A representation is said to be reducible if it can be decomposed into a direct sum of irreducible representations (IRs). Additionally, an irreducible representation cannot be expressed in terms of representations of lower dimensionality. $\Gamma^{'}$ is reducible and its decomposition is given by:

$$\Gamma^{'}(g) = A(g) \oplus 2B(g) \oplus C(g), \tag{6.10}$$

where A(g), B(g) and C(g) are also representations of G and $\oplus$ is the direct sum operator. $\Gamma^{'}$ has been reduced onto representations of lower dimensions. {A, B} and C are respectively two- and one-dimensional irreducible representations (IRs), and can not be further decomposed into lower-dimensional representations. In general, the decomposition[205] of a reducible representation can be written as:

$$\Gamma = \sum_{\nu} n_\nu \Gamma_\nu = n_1\Gamma_1 \oplus n_2\Gamma_3 \oplus ... \oplus n_m\Gamma_m \tag{6.11}$$

Where m is the number of distinct IRs of G, n_ν is the weight or number of IRs of type Γ_ν in the

composition of Γ. Two representations *D(g)* and *D'(g)* are equivalents if there exists a matrix *T* which transforms one into the other. The decomposition of a representation into irreducible representations involves one of the most important theorems of Representation Theory: the Wonderful Orthogonality Theorem. Prior to the description of the Wonderful Orthogonal Theorem one needs to introduce the concepts of characters and the character table.

Definition The character χ^{Γ} (g) of the matrix representation D^{Γ} (g) for a symmetry operation g in a representation Γ, is the trace (the sum over diagonal matrix elements) of the matrix of the representation[202]:

$$\chi^{\Gamma}(g) = \mathrm{Tr}[D^{\Gamma}(g)] = \sum_{\mu=1}^{l} [D^{\Gamma}(g)]_{\mu\mu}, \tag{6.12}$$

where l is the dimension of the representation Γ.

The calculations of the characters of matrices representations for all symmetry elements in all irreducible representations of a space group results in a table, called the character table. In order to reduce a representation Γ into its IRs one first determines the characters of the representation Γ, then the IRs contained in the reducible representation Γ are found using the Wonderful Orthogonality Theorem[30,202,206] which are:

$$\sum_{k} \chi_i(C_k)^* \chi_j(C_k) N_k = h\delta_{ij} \tag{6.13}$$

where $\chi_i(C_k)$ is the character of class C_k written in some representation Γ_i, $*$ denotes the complex conjugate, h is the order - number of elements - of the group, N_k is the number of elements in class C_k, and δ_{ij} is the Kronecker delta[207].

To illustrate the use of the orthogonality theorem, consider the point group *mm2* and an example reducible representation Γ, see Table 6.5. The group *mm2* contains four symmetry elements: the identity, a 2-fold axis and two mirror planes:

$$G = \{1, 2_z, m_x, m_y\}. \tag{6.14}$$

This group (*mm2*) has four classes and Table 5.4 is its character table.

Table 6.5: The character table of the point group *mm2* in first five rows. The last row contains the characters of a reducible representation Γ.

mm2	**1**	**2**	m_x	m_y
Γ_1	1	1	1	1
Γ_2	1	1	-1	-1
Γ_3	1	-1	1	-1
Γ_4	1	-1	-1	1
Γ	9	-1	1	3

In Table 6.5 the first column lists the irreducible representations Γ_i of the group, with i = {1, 2,

3, 4}. The classes are listed in the first row. In this case, each symmetry element is in a distinct class. The numbers 1 and -1 are characters of the symmetry elements written in the corresponding IRs. The application of the Wonderful orthogonal theorem then determines whether or not an IR is part of the decomposition. The number N_k is here equal to 1 for each class. $\sum_k \chi_i(C_k)^* \chi_i(C_l)$ is written as:

For Γ_1: 1*1*9 + 1*1*−1 + 1*1*1 + 1*1*3 = 12 = 3*4.

For Γ_2: 1*1*9 + 1*1*−1 + −1*1*1 + −1*1*3 = 4 = 1*4.

For Γ_3: 1*1*9 + −1*1*−1 + 1*1*1 + −1*1*3 = 8 = 2*4.

For Γ_4: 1*1*9 + −1*1*−1 + −1*1*1 + 1*1*3 = 12 = 3*4.

The blue and green numbers respectively correspond to the characters of the IR and the reducible representation Γ. The numbers in red represent the n_ν in equation (4.11): the number of times an IR appears in the reducible representation. Hence, the decomposition of Γ into IRs can be written:

$$\Gamma = 3\Gamma_1 \oplus 1\Gamma_2 \oplus 2\Gamma_3 \oplus 3\Gamma_4 \tag{6.15}$$

This example illustrates the decomposition of reducible representations into linear combinations of IRs via the wonderful orthogonality theorem. Programs such as the Bilbao Crystallographer Server and *BasIreps* in *Fullprof* suite[115] automate the decomposition of representations into IRs. The character table and orthogonality relations are also useful in determining selection rules for optical absorption in infrared and Raman spectroscopy, where they indicate whether or not some vibrations modes of a crystal lattice are infrared or Raman active.

6.3.3 The little group $G_{\vec{k}}$

The representation analysis method lies on the Representation Theory for the determination of magnetic structures. Before discussing this the propagation vector $\vec{k}$ is introduced.

Magnetic structures combine crystal lattices with magnetic ions. They can be viewed as a periodic repetition of a magnetic unit cell in the three directions of space. An atom/ion within the crystal lattice is identified by its coordinates:

$$\vec{R}_{\vec{t}j} = \vec{t} + \vec{r}_j \tag{6.16}$$

where $\vec{t}$ is a translation vector from an origin to a particular crystal unit cell and $\vec{r_j}$ represents the position of atom in that unit cell. In order to describe a magnetic structure one takes advantage of its periodicity by considering all magnetic moments in the zeroth crystallographic unit cell. Atoms with identical magnetic moments which sit in equivalent crystallographic sites (or Wyckoff positions) in different unit cells are then said to be related by a propagation vector $\vec{k}$, defined by:

$$\vec{m}_j = \vec{\Psi}_j e^{-2\pi i \vec{k}.\vec{t}} \tag{6.17}$$

where $\vec{m}_j$ is the magnetic moment at atomic site j in a unit cell, that is related to the zeroth unit cell by a translation $\vec{t}$, and $\vec{\Psi}_j$ is the magnetic moment in the same atomic site in the zeroth unit cell.

The periodicity of the magnetic structure is associated with a set of points in reciprocal space. These points are associated with the magnetic reflections seen in neutron diffraction patterns recorded below the critical temperature of a material. The points in reciprocal space are shifted from those associated with the periodicity of the nuclear structure by a vector. This vector is the propagation vector $\vec{k}$. For commensurate magnetic structures, $\vec{k}$ relates the magnetic and nuclear unit real space cells. For instance, consider cerium rhodium silicide $CeRh_2Si_2$. The lattice parameters of the unit cell of the nuclear structure are a = b = 4.075 Å and c = 10.13 Å, depicted as the small parallelepiped in Figure 6.7. The larger parallelepiped in Figure 6.7 corresponds to the magnetic unit cell; with lattice parameters are a = b = 8.15 Å and c = 10.13 Å. Therefore the size of the magnetic unit cell is the twice of the nuclear unit cell along the [1 0 0] and [0 1 0] directions.

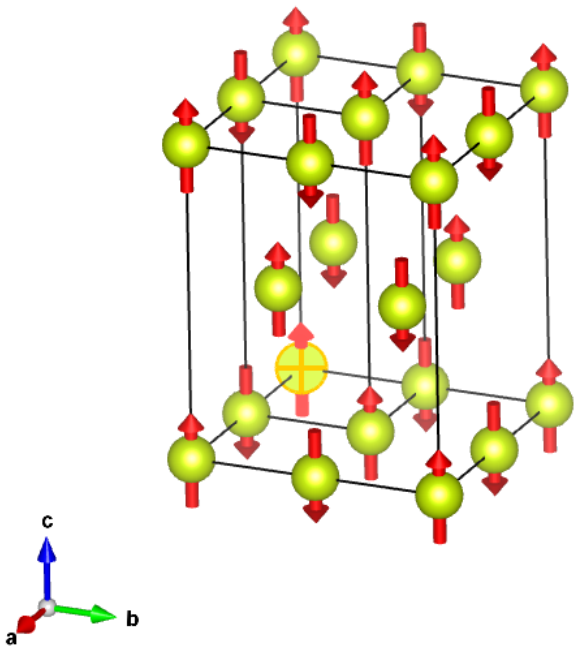

Figure 6.7: The nuclear and magnetic unit cells of $CeRh_2Si_2$. Cerium atoms and their magnetic moments are represented by the light green spheres and the red arrows, respectively. The small and big cells are the nuclear and magnetic unit cells of $CeRhSi_2$, respectively.

The lattice parameters of the magnetic unit with respect to the those of the nuclear structure

can be deduced from the propagation vector and equation (15). In the case of $CeRh_2Si_2$, the magnetic structure is associated with the propagation vector $\vec{k} = (\frac{1}{2}, \frac{1}{2}, 0)$. The three component of $\vec{k}$ are related to the crystallographic $a-$, $b-$ and $c-$axes, respectively. The number 2 in the first and second components of the propagation vector indicates that the lattice parameters along these directions are twice those of the nuclear structure. As $\vec{k}.\vec{z} = 0$ the magnetic moments are unchanged in the [0 0 1] direction. The magnetic structure of MnF_2 in Figure 6.8 illustrates this feature of the propagation vector $\vec{k}$. Manganese atoms and their magnetic moments are represented by the magenta spheres and the red arrows, respectively. The magnetic moments are along the c-direction. The unit cell of the magnetic structure is one of the 8 smalls parallelepipeds in Figure 6.8. The moments order ferromagnetically along the three crystallographic axes. Hence, the propagation vector for this compound is $\vec{k} = (0, 0, 0)$.

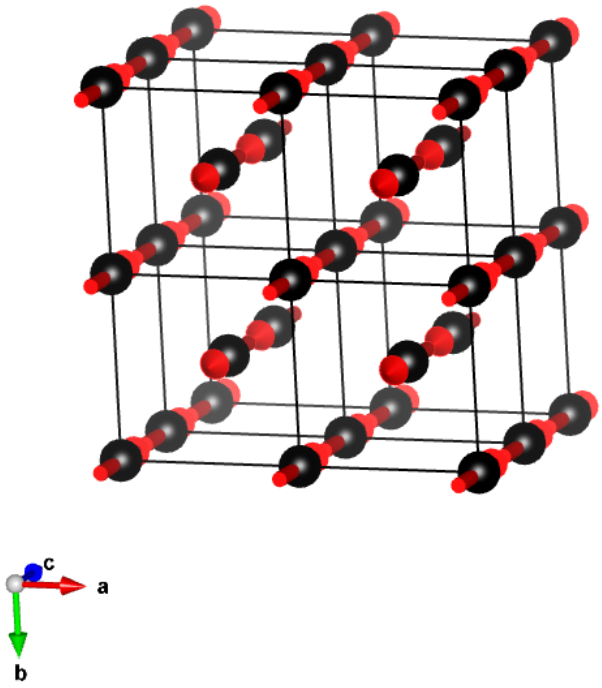

Figure 6.8: Supercell representing the magnetic structure of MnF_2. Manganese atoms and their magnetic moments are represented by the magenta spheres and the red arrows, respectively. The propagation vector associated with this magnetic structure is $\vec{k} = (0, 0, 0)$.

For some magnetic structures more than one propagation vector are needed to account for the periodicity of the magnetic phase, equation (6.17) becomes:

$$\vec{m}_j = \sum_{\vec{k}} \vec{\Psi}_j^{\vec{k}} e^{-2\pi i \vec{k}.\vec{t}} \tag{6.18}$$

The summation in equation (6.18) is over all possible $\vec{k}$ vectors relating equivalent magnetic atoms in different unit cells. For the sake of simplicity we will only consider cases here where a single propagation vector $\vec{k}$ is sufficient to describe the magnetic structure. One can rewrite equation (6.18) in terms of sine and cosine function. The simple condition which needs to be fulfilled for $\vec{m}_j$

to be real is the following: $\vec{\Psi}_j$ is real and the sine part is equal to zero. Hence, equation (6.18) can be written as

$$\vec{m}_j = \vec{\Psi}_j \cos(2\pi \vec{k}.\vec{t}). \tag{6.19}$$

As one travels between equivalent ions, the magnitude of $\vec{m}_j$ varies like a cosine function. This is why magnetic structures are also called modulated structures. The propagation vector $\vec{k}$ controls the modulation and so is also called the modulation vector. Note that in the case of ferromagnetic materials the magnetic cell is identical to that of the nuclear cell: $\vec{k} = (0, 0, 0)$.

To find the symmetries of the magnetic phase one must determine how the propagation vector $\vec{k}$ transforms under the symmetry operations of the space group of the material. All the symmetry elements which leave the propagation vector unchanged up to a reciprocal lattice vector form a group. The latter is known as the little group $G_{\vec{k}}$. The concept of little group will be illustrated with point group 4mm.

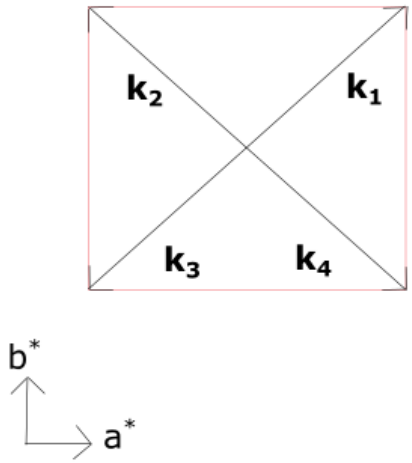

Figure 6.9: Propagation vectors $\vec{k_1}$ and the star of $\vec{k_1}$.

The space group of the square consists of 8 symmetry elements. The application of symmetry operations on the propagation vector $\vec{k_1}$ generates new positions $\vec{k'}$. The little group of $\vec{k_1}$ lying at the boundary is given by:

$$G_k = \{1, m_d\}. \tag{6.20}$$

The set of $\vec{k}$ vectors in Figure 6.9 form the star of the propagation vector $\vec{k_1}$: the number of distinct positions which result from the application of all symmetry elements. In practice in order to extract $\vec{k}$ from neutron diffraction patterns, one follows the process described below:

- One first determines the magnetic reflections, by subtracting a neutron diffractogram measured below the ordering temperature T_N from one measured above. The ordering of the moments

is revealed by the presence of extra reflections in the neutron diffraction patterns (NDPs) measured below T_N.

- From the magnetic reflections one can work out the *d*-spacing associated with each plane.
- The crystal system (orthorhombic, cubic, etc) of the magnetic structure is identified by combining the *d*-spacing values.
- The components of the propagation or modulation vector $\vec{k}$ are given by the ratio between the amplitudes of the basis vectors of the nuclear and magnetic lattices.

Identifying the propagation vector from a powder neutron diffraction pattern involves rather complex numerical calculations. Therefore it is convenient to use software such as *GSAS*, *Jana*, *Fullprof* and *Sarah* to determine the propagation vector(s). For more details on this topic the reader should consult outstanding reports of Wills[208] and Ressouche[209]. The programs *Fullprof* and *Jana* were utilised throughout this research.

6.3.4 Magnetic representation

The determination of the little group $G_{\vec{k}}$ is followed by the derivation of its character table, as see Table 6.5 for the point group mm2. The IRs of the little group $G_{\vec{k}}$ are not "ordinary" irreducible representations. Indeed the functions which generate the IRS, not only describe the symmetry relations between atomic positions but also those between magnetic moments. The IRs of the little group $G_{\vec{k}}$ are also called magnetic representations. Details on a magnetic representation are discussed further below. The action of the functions associated with some IRs of the little group $G_{\vec{k}}$ do not preserve the periodicity of the magnetic structure. Such IRs are magnetically inactive. The other IRs are magnetically active. The functions of these IRs insure a matching between the periodicity of the magnetic and nuclear lattice; in addition they preserve the modulation of the magnetic moments within the magnetic lattice. Hence, the magnetically active IRs and their combinations are potential models for the magnetic structure of the crystal.

As a symmetry element operates on a magnetic ion, it may or may not change the ion's position. It may also alter the orientation of the magnetic moment. The combinations of these two effects are described by a magnetic representation Γ_{mag}.

To account for the spatial transformation due to the application of a symmetry operation on a magnetic ion, the permutation representation Γ_{perm} is introduced. Γ_{perm} is given by:

$$\vec{r_j} \xrightarrow[\Gamma_{perm}]{} \vec{r'_j} \tag{6.21}$$

A phase factor $\theta = e^{2\pi i \vec{k}.\vec{t}}$ is often added to account for a symmetry operation leaving the initial ion at a new position $\vec{r'_j}$ outside the zeroth crystal cell.

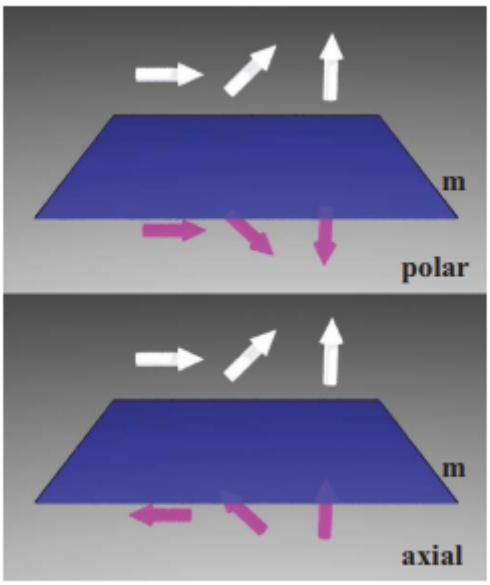

Figure 6.10: Representation of the action of a mirror plane (blue rectangle) on a polar vector (top white arrows) and an axial vector (bottom white arrows).

The axial representation $\Gamma_{\tilde{V}}$ accounts for the change in orientation of a magnetic moment. A magnetic moment is represented by an axial vector. An axial vector is a vector which has an equal magnitude but an opposite direction, to its mirror image. Opposite to a axial vector is a polar vector, whose image after reflection matches its mirror image[202]. For the sake of simplicity the expression vector will be used instead of axial vector. More details on Γ_{perm} and $\Gamma_{\tilde{V}}$ can be found in [8,49]. Figure 6.10 illustrates the difference between a polar vector and an axial vector.

The application of a symmetry operation on a magnetic atom may transform its magnetic moment components (m_x, m_y, m_z) into new components ($m_x^{'}$, $m_y^{'}$, $m_z^{'}$) . The character of the axial representation $\Gamma_{\tilde{V}}$, associated with this symmetry element is given by

$$\chi_{\tilde{V}}^{h} = \sum_{a=b} R_{a=b}^{h} det(h), \tag{6.22}$$

where $R_{a=b}^{h}$ corresponds to a specific element a, b of the rotation matrix h, and $det\,(h)$ represents the determinant of the rotation matrix R^h,and has the value of +1 for a proper and -1 for an improper rotation. To illustrate these two representations, consider the effects of the 4-fold rotation axis passing by the centre of square (4^+) on some magnetic moments located at the edges of the square. In Figure 6.11, the 4-fold rotation axis passes by the red dot. The numbers 1 to 4 and the arrows represent atoms and the magnetic moment they carry, respectively. The rotation transforms atom 1 to atom 2, atom 2 to atom 3, etc. This effect is described by Γ_{perm} (4^+.)

One uses equation (6.22) to determine the character of $\Gamma_{\tilde{V}}$ associated with the 4^+ symmetry operation . The matrix representing the 4-fold rotation axis is given by

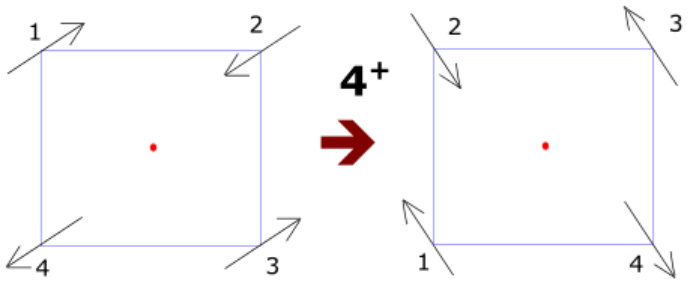

Figure 6.11: Effects of the symmetry operation 4^+ on the atoms of a square and on their respective magnetic moments. The atoms all leave their positions and their respective magnetic moments change orientation.

$$\hat{4^+} = \begin{bmatrix} 0 & -1 & 0 \\ 1 & 0 & 0 \\ 0 & 0 & 1 \end{bmatrix}. \tag{6.23}$$

Its determinant $det\ (\hat{4^+}) = 1$. $\chi_{\tilde{V}}^{4^+}$ is therefore given by the product of the determinant and the trace of the rotation matrix:

$$\chi_{\tilde{V}}^{4^+} = det(4^+)(\mathrm{Tr}[\hat{4^+}]). \tag{6.24}$$

Thus, $\chi_{\tilde{V}}^{4^+} = 1$: the sum of the diagonal components of matrix representing the axial representation $\Gamma_{\tilde{V}}$, associated with the 4-fold rotation axis. This said, equation (6.22) shows that the application of the axial representation on the magnetic moments is similar to that of the permutation representation on the magnetic moments. The *det (h)* accounts for the axial character of the magnetic moments, as it will be equal to -1 for an improper rotation.

It can be shown that a magnetic representation Γ_{mag}, at a particular crystallographic site, is the direct product of the permutation representation and the axial representation [199]:

$$\Gamma_{mag} = \Gamma_{perm} \otimes \Gamma_{\tilde{V}}. \tag{6.25}$$

A magnetic representation can be manipulated using the tools representation theory introduced in section A of appendices. For instance, a decomposed into representations of lower dimensions, as illustrated by the following equation:

$$\Gamma_{mag} = \sum_{\nu} n_\nu \Gamma_\nu \tag{6.26}$$

where the Γ_ν are the IRs of the little group. Γ_{mag} is a l-dimensional matrix, which acts upon l dimensional vector. This components of this vector are the magnetic moment components of the atoms in the zeroth crystallographic cell. One can calculate the number of possible basis vectors

associated with a single IR Γ_ν. These vectors form the basis for the magnetic moments ordered according to a the particular IR Γ_ν of $G_{\vec{k}}$. Therefore the magnetic moments can be expressed as some linear combination of these basis vectors. Rodríguez-Carvajal and Bourée[210] wrote an outstanding article on the derivation of the basis vectors of an IR of the little group $G_{\vec{k}}$. These calculations are not straightforward, therefore it is convenient to utilize programs such as *BasIreps* or ISODISTORT.

In most cases a single magnetic IR can uniquely describe the magnetic structure. This is due to the Landau theorem on second order phase transition[122] which states that a second order transition occurs when a new state of reduced symmetry develops continuously from the disordered phase. The transition must occur homogeneously at critical points where structural change is infinitesimal but only the crystal symmetry varies. John O. Dimmock[211] applied the Landau-Lifshitz theory of second order phase transitions on magnetic structures. Dimmock demonstrated that near the critical temperature as magnetic systems undergo the passage from the paramagnetic phase to magnetically ordered phase the spin density can be described by the basis vectors of a single irreducible representation of the symmetry group of the paramagnetic phase. For an exhaustive mathematical derivation of the Landau theorem and its impact on magnetic structure the reader can consult the seminal work of Cracknell[123] and Dimmock[211].

To summarize, basis tools of representation analysis method and group theory were introduced, along with the concepts of the propagation vector, little group and representations. Magnetic structures combine crystal lattices with atomic magnetic moments. The representation analysis method describes a magnetic structure by relating the periodicity of the nuclear structure with a propagation vector $\vec{k}$. Additonally, a magnetic representation Γ_{mag} acts in the same manner as a "normal" representation. The only difference is that a magnetic representation acts on ensembles of atoms carrying magnetic moments. Γ_{mag} is the direct product of a permutation representation (Γ_{perm}) and an axial representation ($\Gamma_{\vec{V}}$). The little group is the cornerstone of the representation analysis method as its IRs will constitute the models for the magnetic structure. Most of the time, the description of a magnetic structure relies on a single magnetic IR of the little group .

6.4 Magnetic symmetry refinement

This section discusses the magnetic symmetry refinement method for the determination of magnetic structures from neutron diffraction patterns. A review to the history of magnetic space groups is followed by an introduction to the concept of anti-symmetry operations; the derivation and application of magnetic point groups for magnetic structure determination concludes the section.

6.4.1 History of magnetic space groups

Until the Shubnikov's paper in 1954 crystal structures were described by one of the 230 space groups[212]. In this paper Shubnikov introduced the idea of anti-symmetry operations which describe objects whose ensemble of coordinates consists of ordinary position coordinates and an additional coordinate. This extra coordinate takes two values, for example colour (black and white), sign (+ or -) or direction of magnetic moment with respect to an applied field (parallel or anti-parallel). Shubnikov introduced a new symmetry element which inverts the value of the extra coordinate: + to - for example. The new anti-symmetry operations then result from the product of the anti-symmetry operator $\mathcal{R}$ and the ordinary symmetry element. If we let the extra coordinates be the magnetic moments, then described objects are the magnetic structures. In this manner Shubnikov derived a series of magnetic point groups, followed subsequently by the work of Zamorzaev[213]. The field of magnetic space groups was further developed in work by Belov, Nerenova and Smirnova[214], then Tavger and Zaitsev[215].

6.4.2 Definitions

An anti-symmetry operation: When the anti-symmetry element $\mathcal{R}$ is combined with a regular symmetry element, g, one denotes the new symmetry element by a primed symbol, $g^{'}$.

Typically, an anti-symmetry operation is the product of a regular symmetry operator with the time reversal operator:

$$g^{'} = \mathcal{R}g = g\mathcal{R}. \tag{6.27}$$

A grey group: A point group in which the element $\mathcal{R}$ appears by itself is known as a grey point group $\mathbf{M}$, given by:

$$\mathbf{M} = \mathbf{G} + \mathcal{R}\mathbf{G}, \tag{6.28}$$

where $\mathbf{G}$ is any ordinary point group. The anti-symmetry and the identity elements are tied by the following relation:

$$\mathcal{R}^2 = e. \tag{6.29}$$

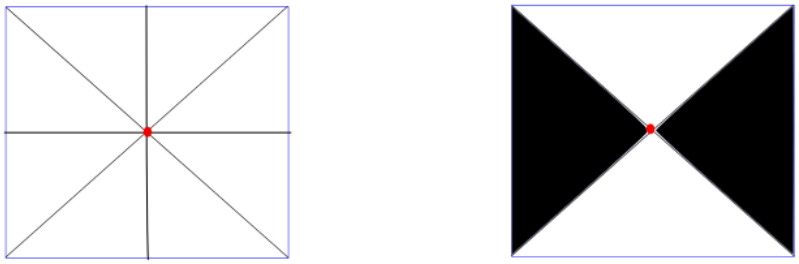

Figure 6.12: Symmetry operations of a square (left). A black and white square (right).

A grey point group is also known as a Shubnikov point group of type II. Note than the order of a grey group is the double of the that of the original point group.

A black or white point group: Point groups, in which the anti-symmetry operator is not an element, but have anti-symmetry operations are called magnetic point group (or black/white point groups).

A black or white point group is given by:

$$\mathbf{M} = \mathbf{H} + \mathcal{R}(\mathbf{G} - \mathbf{H}), \tag{6.30}$$

where $\mathbf{H}$ is a halving of the ordinary point group $\mathbf{G}$. A halving designates half of the elements of $\mathbf{G}$ which are not then multiplied by $\mathcal{R}$. Since one can choose different halvings of a point group, various magnetic space groups can be derived from a single non-magnetic group. A black (or white) group is also known as a Shubnikov point group of type III.

6.4.3 Derivation of a type III point group

The point group of a square will now be used to illustrate the concept of magnetic space groups. The 8 symmetry elements of the square (Figure 5.11 (left)) are illustrated in Figure 6.12. The square on the right in Figure 5.11 consists of black and white units, which colour the vertices.

The point group of the square on the left is $\mathbf{G} = 4\text{mm}$. One has:

$$\mathbf{G} = \{1, 2, 4^+, 4^-, m_x, m_y, m_d, m_d^{'}\}. \tag{6.31}$$

The identity operation (*1*)leaves the vertices unchanged. The 4-fold and a 2-fold rotations respectively rotate the vertices about the centre (red dot) by 90 and 180 °.The four reflection operations perpendicular to *x*- and *y*-axes (m_x and m_y) or accross the two diagonal (m_d and $m_d^{'}$) the vertices

through the mirror planes.

Half of the square in Figure 6.12 is coloured white, while the other half is black. This description of the square requires an additional "colour " coordinate. Hence, each vertex associated with this square is described by either grey or magnetic group. These may be generated by combining the symmetry elements of **G** with the anti-symmetry operator $\mathcal{R}$. The grey group resulting from this combination is:

$$G_1 = \{1, 2, 4^+, 4^-, m_x, m_y, m_d, m_d^{'}, \mathcal{R}, \mathcal{R}2, \mathcal{R}4^+, \mathcal{R}4^-, \mathcal{R}m_x, \mathcal{R}m_y, \mathcal{R}m_d, \mathcal{R}m_d^{'}\}. \tag{6.32}$$

The order of this group is 16: twice that of **G**.

The coloured square is not invariant under the 4-fold rotations 4^+ and 4^- or the reflections mirrors m_d and $m_d^{'}$. Indeed the the black block takes the place of the white block, and vice-versa. Therefore the symmetry elements 4^+, 4^-, m_d and $m_d^{'}$ are no longer symmetry operations. However, the antisymmetric operations $\mathcal{R}4^+$, $\mathcal{R}4^-$,-$\mathcal{R}4^+$ and -$\mathcal{R}4^-$ are good symmetry elements of the colour square. Consequently, the point group G_2 of the coloured square consists of four symmetry elements from **G**, and the above four antisymmetric elements. Thus, G_2 fulfills equation (6.31), as half of the original group elements are included and unmodified, and the half have been combined with $\mathcal{R}$. In other words, the two halves of the group contain uncoloured and coloured symmetry operations. Therefore G_2 is given by:

$$G_2 = \{1, 2, m_d, m_d^{'}, \mathcal{R}4^+, \mathcal{R}4^-, \mathcal{R}m_x, \mathcal{R}m_y\}. \tag{6.33}$$

In the magnetic point groups tabulated by Tavger and Zaitsev[215] this group is denoted as $4^{'}mm^{'}$. The primes indicate the regular point group symmetry elements which are combined with $\mathcal{R}$. One can derive groups similarly to $4^{'}mm^{'}$ to describe any three-dimensional object supplemented with an extra coordinate, such as sign, colour, etc. The 3 spatial and 1 supplementary dimensions lead to 1651 Shubnikov space groups. More details on Shubnikov's work are found in Bradley and Cracknell[205], Miller[216] or various review articles[217,218,219].

6.4.4 Determination of magnetic structure from neutron diffraction

Shubnikov or magnetic space groups are important for the determination of magnetic structures from neutron diffraction pattern, discussed below.

The neutron diffraction pattern (NDP) of a material measured below its Néel temperature (T_N) differs from a NDP measured well above T_N , respectively, by the presence of additional peaks. The extra reflections are due to the ordering of the magnetic moments of the magnetic ions. The Landau

theorem on second order phase transition[122] states that a second order transitions occurs when a new state of reduced symmetry develops continuously from the disordered phase. The transition must occur homogeneously at critical points where but any structural change is infinitesimal but only the crystal symmetry varies. Consequently, the magnetic space group symmetry of such materials is one of the Shubnikov groups derived from the space group of the crystal. These grey, black or white groups are the models for the unknown sublattice magnetization. The magnetic symmetry refinement method is as follows:

- Derivation of the Shubnikov groups related to the studied crystal. The mathematical derivation of the grey, black and white space groups is implemented in programs such as *Jana*. In addition, one can derive the Shubnikov space groups with the Bilbao Crystallographic Server and import them into *Jana*.

- Evaluation of all structural models. One refines the orientations of magnetic moments and positions of the magnetic ions within the lattice of a specific Shubnikov space group, against the neutron diffraction pattern.

- Comparison between the different structural models. One can visualize the sublattice magnetization - associated with a model - with the program VESTA.

The best structural model has the magnetic space group which best fits the measured neutron diffraction pattern - lowest refinement factors.

6.5 The magnetic structure of $NiTa_2O_6$

6.5.1 Discrepancies on the previous magnetic models

Neutrons powder diffraction have been performed on 3 g of the single phase $NiTa_2O_6$. Nickel ditantalate has been previously[81,102] reported to behave like an antiferromagnetic material, which order below $T_N = 10.3$ K. Two magnetic structures were reported for this trirutile compound and there is a discrepancy between the two models. This work aims to shine light on the origin of the differences between the reported sublattice magnetisations for this trirutile.

The first magnetic model (describing the positions, magnitudes and orientations of the magnetic moments of the Ni^{2+} ions within the lattice) was proposed by Ehrenberg *et al.*[102] in 1998. Ehrenberg and coworkers performed neutron diffraction on polycrystalline samples at the High Flux Beam Reactor (HFBR) of the Brookhaven National Laboratory, using the High Resolution Neutron Powder Diffractometer (H1A1) with a wavelength of 1.8857 Å. Their neutron diffraction pattern reveal the presence of a spurious phase within their samples. The additional peaks are reflections of the NiO phase. Nevertheless, the majority of magnetic reflections are indexed by a propagation vector $\vec{k} = (\frac{1}{4}, \frac{-1}{4}, \frac{1}{2})$ or others of its star. The supercell used to describe the magnetic unit cell has an orthorhombic-type crystal system. The lattice parameters of the unit cell are the following: a = 6.677 80 Å, b = 13.355 60 Å and c = 18.30 Å.

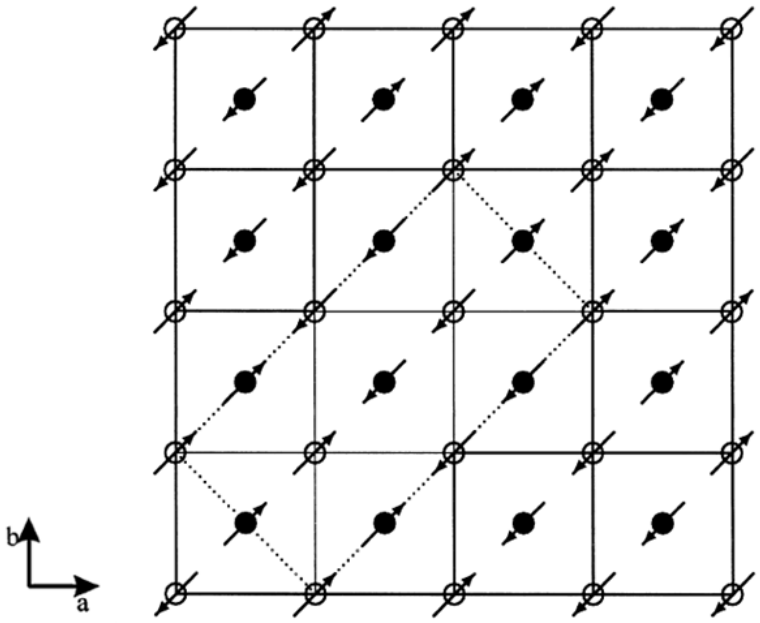

Figure 6.13: The magnetic structure $NiTa_2O_6$ according to Ehrenberg[102].

In Figure 6.13 above, the square represents the unit cell of the nuclear structure. The dotted line outlines the unit cell of the magnetic structure. The open and filled spheres represent the Ni^{2+} ions, which are at z = 0 and z = $\frac{1}{2}$, respectively. The magnetic moments are illustrated by the arrows.

There is a doubling of the nuclear cell along the *c*-axis. There are two magnetically non-equivalent Ni-sites within the lattice. Those at Ni_1 at (0, 0, 0) and Ni_2 at ($\frac{1}{2}$, $\frac{1}{2}$, $\frac{1}{2}$). Within the magnetic lattice the magnetic moments of all Ni^{2+} ions lie in the *ab*-plane and they are collinearly aligned parallel to [1 1 0] and [1 $\bar{1}$ 0]. These magnetic moments form an arrangement of ferromagnetic and antiferromagnetic chains which are perpendicular to each other. There is -up-up-down-down- sequence along the crystallographic axes *a* and *b*. Finally, Ehrenberg and co-workers refined a value of 1.6(1) μ_B per Ni^{2+} ion for the magnetic moments. This value deviates from the theoretical value which is equal to g_o. $m_s = 2\,\mu_B$ per Ni^{2+} ion. g_o is the Landé factor[66]. This discrepancy suggests that the magnetic moments in the samples of Ehrenberg are not completely ordered.

A second model of the magnetic structure of $NiTa_2O_6$ was reported recently, 2014, by Law *et al.*[220]. Law and coworkers investigated the magnetic properties of the nickel ditantalate by means of magnetic susceptibility, specific heat, electron paramagnetic resonance, neutron powder diffraction, and pulse field magnetisation measurements. Additionally, first principles calculations in Density Functional Theory (DFT) determined the spin-exchange constants which describe the magnetic exchange interactions J_i between magnetic ions. According to Law *et al.*[220] $NiTa_2O_6$ has the traits of low-dimensional magnets: it behaves as a quasi-1D system. The chains of Ni^{2+} are well described by a Heisenberg hamiltonian S = 1 with only a nearest-neighbour spin-exchange interaction J of 18.92(2) K. Furthermore, the magnetic susceptibility data and the λ-type anomaly in the specific heat data both indicated long-range antiferromagnetic ordering of Ni^{2+} ions below 10.3(1) K. This Néel temperature is in perfect agreement with that reported by Ehrenberg *et al.*[102]. Like in Ehrenberg's model the magnetic reflections were indexed by propagation vector $\vec{k}$ = ($\frac{1}{4}$, $\frac{-1}{4}$, $\frac{1}{2}$). From neutron powder diffraction pattern Law refined a magnetic moment of 1.93(5) μ_B per Ni^{2+} ion. This value is in good agreement with the expected value for S = 1 systems and it indicates that the magnetic moments of the Ni^{2+} ions within the Law's powders sample are well ordered. There is clear discrepancy between the magnetic moment value refined by Ehrenberg and Law and it is the first difference between the two models. The arrangement of magnetic moments of Ni^{2+} sublattice magnetisation is another difference between the model reported by Law and that of Ehrenberg.

In Figure 6.13 the solid square represents the nuclear unit cell and the dashed box the magnetic unit cell. The grey spheres and the arrows represent the Ni atoms and their respective magnetic moments, respectively. Like in the Ehrenberg model the latter lie in the *ab*-plane, and are collinearly aligned parallel to one of the [±1 ±1, 0] directions. The lattice parameters of their magnetic unit cell - according to the Law model - are the following: a = 18.867 20 Å, c = 18.247 60 Å, indicating that there is a quadrupling and doubling of the nuclear cell along the *a*- and *c*-axes, respectively. The crystal system of the magnetic structure of $NiTa_2O_6$, according to the Law model is monoclinic. This is different to that of the Ehrenberg model where the crystal system was orthorhombic. As a consequence the non-equivalent magnetic Ni^{2+} ions occupy the following Wyckoff sites: Ni_1 at (0, 0, 0) and Ni_2 at ($\frac{1}{8}$, $\frac{1}{8}$, $\frac{1}{4}$). Eventually Law and co-workers refined a value of 1.93(5) μ_B per Ni^{2+} ion for the magnetic moments. This is in agreement with the theoretical value of 2 μ_B per Ni^{2+} ion.

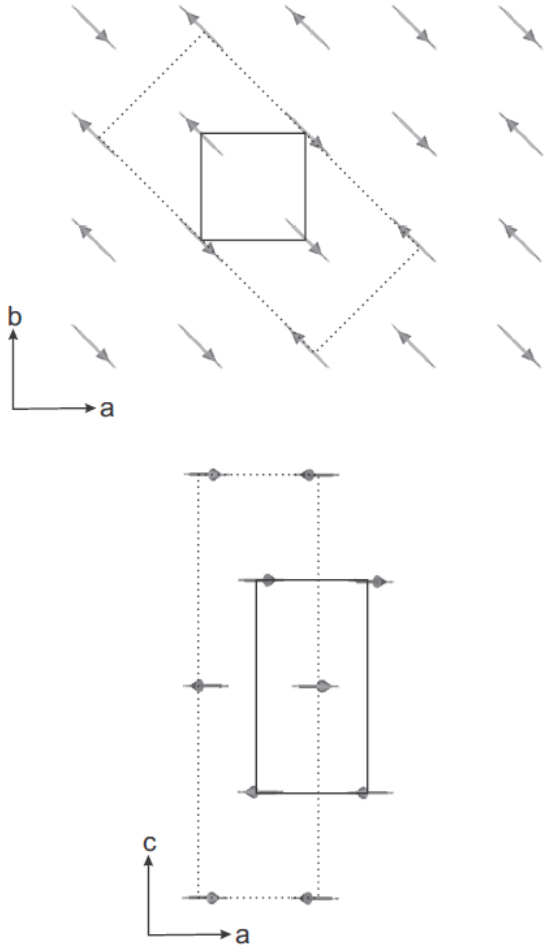

Figure 6.14: The magnetic structure $NiTa_2O_6$ according to Law[220].

It indicates that the magnetic moments in the samples of Law are well ordered.

There are apparent discrepancies between the magnetic structures of $NiTa_2O_6$ reported by Ehrenberg and Law. The crystal system within which the spins ordered themselves are orthorhombic and monoclinic, according to Ehrenberg[102] and Law[220], respectively. Additionally, in the sublattice magnetisations reported by Ehrenebrg and Law the moments are collinearly aligned along the [1 1 0] and [-1, 1 0] directions, respectively. The value of the effective magnetic moment μ_{eff} of Ni^{2+} (1.63(1) and 1.93(5) μ_B) also differ. These differences between the magnetic models proposed for the magnetic structure of $NiTa_2O_6$ motivated the investigations carried on this trirutile material throughout the thesis. First, the Ehrenberg and Law models are assessed, by fitting the magnetic reflections of the measured neutron powder data. A new magnetic model (which best fits the data) is then be introduced. A discussion about the relationship between these magnetic models concludes the chapter.

The magnetic structure of the nickel ditantalate is revisited via neutron diffraction on the $NiTa_2O_6$ polycrystalline samples. Long-range ordering of the magnetic moments of Ni^{2+} is investigated by means of powder neutron diffraction because neutrons wavelengths are comparable to that of the interatomic distance within $NiTa_2O_6$: few angstroms. More importantly thermal neutrons possess a spin $\frac{1}{2}$ which can interact with the magnetic moments of Ni^{2+} cations. Neutron powder diffraction on the prepared sample has been performed at Laboratoire Léon Brillouin (LLB), Saclay (France), using the two-axes G4.1 diffractometer. This system was chosen as it is equipped with a cryostat which enables the determination of the Néel temperature T_N of $NiTa_2O_6$. In addition to that, its resolution at low angle is optimal to investigate the magnetic reflections, as discussed in Chapter 2. The measured diffractograms are depicted in Figure 6.15 on page 162.

The heat map in Figure 6.15 illustrates the NDPs of $NiTa_2O_6$ from 1.5 to 100 K. The axis on the left indicates the temperature at which the NDP was recorded. The intensity an angle of the reflections are on the left and bottom axes, respectively. The vertical lines are Bragg reflections and they are two types of vertical lines (or peaks). They are the intense and weak vertical lines. The intense vertical lines correspond to Bragg peaks which appear on all NDP patterns, for all temperatures, these peaks are the nuclear reflections. On the other hand, the weak vertical lines vanish at about 9.8 K. These vertical lines are the magnetic reflections. Observed on low-temperature NDPs, these reflections are associated with the ordering of the magnetic ions (Ni^{2+}). The most intense magnetic peaks correspond to the following 2θ values: 12.9 °, 25.4 ° and 24.7 °. Figure 6.14 indicates that the Néel temperature of $NiTa_2O_6$ is 9.8 K. This value is very similar to the value reported by both Ehrenberg[102] and Law[220]: 10.3 K.This shift between the current an former T_N may be due to the difference in sintering temperatures.

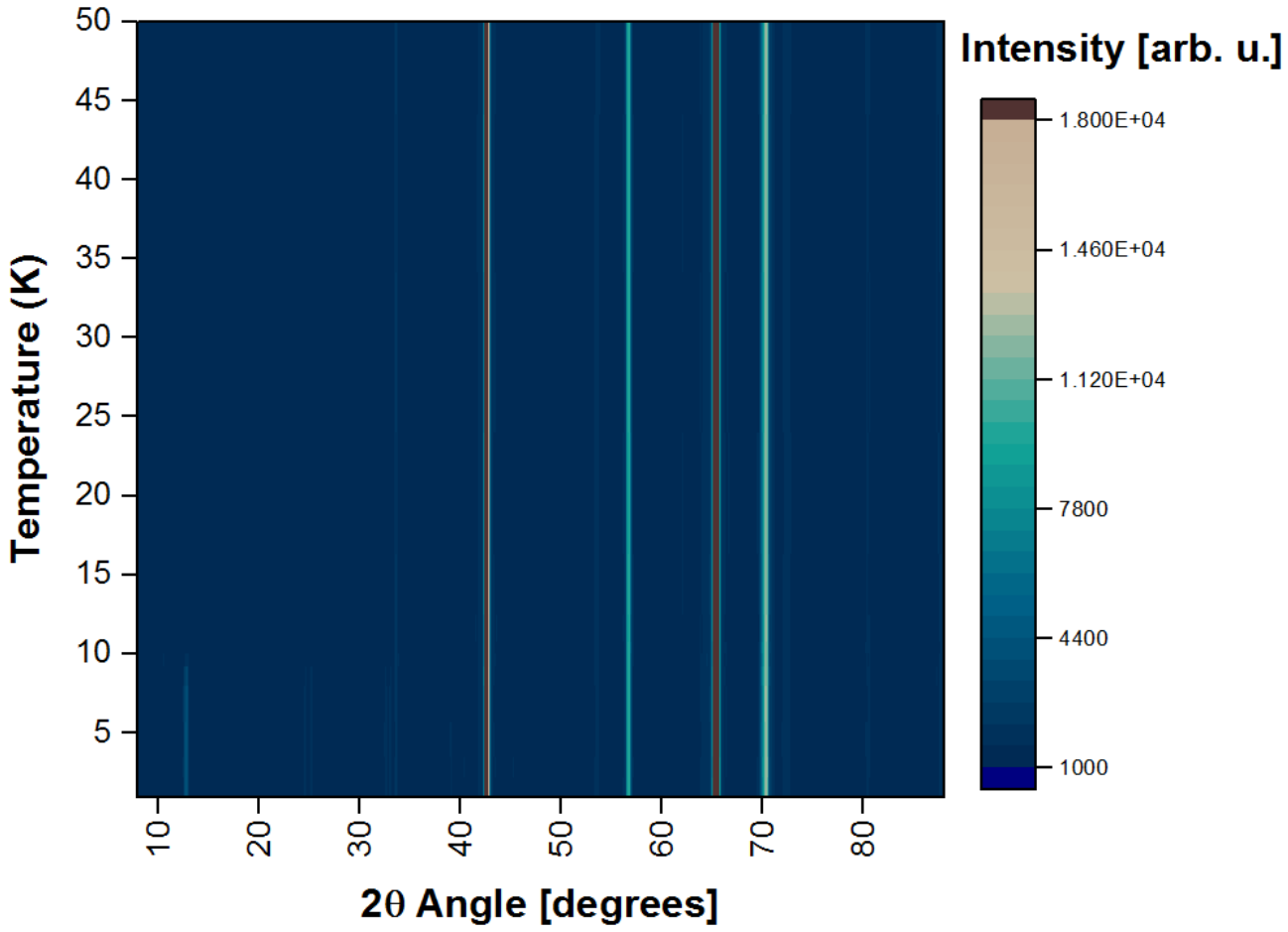

Figure 6.15: Neutron powder diffraction patterns of $NiTa_2O_6$ recorded on the two-axes G4.1 diffractometer in Saclay (France).

6.5.2 Revisiting the magnetic models of Ehrenberg and Law

In the first part of this section the Ehrenberg's[102] model is used as model to fit the magnetic reflections before the Law's[220] model is then accessed. For this purpose Rietveld refinement was performed on the neutron diffraction pattern recorded at 1.5 K. In both models the magnetic reflections are indexed by the modulation vector $\vec{k} = (\frac{1}{4}, \frac{-1}{4}, \frac{1}{2})$.

The space group of the paramagnetic phase - or nuclear phase - is $P4_2/mnm$. This group contains 16 symmetry elements:

$$G = \{1, 4^+, 4^-, 2_z, 2_y, 2_x, 2_{xy}, 2_{-xy}, \bar{1}, m_{xy}, m_{-xy}, n, n, m_x, m_y, m_z\}. \tag{6.34}$$

There are four symmetry operations which keep the propagation vector unchanged. They form the little group $G_{\vec{k}}$. These symmetry elements are the following: the identity (*1*), a 2-fold axes (2_{-xy}), and the two mirrors (m). Hence, one has the following relation:

$$G_{\vec{k}} = \{1, 2_{-xy}, m_{xy}, m_{-xy}\}. \tag{6.35}$$

The program *BasIreps* was utilised for the calculations of the irreducible representations of $G_{\vec{k}}$. The are four irreducible representations for the little group $G_{\vec{k}}$ and they are presented in Table 6.6.

Table 6.6: Magnetic irreducible representations of the little group $G_{\vec{k}}$ associated with the modulation vector $\vec{k} = (\frac{1}{4}, -\frac{1}{4}, \frac{1}{2})$ and the space group number $P4_2/mnm$ (136).

IRREPS	**Symmetry elements**			
	1	**2 x,-x, 0**	**m x,y,0**	**m x, -x, z**
	$\{1\|\|0,0,0\}$	$\{2\|\|0,0,0\}$	$\{m\|\|0,0,0\}$	$\{m\|\|0,0,0\}$
Γ_1	1	-1	1	-1
Γ_2	1	-1	-1	1
Γ_3	1	1	1	1
Γ_4	1	1	-1	-1

This table is essentially the character table of the little group $G_{\vec{k}}$. Γ_1, Γ_2,Γ_3 and Γ_4 are the irreducible representations (IRs) of $G_{\vec{k}}$. The irreducible representations are also known as its primary representations. Note that Γ_3 corresponds to the unitary representation. For the $NiTa_2O_6$ only two irreducible representations of $G_{\vec{k}}$ are magnetically active, they are Γ_2 and Γ_4. Both these primary representation are *4*-dimensional representations. The magnetic model reported by Ehrenberg *et al.*[102] is a combination of Γ_2 and Γ_4. However, these irreducible representations of the little group $G_{\vec{k}}$ were utilised by Law and coworkers for their model. Consequently, the representation analysis method is not relevant to test the two models with the recorded data.

The magnetic symmetry refinement was thus utilised as the internal degrees of freedom of a

representation are fully expressed. Indeed two subspaces (subgroups) can be associated with the same IR if their respective basis vectors generate the same set of matrices *D(g)*. Γ_2 is *4*-dimensional representation. It is therefore possible to choose different sets of basis vectors within this vector space. The latter define subspaces of *4*-dimensional space and each subspace is associated with a subgroup. As one deals with $NiTa_2O_6$ these subgroups are subgroups of $P4_2/mnm$ (136). Furthermore, the Bilbao Crystallography Server enables the visualisation of the sublattice magnetisation associated with the different subgroups of a representation. The tool ISODISTORT in the Bilbao Crystallography server enables the combination of IRs. Hence, the subgroups of the combination between Γ_2 and Γ_4 were studied.

6.5.2.1 The Ehrenberg model

One can visualises the sublattice magnetisation of all the different subgroups of an IR in the Bilbao Crystallography Server. The superposition of the primary representations Γ_2 and Γ_4 gives rise to 25 subgroups. Among these 25 possible subgroup (or distortion modes), one finds the subgroup whose magnetic unit cell is identical to the one reported by Ehrenberg[102]: $A_b$ba2 (41.217). The crystallographic parameters of this magnetic space group were used as model for the Rietveld refinement of the 1.5 K-neutron diffraction pattern. The Rietveld refinement was performed with the program *Jana* and is illustrated in Figure 6.16 on the next page.

In Figure 6.16 the measured and calculated profiles are shown with red dots and black line, respectively. A difference curve (observed-calculated) is shown at the bottom by the blue line. The green tick marks indicate the Bragg peak positions associated with a orthorhombic lattice whose space group is $A_b$ba2 (41.217). For a perfect agreement between the experimental data and the model the blue line would be a straight line. One note the presence of numerous peaks within the blue line. This suggests some discrepancies between the Ehrenberg model and the (actual) magnetic structure of the powder data. This inconsistency is highlighted by the amplitude of the two first reflections, at 12.9 ° and 24.7 °. This is also the case of the peak observed for 2θ equal 33 °.

6.5.2.2 The Law model

The Bilbao Crystallography Server was utilised to determine the Shubnikov group (among the 25) whose symmetry elements were those of the Law[220]'s magnetic structure. This Shubnikov space group is P_b2_1/c (14.82). The procedure performed for the Ehrenberg model was reiterated for the Law model, i.e. the 1.5 K-neutron diffractogram were refined, using the crystallographic parameters of the magnetic unit cell of the subgroup P_b2_1/c (14.82); the Rietveld method, via the program *Jana*, was performed for this task. Figure 6.17 on page 166 exposes the result of this refinement.

In Figure 6.17 the measured and calculated profiles are displayed with red dots and black line, respectively. A difference curve (observed-calculated) is depicted at the bottom of the figure by the blue line. The green tick marks indicate the Bragg peak positions associated with a orthorhombic lattice whose space group is $A_b$ba2 (41.217). Similarly to the Ehrenberg's case, there are discrepancies

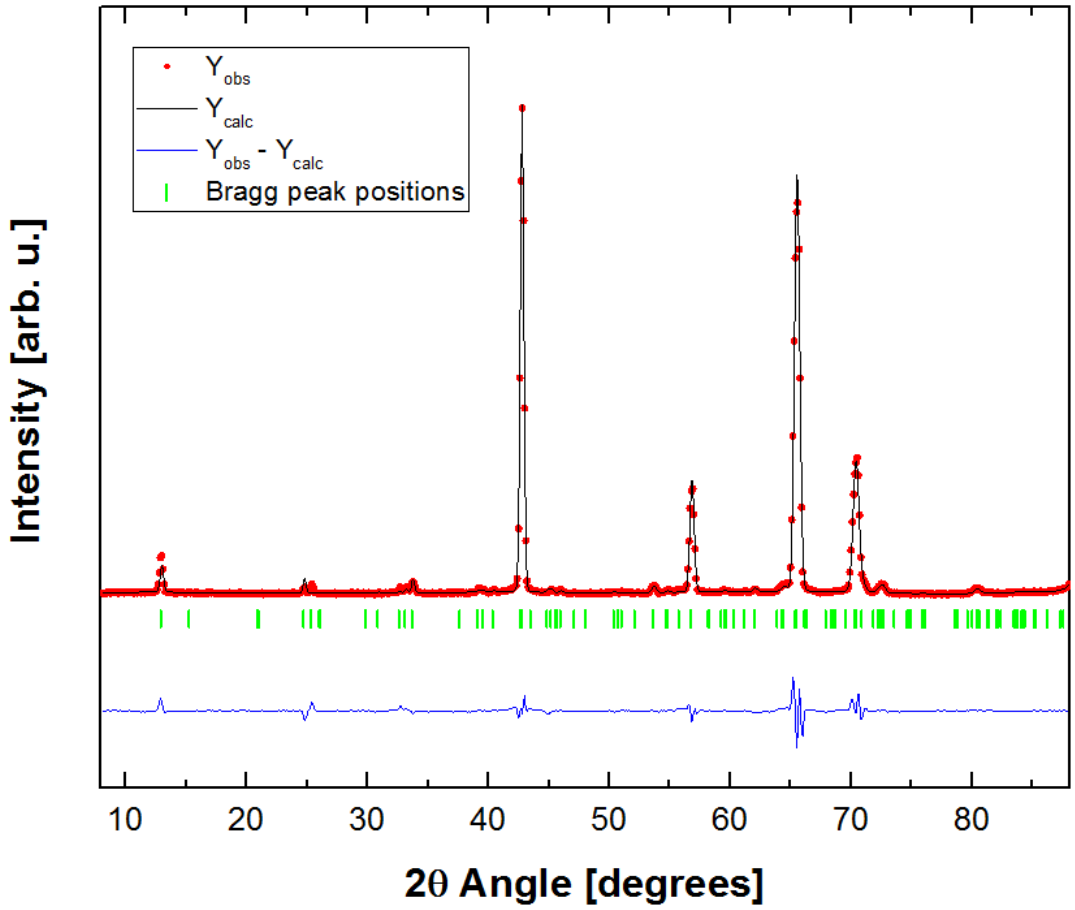

Figure 6.16: Rietveld refinement of the neutron powder diffraction pattern of $NiTa_2O_6$ according to the Ehrenberg model.

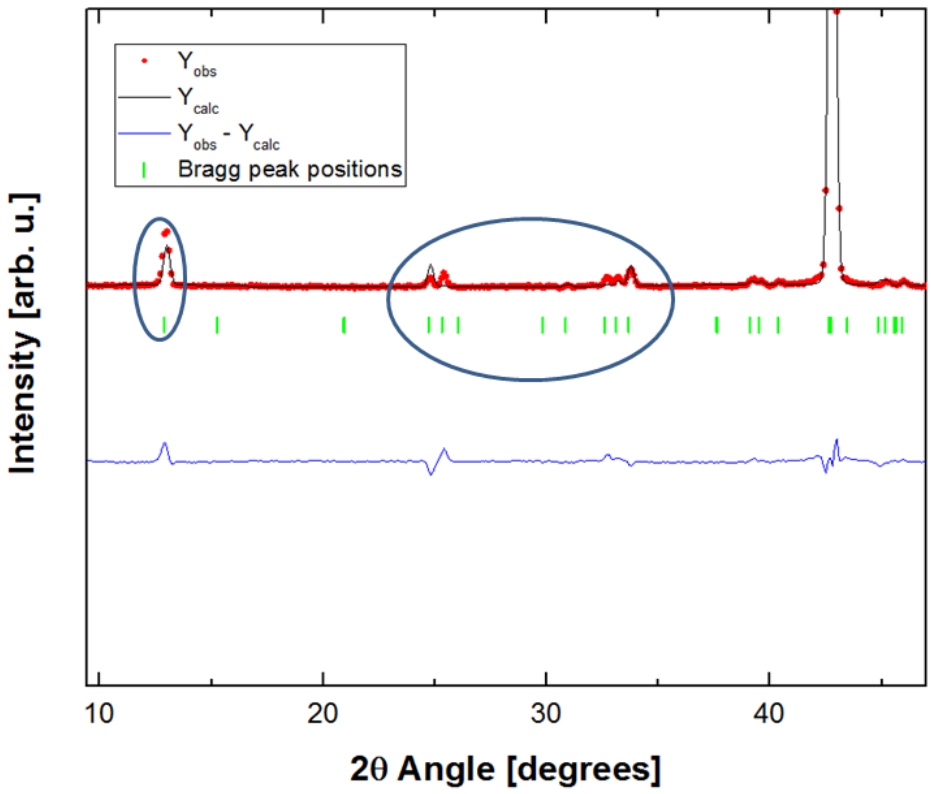

Figure 6.17: Rietveld refinement of the neutron powder diffraction pattern of $NiTa_2O_6$. The Law model was used to fit the experimental pattern.

between the measured pattern (red dots) and the calculated one (black line). These discrepancies between the observed and calculated profiles are similar to those observed for the refinement following the Ehrenberg's model. The discrepancies are highlighted by the blue circles.

It should be noted that the magnetic structure which is derived from Law's model[220] is clearly different to the structure proposed by Ehrenberg *et al.*[102]. The two sublattice magnetisation unit cells derived from the two models are compared in Figure 6.18 on page 167. In both models the blue spheres represent the the Ni^{2+} ions whereas the red arrows correspond to the magnetic moments. These supercells are the unit cell of the magnetic structures associated with Ehrenberg and Law models, respectively. Firstly, the crystal systems for both magnetic structures are different: orthorhombic (Ehrenberg) and monoclinic (Law). Secondly, although one notes the presence of antiferromagnetic chains on both magnetic structures, their sequence of magnetic moments differ. For the Law's model, Figure 6.17 (bottom), one notes an -up-up-down-down- sequence of magnetic moments along the [1 0 0] and [0 1 0] directions. This is not the case for the Ehrenberg model, Figure 6.18 (top) where there is an an -up-down-up-down- sequence within the antiferromagnetic chains. The sublattice magnetisation derived from the Ehrenberg model shows some ferromagnetic chains whereas there are no ferromagnetic chains within the magnetic structure derived from the Law's model. Eventually, the comparison of the two models with the is summed up in Table 6.7 and Table 6.8, for the Ehrenberg and Law models, respectively .

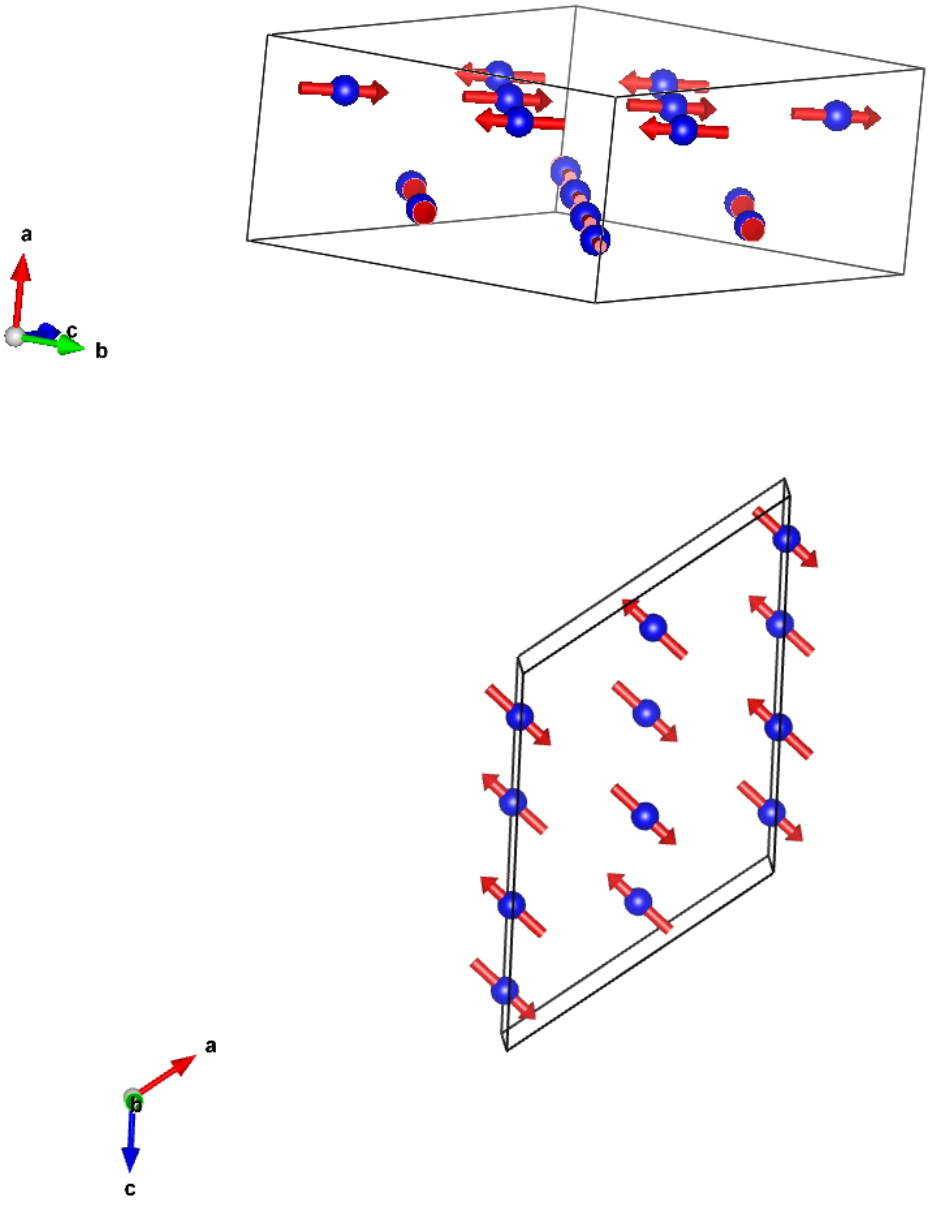

Figure 6.18: Magnetic structure of $NiTa_2O_6$ according to the Ehrenberg's (top) and Law's (bottom) model. The latter has a monoclinic type structure, whereas for the Ehrenberg model the moments are within an orthorhombic lattice.

Table 6.7: Comparison between magnetic structures: refined from Ehrenberg models and reported by Ehrenberg[102].

Date	**1998**	**2016**
Authors	Ehrenberg *et al.*[102]	Us
propagation vector	$\vec{k} = (\frac{1}{4}, \frac{-1}{4}, \frac{1}{2})$	$\vec{k} = (\frac{1}{4}, \frac{-1}{4}, \frac{1}{2})$
Magnetic space group	$A_b$ba2	$A_b$ba2
Lattice system	orthorhombic	orthorhombic
Magnetic moments direction	[1 1 0] and [1 -1 0]	[1 1 0] and [1 -1 0]
Ni1_1 Wyckoff positions	(0, 0, 0)	(0, 0, 0)
Ni2_1 Wyckoff positions	(0, $\frac{1}{4}$, $\frac{1}{4}$)	(0, $\frac{1}{4}$, $\frac{1}{4}$)
Magnetic moment μ_B/Ni^{2+}	1.6(1)	1.488(2)
Relation between ferro- and antiferromagnetic chains	perpendicular	perpendicular
R_B (%)	-	5.42
R_{mag} (%)	-	17.96

Table 6.8: Comparison between magnetic structures: refined from Law's models and reported by Law[220].

Date	**2014**	**2016**
Authors	Law *et al.*[220]	Us
propagation vector	$\vec{k} = (\frac{1}{4}, \frac{-1}{4}, \frac{1}{2})$	$\vec{k} = (\frac{1}{4}, \frac{-1}{4}, \frac{1}{2})$
Magnetic space group	P_c2_1/c	P_c2_1/c
Lattice system	monoclinic	monoclinic
Magnetic moments direction	[1 1 0] and [1 -1 0]	[1 1 0] and [1 -1 0]
Ni1_1 Wyckoff positions	(0, 0, 0)	(0, 0, 0)
Ni2_1 Wyckoff positions	($\frac{1}{8}$, $\frac{1}{8}$, $\frac{1}{4}$)	($\frac{1}{8}$, $\frac{1}{8}$, $\frac{1}{4}$)
Magnetic moment μ_B/Ni^{2+}	1.93(5)	1.473(2)
Relation between ferro- and antiferromagnetic chains	parallel	parallel
R_B (%)	-	5.11
R_{mag} (%) -		18.49

To summarise, the modulation vector for the magnetic structure of $NiTa_2O_6$ was determined from the magnetic reflections in neutron powder patterns below $T_N = 10.3\,K$. The propagation vector $\vec{k} = (\frac{1}{4}, \frac{-1}{4}, \frac{1}{2})$ is identical to that reported by Ehrenberg[220] and Law[220]. The Ehrenberg's and Law's models are both a superposition of the primary IRs Γ_2 and Γ_4. The Shubnikov space group A_b ba2 (41.217) was used as a model to fit the experimental neutron diffractogram below T_N. Law's model was also tested and it was found that the corresponding magnetic space group is P_c2_1/c (14.82). Discrepancies (high values of R_{mag}) between the experimental data and fitting curves indicate that both models are not appropriate for the description of the magnetic structure of the prepared powdered $NiTa_2O_6$ sample.

6.5.3 A new magnetic model for the trirutile $NiTa_2O_6$

As the Ehrenberg's[102] and Law's models[220] were both unsatisfactory for the research purpose further investigations were undertaken. The contribution of other primary IRs and their superpositions was investigated. The representation analysis method was used to determine a magnetic structure which would best fit the data set. There will be a derivation of the Γ_{perm} and Γ_{axial} of the system. The Γ_{mag} will then be decomposed onto IRs. The magnitude and orientations of the magnetic ions will then be refined.

6.5.3.1 Orbits and irreducible representation

The primary IRs of $G_{\vec{k}}$ were derived via the tool *BasIreps* in the program *Fullprof*, see Table 6.6. In addition *BasIreps* informs on the number of non-equivalent positions for magnetic atoms within the magnetic structure. The latter are called orbits. The orbits of the magnetic structure of the nickel ditantalate are shown in Table 6.9. The first orbit $Ni1\_1$ (black font) represents atoms at the edges of the tetragonal unit cell whereas atoms in the centre of the cell are associated with the second and last position $Ni2\_1$ (red font).

Table 6.9: The two orbits of the Ni^{2+} under the operations of the little group $G_{\vec{k}}$.

	Wyckoff positions				
Atom	**Type**	**x**	**y**	**z**	**Occ**
$Ni1\_1$	Ni	0	0	0	1/4
$Ni2\_1$	Ni	1/2	1/2	1/2	1/4

6.5.3.2 Derivation of Γ_{perm} and $\Gamma_{\vec{V}}$

The magnetic representation Γ_{mag} of the whole magnetic structure is obtained by determining the Γ_{mag} at each orbit. Therefore for $Ni1\_1$ and $Ni2\_1$, one needs to derive the magnetic representation related to the symmetry elements of $G_{\vec{k}}$.

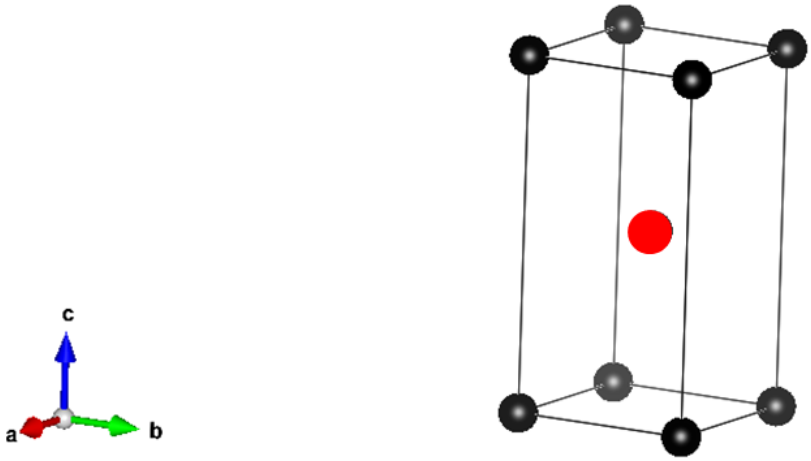

Figure 6.19: Non-equivalent positions of Ni^{2+} within the magnetic structure of $NiTa_2O_6$.$Ni1\_1$ corresponds to the red atom, whereas the blue atoms are all equivalent and represent $Ni2\_1$.

Table 6.10: Characters of the magnetic representation at the orbit $Ni1\_1$.

REPS	**Symmetry elements**			
	1	**2 x,-x, 0**	**m x,y,0**	**m x, -x, z**
	$\{1\|0,0,0\}$	$\{2\|0,0,0\}$	$\{m\|0,0,0\}$	$\{m\|0,0,0\}$
Γ_{mag}	3	-1	-1	-1

BasIreps not only enables the calculations of the IRs and the orbits, it also computes the permutation and axial representations for each magnetic orbit. The permutation and axial vector representations associated with the first orbit $Ni1\_1$ are the following:

$$\Gamma_{perm} = \Gamma_3$$
$$\Gamma_{\tilde{V}} = \Gamma_1 \oplus \Gamma_2 \oplus \Gamma_4$$

Mathematically, Γ_{mag} is the direct product of the permutation Γ_{perm} and $\Gamma_{\tilde{V}}$. The model describing the sublattice magnetisation at $Ni1\_1$ is therefore:

$$\Gamma_{mag} = (\Gamma_3 \otimes \Gamma_1) \oplus (\Gamma_3 \otimes \Gamma_2) \oplus (\Gamma_3 \otimes \Gamma_4). \tag{6.36}$$

To determine the characters of Γ_{mag} (typically $\chi_{\Gamma_{mag}}$) one multiplies the characters $\chi_{\Gamma_{perm\nu}}$ and $\chi_{\tilde{V_\nu}}$, for each symmetry operation. The result can be found in Table 6.10.

The Wonderful Orthogonality Theorem was used to reduce this magnetic representation into IRs of the little group $G_{\vec{k}}$. The calculations to determine whether or not a primary representation contribute to Γ_{mag} are presented below:

For Γ_1: $1*1*3 + -1*1*-1 + 1*1*-1 + -1*1*-1 = 4 = 1*4$.

Table 6.11: The basis vectors of the magnetic irreducible representations for the two orbits of Ni^{2+}.

IRREPS	**2a equivalent sites**		
	basis Vectors	**Ni1_1 (x, y, z)**	**Ni2_1 (x, y, z)**
Γ_1	BASR	(0 0 1)	(1 -1 0)
	BASI	(0 0 0)	(0 0 0)
Γ_2	BASR	(110)	
	BASI	(000)	
Γ_3	BASR		(110)
	BASI		(000)
Γ_4	BASR	(1 -1 0)	(0 0 1)
	BASI	(0 0 0)	(0 0 0)

For Γ_2: $1*1*3 + -1*1*-1 + -1*1*-1 + 1*1*-1 = 4 = 1*4$.

For Γ_3: $1*1*3 + 1*1*-1 + 1*1*-1 + 1*1*-1 = 0 = 0*4$.

For Γ_4: $1*1*3 + 1*1*-1 + -1*1*-1 + -1*1*-1 = 4 = 1*4$.

The numbers in red represent the number of times an IR appears in the reduction of Γ_{mag}.The numbers in blue and in green correspond the characters of the IRs and the representation Γ_{mag}, respectively. Hence, the magnetic representation associated with $Ni1\_1$ (0, 0, 0) is:

$$\Gamma_{mag} = \Gamma_1 \oplus \Gamma_2 \oplus \Gamma_4. \tag{6.37}$$

Likewise the magnetic representation for $Ni2\_1$ $(\frac{1}{2}, \frac{1}{2}, \frac{1}{2})$ is:

$$\Gamma_{mag} = \Gamma_1 \oplus \Gamma_3 \oplus \Gamma_4. \tag{6.38}$$

The permutation representation for this second orbit is Γ_2.

6.5.3.3 From magnetic representations to basis vectors

The last step of the representation analysis method was a mapping from the framework of the IRs to the framework of the parent nuclear structure. One expresses the magnetic moments as function of the basis vectors of the IRs. For this purpose one ought to determine the basis vectors of the four IRs of the little group. The software "*BasIreps*" enables the calculation of the basis vectors of the irreducible representation of a space group. The basis of the IRs of $G_{\vec{k}}$ are presented in Table 6.11.

All basis vectors only have a real part (BASR) contribution, i.e, their imaginary contribution

(BASI) is equal to zero. Consequently, the basis vectors directly represent the projections of the magnetic moments along the crystallographic axes. Nevertheless, the moments orientations of $Ni1\_1$ and $Ni2\_1$ are completely different under the representation Γ_1 and Γ_4. For instance, the moment orientations of the atoms at the orbit $Ni1\_1$ are parallel to the *c*-axis under Γ_1's framework. On the other hand under the same representation the moments of the atoms at the second site ($Ni2\_1$) lie in the *ab*-plane. An ordering of the moments can therefore not be established for this representation. The reverse configuration of moments orientations on both orbits is observed for Γ_4. This is a proof that Γ_1 and Γ_4 are inactive, magnetically. Table 6.10 shows that Γ_2 acts only on the magnetic atoms which are in the $Ni1\_1$ site. Their moments lie in the *ab*-plane. Likewise the Ni^{2+} in the $Ni2\_1$ orbit also have their moments in the *ab*-plane and they are only associated with the IR Γ_3. This coherence in the orientation of the magnetic moments on both orbits suggest that Γ_2 and Γ_3 are magnetically active. Hence, the model to describe the unknown magnetic structure of$NiTa_2O_6$ depends on these two IRs.

The fitting curve and experimental pattern greatly differed, when Γ_2 and Γ_3 were individually used as models. The two models were thus ruled out. However a better match was observed when the two primary IRs were superposed. A Rietveld refinement of the 1.5 K-neutron diffractogram was performed, based on the crystallographic parameters associated with this combination. The result of the refinement is illustrated in Figure 6.20 on the next page.

In Figure 6.20, the measured and calculated profiles are displayed with red dots and black line, respectively. A difference curve (observed-calculated) is illustrated at the bottom by the blue line. The green tick marks indicate the Bragg peak positions associated with an orthorhombic lattice. Figure 6.20 emphasises that the model (the black line) for the magnetic structure of $NiTa_2O_6$ fits well the experimental data (red dots). The agreement between calculated and measured profiles is confirmed by the very low value of the fitting parameters: R_B= 2.51 % and R_{mag} = 7.48 %. The refinement factor values are smaller to those of the refinement by the Ehrenberg and Law models, indicating this model is better than the previous ones.

ISODISTORT was then used to derived all the subgroups associated with the combination between Γ_2 and Γ_3. It turned out the sublattice magnetisation of the subgroup A_bma2 was identical to the one obtained from the Rietveld refinement. Hence, this Shubnikov can be seen as a model for the magnetic structure of $NiTa_2O_6$. To confirm the new model, a refinement of the 1.5 K-neutron diffraction pattern was performed with *Jana*, based on the magnetic space group A_bma2. The result of the latter refinement was identical to that of the one in Figure 6.19. The sublattice magnetisation associated with the black profile in this Figure is depicted in Figure 6.21 on page 174.

In Figure 6.21 the blue spheres represent the nickel ions and the red arrows correspond to the magnetic moments. The smallest lattice represents the nuclear unit cell whereas the largest one is the magnetic structure. Note that the magnetic moments lie in the *ab*-plane, and are along the [1 1

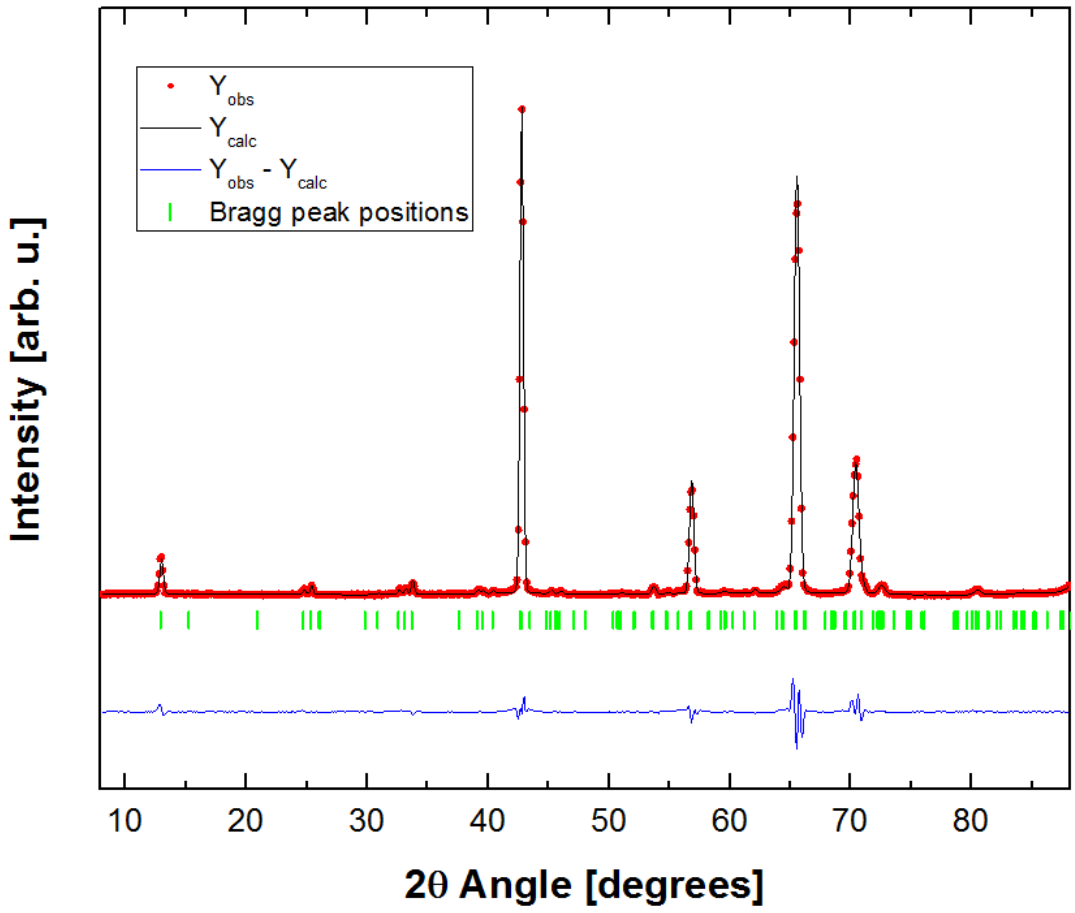

Figure 6.20: Rietveld refinement of the diffractogram recorded at 1.5 K. The theoretical model used for the fitting is a representation which is the superposition of Γ_2 and Γ_3.

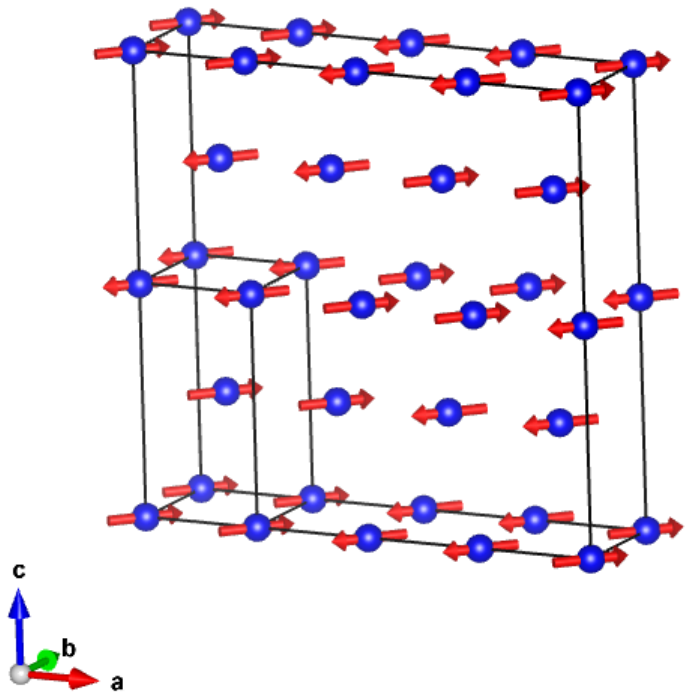

Figure 6.21: Representation of the unit cell of the sublattice magnetisation for $NiTa_2O_6$ following the new model. The latter is a superposition of Γ_1 and Γ_3.

0] direction as predicted by the representation analysis (see Table 1.10). magnetisation crystallises in an orthorhombic-type structure like the one reported by Ehrenberg and coworkers. This is different to the Law's model in which the lattice is monoclinic. The chains show an "-up-up-down-down-" sequence along the *a*- and *b*-axes but there is a "-up-down-" sequence along the *c*-axis. The new magnetic structure and the one reported by Ehrenberg both have a polar symmetry along the *c*-axis. Since $NiTa_2O_6$ is an insulator it is to be expected that it has some magnetically induced electric polarisation along *c*-axis (type II multiferroic). Details on multiferroic can be found in the reports by Khomskii[221,222]or other reviews[223,224].

Since measurements at the LLB, on the G4.1 were carried without the application of any magnetic field one deduces that the extracted structure is the magnetic structure ground state of the system. This ground state magnetic structure exhibits an antiferromagnetic ordering. This finding is in agreement with previous results such as those published by Ehrenberg *et al.*[102], and those from of Law *et al.*[220]. Table 6.12 summarises the relationship between the magnetic structures of $NiTa_2O_6$. One of the striking difference between the three models is the refined magnetic moment of Ni^{2+} ions. The evolution of μ_{eff} is presented and discussed in the following and last section.

6.5.4 Magnetic moment study

All neutron diffraction patterns below the Néel temperature (10.3 K) were refined with the superposition of Γ_1 and Γ_3 (A_bma2) as model. Figure 6.22 shows the temperature dependence of the total

Table 6.12: Comparison between the Ehrenberg, Law and the new models. **a**, **b**, **c** represent the lattice parameters of the nuclear unit cell.

Date	**1998**	**2014**	**2016**
Authors	Ehrenberg *et al.*	Law*et al.*	Us
propagation vector	$\vec{k} = (\frac{1}{4}, \frac{-1}{4}, \frac{1}{2})$	$\vec{k} = (\frac{1}{4}, \frac{-1}{4}, \frac{1}{2})$	$\vec{k} = (\frac{1}{4}, \frac{-1}{4}, \frac{1}{2})$
Magnetic space group	$A_b$ba2	P_c2_1/c	A_b ma2
Lattice system	orthorhombic	monoclinic	orthorhombic
Magnetic moments direction	[1 1 0] and [1 -1 0]	[1 1 0] and [1 -1 0]	[1 1 0] and [1 -1 0]
Ni1_1 Wyckoff positions	(0, 0, 0)	(0, 0, 0)	(0, 0, 0)
Ni2_1 Wyckoff positions	$(0, \frac{1}{4}, \frac{1}{4})$	$(\frac{1}{8}, \frac{1}{8}, \frac{1}{4})$	$(\frac{1}{2}, \frac{1}{2}, \frac{1}{2})$
Magnetic moment μ_B/Ni^{2+}	1.488(2)	1.473(3)	1.85(2)
Relation between ferro- and antiferromagnetic chains	perpendicular	parallel	parallel
R_B (%)	5.42	5.11	2.51
R_{mag} (%)	17.96	18.49	7.48

magnetisation of $NiTa_2O_6$. The intensity of magnetic reflections decreases with increasing temperature it then vanishes as the temperature reaches past 10.3 K. This is agreement with evolution of the magnetisation of an ordered magnetic system as function of the temperature.

An exponential function was used to fit the magnetic moment below the Néel temperature. The function is given by equation (6.38)

$$M(T) = M_o(1 - \frac{T}{T_N})^{\beta} \tag{6.39}$$

Where M_o is the maximal magnitude of the moment and β the critical exponent. β is one of the critical exponents introduced by Landau to describe the critical properties of a magnetic system showing a second order phase transition. Its derivation can be found in the paper by Landau and Lifshitz[225]. $\beta \sim 0.365$ for an Heisenberg Hamiltonian. If the fluctuations are neglected, the Heisenberg Hamiltonian can be approximated to a model known as the Mean field theory model. In this model $\beta = \frac{1}{2}$. The value of the Néel temperature, the exponent and were extracted from the fitting in Figure 1.16. M_o and β are equal to 1.831 μ_B per Ni^{2+} ion and 0.10(0), respectively. The present β value differs from to one reported by Law *et al.* who reported values of 0.22(1). This discrepancy suggests that the Heisenberg model may not be sufficient to explain the magnetic interactions between Ni^{2+} ions. Furthermore, in the above equation T_N is the critical temperature at which the fitting line intercepts the horizontal axes. A value of 9.60(0) K is refined for T_N the prepared $NiTa_2O_6$ polycrystalline samples. This T_N value is in agreement with the previous values. Eventually the resulting magnetic moment of 1.831(5) μ_B per Ni^{2+} ion is in good agreement with the expected value of 2 μ_B for S=1 system with a g-factor of 2.2. It indicates that the prepared $NiTa_2O_6$ is an ordered trirutile.

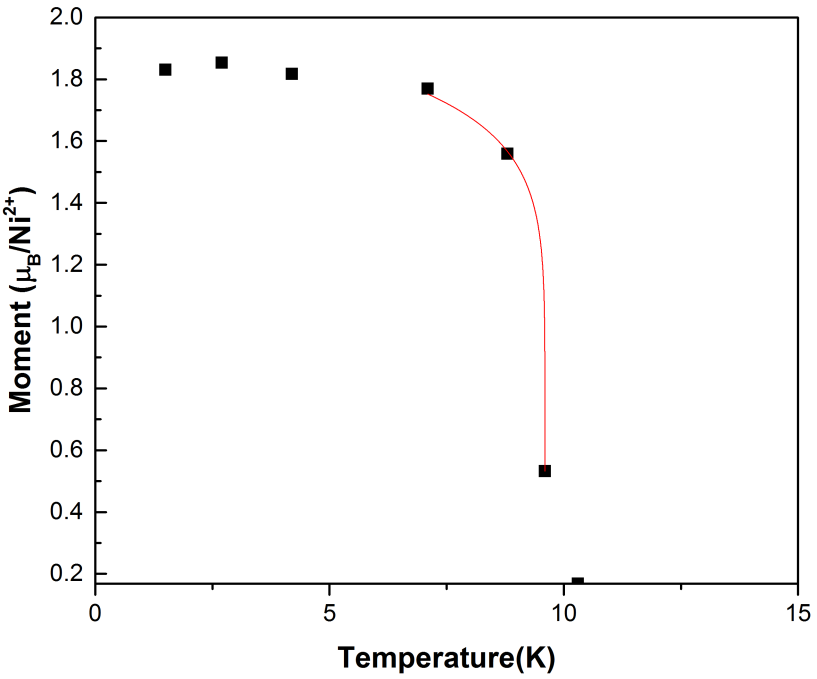

Figure 6.22: Evolution of magnetic moment as function of temperature. The solid line is the fitting curve obtained with the formula in equation (6.40).

6.6 Conclusion

Joint x-ray and neutron refinement confirmed the phase purity of the polycrystalline $NiTa_2O_6$ sample. In addition Rietveld refinement demonstrated that the prepared $NiTa_2O_6$ is a fully ordered trirutile. The highlight of this work is the discovery of a new magnetic structure for this compound. The corresponding Shubnikov space group of the new sublattice magnetisation is A_bma2. There is a polar symmetry along the c-axis within the new model, the one reported by Ehrenberg *et al.*[102]. The breaking of the polar symmetry suggest the multiferroic (type II) character of this material, as it is insulator. Further studies on this sample are envisaged. Firstly, polarisation measurement is envisaged as it will confirm or infirm the ferroelectric behaviour of $NiTa_2O_6$. Secondly this commensurately trirutile is associated with three different magnetic structures below T_N. This gives rises to the following questions: (a) Does the magnetic ions in a given trirutile material order themselves in more than one magnetic structure, below the critical temperature? And (b) Is $NiTa_2O_6$ an exception? Therefore further studies need to be pursued in order to determine the relationship between the modulation of a trirutile and its magnetic structure(s). Eventually, the growth of large single crystals[226] via the floating zone technique is envisaged as measurements on singles crystals inform on the intrinsic properties of a material. Polarised neutron diffraction on these single crystals will shed the orientations of the magnetic moments but also the relationships between the three models.

Chapter 7

The magnetic structure of nickel metaniobate $NiNb_2O_6$

7.1 Motivation

Recently solid state physicists have developed an interest in exploring, theoretically and experimentally, the magnetic properties of AB_2O_6 [227,228,229] materials with M = Fe, Co, Ni. The interplay between the magnetic, electronic, and structural degrees of freedom, within some of the compounds in this family gives rise low-dimensionalities. For instance, $NiTa_2O_6$ [81,102,220] and $FeTa_2O_6$ [71,74,75] are 1D- and quasi-2D antiferromagnets, respectively.

Nickel metaniobate ($NiNb_2O_6$) belongs to the AB_2O_6 family. This material crystallises in a columbite-type structure. The unit cell of its crystal structure is displayed in Figure 7.1. Within the orthorhombic lattice the Ni^{2+} (blue sphere) and Nb^{5+} (grey sphere) ions occupy the *4c* and *8d* sites, respectively. Both cations are surrounded by six oxygen O^{2-} anions (red sphere), forming NiO_6 and NbO_6 octahedra. The transparent and green edge shared octahedra emphasise the -Ni-Nb-Nb-Ni- arrangement along the [1 0 0] direction.

Heid *et al.* [85] investigated the magnetic properties of this columbite compound by means of powder neutron diffraction, magnetic susceptibility and specific heat measurements on polycrystalline $NiNb_2O_6$ samples. The magnetic susceptibility data demonstrated that $NiNb_2O_6$ exhibits an antiferromagnetic ordering below $T_N = 5.7\,\mathrm{K}$. However, Heid and coworkers did not establish its magnetic structure. Since Heid *et al.* [85] early work there have been no further reported studies on magnetic structures for $NiNb_2O_6$. Therefore this investigations carried out on powdered $NiNb_2O_6$ aimed to shine light on the sublattice magnetisation of nickel metaniobate. Firstly, there is a literature review on $NiNb_2O_6$. It is followed by a structural characterization of the prepared polycrystalline sample, by powder x-ray diffraction. The neutron diffraction pattern measured below T_N are refined using both representation and magnetic symmetry analysis methods. The presentation and comparison of several models for the magnetic structure of $NiNb_2O_6$ are discussed in the chapter last sections.

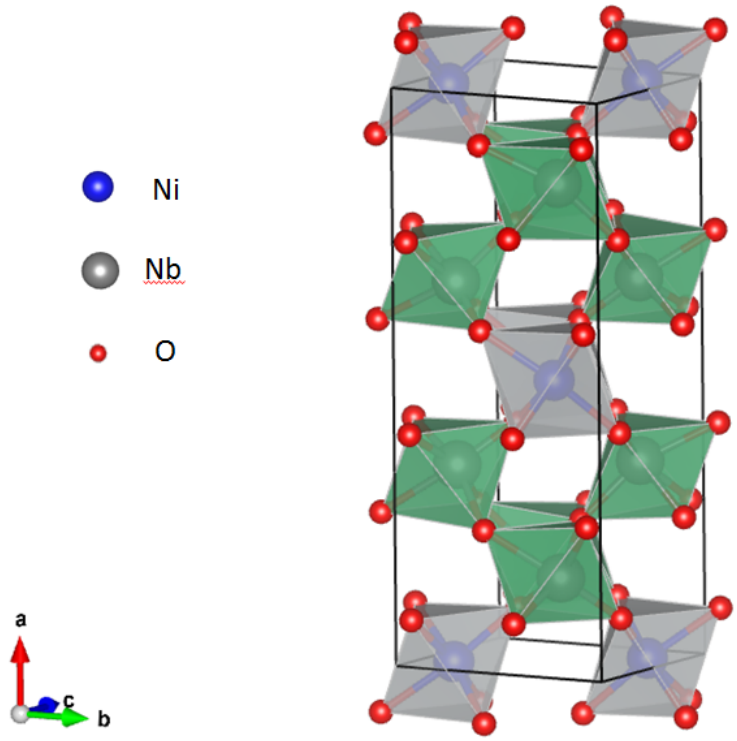

Figure 7.1: The nuclear structure $NiNb_2O_6$ structure. The orthorhombic unit cell consists of nickel (blue), niobium (grey) and oxygen (red) atoms (spheres).

7.2 A literature review of $NiNb_2O_6$

7.2.1 Methods of synthesis

One of the first reports on the properties of $NiNb_2O_6$ was done by Emmenegger and Petermann[230] in 1968. Emmenegger and Petermann investigated the crystal structure of ANb_2O_6 oxides (with A = Mg, Fe, Mn, Zn, Co, Cd, Ca and Ni) by means of x-ray diffraction. Single crystals of nickel metaniobate were prepared by chemical transport technique. Cl_2 was the solvent used the growth process, which occurred in a two-zone furnace. Using the same solvent, the researchers also prepared $NiNb_2O_6$ single crystals by vapor transport pulling technique in a vertical furnace.

Additionally, polycrystalline $NiNb_2O_6$ samples have been prepared via a solid state reaction between stoichiometric amounts of NiO and Nb_2O_5. Stoichiometric amounts of nickel oxide and niobium oxide were heated at 1250 °C for 48 hr[84]. Eventually Prabhakaran and coworkers[84] have grown single crystals of $NiNb_2O_6$ via the floating zone method. The growth was carried out under O_2 atmosphere in a optical vertical furnace.

Recently Lei *et. al.*[87] measured the temperature-dependence susceptibility and magnetisation hysteresis loop of $NiNb_2O_6$ nanoparticles. The nanoparticles were prepared by a hydrothermal method followed by a calcination.

7.2.2 Physical properties

Borromei *et. al.*[231] investigated the optical properties of nickel metaniobate in the range 5000-30 000 cm^{-1} at temperatures from 4.2 to 300 K. The absorption spectrum of Ni^{2+} in $NiNb_2O_6$ is similar to that of the same ion in MWO_4 samples (M = Mg, Zn, Cd)[232]. The main features of the spectra are due to a $\mathcal{O}_h \rightarrow \mathcal{C}_{2v}$ perturbation. This transition corresponds to a reduction of the symmetry which causes a static distortion of the NiO_6 and Nb_2O_5 octahedra. The ground state of nickel ions in the $\mathcal{O}_h$ symmetry environment is $^3\mathcal{A}_{2g}$ ($t_2^6e^2$). This ground state becomes $^3\mathcal{B}_2$ due to the distortion, which gives rise to the $\mathcal{C}_{2v}$ symmetry. In order to fully explain the experimental results Borromei and coworkers added the contributions of the distortion $\mathcal{C}_{2v} \rightarrow \mathcal{C}_2$, the spin-orbit coupling and the vibrational interactions. It should be noted that the state $^3\mathcal{B}_2$ of the Ni^{2+} becomes $^3\mathcal{B}$ as the lattice undergoes a symmetry reduction from $\mathcal{C}_{2v}$ to $\mathcal{C}_2$.

There has been few reports of investigations of the magnetic properties of this AB_2O_6 oxide. Temperature-dependence susceptibility[84,85,87] measurements on polycrystalline $NiNb_2O_6$ samples reveal an antiferromagnetic type curve, which can be fitted by $\chi(T) = \frac{C}{T-\Theta}$. Lei and coworkers[87] reported values of 1.31 and -42.78 for C and Θ, respectively. In addition to that Lei *et. al.*[87] found a value of 6 K as Néel temperature for this antiferromagnet, which is in agreement with 5.7 K reported by Heid *et al.*[85]. Lei and coworkers refined a value of 3.3 μ_B/Ni^{2+} for the effective magnetic moment μ_{eff} of Ni^{2+} ions. This is in agreement with the theoretical value of 3.2 μ_B/Ni^{2+}.

Neutron diffraction and specific heat measurements[85] were also performed on $NiNb_2O_6$ powders. Both confirmed the Néel temperature of this columbite material to be about ∼6 K. The observed magnetic reflections in the neutron powder diffraction (NDP) patterns can be indexed using two propagation vectors: $\vec{k_1} = (\frac{1}{2}, \frac{1}{2}, 0)$ and $\vec{k_2} = (0, \frac{1}{2}, 0)$. The peaks indexed by $\vec{k_1}$ are more intense than those indexed by $\vec{k_2}$. Heid and *et al.* refined a value of 2.4 μ_B for μ_{eff} of Ni^{2+} ions. Heid and coworkers did not establish a model for the magnetic structure of nickel metaniobate, due to broadened Lorentzian-shape type of peaks indexed by the modulation vector $(0, \frac{1}{2}, 0)$. Nevertheless Heid and *et al.* made the hypothesis that the sublattice magnetisation of this compound was similar to that of $FeNb_2O_6$: a non collinear magnetic structure where the magnetic moments lie in the *a*-*c* plane. These magnetic moments have a canting angle of 31° to the *c*-axis.

7.3 Synthesis

In accordance with the solid state reaction by Prabhakaran *et al.*[84]Polycrystalline $NiNb_2O_6$ samples have been prepared, by mixing stoichiometric amounts of NiO (99.9%) and Nb_2O_5 (99.99%). The precursors (nickel oxide (II) and niobium oxide (V)) have green and white colours, respectively. The solid state reaction is described by the following reaction:

$$NiO + Nb_2O_5 \xrightarrow{air} NiNb_2O_6 \tag{7.1}$$

The precursors have been mixed with a pestle in an agate mortar under acetone. The mixture has been heated at 1250 °Cfor 48 h in order to form nickel metaniobate. In order to insure phase purity multiple re-grinding and annealing (at 1300 °C) processes have been performed. The resulting powder has the same colour of that of Prabhakaran and coworkers $NiNb_2O_6$ powders: a dark yellow colour, as seen in Figure 7.2a.

7.4 Powder x-ray diffraction

The crystal structure of the prepared sample has been determined by x-ray diffraction, using a PANalytical diffractometer. Details on this instrument can be found in the Chapter 2. Figure 7.2b presents a Rietveld refinement of a room-temperature x-ray diffraction pattern of $NiNb_2O_6$. *Jana* program has been used to perform the Rietveld refinement.

In Figure 7.2b the red dots correspond to the measured or experimental x-ray diffraction pattern, whereas the continuous black line is the calculated profile. The difference between these two curves is illustrated by the blue line. It was noted that there were some discrepancies between measured and calculated profiles for $2\theta \sim 35°$ and at 45°. The plane associated with the peak at 35° is (3 1 1); and (6 0 0) is the corresponding plane for the peak at 45°. The intensity of this peak is greater than that its theoretical value, whereas the the calculated value for the (3 1 1) reflection is higher than its theoretical value. These two mismatches suggest the presence of preferential orientations within the lattice. Nevertheless, there is good level of agreement be the measured and theoretical profiles. As all reflections in the x-ray diffractogram, in Figure 7.2b, are those of a orthorhombic lattice, whose space group symmetry is Pbcn (60).The Bragg peak positions of such lattice are indicated by the green ticks. The good level of agreement is indicated by the low values of the "R" coefficients: χ^2 = 1.93, R_B = 11.35 % and R_F = 15.34 %.

The Wyckoff positions of Ni, Nb and O - extracted from the joint x-ray and neutron diffraction - are presented in Table 7.1.

Table 7.1: Wyckoff positions of atoms within the orthorhombic unit cell of $NiNb_2O_6$, obtained from Rietveld refinement of a room-temperature x-ray diffraction patterns. Site occupancy (site occu.) is the ratio between the site multiplicity and the general multiplicity. Space group: Pbcn (60).

atom label	**atom type**	**Wyckoff symbol**	**x**	**y**	**z**	**site occu.**
Ni	Ni	4c	0	0.15718(4)	1/4	0.500
Nb	Nb	8d	0.15931(1)	0.31997(3)	0.75578(9)	1.000
O_1	O	8d	0.09525(2)	0.39321(5)	0.42280(8)	1.000
O_2	O	8d	0.07945(3)	0.11693(6)	0.90819(8)	1.000
O_3	O	8d	0.25599(3)	0.12205(7)	0.57673(8)	1.000

The low values of R_B and R_F confirm the phase purity of the prepared nickel metaniobate powder. Its physical properties can then be investigated. The physical property examined in this chapter is the sublattice magnetisation of the columbite $NiNb_2O_6$, as there is not yet reports of it in the literature.

(a)

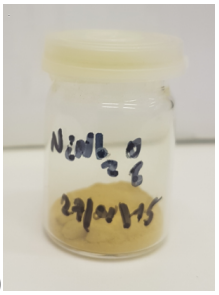

(b)

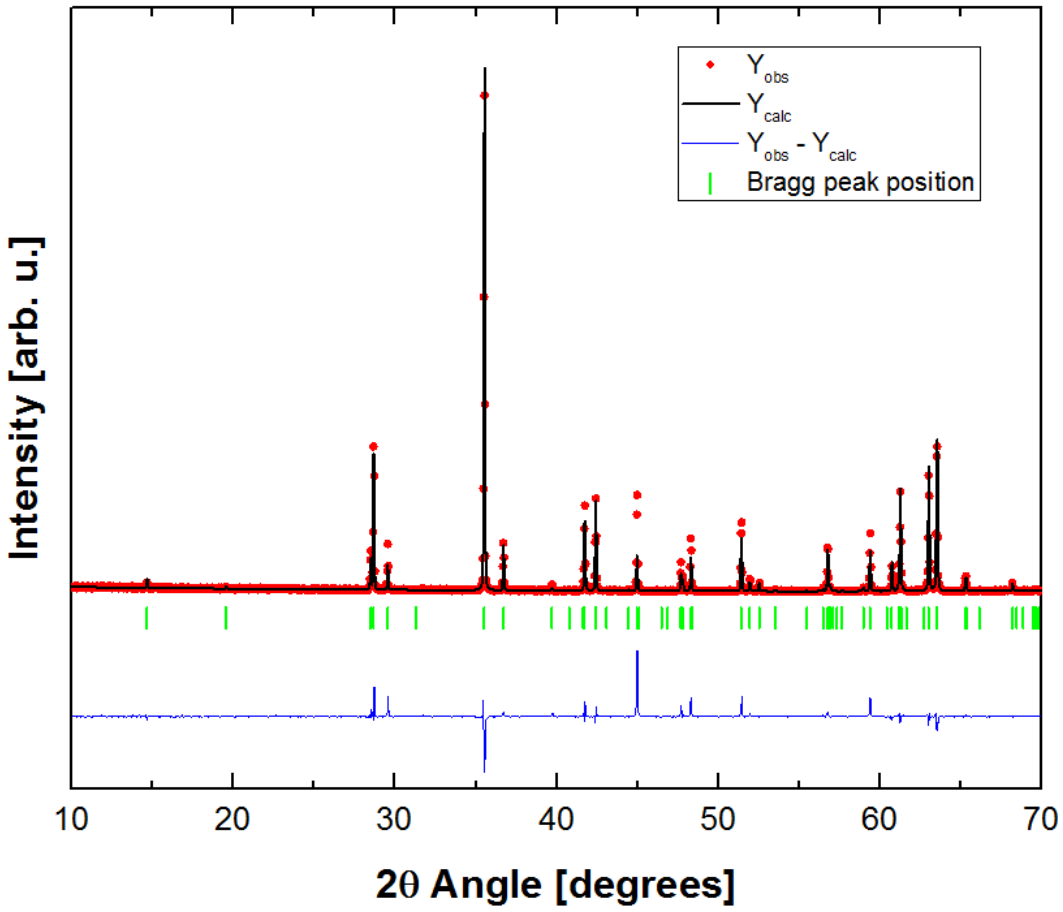

Figure 7.2: a) Powdered $NiNb_2O_6$ sample. (b) Rietveld refinement of a room-temperature x-ray diffraction pattern of $NiNb_2O_6$. The red dots and the black line correspond to the measured and calculated profiles. The difference between these two curves is the blue line. The green ticks represent the Bragg peak positions.

7.5 The magnetic structure of $NiNb_2O_6$

7.5.1 The Néel temperature

Neutron powder diffraction (NDP) has been performed on the prepared powder sample. Informations on the orientations of moments in $NiNb_2O_6$ can be obtained from this experiment, as the spin $\frac{1}{2}$ of neutrons can interact with the unpaired electrons of Ni^{2+}. In addition, the neutrons can tell on the sublattice magnetisation. This is due to the fact that their wavelength is similar to that of the distances between atoms within this columbite. Zero-field neutron powder diffraction has therefore been performed on the two-axes G4.1 diffractometer, across a temperature range between 1.5 and 300 K. Details on this instrument are given in the Chapter 2. They are depicted in Figure 7.3.

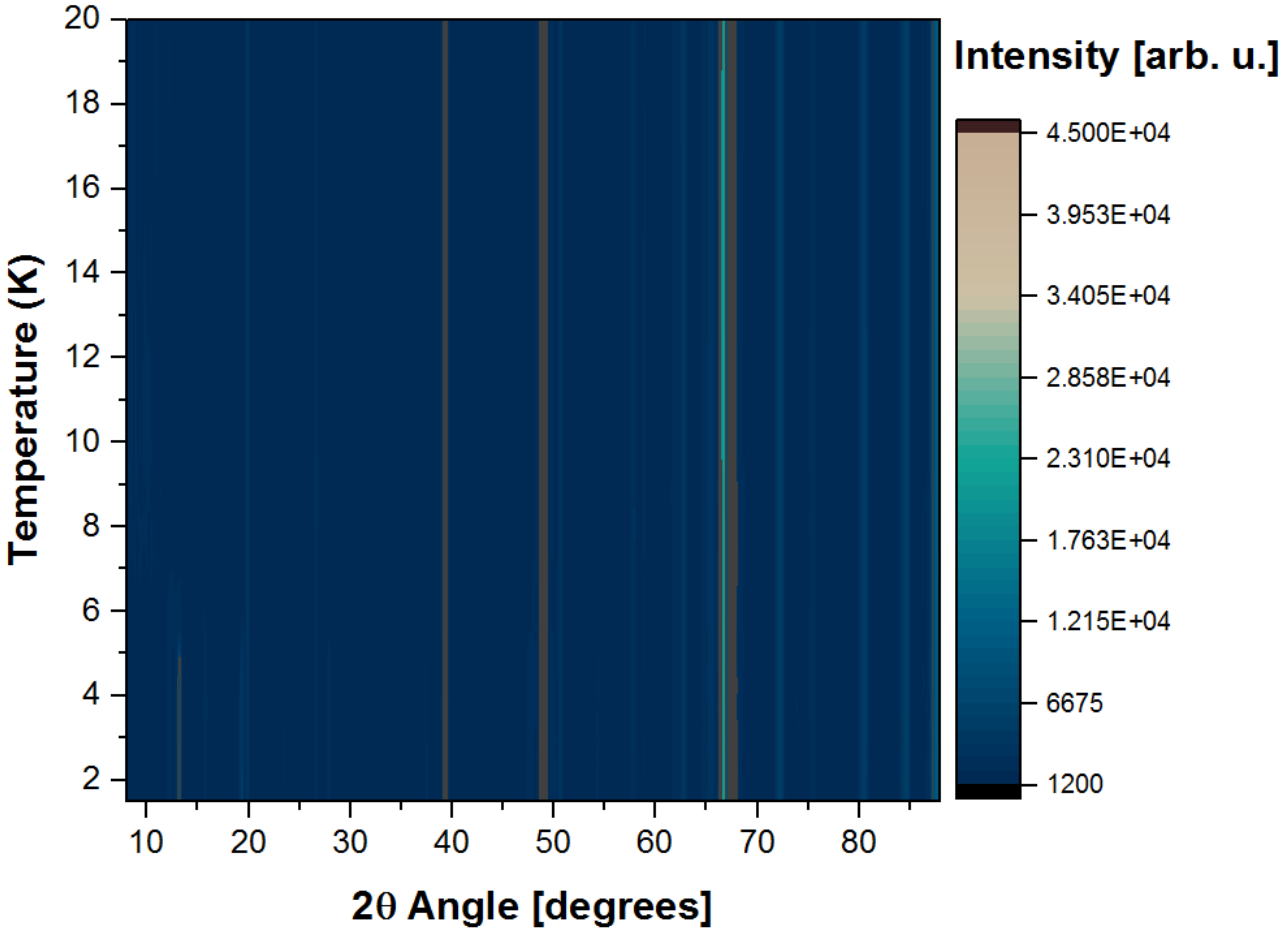

Figure 7.3: Neutron powder diffraction patterns of $NiNb_2O_6$ recorded on the two-axes G4.1 diffractometer in Saclay (France).

The diffractograms measured from 1.5 K to 9.6 K are displayed in the heat map in Figure 7.3. The heat map in Figure 7.3 illustrates the NDPs of $NiTa_2O_6$ from 1.5 to 300 K. The axis on the left indicates the temperature at which the NDP was recorded, the intensity an angle of the reflections are on the left and bottom axes, respectively. The vertical lines are Bragg reflections and they are two types of vertical lines (or peaks). They are the intense and weak vertical lines. The intense vertical lines correspond to Bragg peaks which appear on all NDP patterns, for all temperatures: these peaks are the nuclear reflections. On the other hand, the weak vertical lines vanish at about 5.6 K.

Like in Figure 6.15, these vertical lines are the magnetic reflections. Observed on low-temperature NDPs, these reflections are associated with the ordering of Ni^{2+} ions. From Figure 7.3 one deduces that the Néel temperature T_N of $NiNb_2O_6$ is about 5.6 K. This is in agreement wit the results from Heid and coworkers[85], who reported a value of 5.7 K.

7.5.2 Magnetic representations and magnetic models

The representation analysis was used to determine the magnetic structure of the columbite $NiNb_2O_6$. This method describes the magnetic structure of a material as function of a modulation vector and its nuclear structure. Consequently the first step of this approach is to identify the propagation vector(s) related to the sublattice magnetisation. The program k_search enables the calculation of a modulation vector from a sets of magnetic reflections. It was not possible to index all the magnetic peaks using a single modulation vector $\vec{k}$. Nevertheless this was possible using the modulation vectors $\vec{k_1} = (\frac{1}{2}, \frac{1}{2}, 0)$ and $\vec{k_2} = (0, \frac{1}{2}, 0)$. This is in agreement with the work of Heid *et. al.*[85].

The derivation of the little group $G_{\vec{k}}$ associated with the propagator vector(s) is the second step of the representation analysis. One focuses on the magnetic irreducible representations of G_{veck}, especially those whose periodicity matches the nuclear structure's periodicity. These primary IRs and their superposition are potential models for the magnetic structure of a material. In the case of nickel metaniobate there are two modulation vectors $\vec{k_1} = (\frac{1}{2}, \frac{1}{2}, 0)$ and $\vec{k_2} = (0, \frac{1}{2}, 0)$. Hence, one needs to first treat these modulation vectors separately. The Bilbao Crystallographic server was used for the derivation of the magnetic irreducible representations (IRs) associated with each propagation. There are two primary IRs derived related to $\vec{k_1}$ and the latter are $mS1^+$ and $mS1^-$. Similarly $\vec{k_2}$ generates two primary irreducible representations, which are *mY1* and *mY2*. The magnetic model for the magnetic structure of $NiNb_2O_6$ is therefore the result of a combination between the primary IRs of $\vec{k_1}$ and those of $\vec{k_2}$. *ISODISTORT* is a versatile tool of the Bilbao Crystallographic Server, as it enables one to combine two IRs, and also to explore the different isotropy subgroups generated from this mixture. Figure 7.4 summarises the derivation of magnetic models from the primary irreducible representations of the two propagation vectors.

In Figure 7.4 the symbols Is_1, Is_2, Is_3 andIs_4 represent the four groups derived from the mixture of the IRs of the propagation vectors $\vec{k_1} = (\frac{1}{2}, \frac{1}{2}, 0)$ and $\vec{k_2} = (0, \frac{1}{2}, 0)$. Each of these I_i contains isotropy subgroups. The latter can all be derived from the nuclear structure space group Pbcn (60), according to the powerful Landau theorem[122,225] on second order phase transitions. Since one deals with a magnetic structure these isotropy subgroups are in fact Shubnikov groups derived *Pbcn (60)*.

Each group Is_i (i = 1, 2, 3, 4) consists of 6 isotropy groups so there are 24 possible subgroups for the magnetic structure of $NiNb_2O_6$. Four of these 6 subgroups have a monoclinic symmetry whereas the two others have a triclinic symmetry. One of the four monoclinic subgroups appears twice in each Is_i. The two monoclinic subgroups in each group Is_i differ by the origin of the unit cell. In addition to that $mS1^+$ and $mS1^-$ are co-primary irreducible representations. In others words acting

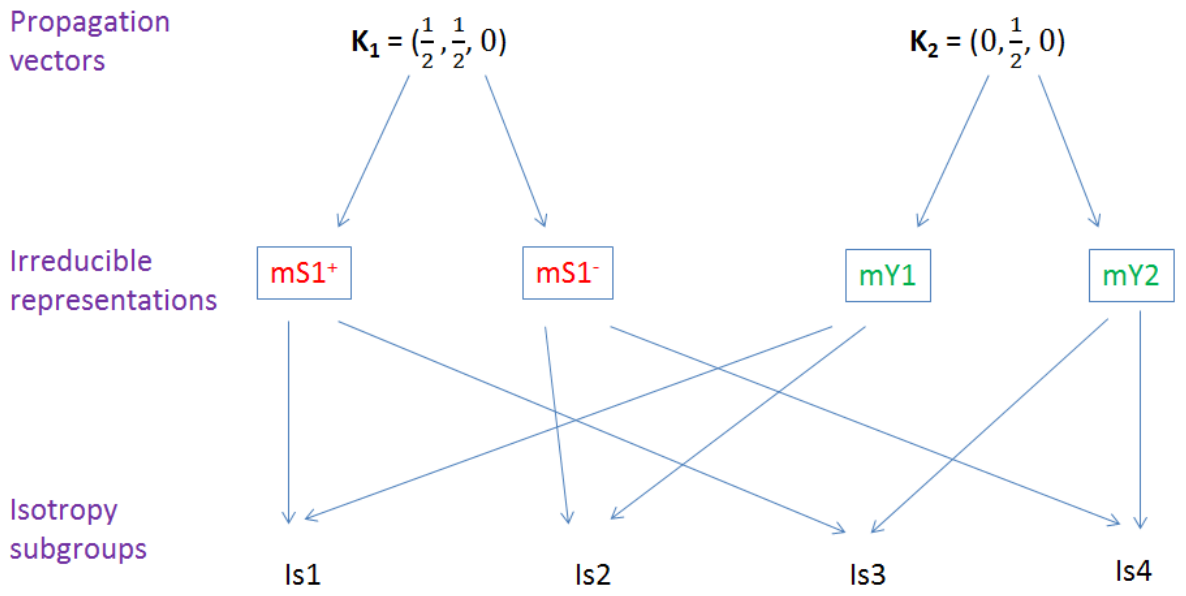

Figure 7.4: Tree of isotropy subgroups of $NiNb_2O_6$ derived from the irreducible representations of the two modulation vectors.

Table 7.2: Isotropy subgroups derived from the mixture of the primary IRs of the propagation vectors $\vec{k_1} = (\frac{1}{2}, \frac{1}{2}, 0)$ and $\vec{k_2} = (0, \frac{1}{2}, 0)$.

	Is_1	Is_2	Is_3	Is_4
Number of subgroups	6	6	6	6
Repetition subgroup	P_b2/c	P_b2/c	P_b2_1/c	P_b2_1/c

Distinct subgroups: P_b2_1/c, P_b2/c, P_a2_1, P_b2_1, P_b2, P_S-1 and P_S1

alone, either one leads to the same isotropy subgroup. When one of them acts to lower the symmetry, the other is able to follow along without lowering the symmetry further. There are therefore several equivalent subgroups within the 24 subgroups. By taking into account the redondance of subgroups and the co-primary characters of $mS1^+$ and $mS1^-$, there are only 7 unique isotropy subgroups. These subgroups are models for the sublattice magnetisation of $NiNb_2O_6$. Table 7.2 summarises the relationship between the isotropy subgroups of the mixture between $mS1^+$, $mS1^-$ and $mY1$, $mY2$.

The 7 distinct subgroups derived from the mixture of the IRs of $\vec{k_1}$ and $\vec{k_2}$ are: P_b2_1/c, P_b2/c, P_a2_1, P_b2_1, P_b2, P_S-1 and P_S1. The subgroups P_S-1 and P_S1 are associated with a triclinic-type structure and have the lowest symmetry. On the other hand the first five subgroups have a monoclinic-type structure and have a higher symmetry than the "triclinic subgroups". Note that P_b2_1/c has the highest symmetry.

7.5.3 $NiNb_2O_6$: a multi-$\vec{k}$ magnetic structure

Prior to the establishment of the magnetic structure of the columbite $NiNb_2O_6$ several discussion questions need to be addressed. Is a combination of $\vec{k_1}$ and $\vec{k_2}$ necessary to describe the magnetic

structure from all magnetic peaks? Does the magnetic structure consist of domains? It domains there are, how do they relate to two propagation propagation vector? Investigations related to these questions were carried out and the results are presented in the next lines of this subsection. Lebail fits have been performed for these two cases and the results are presented below. The case for a one-$\vec{k}$ structure are first assessed.

Firstly a Lebail fit - bases on $\vec{k_1}$ - was performed in order to fit all reflections of the a neutron diffraction pattern measured below 5.6 K. Parallely to that another Lebail fit associated with the $\vec{k_2}$ was also performed with the program *Jana*. The result for $\vec{k_1}$ is illustrated in Figure 7.5.

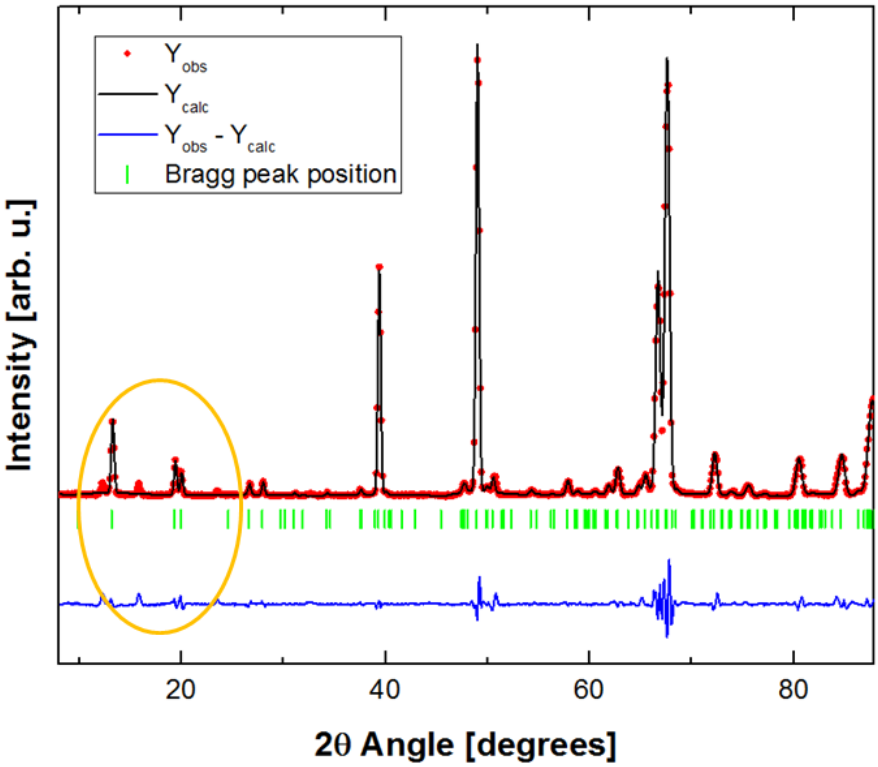

Figure 7.5: LeBail fit of 1.5 K-neutron diffraction pattern, associated with $\vec{k_1} = (\frac{1}{2}, \frac{1}{2}, 0)$. The red dots and the continuous black line correspond the experimental data and the theoretical profile, respectively. The difference between these two curves is indicated by the blue line. The green ticks index the Bragg reflections associated with the propagation vector $(\frac{1}{2}, \frac{1}{2}, 0)$.

Figure 7.5 displays a Lebail fit of the SI1.5K-neutron diffraction pattern. The red dots and the continuous black line correspond the measured and calculated profiles, respectively. The blue line corresponds to a difference between the experimental and theoretical data. The latter is and is a straight line for a perfect matching between the red dots and the black line. The green ticks correspond to the reflections indexed by $\vec{k_1} = (\frac{1}{2}, \frac{1}{2}, 0)$. There are apparent differences between the observed intensities (red dots) and calculated ones (black line), as the blue line is not a straight line. These discrepancies are highlighted by the yellow ellipse. The reflections which occur at 2θ equal 12.2, 15.7 and 23.4° are not at taking into account by the Lebail fit. One encounters similar issues as one performs a Lebail fit of the same neutron diffraction pattern based on $\vec{k_2} = (0, \frac{1}{2}, 0)$. Figure 6.6 illustrates a Lebail fit of the 1.5 K-neutron diffraction, with $\vec{k_2}$ as framework. The discrepancy

between the red dots and the black line are observed for the reflections at 2θ equal 13.1, 19.3 and 27.9°. Note there is a good agreement between the Lebail fit and the experimental pattern for 2θ equal 12.2, 15.7 and 23.4°. Consequently all magnetic reflections can not be indexed with only either $(\frac{1}{2}, \frac{1}{2}, 0)$ or $(0, \frac{1}{2}, 0)$. Hence, these cases can not be considered as framework for models for the magnetic structure of $NiNb_2O_6$.

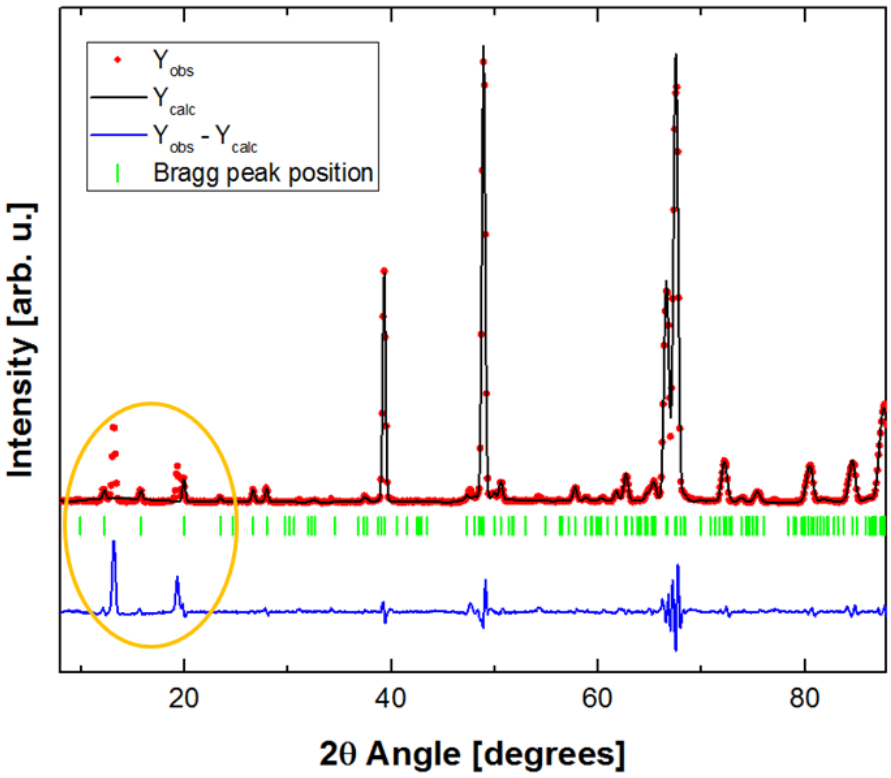

Figure 7.6: LeBail fit of 1.5 K-neutron diffraction pattern, associated with only $\vec{k_2} = (0, \frac{1}{2}, 0)$. The red dots and the continuous black line correspond the experimental data and the theoretical profile, respectively. The difference between these two curves is indicated by the blue line. The green ticks index the Bragg reflections associated with the propagation vector $(0, \frac{1}{2}, 0)$.

Furthermore the frameworks involving both $\vec{k_1}$ and $\vec{k_2}$ were explored. The first one is the two-phase framework. In such case the magnetic structure of $NiNb_2O_6$ consists of two types of domains. Each type of domain is related to only one of the modulation vectors: either $\vec{k_1}$ or $\vec{k_1}$. Consequently the peaks associated with this model are the sum of the reflections generated by $(\frac{1}{2}, \frac{1}{2}, 0)$ and those by $(0, \frac{1}{2}, 0)$. These reflections can be called "pure" reflections. The second framework corresponds to $\vec{k_1}+\vec{k_2}$ model. It is called the $2\vec{k}$-structure. Within this framework one expects to observe the "pure" reflections and some extra ones. The latter are mixed terms which originate from the combination of the propagation vectors. Both models were tested and the results of their respective Lebail fit are displayed in Figure 7.7 on page 187.

The diagrams in Figure 7.7 correspond to the Lebail fits associated with the two phases (a) and $2\vec{k}$-structure frameworks (b), respectively. The red dots and the continuous black line correspond the experimental data and the theoretical profile, respectively. The blue line is expected to be a straight line if the theoretical model (black line) fits perfectly the experimental data. The green and magenta ticks in Figure 7.7 a) refer to "pure" reflections generated by $\vec{k_1}$ and $\vec{k_2}$, respectively.

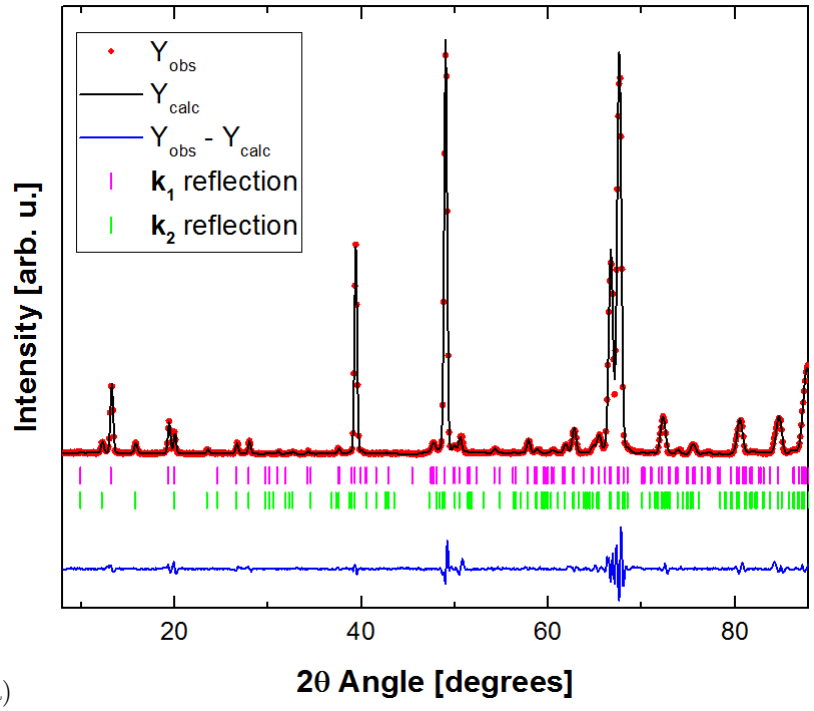

(a)

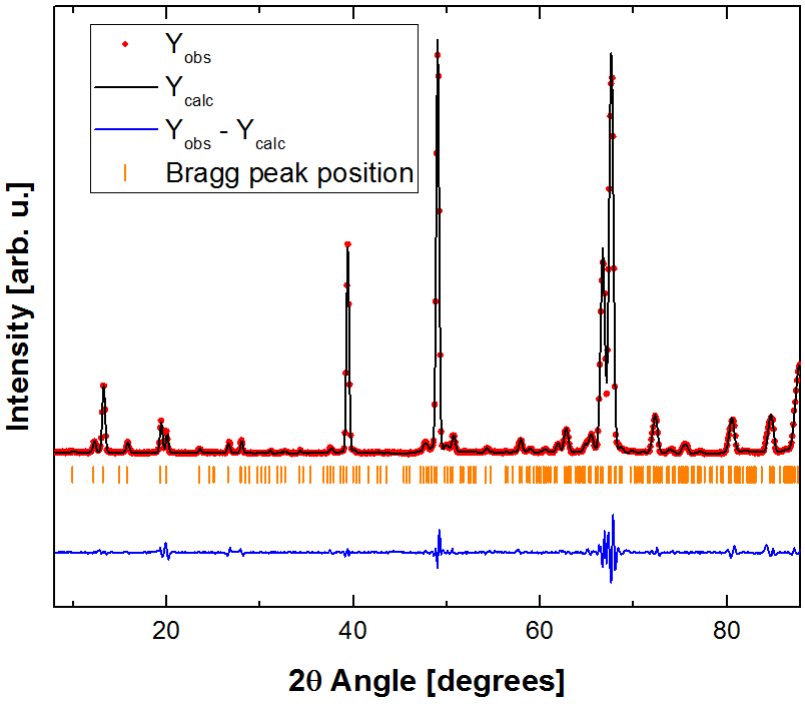

(b)

Figure 7.7: LeBail fits of 1.5 K-neutron diffraction pattern, associated with the two-phase (a) and one phase (b) frameworks. The red dots and the continuous black line correspond the experimental data and the theoretical profile, respectively. The difference between these two curves is indicated by the blue line. The green, magenta and orange ticks index the magnetic Bragg reflections.

The mixture between two modulation vectors generate the orange Bragg peaks in Figure 7.7 b). All magnetic reflections in both Lebail fits are well fitted. This is different to the Lebail presented in Figure 7.5 and Figure 7.6. Low values of the refinement factors indicated a good agreement between measured pattern and calculated profile, see Table 7.3. The GOF, R_B, and R_{wp} are the lowest for the $2\vec{k}$-structure. Hence, this framework is better than the three other frameworks, see Table 6.3. GOF stands for the goodness of fit and is defined as:

$$GOF = \sum_i \frac{wi(y_{io} - y_{ic})^2}{N - P}, \tag{7.2}$$

where N is the number of data points in the diffraction pattern and P is the number of parameters refined. y_{io} (y_{ic}) is the observed (calculated) intensity at the i^{th} incremental step of the pattern.

Note that the mixed terms, although weak, are present in Figure 7.7 b). This low intensity may be due to a lost of magnetic information, which originates from an average of the intensity over all directions as one performs powder diffraction. The one phase ($2\vec{k}$-structure) was therefore used as framework for the determination of the magnetisation of $NiNb_2O_6$.

Table 7.3: Fitting parameters associated with different $\vec{k}$-models for the refinement of $NiNb_2O_6$'s magnetic structure. The volume fractions of the two types of domains are presented at the bottom of the table.

propagation vector	GOF	R_p (%)	R_{wp} (%)
$(\frac{1}{2}, \frac{1}{2}, 0)$	3.64	5.11	7.44
$(0, \frac{1}{2}, 0)$	6.04	6.75	12.35
$(\frac{1}{2}, \frac{1}{2}, 0)$+$(0, \frac{1}{2}, 0)$	2.96	4.12	6.06
Two phases	3.17	4.52	6.48

7.5.4 A new model for the magnetic structure of $NiNb_2O_6$

The 7 isotropy subgroups were utilised as models (within the $2\vec{k}$-structure framework) for the determination of the magnetic structure of $NiNb_2O_6$. Rietveld refinements of the 1.5 K-neutron diffraction pattern, with *Jana*, were thus performed for each Shubnikov space groups.

Consider the case where the model is the isotropy subgroup P_b2/c. The Rietveld refinement of a NDP based on this model is presented in Figure 7.8. The red dots and the continuous black represent the measured and theoretical patterns, respectively. The green ticks are the Bragg peak positions of a lattice with the space symmetry P_b2/c. The blue line at the bottom of Figure 7.8 is derived by subtracting the measured profile from the calculated profile.

There are clear discrepancies between the experimental (red dots) and calculated (black line) profiles. This is illustrated by the presence of peaks in the blue curve. The dissimilarities occur at 2θ equal 12.2, 39.3, 49.1 and around 67.7°. For instance, the fit doesn't take into account the reflection (0 1 0) at 12.2°. Elsewhere there is a difference between the intensity of the experimental data (red dots) and the theoretical model (black line), for the reflection (0 2 6) at 39.3°;in fact

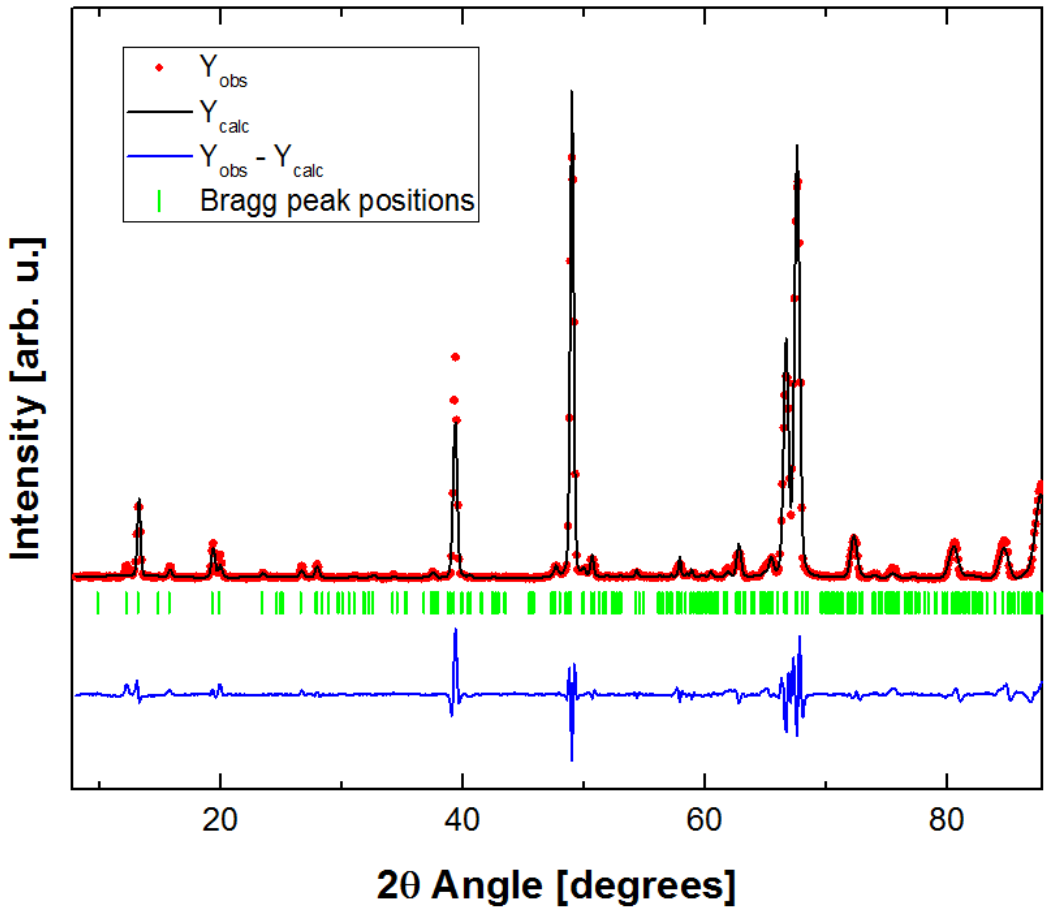

Figure 7.8: Rietveld refinement of the 1.5 K-neutron powder diffraction, using the isotropy subgroup P_b2/c as model. The red dots and the continuous black represent the measured and theoretical patterns, respectively. The difference between the measured and calculated profile is illustrated by the blue line. The green ticks are the Bragg peak positions.

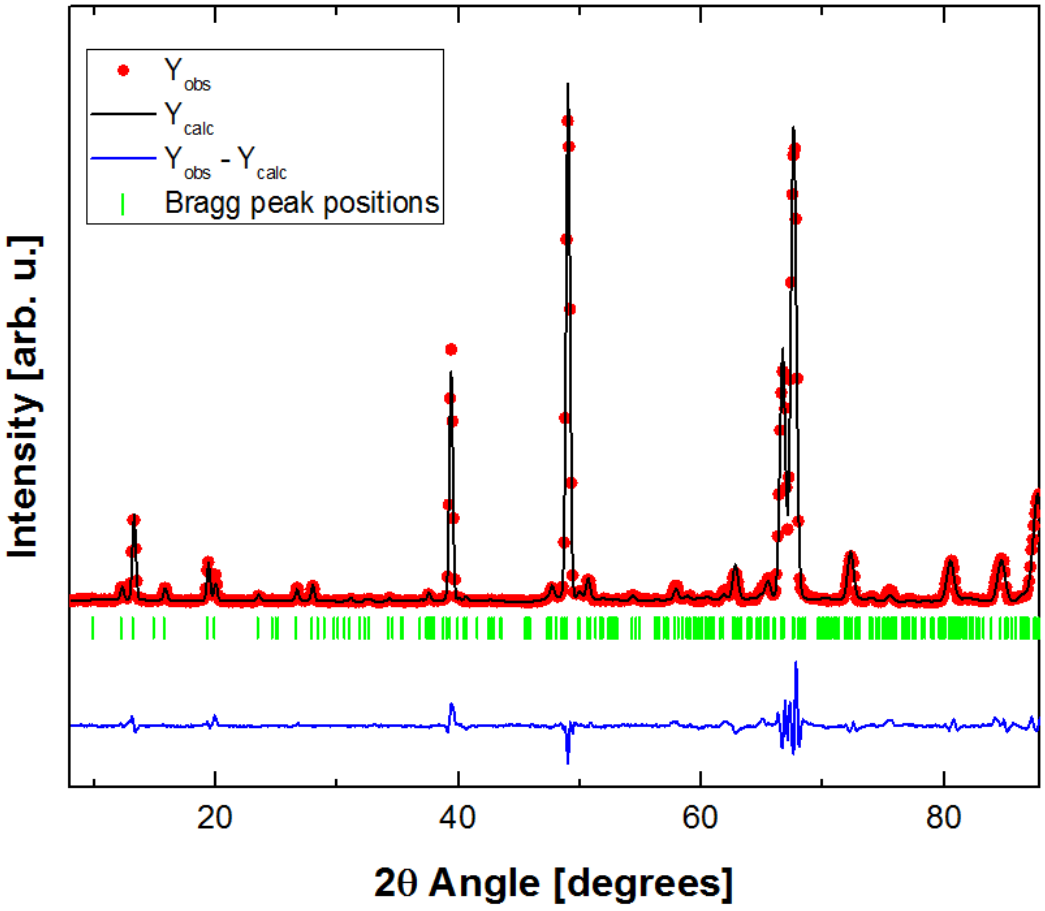

Figure 7.9: Rietveld refinement of the 1.5 K-neutron powder diffraction, using the isotropy subgroup P_b2_1 as model. The red dots and the continuous black represent the measured and theoretical patterns, respectively. The green ticks are the Bragg peak positions and the blue line corresponds to the difference between the measured and calculated profile.

the calculated intensity value is about two thirds of the measured value. All these discrepancies indicate that the subgroup P_b2/c can not be considered as model for the sublattice magnetisation of $NiNb_2O_6$. Consequently Rietveld refinements based on the other 6 subgroups have been performed.

Additionally, a Rietveld refinement based isotropy subgroup P_b2_1 was performed with *Jana*. The result is presented in Figure 7.9. The red dots and black line illustrate the experimental and calculated data, respectively. The difference between these two values at each 2θ angle corresponds to the blue line. The Bragg peak positions of a lattice whose space group symmetry is P_b2_1 are indicated by the green ticks.

The fit (black line) in Figure 7.9 fits well the experimental data recorded at 1.5 K, as the blue line is almost a straight line except at 39.3 and 67.7°. The reflection (0 1 0) which appears 12.2° is well fitted in comparison with the fit in Figure 7.8. Although some of discrepancies in intensity encountered in Figure 7.8 persist, they are improved. For instance, the ratio between the intensity values of the calculated and experimental profile at 39.3° is no longer $\frac{2}{3}$ but $\frac{9}{10}$. However, the refinement factors associated with P_b2_1 fluctuate throughout the refinement. GOF, R_p, R_{nucl} and

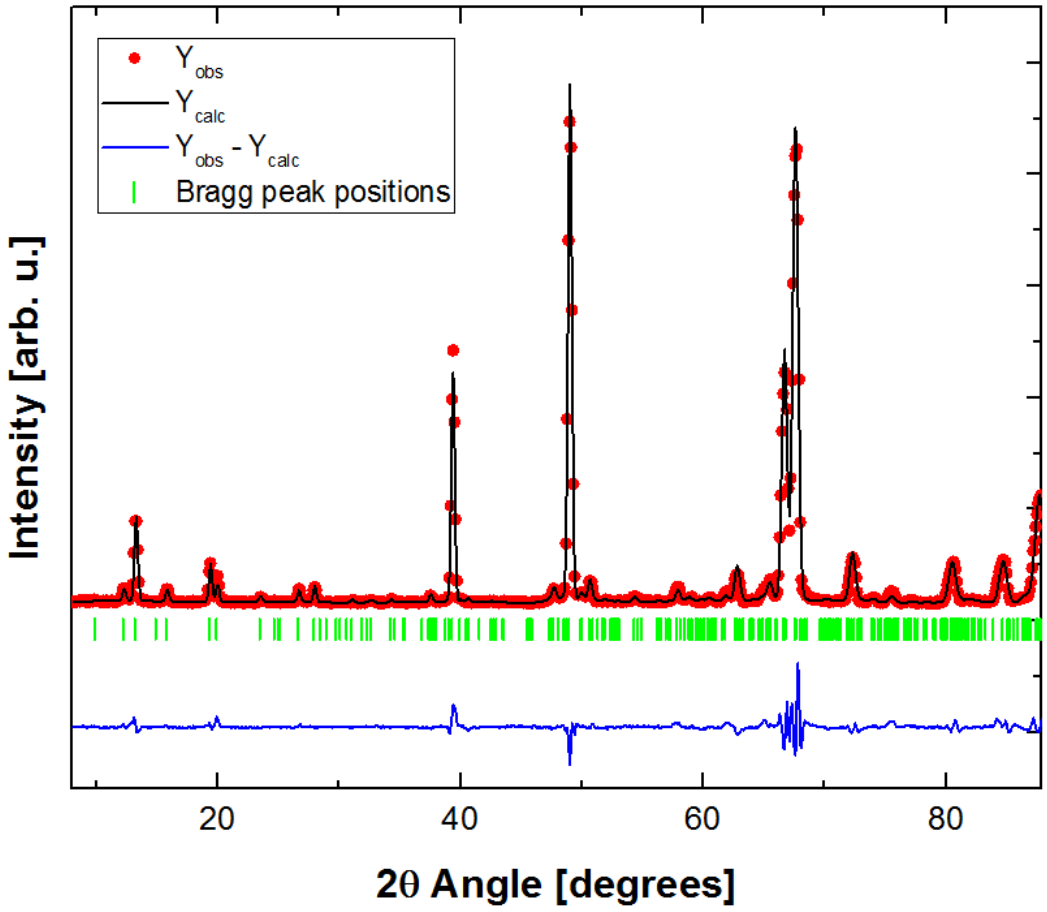

Figure 7.10: Rietveld refinement of the 1.5 K-neutron powder diffraction, using the isotropy subgroup P_b2_1/c as model. The red dots and the continuous black represent the measured and theoretical patterns, respectively. The green ticks are the Bragg peak positions and the blue line corresponds to the difference between the measured and calculated profile.

R_{mag} oscillate around the respective following values: 4.29, 5.54 %, 5.82 % and 14.62 %. GOF is the goodness of fit. As the refinement did not converge this Shubnikov subgroup was ruled out.

The best fitting of the neutron diffraction patterns measured below T_N was obtained for the isotropy subgroup P_b2_1/c. The latter is the subgroup with the highest symmetry space group. The result of the Rietveld refinement of the 1.5 K-neutron diffraction pattern, is presented in Figure 7.10.

The fitting curves (black and blue lines) in Figure 7.10 are very similar to those in Figure 6.9. For instance, the ratio between the intensity values of the calculated and measured profile at 39.3° is around $\frac{9}{10}$. This refinement differs from the previous as the refinements converge; in addition the values of GOF, R_p, R_{nucl} and R_{mag} obtained at the end of the refinement were the lowest ones. GOF, R_p, R_{nucl} and R_{mag} converge to 3.71, 5.39 %, 5.47 % and 12.80 % respectively. Hence, the best candidate (model) for the magnetic structure of $NiNb_2O_6$ is P_b2_1/c.

The magnetic structure associated with this model is presented in Figure 7.11. In this figure the bigger cell represents the unit cell of the magnetic structure and its lattice parameters are a

Table 7.4: Wyckoff positions and projections of magnetic moments of Ni^{2+} ions in the monoclinic unit cell.

Atom	**Wyckoff positions**		
	x	**y**	**z**
Ni_1	0	0.0776(0)	1/4
Ni_2	1/2	0.0776(0)	1/4
Ni_3	1/4	0.1724(0)	3/4
	Magnetic moments projections		
	M_x	M_y	M_z
Ni_1	-0.891(6)	0	-3.547(2)
Ni_2	1.715(3)	0	1.208(1)
Ni_3	0.288(5)	0.108(2)	-0.032(2)

= 27.941(4) Å, b = 11.326(0) Å and c = 5.005(0) Å. The small cell is the unit cell of the nuclear structure.The magnetic unit cell is obtained from the nuclear unit cell by doubling the lengths along the [1 0 0] and [0 1 0] directions. The blue spheres and the red arrows represent the magnetic Ni^{2+} ions and their magnetic moments, respectively. The magnetic moments lie in the a-c plane. In addition the magnetic moments (red arrows) do not all have the same magnitude nor the same orientations. The magnitude of the magnetic moments of Ni^{2+} ions which are situated at x = 0 and x = 1 is higher than those which are in the middle of unit the unit cell. However, the magnitude and orientation of Ni^{2+} ions located at x = 0 and x = 1 are identical. For the sake of simplicity these ions will be called Ni_1.These ions have an antiferromagnetic arrangement of the magnetic moments with the sequence -up-up-down- along the b-axis.

There are three orbits or non-equivalent Ni^{2+} in the magnetic structure of $NiNb_2O_6$. The first orbit corresponds to the position on the facets of the monoclinic unit cell along the b-$\not c$ plane. These nickel ions are represented by atom 1 in Figure 7.11 and refer to Ni_1. Ni_2 refer to Ni^{2+} ions located at the middle of the unit cell: x = $\frac{1}{2}$. The other non-equivalent nickel ions are designated by Ni_3 and corresponds to nickel ions located at x = $\frac{1}{4}$. Ni_2 and Ni_3 are illustrated by the numbers 2 and 3 in Figure 7.11, respectively. The magnitudes of the magnetic moments of Ni^{2+} ions located in the parallelepiped in Figure 7.11 are lower than that of those which belong to the facets of the parallelepiped. Ni_2 have a bigger magnetic moment than that of Ni_3. The Wyckoff positions and the magnetic moments of orbits of $NiNb_2O_6$ are displayed in Table 7.4.
M_x, M_y and M_z are the projections of a magnetic moment along the [1 0 0], [0 1 0] and [0 0 1] directions. Table 7.4 shows that the magnitude of the magnetic moments is not uniform throughout the unit cell. Ni_1, Ni_2 and Ni_3 exhibit a magnetic moment of the order of 3.657(6), 2.098(6) and 0.309(5) μ_B/Ni^{2+}, respectively. For the sake of simplicity an uniform magnitude of the magnetic moments within the lattice is one of the assumptions often made. Several Rietveld refinements were made under that constraints. However these refinements were mostly not successful, as the calculations did not converge.

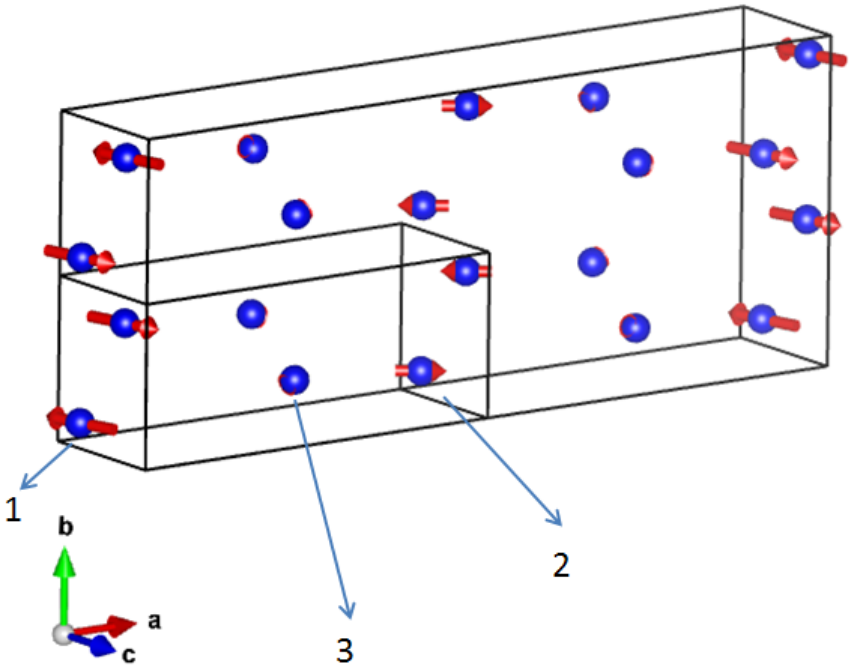

Figure 7.11: Magnetic structure unit cell of $NiNb_2O_6$ with P_b2_1/c as model. The blue spheres represent the Ni^{2+} ions and a red arrow is the magnetic moment it carries. 1, 2 and 3 refer to non-equivalent magnetic Ni^{2+} ions: Ni_1, Ni_2 and Ni_3, respectively.

7.6 Conclusion

Representation analysis and magnetic symmetry methods were both used to determine a model for the magnetic structure of $NiNb_2O_6$. Rietveld refinements suggest that the Shubnikov subgroup P_b2_1/c is the best model to describe the ordering of Ni^{2+} below $T_N = 5.6\,K$. The growth of $NiNb_2O_6$ single crystals via the floating zone technique[84] is highly considered as perspective work. It is due to the fact that single crystals are the best type of crystal solid there exists to investigate the intrinsic properties of a material. For better understanding of the sublattice magnetic structure of the columbite $NiNb_2O_6$ polarised neutron diffraction on the grown single crystals is envisaged. This measurement will help establish the relationship between the two modulation vectors $\vec{k_1}$ and $\vec{k_1}$; but also the relationship between magnetic ion and propagation vectors. Polarised neutron diffraction will also enable the determination of the direction of the magnetic moments. Finally, magnetic susceptibility and field dependence magnetisation on the single crystals are envisaged, as they will shine light on the magnetic anisotropy in $NiNb_2O_6$.

Chapter 8

Conclusions and Outlook

This PhD thesis was about the measurement of thermoelectric transport properties - Seebeck coefficient, electrical and thermal conductivities - and the determination of the magnetic properties of some polycrystalline AB_2O_6 oxides. The temperature dependence of the thermoelectric properties and their analysis with several models helped to make significant conclusions, in the scope of the use of the AB_2O_6 semiconducting oxides in high-temperature thermoelectric applications. The core of this work was dedicated to magnetic structure determination from neutron powder diffraction. Two methods were used for this purpose and they are the representation analysis and magnetic symmetry refinement. These methods helped to shine a light on the magnetic structures of two nickel-based AB_2O_6 oxides. This Chapter briefly recounts the main contributions that the work contained in this thesis has made to the fields of thermoelecrtrics and powder neutron diffraction. It also throws light on few unanswered questions, which can be the beginning of future investigations.

The first novel contribution of the work contained herein is the determination a new magnetic structure for $NiTa_2O_6$. As previously never done before for this antiferromagnetic compound, both a Shubnikov group and a magnetic structure are attributed to the ordering of the magnetic moments within the magnetic lattice. In addition, the two previous magnetic models are compared to the new model derived in this study. Eventually the symmetry of the magnetic lattice indicates that the insulator $NiTa_2O_6$ has some magnetically induced electric polarisation along the c-axis.

The second novel contribution, previously never reported before, is the establishment of a magnetic model for the magnetic structure of the columbite $NiNb_2O_6$. Two propagation vectors are needed to describe the antiferromagnetic ordering below the Néel temperature. The 2-$\vec{k}$ sublattice magnetisation is characterised by non collinear magnetic moments, whose magnitude varies with respect to the Wyckoff positions in the magnetic lattice.

However, a few points related to these two new magnetic structures need to be addressed. The models were derived from powder neutron diffraction. Hence, these sublattice magnetisations are not intrinsic properties of $NiTa_2O_6$, nor $NiNb_2O_6$. Single crystals neutron diffraction is therefore

highly envisaged to confirm or refute the herein results. For instance, the use of polarised neutrons on $NiNb_2O_6$ single crystals will help better understand the relationship between the two modulation vectors and the magnetic moments. It will also shine light on the magnitude of the Ni^{2+} magnetic moments within the lattice. Polarisation measurements on $NiTa_2O_6$ should confirm the multiferroic character of the new magnetic structure model. To go further, the present work can be resumed by establishing a model, which will systematically relates the transitions between the possible sublattice magnetizations of a trirutile and its modulation in trirutile. It seems that the distribution of the cations in $NiTa_2O_6$ is at the origin of the discrepancies between the three magnetic structures.

The third novel contribution of this PhD thesis is the report of thermoelectric properties of Y-doped $CdSb_2O_6$ and WV_2O_6. This study aimed to identify new materials for thermoelectric technology, which may impact our society positively, in the foreseeable future. The temperature dependence of the thermopower data reveal that these compounds behave as *n*-type semiconductor materials. Analysis of the thermal conductivity of tungsten divanadate oxide indicates that the lattice contribution dominates the electronic contribution. The electrical conductivity data of WV_2O_6 was well reproduced by the variable range hopping (tunneling process) and the band model (delocalised electrons in closely stacked energy levels). These models are valid at low and high temperature, respectively. The power factors of both compounds, although few orders of magnitude lower than that of the state-of-the-art thermoelectric oxides, are comparable to that of some established TE materials.

In order for these two oxides to reach and/or outperform the best TE oxides, few points need to be addressed. First and foremost, the thermal conductivities of Y-doped $CdSb_2O_6$ need to measure for a complete characterization of their thermoelectric properties. It would thus lead to the determination of their figures of merit (ZT) for each of the compounds. Besides, the search for $Cd_{1-x}Y_xSb_2O_6$ systems with optimal thermoelectric properties will be restricted to compositions in which x is between 0 and 0.05 %. Regarding the trirutile WV_2O_6, this herein work discusses the TE properties of the intrinsic WV_2O_6. Appropriate doping of this columbite may therefore lead to an enhance of its thermoelectric properties. Single crystals growth of various compositions of the trirutile $V_xW_{1-x}O_6$ (with $1.7 \leq x \leq 2$) are envisaged. The study of the effect of the compositions on their Seebeck coefficient, electrical and thermal conductivities will then be explored.

Finally, this thesis emphasizes the importance of the structural-property relationship; as understanding the bond between microscopic (atoms) and macroscopic scales (physical properties) is essential to tailor materials for specific applications. For the herein work the application is the power generation via the thermoelectric effect. To understand and predict the properties of a material one ought to seek for the intrinsic transformations which are embedded in the studied material itself: the crystal structure symmetries.

Poster presentation

During my doctorate in physics I have participated at various conferences. I presented a poster on the work on Y-doped $CdSb_2O_6$ at the following conferences:

- Electro Ceramics XV in Limoges, 27-29 June in 2016.
- NANOENERGY 2016 programme in Liverpool, 27-29 July 2016 .
- EPSRC Thermoelectric Network UK Meeting, 14-15 Feb 2017, Manchester.
- Electro-chemistry (ECS) conference, 8^{th} June 2017, Liverpool.

Articles

Paper, on the magnetic structure of $NiTa_2O_6$, in progress.

Appendices

Appendix A

Group Theory fundamentals

The application of a symmetry operation leaves an object unchanged. A set of symmetry elements {g1, g2, ...,gn} form a group if there exists an operation which assigns to each ordered pair g_i, $g_j \in$ G another element of G[202]. In addition, a group must fulfill the following four criteria:

- The product of any two elements of the group is itself an element of the group, e.g. $g_i g_j = g_k$, where g_k is another member of the group.
- The associative law must be valid: $(g_i g_j)g_k = g_i(g_j g_k)$.
- There exists a unit element e (also called the identity element) such that the product of e with any element of the group leaves that element unchanged[202], i.e. $g_i e = e g_i = g_i$.
- Finally for every member g_i of G there exists an inverse element g_i^{-1}, such that $g_i^{-1} g_i = g_i g_i^{-1} = e$.

Definition: A class is defined as all the elements in the group that are related by conjugation[202,207]. Two elements g_i and g_j are conjugate to each other if they fulfill the relation:

$$g_i = g_k^{-1} g_j g_k \tag{A.1}$$

where g_k is any arbitrary element of the group.

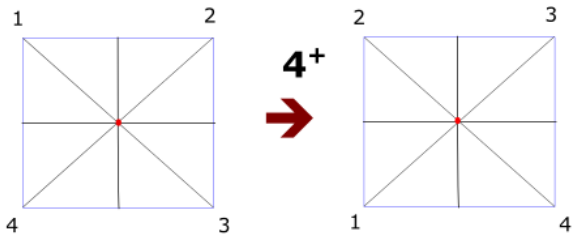

Figure A.1: Symmetry operations of a square. An object exhibits a symmetry if the application of the corresponding symmetry operation leaves the object unchanged. This is the case of a rotation of 90°, 4^+, which transforms the square on the left into the second on the right.

There exist different types of symmetry operations: rotations, reflections, inversions and improper rotations[202]. A symmetry operation transforms an object into a new object which is identical to the original one - it leaves it invariant. For example consider the group associated with a square, see Figure 1.7. The numbers 1, 2, 3 and 4 label the vertices and help to visualize the symmetry operations. There are 8 symmetry operations which transform the vertices but leave the square unchanged and they form a group:

$$G = \{1, 2, 4^+, 4^-, m_x, m_y, m_d, m_d^{'}\}. \tag{A.2}$$

The first four symmetry elements are the identity, and 4-fold and 2-fold rotation axes, respectively. The 4-fold and 2-fold rotations rotate the square about its centre by ∼90 and 180 °, respectively. m_x and m_y represent two mirror planes - perpendicular to each other - intersecting the middle of two opposites sides of the square. The diagonal mirror planes m_d and $m_d^{'}$ are located along the diagonal lines in black in Figure 1.7. In condensed matter physics one deals with crystallographic structures, also called nuclear structures, which arrange atoms within a specific lattice (orthorhombic, cubic, monoclinic, etc). The symmetries of the crystal then place it in a specific group. A group of symmetry operations which leave a fixed point in space are called point group operations. Certain symmetry operations may require translations which leave no point fixed. All crystal structures can be described by one of the 230 space groups, tabulated in the International Tables for Crystallography[233]. The point group of the square shown in Figure 1.2 is 4mm.

Appendix B

Magnetism Fundamental

B.1 Introduction

In 1907 Pierre Weiss published his work on magnetic materials[234]. This work highlighted the idea of a molecular field: it stipulates that the observed magnetization (sum of all magnetic moments) originates from an intense magnetic field of internal origin. This was the birth of the concept of ferromagnetism and ultimately the start of the study of magnetic structure. Magnetic structures comprise an ensemble of ordered magnetic atoms within a particular crystallographic lattice. The magnetism originates from the presence of unpaired electrons in these atoms. This is typically seen in some transition metal elements such as Fe, Ni and Co. Below a critical temperature - the Curie temperature - the internal field forces the moments to align in the same direction. Later on Louis Néel[235] extended this idea by conjecturing that the internal field can take a positive or negative value. In the latter case he showed that below a critical temperature known as the Néel temperature it was possible to observe an ordered arrangement of equal numbers of oppositely directed magnetic moments. Materials showing such behaviour are called antiferromagnetic systems. The blue arrows in Figure 1.6 represent the magnetic moments of some magnetic atoms. In the first configuration Figure 1.6a) one deals with a ferromagnetic ensemble, as all ordered magnetic moments have the same direction. On the other hand the number of arrows pointing up is an equal to the number of arrows pointing down: it is an antiferromagnetic ensemble.

B.2 Magnetic interactions in magnetic ordered systems

To understand the different magnetic states, it is important to review the different microscopic mechanisms related to the magnetic moments. Hence this section reviews the types of interactions which lead to a long-range ordering of the moments.

B.2.1 The direct exchange interaction

The direct exchange arises from the overlap of the wave functions of two neighbouring magnetic atoms. It is known as direct exchange because the interaction occurs without the need for an

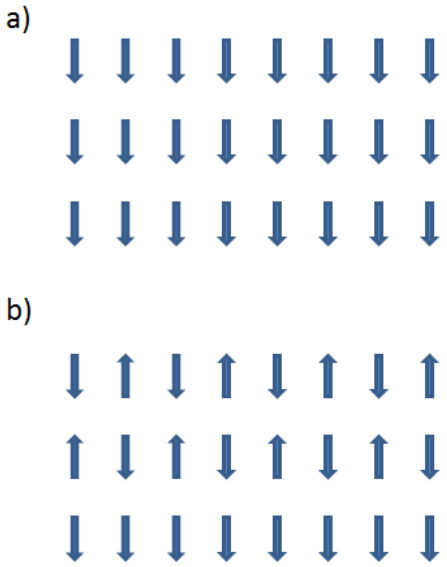

Figure B.1: Illustration of two magnetic states. An arrow represents a magnetic moment. The top part a) shows an ensemble of blue arrows all pointing down: one deals with a ferromagnetic system. b) corresponds to a antiferromagnetic system, as there is an equal number of oppositely directed magnetic moments.

intermediary[66]. It is due to the electrostatic or Coulomb potential, and Pauli principle between the electrons. The Pauli principle states that two or more identical fermions (particles with half-integer spin) cannot occupy the same quantum state within a quantum system simultaneously. For instance, if two electrons reside in the same orbital they must have opposite half-integer spins of $\frac{1}{2}$ ($\uparrow$) and -$\frac{1}{2}$ ($\downarrow$). Consider the system which consists of two orbitals ϕ_i and ϕ_j centred on two different atoms (A and B) and two electrons (1 and 2), see Figure B.1.

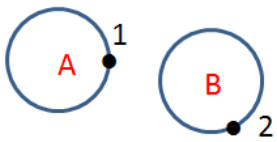

Figure B.2: Electrons 1 and 2 orbiting around the nucleus of atoms A and B, respectively.

The resulting wave function ψ_i is given by:

$$\psi(\mathbf{r_1}, \mathbf{r_2}) = \frac{1}{\sqrt{2}}[\phi_i(\mathbf{r_1})\phi_j(\mathbf{r_2}) \pm \phi_i(\mathbf{r_2})\phi_j(\mathbf{r_1})]. \tag{B.1}$$

This function must be symmetrical (+) or anti-symmetrical (-) according to the Pauli principle. The distance r_1 is the distance between electron 1 and the nuclei of atom A. r_2 plays the same role for electron 2 and atom B. The Coulomb repulsion between electrons 1 and 2 can be expressed by:

$$\langle \frac{e^2}{4\pi\epsilon_0|\mathbf{r_1} - \mathbf{r_1}|} \rangle = J \pm K, \tag{B.2}$$

with J been the exchange integral between the two electrons over the two orbitals, and K been a constant. J is also known as the exchange coupling constant. Eq. (1.1) shows that the magnitude of the direct exchange becomes negligible as the distance between the atoms (hence electrons) increases. Nevertheless the exchange is valid for all neighbouring atoms. This is expressed by the following Hamiltonian:

$$\mathcal{H} = -\frac{1}{2}\sum_{i,j} J_{i,j}\mathbf{S_i}.\mathbf{S_j}. \tag{B.3}$$

Eq. (1.3) is known as the Heisenberg Hamiltonian. J_{ij} is the exchange coupling constant between the i^{th} and j^{th}. The pre-factor $\frac{1}{2}$ is there to avoid the double-counting over the set of spins. Note that this equation corresponds to the Ising model of ferromagnetism except that in the Ising model one deals with a one- or two-dimensional systems[236,237]. However in many materials, such as the transition metal compounds, the magnetic ions are separated by non-magnetic ions . The magnitude of the direct exchange becomes negligible because of the larger distance between magnetic ions. Another mechanisms are, therefore, required to explain the magnetism in these structures.

B.2.2 The indirect exchange interaction

In ionic solids the indirect exchange is one of the interactions between magnetic ions, which need to be taken into account to explain the long-range order in these systems. One speaks of indirect exchange as an intermediate is required for "the communication" between magnetic ions. The intermediate are typically non-magnetic ions (for instance O^{2-}) placed between the magnetic ions. Since the interaction operates over longer-ranged distances with respect to the short-ranged distances of the direct exchange the indirect exchange interaction is often called superexchange interaction.
The ordering of the magnetic moments in MnO illustrates well the importance of the superexchange. MnO crystallizes in a face centered cubic lattice, as shown in Figure B.2(a). The black and red spheres represent the Mn and O atoms, respectively.

Superexchange occurs as there is overlap between the p orbitals of O^{2-} ions and d orbitals of Mn^{2+} ions. Consider the case where the magnetism in a Mn^{2+} ion is due to a single unpaired electron. In the antiferromagnetic configuration, electrons of two neighbouring manganese ions can both hybridize with 1 p-electron of ceO^{2-}, see Figure 1.2(b). Hence the antiferromagnetic ordering is favoured in this compound, as it lowers the energy of the system; and allows a delocalization of electrons over the whole structure. Note that the p- and d-orbitals are said to be hybridized. The superexchange[66] is a second-order process and is derived from second-order perturbation theory. From second order pertubation theory, it can be shown that the energy of the indirect exchange interaction is related to the hopping t of the electron between magnetic and non-magnetic ions, with the average repulsive Coulomb interaction U between electrons. More details on the superexchange interaction can be found in the papers by Anderson[238,239], Goodenough[240,241] and Kanamori[242].

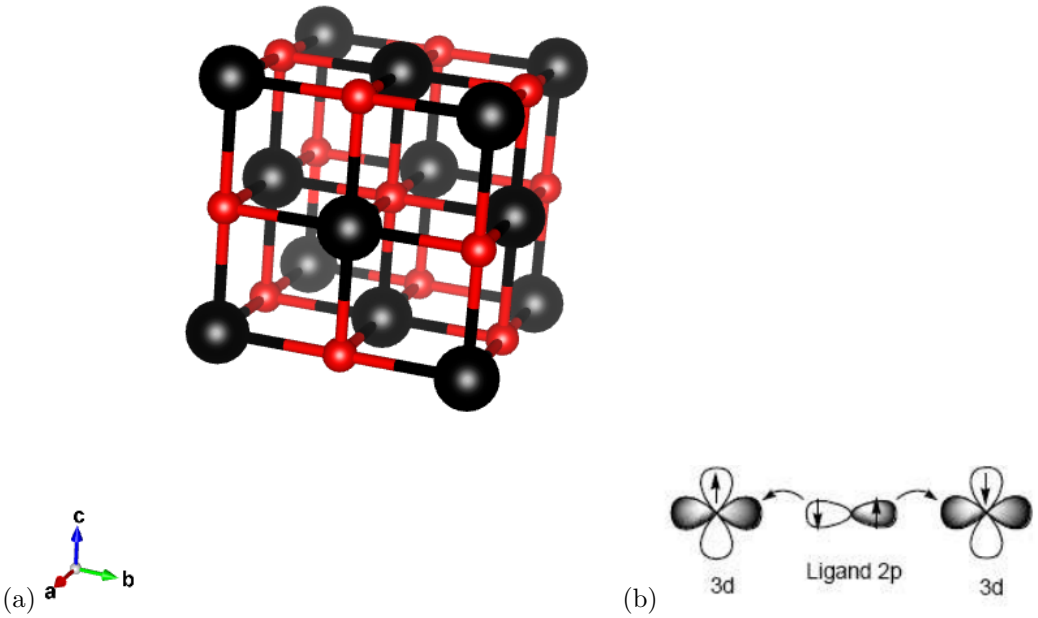

(a) (b)

Figure B.3: (a) Unit cell of the crystal structure of MnO. Neighbouring manganese Mn^{2+} ions are connected via O^{2-} ions. (b) Superexchange between O *p*-orbital and Mn *d*-orbitals. Source: *http://magnetism.eu/esm/2013/*.

B.2.3 The Ruderman-Kittel-Kassuya-Yosida (RKKY) interaction

In some materials the conduction electrons are responsible for the ordering of the magnetic moments. A localized magnetic moment polarizes the conduction electrons . The polarization of the conduction electrons is then transferred to a localized magnetic moment at distance r away from the original magnetic moment. This interaction is therefore indirect like the superexchange, as there is no direct connection between the magnetic ions. This interaction is known as the RKKY interaction, after the discoverers of the phenomena: Ruderman and Kittel[243], Kasuya[244] and Yosida[244]. It is the dominant exchange interaction in metals. For a 3-dimensional free electron gas the coupling constant of the RKKY interaction is given by :

$$J^{3D}_{RKKY}(r) = -\frac{1}{\pi} J n_o(\epsilon_F) \frac{cos(2k_F r)}{(2k_F r)^3}, \tag{B.4}$$

where k_F is the radius of the conduction electrons Fermi surface, n_o (ϵ_F) is the density of states of electrons near the Fermi energy. J is the direct exchange coupling. Eq. (1.4) shows that the RKKY is a long range interaction. Moreover the interaction strength J^{3D}_{RKKY} oscillates with distance r from between the spins due to a specific Fermi wavelength of electrons.

Bibliography

[1] N Nakićenović, A Grübler, and A McDonald. *Global energy perspectives*. Cambridge University Press, 1998.

[2] N Nakicenovic and M Jefferson. Global energy perspectives to 2050 and beyond. 1995.

[3] A Grubler, M Jefferson, A McDonald, S Messner, N Nakicenovic, H-H Rogner, and L Schrattenholzer. Global energy perspectives to 2050 and beyond. 1995.

[4] LE Bell. Cooling, heating, generating power, and recovering waste heat with thermoelectric systems. *Science*, 321(5895):1457–1461, 2008.

[5] J Yang and FR Stabler. Automotive applications of thermoelectric materials. *Journal of Electronic Materials*, 38(7):1245–1251, 2009.

[6] J Yang. Potential applications of thermoelectric waste heat recovery in the automotive industry. In *Thermoelectrics, 2005. ICT 2005. 24th International Conference on*, pages 170–174. IEEE, 2005.

[7] HJ Goldsmid. *Introduction to thermoelectricity*, volume 121. Springer, 2010.

[8] GS Nolas, J Sharp, and J Goldsmid. *Thermoelectrics: basic principles and new materials developments*, volume 45. Springer Science & Business Media, 2013.

[9] H Goldsmid. *Thermoelectric refrigeration*. Springer, 2013.

[10] HJ Goldsmid. The thermoelectric and related effects. In *Introduction to Thermoelectricity*, pages 1–7. Springer, 2016.

[11] TM Tritt. Thermoelectric phenomena, materials, and applications. *Annual Review of Materials Research*, 41:433–448, 2011.

[12] J Zheng. Recent advances on thermoelectric materials. *Frontiers of Physics in China*, 3(3):269–279, 2008.

[13] A Shakouri. Recent developments in semiconductor thermoelectric physics and materials. *Annual Review of Materials Research*, 41, 2011.

[14] GJ Snyder and ES Toberer. Complex thermoelectric materials. *Nature Materials*, 7(2):105–114, 2008.

[15] JW Fergus. Oxide materials for high temperature thermoelectric energy conversion. *Journal of the European Ceramic Society*, 32(3):525–540, 2012.

[16] M Ohtaki. Oxide thermoelectric materials for heat-to-electricity direct energy conversion. *Kyushu University Global COE Program Novel Carbon Resources Sciences Newsletter*, 3, 2010.

[17] AF Ioffe, LS Stil'Bans, EK Iordanishvili, TS Stavitskaya, A Gelbtuch, and G Vineyard. Semiconductor thermoelements and thermoelectric cooling. *Physics Today*, 12:42, 1959.

[18] GD Mahan and JO Sofo. The best thermoelectric. *Proceedings of the National Academy of Sciences*, 93(15):7436–7439, 1996.

[19] MW Gaultois, TD Sparks, CKH Borg, R Seshadri, WD Bonificio, and DR Clarke. Data-driven review of thermoelectric materials: performance and resource considerations. *Chemistry of Materials*, 25(15):2911–2920, 2013.

[20] FD Rosi. Thermoelectricity and thermoelectric power generation. *Solid-State Electronics*, 11(9):833IN1849–848IN2868, 1968.

[21] C Wood. Materials for thermoelectric energy conversion. *Reports on Progress in Physics*, 51(4):459, 1988.

[22] DM Rowe. *Thermoelectrics handbook: macro to nano*. CRC press, 2005.

[23] D Champier. Thermoelectric generators: A review of applications. *Energy Conversion and Management*, 140:167–181, 2017.

[24] A Killander and JC Bass. A stove-top generator for cold areas. In *Thermoelectrics, 1996., Fifteenth International Conference on*, pages 390–393. IEEE, 1996.

[25] RY Nuwayhid, DM Rowe, and Ga Min. Low cost stove-top thermoelectric generator for regions with unreliable electricity supply. *Renewable Energy*, 28(2):205–222, 2003.

[26] R *Bjørk* and KK Nielsen. The performance of a combined solar photovoltaic (pv) and thermoelectric generator (teg) system. *Solar Energy*, 120:187–194, 2015.

[27] D Kraemer, L Hu, A Muto, X Chen, G Chen, and M Chiesa. Photovoltaic-thermoelectric hybrid systems: a general optimization methodology. *Applied Physics Letters*, 92(24):243503, 2008.

[28] R Amatya and RJ Ram. Trend for thermoelectric materials and their earth abundance. *Journal of Electronic Materials*, 41(6):1011–1019, 2012.

[29] SE Kesler and AC Simon. *Mineral resources, economics and the environment*. Cambridge University Press, 2015.

[30] K Koumoto, I Terasaki, and R Funahashi. Complex oxide materials for potential thermoelectric applications. *Mrs Bulletin*, 31(3):206–210, 2006.

[31] I Terasaki, Y Sasago, and K Uchinokura. Large thermoelectric power in $NaCo_2O_4$ single crystals. *Physical Review B*, 56(20):R12685, 1997.

[32] TD Sparks. *Oxide Thermoelectrics: The Role of Crystal Structure on Thermopower in Strongly Correlated Spinels*. PhD thesis, Harvard University, 2012.

[33] W Koshibae, K Tsutsui, and S Maekawa. Thermopower in cobalt oxides. *Physical Review B*, 62(11):6869, 2000.

[34] M Ito, T Nagira, D Furumoto, S Katsuyama, and H Nagai. Synthesis of $Na_xCo_2O_4$ thermoelectric oxides by the polymerized complex method. *Scripta Materialia*, 48(4):403–408, 2003.

[35] Ryoji Funahashi, Ichiro Matsubara, Hiroshi Ikuta, T Takeuchi, U Mizutani, and S Sodeoka. An oxide single crystal with high thermoelectric performance in air. *Japanese Journal of Applied Physics*, 39(11B):L1127, 2000.

[36] R Funahashi and M Shikano. $Bi_2Sr_2Co_2Oy$ whiskers with high thermoelectric figure of merit. *Applied Physics Letters*, 81(8):1459–1461, 2002.

[37] RR Heikes and RW Ure. *Thermoelectricity: science and engineering*. Interscience Publishers, 1961.

[38] K Shirai and K Yamanaka. Mechanism behind the high thermoelectric power factor of $SrTiO_3$ by calculating the transport coefficients. *Journal of Applied Physics*, 113(5):053705, 2013.

[39] ME Melo Jorge, MR Nunes, R Silva Maria, and D Sousa. Metal- insulator transition induced by Ce doping in $CaMnO_3$. *Chemistry of Materials*, 17(8):2069–2075, 2005.

[40] R Funahashi, A Kosuga, N Miyasou, E Takeuchi, S Urata, K Lee, H Ohta, and K Koumoto. Thermoelectric properties of $CaMnO_3$ system. In *Thermoelectrics, 2007. ICT 2007. 26th International Conference on*, pages 124–128. IEEE, 2007.

[41] M Molinari, DA Tompsett, SC Parker, F Azough, and R Freer. Structural, electronic and thermoelectric behaviour of $CaMnO_3$ and $CaMnO_{3-\delta}$. *Journal of Materials Chemistry A*, 2(34):14109–14117, 2014.

[42] FP Zhang, QM Lu, X Zhang, and JX Zhang. First principle investigation of electronic structure of $CaMnO_3$ thermoelectric compound oxide. *Journal of Alloys and Compounds*, 509(2):542–545, 2011.

[43] C Li, KCK Soh, and P Wu. Formability of ABO_3 perovskites. *Journal of Alloys and Compounds*, 372(1):40–48, 2004.

[44] AS Bhalla, R Guo, and R Roy. The perovskite structure—a review of its role in ceramic science and technology. *Materials Research Innovations*, 4(1):3–26, 2000.

[45] H Taguchi, M Nagao, T Sato, and M Shimada. High-temperature phase transition of $CaMnO_{3-\delta}$. *Journal of Solid State Chemistry*, 78(2):312–315, 1989.

[46] L Bocher, MH Aguirre, R Robert, D Logvinovich, S Bakardjieva, J Hejtmanek, and A Weidenkaff. High-temperature stability, structure and thermoelectric properties of $CaMn_{1-x}Nb_xO_3$ phases. *Acta Materialia*, 57(19):5667–5680, 2009.

[47] L Bocher, MH Aguirre, D Logvinovich, A Shkabko, R Robert, M Trottmann, and A Weidenkaff. $CaMn_{1-x}Nb_xO_3$ ($x \leq 0.08$) perovskite-type phases as promising new high-temperature n-type thermoelectric materials. *Inorganic Chemistry*, 47(18):8077–8085, 2008.

[48] T Okuda, K Nakanishi, S Miyasaka, and Y Tokura. Large thermoelectric response of metallic perovskites: $Sr_{1-x}La_xTiO_3$ ($0 < x < 0.1$). *Physical Review B*, 63(11):113104, 2001.

[49] LF Mattheiss. Energy bands for $KNiF_3$, $SrTiO_3$, $KMoO_3$, and $KTaO_3$. *Physical Review B*, 6(12):4718, 1972.

[50] S Ohta, T Nomura, H Ohta, and K Koumoto. High-temperature carrier transport and thermoelectric properties of heavily la-or Nb-doped $SrTiO_3$ single crystals. *Journal of Applied Physics*, 97(3):034106, 2005.

[51] S Ohta, T Nomura, H Ohta, M Hirano, H Hosono, and K Koumoto. Large thermoelectric performance of heavily Nb-doped $SrTiO_3$ epitaxial film at high temperature. *Applied Physics Letters*, 87(9):092108, 2005.

[52] KH Lee, SW Kim, H Ohta, and K Koumoto. Ruddlesden-popper phases as thermoelectric oxides: Nb-doped SrO $(SrTiO_3)_n$ (n= 1, 2). *Journal of Applied Physics*, 100(6):063717, 2006.

[53] YF Wang, KH Lee, H Ohta, and K Koumoto. Fabrication and thermoelectric properties of heavily rare-earth metal-doped $SrO(SrTiO_3)_n$ (n= 1, 2) ceramics. *Ceramics International*, 34(4):849–852, 2008.

[54] N Wang, H Chen, H He, W Norimatsu, M Kusunoki, and K Koumoto. Enhanced thermoelectric performance of Nb-doped $SrTiO_3$ by nano-inclusion with low thermal conductivity. *Scientific Reports*, 3, 2013.

[55] KP Ong, DJ Singh, and P Wu. Analysis of the thermoelectric properties of n-type ZnO. *Physical Review B*, 83(11):115110, 2011.

[56] BG Lewis and DC Paine. Applications and processing of transparent conducting oxides. *Mrs Bulletin*, 25(8):22–27, 2000.

[57] T Minami. Transparent conducting oxide semiconductors for transparent electrodes. *Semiconductor Science and Technology*, 20(4):S35, 2005.

[58] T Tsubota, M Ohtaki, K Eguchi, and H Arai. Thermoelectric properties of Al-doped ZnO as a promising oxidematerial for high-temperature thermoelectric conversion. *Journal of Materials Chemistry*, 7(1):85–90, 1997.

[59] M Ohtaki, K Araki, and K Yamamoto. High thermoelectric performance of dually doped ZnO ceramics. *Journal of Electronic Materials*, 38(7):1234–1238, 2009.

[60] N Ma, J-F Li, BP Zhang, YH Lin, LR Ren, and GF Chen. Microstructure and thermoelectric properties of $Zn_{1-x}Al_xO$ ceramics fabricated by spark plasma sintering. *Journal of Physics and Chemistry of Solids*, 71(9):1344–1349, 2010.

[61] HP Beck. A study on AB_2O_6 compounds, part ii: the branches of the hcp family. *Zeitschrift für Kristallographie-Crystalline Materials*, 227(12):843–858, 2012.

[62] H Bärnighausen. Group-subgroup relations between space groups: a useful tool in crystal chemistry. *Commun. Math. Chem*, 9:139–175, 1980.

[63] O Bock and U Müller. Symmetrieverwandtschaften bei varianten des ReO_3-typs. *Zeitschrift für Anorganische und Allgemeine Chemie*, 628(5):987–992, 2002.

[64] HD Megaw. *Crystal structures: a working approach*. Number 10. Saunders Limited., 1973.

[65] WH Baur. The rutile type and its derivatives. *Crystallography Reviews*, 13(1):65–113, 2007.

[66] S Blundell. Magnetism in condensed matter, 2003.

[67] JT Szymanski and JD Scott. A crystal-structure refinement of synthetic brannerite, UTi_2O_6, and its bearing on rate of alkaline-carbonate leaching of brannerite in ore. *The Canadian Mineralogist*, 20(2):271–280, 1982.

[68] FR Ahmed and WH Barnes. The crystal structure of rossite. *The Canadian Mineralogist*, 7(5):713–726, 1963.

[69] S Katsura. Statistical mechanics of the anisotropic linear heisenberg model. *Physical Review*, 127(5):1508, 1962.

[70] SM Eicher, JE Greedan, and KJ Lushington. The magnetic properties of $FeTa_2O_6$. magnetic structure and low-dimensional behavior. *Journal of Solid State Chemistry*, 62(2):220–230, 1986.

[71] LI Zawislak, JBM da Cunha, A Vasquez, and CA Dos Santos. Mössbauer study of the planar antiferromagnet $FeTa_2O_6$. *Solid State Communications*, 94(5):345–348, 1995.

[72] M Takano and T Takada. Magnetic properties of MTa_2O_6 (M= Fe, Co or Ni). *Materials Research Bulletin*, 5(6):449–454, 1970.

[73] H Weitzel and S Klein. Magnetische struktur des trirutils $FeTa_2O_6$. *Acta Crystallographica Section A: Crystal Physics, Diffraction, Theoretical and General Crystallography*, 30(3):380–384, 1974.

[74] EML Chung, MR Lees, GJ McIntyre, C Wilkinson, G Balakrishnan, JP Hague, D Visser, and D McK Paul. Magnetic properties of tapiolite ($FeTa_2O_6$); a quasi two-dimensional (2d) antiferromagnet. *Journal of Physics: Condensed Matter*, 16(43):7837, 2004.

[75] Y Muraoka, T Idogaki, and N Uryû. Susceptibility analysis of two-dimensional antiferromagnet $FeTa_2O_6$. *Journal of the Physical Society of Japan*, 57(5):1758–1761, 1988.

[76] GA Baker Jr. Application of the padé approximant method to the investigation of some magnetic properties of the ising model. *Physical Review*, 124(3):768, 1961.

[77] GA Baker Jr, GS Rushbrooke, and HE Gilbert. High-temperature series expansions for the spin-$\frac{1}{2}$ heisenberg model by the method of irreducible representations of the symmetric group. *Physical Review*, 135(5A):A1272, 1964.

[78] GA Baker Jr, HE Gilbert, J Eve, and GS Rushbrooke. High-temperature expansions for the spin-$\frac{1}{2}$ heisenberg model. *Physical Review*, 164(2):800, 1967.

[79] C Fan and FY Wu. Ising model with second-neighbor interaction. i. some exact results and an approximate solution. *Physical Review*, 179(2):560, 1969.

[80] JN Reimers, JE Greedan, CV Stager, and R Kremer. Crystal structure and magnetism in $CoSb_2O_6$ and $CoTa_2O_6$. *Journal of Solid State Chemistry*, 83(1):20–30, 1989.

[81] RK Kremer and JE Greedan. Magnetic ordering in $CoTa_2O_6$ and $NiTa_2O_6$. *Journal of Solid State Chemistry*, 73(2):579–582, 1988.

[82] EJ Kinast, CA Dos Santos, D Schmitt, Olivier Isnard, MA Gusmao, and JBM da Cunha. Magnetic structure of the quasi-two-dimensional compound $CoTa_2O_6$. *Journal of Alloys and Compounds*, 491(1):41–44, 2010.

[83] M Saes, NP Raju, and JE Greedan. Structure and magnetism in $CrTa_2O_6$: A trirutile oxide based on Cr^{2+}. *Journal of Solid State Chemistry*, 140(1):7–13, 1998.

[84] D Prabhakaran, FR Wondre, and AT Boothroyd. Preparation of large single crystals of ANb_2O_6 (A= Ni, Co Fe, Mn) by the floating-zone method. *Journal of Crystal Growth*, 250(1):72–76, 2003.

[85] C Heid, H Weitzel, F Bourdarot, R Calemczuk, T Vogt, and H Fuess. Magnetism in and. *Journal of Physics: Condensed Matter*, 8(49):10609, 1996.

[86] I Yaeger, AH Morrish, BM Wanklyn, and BJ Garrard. Magnetization studies in transition-metal niobates. ii. $FeNb_2O_6$. *Physical Review B*, 16(5):2289, 1977.

[87] S Lei, C Wang, D Guo, X Gao, Di Cheng, J Zhou, B Cheng, and Y Xiao. Synthesis and magnetic properties of MNb_2O_6 (m= Fe, Co, Ni) nanoparticles. *RSC Advances*, 4(95):52740–52748, 2014.

[88] D Weitzel. Magnetische struktur von columbit, $FeNb_2O_6$. *Zeitschrift für Anorganische und Allgemeine Chemie*, 380(2):119–127, 1971.

[89] I Yaeger, AH Morrish, C Boumford, CP Wong, BM Wanklyn, and BJ Garrard. Low-temperature mössbauer studies of $FeNb_2O_6$. *Solid State Communications*, 28(8):651–653, 1978.

[90] T Hanawa, M Ishikawa, and K Miyatani. Disappearance of ferromagnetism at low temperatures in $CoNb_2O_6$. *Journal of the Physical Society of Japan*, 61(12):4287–4289, 1992.

[91] T Hanawa, K Shinkawa, M Ishikawa, K Miyatani, K Saito, and K Kohn. Anisotropic specific heat of $CoNb_2O_6$ in magnetic fields. *Journal of the Physical Society of Japan*, 63(7):2706–2715, 1994.

[92] W Scharf, H Weitzel, I Yaeger, I Maartense, and BM Wanklyn. Magnetic structures of $CoNb_2O_6$. *Journal of Magnetism and Magnetic Materials*, 13(1-2):121–124, 1979.

[93] C Heid, H Weitzel, P Burlet, M Bonnet, W Gonschorek, T Vogt, J Norwig, and H Fuess. Magnetic phase diagram of $CoNb_2O_6$: A neutron diffraction study. *Journal of Magnetism and Magnetic Materials*, 151(1-2):123–131, 1995.

[94] S Kobayashi, S Mitsuda, K Hosoya, H Yoshizawa, T Hanawa, M Ishikawa, K Miyatani, K Saito, and K Kohn. Competition between the inter-chain interaction and single-ion anisotropy in $CoNb_2O_6$. *Physica B: Condensed Matter*, 213:176–178, 1995.

[95] I Maartense, I Yaeger, and BM Wanklyn. Field-induced magnetic transitions of $CoNb_2O_6$ in the ordered state. *Solid State Communications*, 21(1):93–96, 1977.

[96] PWC Sarvezuk, EJ Kinast, CV Colin, MA Gusmao, JBM Da Cunha, and O Isnard. New investigation of the magnetic structure of $CoNb_2O_6$ columbite. *Journal of Applied Physics*, 109(7):07E160, 2011.

[97] S Mitsuda, K Hosoya, T Wada, H Yoshizawa, T Hanawa, M Ishikawa, K Miyatani, K Saito, and K Kohn. Magnetic ordering in one-dimensional system $CoNb_2O_6$ with competing interchain interactions. *Journal of the Physical Society of Japan*, 63(10):3568–3571, 1994.

[98] C Heid, H Weitzel, P Burlet, M Winkelmann, H Ehrenberg, and H Fuess. Magnetic phase diagrams of $CoNb_2O_6$. *Physica B: Condensed Matter*, 234:574–575, 1997.

[99] S Kobayashi, S Mitsuda, and K Prokes. Low-temperature magnetic phase transitions of the geometrically frustrated isosceles triangular ising antiferromagnet $CoNb_2O_6$. *Physical Review B*, 63(2):024415, 2000.

[100] SB Lee, RK Kaul, and L Balents. Interplay of quantum criticality and geometric frustration in columbite. *arXiv preprint arXiv:0911.0038*, 2009.

[101] AB Christian, CD Hunt, and JJ Neumeier. Local and long-range order and the influence of applied magnetic field on single-crystalline $NiSb_2O_6$. *Physical Review B*, 96(2):024433, 2017.

[102] H Ehrenberg, G Wltschek, J Rodiguez-Carvajal, and T Vogt. Magnetic structures of the tri-rutiles $NiTa_2O_6$ and $NiSb_2O_6$. *Journal of Magnetism and Magnetic Materials*, 184(1):111–115, 1998.

[103] J Kikuchi, K Ishiguchi, K Motoya, M Itoh, K Inari, N Eguchi, and J Akimitsu. Nmr and neutron scattering studies of quasi one-dimensional magnet CuV_2O_6. *Journal of the Physical Society of Japan*, 69(8):2660–2668, 2000.

[104] AN Vasil'ev, LA Ponomarenko, AI Smirnov, EV Antipov, Yu A Velikodny, M Isobe, and Y Ueda. Short-range and long-range magnetic ordering in α-CuV_2O_6. *Physical Review B*, 60(5):3021, 1999.

[105] AV Prokofiev, RK Kremer, and W Assmus. Crystal growth and magnetic properties of α-CuV_2O_6. *Journal of Crystal Growth*, 231(4):498–505, 2001.

[106] M Lenertz, J Alaria, D Stoeffler, S Colis, A Dinia, O Mentré, G André, F Porcher, and E Suard. Magnetic structure of ground and field-induced ordered states of low-dimensional α-CoV_2O_6: Experiment and theory. *Physical Review B*, 86(21):214428, 2012.

[107] Z He and W Cheng. Magnetic phase diagram of an ising spin-chain system α-CoV_2O_6 with $\frac{1}{3}$ magnetization plateau. *Journal of Magnetism and Magnetic Materials*, 362:27–30, 2014.

[108] X Yao. 1/3 magnetization plateau induced by magnetic field in monoclinic CoV_2O_6. *The Journal of Physical Chemistry A*, 116(9):2278–2282, 2012.

[109] M Markkula, AM Arévalo-López, and JP Attfield. Field-induced spin orders in monoclinic CoV_2O_6. *Physical Review B*, 86(13):134401, 2012.

[110] BE Warren. *X-ray Diffraction*. Courier Corporation, 1969.

[111] LD Whittig and WR Allardice. X-ray diffraction techniques. *Methods of Soil Analysis: Part 1—Physical and Mineralogical Methods*, (methodsofsoilan1):331–362, 1986.

[112] M Birkholz. Principles of x-ray diffraction. *Thin Film Analysis by X-Ray Scattering*, pages 1–40, 2006.

[113] WH Bragg and WL Bragg. The reflection of x-rays by crystals. *Proceedings of the Royal Society of London. Series A, Containing Papers of a Mathematical and Physical Character*, 88(605):428–438, 1913.

[114] M Von Laue. *Röntgenstrahl-interferenzen*, volume 6. Akad. VerlagGes., 1960.

[115] J Rodriguez-Carvajal. Fullprof: a program for rietveld refinement and pattern matching analysis. In *satellite meeting on powder diffraction of the XV congress of the IUCr*, volume 127. Toulouse, France:[sn], 1990.

[116] HM Rietveld. Line profiles of neutron powder-diffraction peaks for structure refinement. *Acta Crystallographica*, 22(1):151–152, 1967.

[117] HM Rietveld. A profile refinement method for nuclear and magnetic structures. *Journal of Applied Crystallography*, 2(2):65–71, 1969.

[118] PW Stephens. Phenomenological model of anisotropic peak broadening in powder diffraction. *Journal of Applied Crystallography*, 32(2):281–289, 1999.

[119] T Chatterji. *Neutron scattering from magnetic materials*. Gulf Professional Publishing, 2005.

[120] BTM Willis and CJ Carlile. *Experimental neutron scattering*. Oxford University Press, 2017.

[121] MO Jones, AD Taylor, and SF Parker. Neutron scattering studies of catalyst systems at the isis neutron spallation source. *Applied Petrochemical Research*, 2(3-4):97–104, 2012.

[122] Y Mnyukh. Second-order phase transitions, l. landau and his successors. *arXiv preprint arXiv:1102.1085*, 2011.

[123] AP Cracknell, J Lorenc, and JA Przystawa. Landau's theory of second-order phase transitions and its application to ferromagnetism. *Journal of Physics C: Solid State Physics*, 9(9):1731, 1976.

[124] DB Litvin. Magnetic space-group types. *Acta Crystallographica Section A: Foundations of Crystallography*, 57(6):729–730, 2001.

[125] CJ Bradley and BL Davies. Magnetic groups and their corepresentations. *Reviews of Modern Physics*, 40(2):359, 1968.

[126] P Baláž. High-energy milling. In *Mechanochemistry in Nanoscience and Minerals Engineering*, pages 103–132. Springer, 2008.

[127] D Shindo and T Oikawa. Energy dispersive x-ray spectroscopy. In *Analytical Electron Microscopy for Materials Science*, pages 81–102. Springer, 2002.

[128] J Goldstein, DE Newbury, P Echlin, DC Joy, AD Romig Jr, CE Lyman, C Fiori, and E Lifshin. *Scanning electron microscopy and X-ray microanalysis: a text for biologists, materials scientists, and geologists*. Springer Science & Business Media, 2012.

[129] H Fritzsche. A general expression for the thermoelectric power. *Solid State Communications*, 9(21):1813–1815, 1971.

[130] NF Mott and H Jones. *The theory of the properties of metals and alloys*. Courier Corporation, 1958.

[131] DA Greenwood. The boltzmann equation in the theory of electrical conduction in metals. *Proceedings of the Physical Society*, 71(4):585, 1958.

[132] GD Mahan. Good thermoelectrics. *Solid State Phys.*, 51:81–157, 1979.

[133] W Koshibae and S Maekawa. Effects of spin and orbital degeneracy on the thermopower of strongly correlated systems. *Physical Review Letters*, 87(23):236603, 2001.

[134] A Nag and V Shubha. Oxide thermoelectric materials: A structure–property relationship. *Journal of Electronic Materials*, 43(4):962–977, 2014.

[135] PM Chaikin and G Beni. Thermopower in the correlated hopping regime. *Physical Review B*, 13(2):647, 1976.

[136] JA Pople and DL Beveridge. Molecular orbital theory. *C0., NY*, 1970.

[137] LD Landau. Uber die bewegung der elektronen in kristalgitter. *Phys. Z. Sowjetunion*, 3:644–645, 1933.

[138] EM Conwell. Impurity band conduction in germanium and silicon. *Physical Review*, 103(1):51, 1956.

[139] NF Mott. Canad. *J: Phys*, 34:1356, 1956.

[140] A Miller and E Abrahams. Impurity conduction at low concentrations. *Physical Review*, 120(3):745, 1960.

[141] NF Mott. Conduction in non-crystalline materials: Iii. localized states in a pseudogap and near extremities of conduction and valence bands. *Philosophical Magazine*, 19(160):835–852, 1969.

[142] V Ambegaokar, BI Halperin, and JS Langer. Hopping conductivity in disordered systems. *Physical Review B*, 4(8):2612, 1971.

[143] M Pollak. A percolation treatment of dc hopping conduction. *Journal of Non-Crystalline Solids*, 8:486–491, 1972.

[144] VKS Shante and S Kirkpatrick. An introduction to percolation theory. *Advances in Physics*, 20(85):325–357, 1971.

[145] M Sahimi. *Applications of percolation theory*. CRC Press, 1994.

[146] JW Essam. Percolation theory. *Reports on Progress in Physics*, 43(7):833, 1980.

[147] BI Shklovskii and AL Efros. *Electronic properties of doped semiconductors*, volume 45. Springer Science & Business Media, 2013.

[148] N Apsley and HP Hughes. Temperature-and field-dependence of hopping conduction in disordered systems, ii. *Philosophical Magazine*, 31(6):1327–1339, 1975.

[149] N Apsley and HP Hughes. Temperature-and field-dependence of hopping conduction in disordered systems. *Philosophical Magazine*, 30(5):963–972, 1974.

[150] NF Mott. Electrons in disordered structures. *Advances in Physics*, 16(61):49–144, 1967.

[151] KD Schotte. The thermoelectric properties of the small polaron. *Zeitschrift für Physik A Hadrons and Nuclei*, 196(4):393–414, 1966.

[152] Y Yin, B Tudu, and A Tiwari. Recent advances in oxide thermoelectric materials and modules. *Vacuum*, 2017.

[153] GA Slack. Nonmetallic crystals with high thermal conductivity. *Journal of Physics and Chemistry of Solids*, 34(2):321–335, 1973.

[154] GA Slack. The thermal conductivity of nonmetallic crystals. *Solid State Physics*, 34:1–71, 1979.

[155] TM Tritt. *Thermal conductivity: theory, properties, and applications*. Springer Science & Business Media, 2005.

[156] DG Cahill, SK Watson, and RO Pohl. Lower limit to the thermal conductivity of disordered crystals. *Physical Review B*, 46(10):6131, 1992.

[157] V Murashov, MA White, and TM Tritt. Thermal conductivity: Theory, properties, and applications. 2004.

[158] SL Shindé and J Goela. *High thermal conductivity materials*, volume 91. Springer, 2006.

[159] A Einstein. Planck's theory of radiation and the theory of specific heat. *Ann. Phys*, 22:180–190, 1907.

[160] J Callaway. Model for lattice thermal conductivity at low temperatures. *Physical Review*, 113(4):1046, 1959.

[161] J Callaway and HC von Baeyer. Effect of point imperfections on lattice thermal conductivity. *Physical Review*, 120(4):1149, 1960.

[162] JS Dugdale and ZS Basinski. Mathiessen's rule and anisotropic relaxation times. *Physical Review*, 157(3):552, 1967.

[163] K Watari and SL Shinde. High thermal conductivity materials. *MRS Bulletin*, 26(6):440–444, 2001.

[164] AN Banerjee and KK Chattopadhyay. Recent developments in the emerging field of crystalline p-type transparent conducting oxide thin films. *Progress in Crystal Growth and Characterization of Materials*, 50(1):52–105, 2005.

[165] K Yanagawa, Y Ohki, T Omata, H Hosono, N Ueda, and H Kawazoe. Preparation of $Cd_{1-x}Y_xSb_2O_6$ thin film on glass substrate by radio frequency sputtering. *Applied Physics Letters*, 65(4):406–408, 1994.

[166] T Minami. New n-type transparent conducting oxides. *Mrs Bulletin*, 25(08):38–44, 2000.

[167] K Yanagawa, Y Ohki, N Ueda, T Omata, T Hashimoto, and H Kawazoe. New oxide phase $Cd_{1-x}Y_xSb_2O_6$ with a wide band gap and high electrical conductivity. *Applied Physics Letters*, 63(24):3335–3337, 1993.

[168] H Mizoguchi and PM Woodward. Electronic structure studies of main group oxides possessing edge-sharing octahedra: implications for the design of transparent conducting oxides. *Chemistry of materials*, 16(25):5233–5248, 2004.

[169] A Castro, I Rasines, MC Sanchez-Martos, and P Garcia-Casado. Refinement of structural parameters for polycrystalline $CdSb_2O_6$: A comparison of two methods. *Powder Diffraction*, 3(04):219–221, 1988.

[170] H Todokoro and M Ezumi. Scanning electron microscope, 1999. US Patent 5,872,358.

[171] J Singh, N Bhardwaj, and S Uma. Single step hydrothermal based synthesis of $m(ii)Sb_2O_6$ (m= Cd and Zn) type antimonates and their photocatalytic properties. *Bulletin of Materials Science*, 36(2):287–291, 2013.

[172] K Kurosaki, H Kobayashi, and S Yamanaka. Thermoelectric properties of ni-and zn-doped nd 2 cuo 4. *Journal of Alloys and Compounds*, 350(1):340–343, 2003.

[173] M Yan, M Lane, CR Kannewurf, and RPH Chang. Highly conductive epitaxial CdO thin films prepared by pulsed laser deposition. *Applied Physics Letters*, 78(16):2342–2344, 2001.

[174] MN Rahaman. *Sintering of ceramics*. CRC press, 2007.

[175] RL Coble and JE Burke. Sintering in ceramics. *Progress in ceramic science*, 3(199):24, 1963.

[176] A Magneli. The crystal structure of lead metantimonate and isomorphous compounds. *Arkiv for Kemi, Mineralogi O Geologi*, 1941.

[177] JL Hodeau, M Gondrand, M Labeau, and JC Joubert. Structure cristalline de WV_2O_6 sur monocristal à 298 et 383 k. *Acta Crystallographica Section B: Structural Crystallography and Crystal Chemistry*, 34(12):3543–3547, 1978.

[178] JC Bernier and P Poix. Structure of two trirutile oxides containing vanadium. In *Annales de Chimie France*, volume 3, page 119, 1968.

[179] P Schmidt, M Binnewies, R Glaum, and M Schmidt. Chemical vapor transport reactions–methods, materials, modeling. In *Advanced Topics on Crystal Growth*. InTech, 2013.

[180] M Binnewies, R Glaum, M Schmidt, and P Schmidt. Chemical vapor transport reactions–a historical review. *Zeitschrift für Anorganische und Allgemeine Chemie*, 639(2):219–229, 2013.

[181] D Fruchart, MC Montmory, EF Bertaut, and JC Bernier. Structures magnétiques de Mn_2TeO_6 et WV_2O_6. stabilité des modes magnétiques observés. *Journal de Physique*, 41(2):141–147, 1980.

[182] Mme MC Montmory, EF Bertaut, and P Mollard. Structure magnetique de WCr_2O_6. *Solid State Communications*, 4(5):249–253, 1966.

[183] Mme MC Montmory and R Newnham. Structures magnétiques des composes trirutiles $TeCr_2O_6$ et WCr_2O_6. *Solid State Communications*, 6(5):323–326, 1968.

[184] S Hansen, A Landa-Cánovas, K Ståhl, and J Nilsson. Cation ordering waves in trirutiles. when x-ray crystallography fails? *Acta Crystallographica Section A: Foundations of Crystallography*, 51(4):514–519, 1995.

[185] AD Becke. A new mixing of hartree–fock and local density-functional theories. *The Journal of Chemical Physics*, 98(2):1372–1377, 1993.

[186] W Setyawan and S Curtarolo. High-throughput electronic band structure calculations: Challenges and tools. *Computational Materials Science*, 49(2):299–312, 2010.

[187] J Singleton. *Band theory and electronic properties of solids*, volume 2. Oxford University Press, 2001.

[188] M Ohtaki, T Tsubota, K Eguchi, and H Arai. High-temperature thermoelectric properties of $(Zn_{1-x}Al_x)O$. *Journal of Applied Physics*, 79(3):1816–1818, 1996.

[189] D Feng and G Jin. *Introduction to condensed matter physics*, volume 1. World Scientific, 2005.

[190] SK Chatterjee. *Crystallography and the World of Symmetry*, volume 113. Springer Science & Business Media, 2008.

[191] M Eckert. Max von laue and the discovery of x-ray diffraction in 1912. *Annalen der Physik*, 524(5), 2012.

[192] AL Patterson. Homometric structures. *Nature*, 143(3631):939–940, 1939.

[193] AL Patterson. Ambiguities in the x-ray analysis of crystal structures. *Physical Review*, 65(5-6):195, 1944.

[194] JM Perez-Mato, FJ Zuniga, and G Madariaga. Methods of structural analysis of modulated structures and quasicrystals, 1991.

[195] JM Perez-Mato, D Orobengoa, and MI Aroyo. Mode crystallography of distorted structures. *Acta Crystallographica Section A: Foundations of Crystallography*, 66(5):558–590, 2010.

[196] AI Liechtenstein, MI Katsnelson, and VA Gubanov. Exchange interactions and spin-wave stiffness in ferromagnetic metals. *Journal of Physics F: Metal Physics*, 14(7):L125, 1984.

[197] I Turek, J Kudrnovskỳ, V Drchal, and P Bruno. Exchange interactions, spin waves, and transition temperatures in itinerant magnets. *Philosophical Magazine*, 86(12):1713–1752, 2006.

[198] J Rodríguez-Carvajal. Recent advances in magnetic structure determination by neutron powder diffraction. *Physica B: Condensed Matter*, 192(1-2):55–69, 1993.

[199] A Wills. Magnetic structures and their determination using group theory. *Le Journal de Physique IV*, 11(PR9):Pr9–133, 2001.

[200] HJ Goldsmid. Bismuth telluride and its alloys as materials for thermoelectric generation. *Materials*, 7(4):2577–2592, 2014.

[201] EF Bertaut. Representation analysis of magnetic structures. *Acta Crystallographica Section A: Crystal Physics, Diffraction, Theoretical and General Crystallography*, 24(1):217–231, 1968.

[202] MS Dresselhaus, G Dresselhaus, and A Jorio. *Group theory: application to the physics of condensed matter*. Springer Science & Business Media, 2007.

[203] W Fulton and J Harris. *Representation theory: a first course*, volume 129. Springer Science & Business Media, 2013.

[204] H Kamp and U Reyle. *From discourse to logic: Introduction to modeltheoretic semantics of natural language, formal logic and discourse representation theory*, volume 42. Springer Science & Business Media, 2013.

[205] Gregor Posnjak. Magnetic symmetry and determination of magnetic structures. 2012.

[206] Y Takahashi, J Akimoto, N Kijima, and Y Gotoh. Structure and electron density analysis of $Na_{0.74}CoO_2$ by single-crystal x-ray diffraction. *Solid State Ionics*, 172(1):505–508, 2004.

[207] P Yu and M Cardona. *Fundamentals of semiconductors: physics and materials properties*. Springer Science & Business Media, 2010.

[208] AS Wills. Indexing magnetic structures and crystallographic distortions from powder diffraction: Brillouin zone indexing. *arXiv preprint arXiv:0905.0873*, 2009.

[209] E Ressouche. Reminder: Magnetic structures description and determination by neutron diffraction. *École thématique de la Société Française de la Neutronique*, 13:02001, 2014.

[210] J Rodríguez-Carvajal and F Bourée. Symmetry and magnetic structures. In *EPJ Web of Conferences*, volume 22, page 00010. EDP Sciences, 2012.

[211] JO Dimmock. Use of symmetry in the determination of magnetic structures. *Physical Review*, 130(4):1337, 1963.

[212] International Union of Crystallography. *International tables for X-ray crystallography*, volume 2. Kynock Press, 1959.

[213] AM Zamorzaev. *Generalization of the space groups.* PhD thesis, Dissertation Leningrad Univ., 1953 (in Russian), 1953.

[214] NV Belov, NN Neronova, and TS Smirnova. Shubnikov groups. *Kristallografiya*, 2(3):315–325, 1957.

[215] BA Tavger and VM Zaitsev. Magnetic symmetry of crystals. *Soviet Physics JETP-USSR*, 3(3):430–436, 1956.

[216] SC Miller and WF Love. *Tables of irreducible representations of space groups and co-representations of magnetic space groups.* Pruett Press, 1967.

[217] DB Litvin. Tables of crystallographic properties of magnetic space groups. *Acta Crystallographica Section A: Foundations of Crystallography*, 64(3):419–424, 2008.

[218] W Opechowski and Rosalia Guccione. Magnetic symmetry. *Magnetism*, 2:105–165, 1965.

[219] J Zak. Magnetic translation group. ii. irreducible representations. *Physical Review*, 134(6A):A1607, 1964.

[220] JM Law, H-J Koo, M-H Whangbo, E Brücher, V Pomjakushin, and RK Kremer. Strongly correlated one-dimensional magnetic behavior of $NiTa_2O_6$. *Physical Review B*, 89(1):014423, 2014.

[221] D Khomskii. Trend: Classifying multiferroics: Mechanisms and effects. *Physics*, 2:20, 2009.

[222] DI Khomskii. Multiferroics: Different ways to combine magnetism and ferroelectricity. *Journal of Magnetism and Magnetic Materials*, 306(1):1–8, 2006.

[223] NA Spaldin and M Fiebig. The renaissance of magnetoelectric multiferroics. *Science*, 309(5733):391–392, 2005.

[224] S-W Cheong and M Mostovoy. Multiferroics: a magnetic twist for ferroelectricity. *Nature Materials*, 6(1):13, 2007.

[225] LD Landau and EM Lifshitz. Statistical physics. *Course of theoretical physics-Pergamon International Library of Science, Technology, Engineering and Social Studies, Oxford: Pergamon Press, and Reading: Addison-Wesley,— c1969, 2nd rev.-enlarg. ed.*, 1, 1969.

[226] K Ando, M Higuchi, J Takahashi, and K Kodaira. Floating zone growth and optical properties of nickel tantalum oxide single crystals. *Materials Research Bulletin*, 29(4):385–391, 1994.

[227] HP Beck, H Seup-Ra, R Haberkorn, H Kohlmann, M Eul, T Harmening, and R Pöttgen. A study on AB_2O_6 compounds: part i, synthesis, structure, magnetic properties and 151eu mössbauer spectroscopic data of $EuNb_2O_6$. *Zeitschrift für Anorganische und Allgemeine Chemie*, 636(6):1069–1073, 2010.

[228] HP Beck. A study on AB_2O_6 compounds, part v: a dft study on charge balance as driving force for structural organisation. *Zeitschrift für Kristallographie-Crystalline Materials*, 230(7):449–458, 2015.

[229] Edg Santos. *Theoretical and experimental study of the magnetic properties of transition-metal oxides of the type AB_2O_6.* PhD thesis, Université de Grenoble, 2012.

[230] F Emmenegger and A Petermann. Transport reactions and crystal growth of transition metal niobates. *Journal of Crystal Growth*, 2(1):33–39, 1968.

[231] R Borromei, G Ingletto, L Oleari, and P Day. Low-temperature absorption spectrum of the nickel (ii) ion in single crystals of the columbite $NiNb_2O_6$. *Journal of the Chemical Society, Faraday Transactions 2: Molecular and Chemical Physics*, 79(6):847–863, 1983.

[232] R Borromei, L Oleari, and P Day. Electronic spectrum of the manganate (v) ion in different host lattices. *Journal of the Chemical Society, Faraday Transactions 2: Molecular and Chemical Physics*, 77(9):1563–1578, 1981.

[233] E Prince and AJC Wilson. International tables for crystallography. 2004.

[234] P Weiss. L'hypothèse du champ moléculaire et la propriété ferromagnétique. *J. Phys. Theor. Appl.*, 6(1):661–690, 1907.

[235] L Néel. Antiferromagnetism and ferrimagnetism. *Proceedings of the Physical Society. Section A*, 65(11):869, 1952.

[236] SG Brush. History of the lenz-ising model. *Reviews of Modern Physics*, 39(4):883, 1967.

[237] BM McCoy and TT Wu. *The two-dimensional Ising model*. Courier Corporation, 2014.

[238] PW Anderson. New approach to the theory of superexchange interactions. *Physical Review*, 115(1):2, 1959.

[239] PW Anderson. Antiferromagnetism. theory of superexchange interaction. *Physical Review*, 79(2):350, 1950.

[240] JB Goodenough. Theory of the role of covalence in the perovskite-type manganites [La, m (ii)]MnO_3. *Physical Review*, 100(2):564, 1955.

[241] FA Cotton and JB Goodenough. Magnetism and the chemical bond. *Vol. I, Interscience—John Wiley, New York*, 1963.

[242] J Kanamori. Superexchange interaction and symmetry properties of electron orbitals. *Journal of Physics and Chemistry of Solids*, 10(2):87–98, 1959.

[243] MA Ruderman and C Kittel. Indirect exchange coupling of nuclear magnetic moments by conduction electrons. *Physical Review*, 96(1):99, 1954.

[244] K Yosida. Magnetic properties of Cu-Mn alloys. *Physical Review*, 106(5):893, 1957.

[245] I Dincer. Renewable energy and sustainable development: a crucial review. *Renewable and Sustainable Energy Reviews*, 4(2):157–175, 2000.

[246] HJ Goldsmid and RW Douglas. The use of semiconductors in thermoelectric refrigeration. *British Journal of Applied Physics*, 5(11):386, 1954.

[247] C Gayner and KK Kar. Recent advances in thermoelectric materials. *Progress in Materials Science*, 83:330–382, 2016.

[248] GD Mahan. Figure of merit for thermoelectrics. *Journal of Applied Physics*, 65(4):1578–1583, 1989.

[249] HJ Goldsmid. Electronic refrigeration (london: Pion limited, 1986). *Google Scholar*, pages 58–64.

[250] B Poudel, Q Hao, Y Ma, Y Lan, A Minnich, B Yu, X Yan, D Wang, A Muto, D Vashaee, et al. High-thermoelectric performance of nanostructured bismuth antimony telluride bulk alloys. *Science*, 320(5876):634–638, 2008.

[251] SK Yee, S LeBlanc, KE Goodson, and C Dames. per w metrics for thermoelectric power generation: beyond zt. *Energy & Environmental Science*, 6(9):2561–2571, 2013.

[252] HJ Schwartz and LI Shure. Survey of electric power plants for space applications. 1965.

[253] B Mazar. State of the art prototype vehicle with a thermoelectric generator. In *TE Application Workshop, Baltimore, March*, 2012.

[254] J He, Y Liu, and R Funahashi. Oxide thermoelectrics: The challenges, progress, and outlook. *Journal of Materials Research*, 26(15):1762–1772, 2011.

[255] X Zhang and LD Zhao. Thermoelectric materials: energy conversion between heat and electricity. *Journal of Materiomics*, 1(2):92–105, 2015.

[256] S Shamoto, Y Hasegawa, and T Kajitani. Two-dimensional sodium fluctuation at high temperatures in high-temperature thermoelectric material γ-$Na_{0.7}CoO_2$. *Japanese Journal of Applied Physics*, 45(8R):6395, 2006.

[257] N Li, Y Jiang, G Li, C Wang, J Shi, and D Yu. Self-ignition route to Ag-doped $Na_{1.7}Co_2O_4$ and its thermoelectric properties. *Journal of Alloys and Compounds*, 467(1):444–449, 2009.

[258] E Maeda and M Ohtak. Effect of preparation process on thermoelectric performance of $NaCo_2O_4$. *Transactions-Materials Research Society of Japan*, 25(1):237–240, 2000.

[259] M Mikami, N Ando, and R Funahashi. The effect of ag addition on electrical properties of the thermoelectric compound $Ca_3Co_4O_9$. *Journal of Solid State Chemistry*, 178(7):2186–2190, 2005.

[260] Y Liu, Y Lin, Z Shi, CW Nan, and Z Shen. Preparation of $Ca_3Co_4O_9$ and improvement of its thermoelectric properties by spark plasma sintering. *Journal of the American Ceramic Society*, 88(5):1337–1340, 2005.

[261] G Xu, R Funahashi, M Shikano, I Matsubara, and Y Zhou. Thermoelectric properties of the Bi-and Na-substituted $Ca_3Co_4O_9$ system. *Applied Physics Letters*, 80(20):3760–3762, 2002.

[262] S Li, R Funahashi, I Matsubara, K Ueno, S Sodeoka, and H Yamada. Synthesis and thermoelectric properties of the new oxide materials $Ca_{3-x}Bi_xCo_4O_9{}^+ \delta$ ($0.0< x < 0.75$). *Chemistry of Materials*, 12(8):2424–2427, 2000.

[263] P Zou, Z Li, and K Zhao. Preparation and electric property of $Bi_2Sr_2Co_2Oy$ thermoelectric ceramics [j]. *Development and Application of Materials*, 1:007, 2009.

[264] K Fujita, T Mochida, and K Nakamura. High-temperature thermoelectric properties of $NaxCoO_{2-\delta}$ single crystals. *Japanese Journal of Applied Physics*, 40(7R):4644, 2001.

[265] S Populoh, M Trottmann, MH Aguire, and A Weidenkaff. Nanostructured nb-substituted $CaMnO_3$ n-type thermoelectric material prepared in a continuous process by ultrasonic spray combustion. *Journal of Materials Research*, 26(15):1947–1952, 2011.

[266] A Weidenkaff, MH Aguirre, L Bocher, M Trottmann, P Tomes, and R Robert. Development of perovskite-type cobaltates and manganates for thermoelectric oxide modules. *Journal of the Korean Ceramic Society*, 47(1):47–53, 2010.

[267] P Tome, M Trottmann, C Suter, MH Aguirre, A Steinfeld, P Haueter, and A Weidenkaff. Thermoelectric oxide modules (toms) for the direct conversion of simulated solar radiation into electrical energy. *Materials*, 3(4):2801–2814, 2010.

[268] C Liu, F Ren, H Wang, ED Case, and DT Morelli. Solid-state synthesis and some properties of magnesium-doped copper aluminum oxides. *MRS Online Proceedings Library Archive*, 1218, 2009.

[269] S Yanagiya, N Van Nong, J Xu, and N Pryds. The effect of (Ag, Ni, Zn)-addition on the thermoelectric properties of copper aluminate. *Materials*, 3(1):318–328, 2010.

[270] Y Wang, Y Sui, X Wang, and W Su. Enhancement of thermoelectric efficiency in (Ca, Dy) MnO_3 - (Ca, Yb) MnO_3 solid solutions. *Applied Physics Letters*, 97(5):052109, 2010.

[271] A Kosuga, Y Isse, Y Wang, K Koumoto, and R Funahashi. High-temperature thermoelectric properties of $Ca_{0.9-x}Sr_xYb_{0.1}MnO_{3-\delta}$ ($0 \leq x \leq 0.2$). *Journal of Applied Physics*, 105(9):093717, 2009.

[272] KF Cai, E Muller, C Drasar, and A Mrotzek. Preparation and thermoelectric properties of Al-doped ZnO ceramics. *Materials Science and Engineering: B*, 104(1):45–48, 2003.

[273] H Colder, E Guilmeau, C Harnois, S Marinel, R Retoux, and E Savary. Preparation of Ni-doped ZnO ceramics for thermoelectric applications. *Journal of the European Ceramic Society*, 31(15):2957–2963, 2011.

[274] H Ohta, W-S Seo, and K Koumoto. Thermoelectric properties of homologous compounds in the ZnO-In_2O_3 system. *Journal of the American Ceramic Society*, 79(8):2193–2196, 1996.

[275] KH Kim, SH Shim, KB Shim, K Niihara, and J Hojo. Microstructural and thermoelectric characteristics of zinc oxide-based thermoelectric materials fabricated using a spark plasma sintering process. *Journal of the American Ceramic Society*, 88(3):628–632, 2005.

[276] K Park and JK Seong. Influence of simultaneous addition of Sb_2O_3 and SnO_2 on thermoelectric properties of $Zn_{1-x-y}Sb_xSn_yO$ prepared by tape casting. *Journal of Alloys and Compounds*, 464(1):1–5, 2008.

[277] H Muta, K Kurosaki, and S Yamanaka. Thermoelectric properties of reduced and la-doped single-crystalline SrTiO3. *Journal of Alloys and Compounds*, 392(1):306–309, 2005.

[278] J Liu, CL Wang, WB Su, HC Wang, P Zheng, JC Li, JL Zhang, and LM Mei. Enhancement of thermoelectric efficiency in oxygen-deficient $Sr_{1-x}La_xTiO_{3-\delta}$ ceramics. *Applied Physics Letters*, 95(16):162110, 2009.

[279] J Ravichandran, W Siemons, D-W Oh, JT Kardel, A Chari, H Heijmerikx, ML Scullin, A Majumdar, R Ramesh, and DG Cahill. High-temperature thermoelectric response of double-doped $SrTiO_3$ epitaxial films. *Physical Review B*, 82(16):165126, 2010.

[280] A Kikuchi, N Okinaka, and T Akiyama. A large thermoelectric figure of merit of La-doped $SrTiO_3$ prepared by combustion synthesis with post-spark plasma sintering. *Scripta Materialia*, 63(4):407–410, 2010.

[281] P-P Shang, B-P Zhang, J-F Li, and N Ma. Effect of sintering temperature on thermoelectric properties of La-doped $SrTiO_3$ ceramics prepared by sol–gel process and spark plasma sintering. *Solid State Sciences*, 12(8):1341–1346, 2010.

[282] H Muta, K Kurosaki, and S Yamanaka. Thermoelectric properties of rare earth doped $SrTiO_3$. *Journal of Alloys and Compounds*, 350(1):292–295, 2003.

[283] SC Tarantino, M Zema, M Pistorino, and MC Domeneghetti. High-temperature x-ray investigation of natural columbites. *Physics and Chemistry of Minerals*, 30(10):590–598, 2003.

[284] RWG Wyckoff. Fluorite structure. *Interscience Publishers, New York, NY, Crystal Structures*, 1:239, 1963.

[285] A Palenzona. Rosiaite, $PbSb_2O_6$, new mineral from the cetine mine, siena, italy. *Eur. J. Mineral*, 8:487–492, 1996.

[286] U Müller. *Symmetriebeziehungen zwischen verwandten Kristallstrukturen: Anwendungen der kristallographischen Gruppentheorie in der Kristallchemie; unter Verwendung von Textvorlagen von Hans Wondratschek und Hartmut Bärnighausen*. Vieweg+ Teubner ko* 5109279, 2012.

[287] U Müller. Setting up trees of group–subgroup relations, 2005.

[288] MA White and G Neshvad. The heat capacities of the tantalates MTa_2O_6, M= Mg, Fe, Co, Ni. *The Journal of Chemical Thermodynamics*, 23(5):455–460, 1991.

[289] ES Kim and CJ Jeon. Crystal structure and microwave dielectric properties of $ATiO_3$, ATa_2O_6, AWO_4 (A= Ni, Mg, Co) ceramics. In *Applications of Ferroelectrics, 2009. ISAF 2009. 18th IEEE International Symposium on the*, pages 1–6. IEEE, 2009.

[290] JP Hague, EML Chung, D Visser, G Balakrishnan, E Clementyev, D McK Paul, and MR Lees. Spin wave dispersion and magnons from short range order in tapiolite ($FeTa_2O_6$); a quasi-two-dimensional antiferromagnet. *Journal of Physics: Condensed Matter*, 17(46):7227, 2005.

[291] Y Mnyukh. Lambda-and schottky-anomalies in solid-state phase transitions. *arXiv preprint arXiv:1104.4637*, 2011.

[292] ME Fisher. Relation between the specific heat and susceptibility of an antiferromagnet. *Philosophical Magazine*, 7(82):1731–1743, 1962.

[293] ME Fisher. The theory of equilibrium critical phenomena. *Reports on progress in physics*, 30(2):615, 1967.

[294] T Nagamiya. Helical spin ordering—1 theory of helical spin configurations. *Solid State Physics*, 20:305–411, 1968.

[295] RC Pullar. The synthesis, properties, and applications of columbite niobates ($M^{2+}Nb_2O_6$): a critical review. *Journal of the American Ceramic Society*, 92(3):563–577, 2009.

[296] I Tanaka, R Inoue, H Kojima, and R Oyamada. Single crystal growth of tantalite ((Fe, Mn)(Ta, $Nb)_2o_6$) solid solutions. *Journal of Crystal Growth*, 91(1-2):141–146, 1988.

[297] IS Mulla, N Natarajan, AB Gaikwad, V Samuel, UN Guptha, and V Ravi. A coprecipitation technique to prepare $CoTa_2O_6$ and $CoNb_2O_6$. *Materials Letters*, 61(11):2127–2129, 2007.

[298] M Greenblatt, BM Wanklyn, and BJ Garrard. Flux growth of MNb_2O_6 (M= Mg, Zn, Ba) single crystals. *Journal of Crystal Growth*, 58(2):463–466, 1982.

[299] H Weitzel. Magnetische strukturen von $NiNb_2O_6$ und Fe_2WO_6. *Acta Crystallographica Section A: Crystal Physics, Diffraction, Theoretical and General Crystallography*, 32(4):592–597, 1976.

[300] H-J Lee, I-T Kim, and KS Hong. Dielectric properties of AB_2O_6 compounds at microwave frequencies (a= Ca, Mg, Mn, Co, Ni, Zn, and b= Nb, Ta). *Japanese Journal of Applied Physics*, 36(10A):L1318, 1997.

[301] RC Pullar, JD Breeze, and NMcN Alford. Characterization and microwave dielectric properties of $M^{2+}Nb_2O_6$ ceramics. *Journal of the American Ceramic Society*, 88(9):2466–2471, 2005.

[302] PWC Sarvezuk, MA Gusmão, JBM Da Cunha, and O Isnard. Magnetic behavior of the $Ni_xFe_{1-x}Nb_2O_6$ quasi-one-dimensional system: Isolation of ising chains by frustration. *Physical Review B*, 86(5):054435, 2012.

[303] H Weitzel and S Klein. Magnetische struktur von columbiten $MnTa_2O_6$ und $CoNb_2O_6$. *Solid State Communications*, 12(2):113–116, 1973.

[304] S Kobayashi, S Mitsuda, T Jogetsu, J Miyamoto, H Katagiri, and K Kohn. Anisotropic growth kinetics in the geometrically frustrated isosceles triangular ising antiferromagnet $CoNb_2O_6$. *Physical Review B*, 60(14):R9908, 1999.

[305] AM Nakua and JE Greedan. Single crystal growth of transition metal antimonates AB_2O_6 from V_2O_5-B_2O_3 fluxes. *Journal of Crystal Growth*, 154(3-4):334–338, 1995.

[306] S Shimada, K Kodaira, and T Matsushita. Crystal growth of $CuSb_2O_6$ by flux method. *Journal of Crystal Growth*, 72(3):753–755, 1985.

[307] A Nakua, H Yun, JN Reimers, JE Greedan, and CV Stager. Crystal structure, short range and long range magnetic ordering in $CuSb_2O_6$. *Journal of Solid State Chemistry*, 91(1):105–112, 1991.

[308] H-B Kanga CD Lingb and T Söhnela. Exploring the structural and magnetic phase transition of $Cu_{1-x}Co_xSb_2O_6$.

[309] AB Christian, A Rebello, MG Smith, and JJ Neumeier. Local and long-range magnetic order of the spin- $\frac{3}{2}$ system $CoSb_2O_6$. *Physical Review B*, 92(17):174425, 2015.

[310] K Mocala and A Navrotsky. Energetics of brannerite-type solid solutions: The systems ZnV_2O_6-$LiMoVO_6$ and MgV_2O_6-$LiMoVO_6$. *Journal of Solid State Chemistry*, 73(1):224–234, 1988.

[311] K Mocała and J Ziółkowski. Polymorphism of the bivalent metal vanadates MeV_2O_6 (Me= Mg, Ca, Mn, Co, Ni, Cu, Zn, Cd). *Journal of Solid State Chemistry*, 69(2):299–311, 1987.

[312] S Gupta, YP Yadava, and RA Singh. Electrical transport properties of polycrystalline nickel vanadate. *Zeitschrift für Physik B Condensed Matter*, 74(2):221–226, 1989.

[313] Z He, J-I Yamaura, Y Ueda, and W Cheng. CoV_2O_6 single crystals grown in a closed crucible: unusual magnetic behaviors with large anisotropy and 1/3 magnetization plateau. *Journal of the American Chemical Society*, 131(22):7554–7555, 2009.

[314] M Lenertz, A Dinia, S Colis, O Mentré, G André, F Porcher, and E Suard. Magnetic structure of ground and field induced ordered states of low-dimensional γ-CoV_2O_6. *The Journal of Physical Chemistry C*, 118(25):13981–13987, 2014.

[315] SAJ Kimber, DN Argyriou, and JP Attfield. Metamagnetism and 1/3 plateau in the spin chain compound CoV_2O_6. *arXiv preprint arXiv:0804.2966*, 2008.

[316] SAJ Kimber, H Mutka, T Chatterji, T Hofmann, PF Henry, HN Bordallo, DN Argyriou, and J P Attfield. Metamagnetism and soliton excitations in the modulated ferromagnetic ising chain CoV_2O_6. *Physical Review B*, 84(10):104425, 2011.

[317] Z Lenarčič. Magnetic groups.

[318] K Momma and F Izumi. Vesta 3 for three-dimensional visualization of crystal, volumetric and morphology data. *Journal of Applied Crystallography*, 44(6):1272–1276, 2011.

[319] V Petricek, M Dusek, and L Palatinus. Jana 2006 software, 2006.

[320] J Rossat-Mignod. 19. magnetic structures. *Methods in Experimental Physics*, 23:69–157, 1987.

[321] AS Wills. A new protocol for the determination of magnetic structures using simulated annealing and representational analysis (sarah). *Physica B: Condensed Matter*, 276:680–681, 2000.

[322] SM Eicher. *Quasi two-dimensional magnetic properties of the tri-rutile phases MTa_2O_6, M= V, Fe, Co,Ni.* PhD thesis, 1985.

[323] P. Massard, J.C. Bernier, and A. Michel. Structure cristalline et proprietes de l'oxyde $CrTa_2O_6$. *Annales de Chimie (Paris) (Vol=Year)*, 1971:41–52, 1971.

[324] HT Stokes and DM Hatch. *Isotropy subgroups of the 230 crystallographic space groups*. World Scientific, 1988.

[325] R Borromei, E Cavalli, and L Oleari. The electronic spectrum of $NiTa_2O_6$. *Inorganica Chimica Acta*, 204(2):159–170, 1993.

[326] JM Law, H Benner, and RK Kremer. Padé approximations for the magnetic susceptibilities of heisenberg antiferromagnetic spin chains for various spin values. *Journal of Physics: Condensed Matter*, 25(6):065601, 2013.

[327] PD Olmsted. Lectures on landau theory of phase transitions. *University of Leeds, Department of Physics and Astronomy*, 2000.

[328] J Humphreys. *Introduction to Lie algebras and representation theory*, volume 9. Springer Science & Business Media, 2012.

[329] BH Grier, JM Lawrence, V Murgai, and RD Parks. Magnetic ordering in CeM_2Si_2 (m= Ag, Au, Pd, Rh) compounds as studied by neutron diffraction. *Physical Review B*, 29(5):2664, 1984.

[330] JN Franklin. Ambiguities in the x-ray analysis of crystal structures. *Acta Crystallographica Section A: Crystal Physics, Diffraction, Theoretical and General Crystallography*, 30(6):698–702, 1974.

[331] RL Withers, S Schmid, and JG Thompson. A composite modulated structure approach to the lanthanide oxide fluoride, uranium nitride fluoride and zirconium nitride fluoride solid-solution fields. *Acta Crystallographica Section B: Structural Science*, 49(6):941–951, 1993.

[332] Y-H Chu, LW Martin, MB Holcomb, and R Ramesh. Controlling magnetism with multiferroics. *Materials Today*, 10(10):16–23, 2007.

[333] AV Shubnikov. Symmetry and antisymmetry of finite figures. *USSR Academy of Sciences, Moscow*, 1951.

[334] R Mirman. *Point groups, space groups, crystals, molecules*. World Scientific Publishing Co Inc, 1999.

[335] AS Wills. A historical introduction to the symmetries of magnetic structures. part 1. early quantum theory, neutron powder diffraction and the coloured space groups. *Powder Diffraction*, pages 1–8, 2017.

[336] V Kopskỳ. Crystallography and magnetic phenomena. *Symmetry*, 7(1):125–145, 2015.

[337] C Bradley and A Cracknell. *The mathematical theory of symmetry in solids: representation theory for point groups and space groups*. Oxford University Press, 2010.

[338] F Von Laves, G Bayer, and A Panagos. Structural relation between α-PbO_2, $FeWO_4$ (wolframite), and $FeNb_2O_6$ (columbite) and the polymorphism of $FeNbO_4$. *Schweiz. Mineral. Petrog. Mitt*, 43:217–234, 1963.

[339] O Khamman, R Yimnirun, Y Laosiritaworn, and S Ananta. Preparation and characterization of nickel niobate ($NiNb_2O_6$) nanopowders. *Editorial Policy*, page 35.

[340] R Wichmann and Hk Müller-Buschbaum. Synthese und untersuchung von $NiNb_2O_6$-einkristallen mit columbit-und rutilstruktur. *Zeitschrift für anorganische und allgemeine Chemie*, 503(8):101–105, 1983.

[341] I Yaeger, AH Morrish, and BM Wanklyn. Magnetization studies in transition-metal niobates: I. $NiNb_2O_6$. *Physical Review B*, 15(3):1465, 1977.

[342] TJS Munsie, A Millington, PA Dube, HA Dabkowska, J Britten, GM Luke, and JE Greedan. Crystal growth and magnetic characterization of a tetragonal polymorph of $NiNb_2O_6$. *Journal of Solid State Chemistry*, 236:19–23, 2016.

[343] R Pynn. Neutron scattering—a non-destructive microscope for seeing inside matter. In *Neutron Applications in Earth, Energy and Environmental Sciences*, pages 15–36. Springer, 2009.

[344] W Schweika. Polarized neutron scattering. *Neutron Scattering*.

[345] F Mezei. La nouvelle vague in polarized neutron scattering. *Physica B+ C*, 137(1-3):295–308, 1986.

[346] RM Moon, T Riste, and WC Koehler. Polarization analysis of thermal-neutron scattering. *Physical Review*, 181(2):920, 1969.

[347] S Kobayashi, S Mitsuda, M Ishikawa, K Miyatani, and K Kohn. Three-dimensional magnetic ordering in the quasi-one-dimensional ising magnet $CoNb_2O_6$ with partially released geometrical frustration. *Physical Review B*, 60(5):3331, 1999.

[348] T Hanawa, M Ishikawa, and K Miyatani. Disappearance of ferromagnetism at low temperatures in $CoNb_2O_6$. *Journal of the Physical Society of Japan*, 61(12):4287–4289, 1992.

[349] A Hubert and R Schäfer. *Magnetic domains: the analysis of magnetic microstructures*. Springer Science & Business Media, 2008.

[350] LM Holmes, AA Ballman, and RR Hecker. Antiferromagnetic ordering in $MnNb_2O_5$ studied by magnetoelectric and magnetic susceptibility measurements. *Solid State Communications*, 11(3):409–413, 1972.

[351] A Le Bail. Whole powder pattern decomposition methods and applications: A retrospection. *Powder Diffraction*, 20(04):316–326, 2005.

[352] A Altomare, MC Burla, M Camalli, GL Cascarano, C Giacovazzo, A Guagliardi, AGG Moliterni, G Polidori, and R Spagna. Sir97: a new tool for crystal structure determination and refinement. *Journal of Applied Crystallography*, 32(1):115–119, 1999.

[353] HJ Zeiger and GW Pratt. Magnetic interactions in solids. 1973.

[354] RJ Glauber. Time-dependent statistics of the ising model. *Journal of Mathematical Physics*, 4(2):294–307, 1963.

[355] T-D Lee and C-N Yang. Statistical theory of equations of state and phase transitions. ii. lattice gas and ising model. *Physical Review*, 87(3):410, 1952.

[356] T Kasuya. A theory of metallic ferro-and antiferromagnetism on zener's model. *Progress of Theoretical Physics*, 16(1):45–57, 1956.

[357] SC Dixon, DO Scanlon, CJ Carmalt, and IP Parkin. n-type doped transparent conducting binary oxides: an overview. *Journal of Materials Chemistry C*, 4(29):6946–6961, 2016.

[358] E Fortunato, D Ginley, H Hosono, and DC Paine. Transparent conducting oxides for photovoltaics. *MRS bulletin*, 32(03):242–247, 2007.

[359] FU Hamelmann. *Transparent conductive oxides in thin film photovoltaics*, volume 559. 2014.

[360] K Ellmer. Past achievements and future challenges in the development of optically transparent electrodes. *Nature Photonics*, 6(12):809–817, 2012.

[361] KL Chopra, S Major, and DK Pandya. Transparent conductors—a status review. *Thin Solid Films*, 102(1):1–46, 1983.

[362] T Tsubota, M Ohtaki, K Eguchi, and H Arai. Transport properties and thermoelectric performance of $(Zn_{1-y}Mg_y)_{1-x}Al_xO$. *Journal of Materials Chemistry*, 8(2):409–412, 1998.

[363] OK Andersen, Z Pawlowska, and O Jepsen. Illustration of the linear-muffin-tin-orbital tight-binding representation: Compact orbitals and charge density in si. *Physical Review B*, 34(8):5253, 1986.

[364] LB Borovkova, ES Lukin, DN Poluboyarinov, and EB Sapozhnikova. Sintering and properties of yttrium oxide ceramics. *Tractories and Industrial Ceramics*, 11(11):717–722, 1970.

[365] X Zhang, H Li, and J Wang. Effect of sintering temperature on thermoelectric properties of CdO ceramics. *Journal of Advanced Ceramics*, 4(3):226, 2015.

[366] RM German. Sintering theory and practice. *Solar-Terrestrial Physics (Solnechno-zemnaya fizika)*, page 568, 1996.

[367] DC Joy. *Scanning electron microscopy*. Wiley Online Library, 2006.

[368] SW Hughes. Measuring liquid density using archimedes' principle. *Physics Education*, 41(5):445, 2006.

[369] Y Tokura and N Nagaosa. Orbital physics in transition-metal oxides. *science*, 288(5465):462–468, 2000.

[370] N Tsuda, K Nasu, A Fujimori, and K Siratori. *Electronic conduction in oxides*, volume 94. Springer Science & Business Media, 2013.

[371] M Cutler and NF Mott. Observation of anderson localization in an electron gas. *Physical Review*, 181(3):1336, 1969.

[372] L Onsager. Reciprocal relations in irreversible processes. i. *Physical Review*, 37(4):405, 1931.

[373] L Onsager. Reciprocal relations in irreversible processes. ii. *Physical Review*, 38(12):2265, 1931.

[374] I Terasaki. High-temperature oxide thermoelectrics. *Journal of Applied Physics*, 110(5):053705, 2011.

[375] G Ren, J Lan, C Zeng, Y Liu, B Zhan, S Butt, Y-H Lin, and C-W Nan. High performance oxides-based thermoelectric materials. *JOM*, 67(1):211–221, 2015.

[376] SI Pekar. Investigations in the electron theory of crystals. *Gostekhizdat, Moscow*, 1951.

[377] M Jaime, HT Hardner, MB Salamon, M Rubinstein, P Dorsey, and D Emin. Hall-effect sign anomaly and small-polaron conduction in $(La_{1-x}Gd_x)_{0.67}Ca_{0.33}MnO_3$. *Physical Review Letters*, 78(5):951, 1997.

[378] JR Sootsman, DY Chung, and MG Kanatzidis. New and old concepts in thermoelectric materials. *Angewandte Chemie International Edition*, 48(46):8616–8639, 2009.

[379] EF Bertaut and N Vannhung. Structures magnétiques de vanadite monocalcique CaV_2O_4. *Comptes Rendus Hebdomadaires des Seances de l'Academie des Sciences Serie B*, 264(20):1416, 1967.

[380] PG Klemens. Thermal conductivity and lattice vibrational modes. *Solid State Physics*, 7:1–98, 1958.

[381] HS Lee. *Thermoelectrics: Design and Materials*. John Wiley & Sons, 2016.

[382] BI Shklovskii and AL Efros. Variable-range hopping conduction. In *Electronic Properties of Doped Semiconductors*, pages 202–227. Springer, 1984.

[383] J-H Park and TS Sudarshan. *Chemical vapor deposition*, volume 2. ASM international, 2001.

[384] J Benesty, J Chen, Y Huang, and I Cohen. Pearson correlation coefficient. In *Noise reduction in speech processing*, pages 1–4. Springer, 2009.

[385] K Hamrin, C Nordling, and L Kihlborg. Esca studies of oxidation states in W–V–O phases. *Ann. Acad. Regieae Sci., Upsala*, 14:1–7, 1970.

[386] PY Yu et al. Electronic band structures. In *Fundamentals of Semiconductors*, pages 13–98. Springer, 1996.

[387] NW Ashcroft and ND Mermin. Solid state physics (holt, rinehart and winston, new york, 1976). *Google Scholar*, 403, 2005.